

**Transition metal nitrides, nitridometalates and  
carbodiimides, as well as strontium acetonitriletriides:  
Chemical, structural and physical characteristics**

Von der Fakultät Chemie  
der Universität Stuttgart zur Erlangung der Würde eines

DOKTORS DER NATURWISSENSCHAFTEN

– Dr. rer. nat. –

genehmigte Abhandlung

Vorgelegt von

William P. Clark

aus Derby, Großbritannien

Hauptberichter:	Prof. Dr. Rainer Niewa
Mitberichter:	Prof. Dr. Hans-Joachim Massonne
Prüfungsvorsitzender:	Prof. Dr. Thomas Schleid

Tag der mündlichen Prüfung: 07.06.2019

Institut für Anorganische Chemie der Universität Stuttgart  
2019



“A straight line may be the shortest distance between two points,  
but it is by no means the most interesting.”

-The Doctor, *Doctor Who*



# Contents

<b>Abstract.....</b>	<b>I</b>
<b>Zusammenfassung.....</b>	<b>V</b>
<b>1. Introduction .....</b>	<b>1</b>
<b>2. Experimental methods .....</b>	<b>7</b>
2.1. Chemicals used .....	7
2.2. Glove box.....	8
2.3. Arc furnace .....	9
2.4. High temperature apparatus .....	9
2.4.1. Tube furnace .....	9
2.4.2. Ammonia flow furnace .....	11
2.5. Crystal growth with ampoules .....	12
2.6. Methods of high pressure and temperature synthesis .....	14
2.6.1. Diamond anvil cell .....	14
2.6.2. Voggenreiter press with a Walker-type Multi-anvil module .....	16
<b>3. Analytical techniques .....</b>	<b>19</b>
3.1. Structural characterisation by X-ray diffraction .....	19
3.1.1. Generation and properties of X-rays .....	19
3.1.2. Diffraction of X-rays.....	21
3.1.3. Single crystal X-ray diffraction.....	23
3.1.4. Powder X-ray diffraction .....	27
3.2. Magnetism and magnetic measurements .....	29
3.2.1. Overview .....	29
3.2.2. Curie-Weiss Law.....	30
3.3. Raman spectroscopy .....	32
3.4. Mössbauer Spectroscopy .....	33
3.5. Elemental Analysis .....	34
3.5.1. Energy dispersive X-ray analysis.....	34

3.5.2.	Wavelength dispersive X-ray spectroscopy .....	34
3.6.	Thermal Analysis .....	35
3.6.1.	Differential Thermal Analysis .....	35
3.6.2.	Differential Scanning Calorimetry .....	35
<b>4.</b>	<b>High pressure synthesis of iron containing nitrides .....</b>	<b>37</b>
4.1.	Overview of iron nitrides .....	37
4.2.	Synthesis and characterisation of NiAs-type FeN .....	39
4.2.1.	Introduction .....	39
4.2.2.	Synthesis of NiAs-type FeN .....	42
4.2.3.	Characterisation .....	43
4.2.3.1.	Structure determination of NiAs-type FeN .....	43
4.2.3.2.	Crystal structure .....	46
4.2.3.3.	Mössbauer Spectroscopy .....	48
4.2.3.4.	Electronic structure calculations .....	50
4.2.4.	Summary .....	52
4.3.	High pressure synthesis and characterisation of $\epsilon$ -Fe <sub>2</sub> MnN .....	53
4.3.1.	Introduction .....	53
4.3.2.	Synthesis .....	54
4.3.3.	Characterisation .....	55
4.3.3.1.	Structure determination and crystal structure of $\epsilon$ -Fe <sub>2</sub> MnN .....	55
4.3.3.2.	Energy dispersive X-ray analysis .....	58
4.3.3.3.	Magnetic susceptibility .....	59
4.3.3.4.	Differential thermal analysis and thermogravimetry .....	61
4.3.3.5.	Microhardness .....	62
4.3.4.	Summary .....	63
<b>5.</b>	<b>Transition metal nitridometalates containing infinite linear chains .....</b>	<b>65</b>
5.1.	Overview of nitridometalates .....	65
5.2.	Synthesis and characterisation of SrLi <sub>2</sub> {Li[CoN <sub>2</sub> ] } .....	66
5.2.1.	Introduction .....	66
5.2.2.	Synthesis .....	67
5.2.3.	Characterisation .....	68
5.2.3.1.	Structure Determination .....	68

5.2.3.2. Crystal Structure.....	78
5.2.4. Magnetic Susceptibility.....	80
5.2.5. Summary .....	82
5.3. Synthesis and characterisation of $\text{Sr}_2[(\text{Li}_{1-x}\text{Ni}_x)\text{Ni}_2\text{N}_2]$ .....	83
5.3.1. Introduction.....	83
5.3.2. Synthesis .....	84
5.3.3. Characterisation .....	85
5.3.3.1. Structure determination and crystal structure of $\text{Sr}_2[(\text{Li}_{1-x}\text{Ni}_x)\text{Ni}_2\text{N}_2]$ .....	85
5.3.3.2. Energy dispersive spectroscopy .....	93
5.3.4. Discussion and conclusion .....	95
<b>6. Synthesis and characterisation of <math>\text{Sr}_6\text{N}[\text{CuN}_2][\text{CN}_2]_2</math>.....</b>	<b>99</b>
6.1. Overview.....	99
6.2. Synthesis.....	102
6.3. Structure determination and characterisation of $\text{Sr}_6\text{N}[\text{CuN}_2][\text{CN}_2]_2$ .....	103
6.3.1. Structure Determination.....	103
6.3.2. Magnetic susceptibility .....	109
6.3.3. Raman spectroscopy .....	110
6.4. Discussion and conclusion.....	112
<b>7. Synthesis and characterisation of strontium acetonitriletrides .....</b>	<b>117</b>
7.1. Introduction.....	117
7.2. Synthesis and characterisation of $\text{Sr}_4\text{N}[\text{C}_2\text{N}][\text{CN}_2]$ .....	119
7.2.1. Synthesis .....	119
7.2.2. Structure determination and characterisation.....	119
7.2.3. Raman spectroscopy .....	124
7.3. Structure determination and crystal structure of $\text{Sr}_3[\text{C}_2\text{N}]_2$ .....	127
7.3.1. Synthesis .....	127
7.3.2. Structure determination and characterisation.....	127
7.3.3. Raman Spectroscopy.....	132
7.3.4. Energy dispersive spectroscopy .....	133
7.4. Discussion and Conclusion.....	134

<b>8. Substitution and property investigations of lead germanates .....</b>	<b>137</b>
8.1. Overview.....	137
8.2. Synthesis and characterisation of $Pb_{5-x}Ba_xGe_3O_{11}$ .....	141
8.2.1. Introduction.....	141
8.2.2. Synthesis of $Pb_{5-x}Ba_xGe_3O_{11}$ .....	142
8.2.3. Characterisation .....	142
8.2.3.1. Structure determination and crystal structure of $Pb_{5-x}Ba_xGe_3O_{11}$ .....	142
8.2.3.2. Energy dispersive spectroscopy .....	148
8.2.3.3. Differential scanning calorimetry.....	148
8.2.4. Discussion and conclusion .....	150
8.3. Synthesis and characterisation of $Pb_5Ge_{3-x}Si_xO_{11}$ .....	152
8.3.1. Introduction.....	152
8.3.2. Synthesis of $Pb_5Ge_{3-x}Si_xO_{11}$ .....	153
8.3.3. Characterisation .....	153
8.3.3.1. Structure determination and crystal structure of $Pb_5Ge_{3-x}Si_xO_{11}$ .....	153
8.3.3.2. Wavelength dispersive spectroscopy.....	160
8.3.3.3. Differential scanning calorimetry.....	161
8.3.4. Discussion and conclusion .....	162
8.4. Synthesis and characterisation of $Pb_{3-x}Ba_x[Ge_2O_7]$ .....	165
8.4.1. Introduction.....	165
8.4.2. Synthesis of $Pb_{3-x}Ba_x[Ge_2O_7]$ .....	166
8.4.3. Characterisation .....	166
8.4.3.1. Structure determination and crystal structure of $Pb_{3-x}Ba_x[Ge_2O_7]$ .....	166
8.4.3.2. Energy Dispersive Spectroscopy .....	173
8.4.3.3. Differential scanning calorimetry.....	174
8.4.4. Discussion and conclusion .....	176
<b>9. Summary &amp; outlook.....</b>	<b>179</b>
<b>References.....</b>	<b>181</b>
<b>Appendix.....</b>	<b>195</b>



## **Foreword & Declaration of Authorship**

The experimental work presented in this doctoral thesis was conducted between November 2014 and January 2019 at the Institute of Inorganic Chemistry at the University of Stuttgart under the supervision of Prof. Rainer Niewa.

I certify that the doctoral thesis entitled “Transition metal nitrides, nitridometalates and carbodiimides, as well as strontium acetonitriletriides: Chemical, structural and physical characteristics.” is entirely my own work, unless otherwise indicated. All passages and ideas obtained from other sources have been clearly indicated.

## **Vorwort & Eigenständigkeitserklärung**

Die experimentellen Arbeiten und die Auswertungen zur vorliegenden Doktorarbeit wurden im Zeitraum zwischen November 2014 und Januar 2019 am Institut für Anorganische Chemie der Universität Stuttgart unter Prof. Dr. Rainer Niewa durchgeführt.

Ich versichere, dass ich die vorliegende Doktorarbeit mit dem Titel „Transition metal nitrides, nitridometalates and carbodiimides, as well as strontium acetonitriletriides: Chemical, structural and physical characteristics.“ selbständig verfasst und keine anderen als angegebenen Quellen und Hilfsmittel benutzt habe. Aus fremden Quellen entnommene Passagen und Gedanken sind als solche kenntlich gemacht.



## Acknowledgments

I would first like to thank my supervisor, Prof. Rainer Niewa, for the opportunity for me to join his research group and contribute in the field of nitride chemistry, as well as for his mentoring and guidance during the past few years, which has made me grow and learn so much as a chemist.

Secondly, my thanks go to Prof. Hans-Joachim Massonne for taking the time to be my secondary examiner and Prof. Thomas Schleid for taking on the role of “Prüfungsausschussvorsitz”.

The research presented here would not have been possible if it were not for the numerous collaboration partners that have contributed their ideas and expertise during this research. I want to thank each of them for their contributions, especially Priv. -Doz. Dr. Ulrich Schwarz, Dr. Peter Höhn and Dr. Denis Vinnik.

My thanks go out to Dr. Sabine Strobel, Dr. Falk Lissner and Priv. -Doz. Dr. Ingo Hartenbach for the measuring of single crystal samples with X-ray diffraction. For elemental analysis I want to thank Tanja Lehmann M. Sc., Felix Goerigk M. Sc., Manuel Häßner M. Sc. and Christian Bäucker M. Sc. My appreciation goes to Dr. Björn Blaschkowski and Manuel Häßner M. Sc. for magnetic susceptibility measurements and their patience with uncooperative samples. For Raman spectroscopy measurements, I would like to thank Dipl. -Chem. Adrian Geyer and Kevin Bareiß M. Sc. Finally, I would like to thank both Christof Schneck and Christian Funk M. Sc. for conducting thermal analysis investigations of particular samples.

Overall, I would like to thank everyone I have gotten to know in AK Niewa, AK Schleid, AK Gudat and AK Kaim for the friendly working environment and memorable events. In addition, I want to thank Dipl. -Chem. Dominik Stoiber for helping to make our shared office a relaxed working environment and for the interesting scientific discussions.

I want to express a special thank you to Dr. Sabine Strobel for all of her time and patience with the numerous crystallographic issues that presented themselves during this work. Another special thanks goes to Tanja Haag for taking the time to help with the German translation of the abstract.

Finally, my heartfelt thanks and gratitude goes to my parents and Nana, who helped shape me to be the person I am and have constantly supported me in everything I have chosen to do, and also to my partner Damla for her love and support during everything and for changing my life.



## Abstract

The scope of this doctoral thesis involves the development and characterisation of novel binary and higher nitrides, with a focus on exploring the chemistry of late 3d transition metal nitrides. These investigations naturally lead to the discovery and characterisation of new nitridometalate compounds and later the production of compounds with the exotic C and N containing anion  $[\text{C}_2\text{N}]^{3-}$ .

Currently, there is a large interest in the development of new nitride containing compounds. A large number of binary nitrides are used for their electrical conductivity, semiconducting, insulating and superconducting properties, as well as their catalytic activity, corrosion resistance, magnetic properties and hardness. The more complex nitridometalate compounds have shown potential applications as anode materials in batteries, electrocatalysts and data storage materials. Exotic C and N containing compounds, such as carbodiimides, have also shown corrosion resistance, as well as other potential applications like photovoltaic cells, light emitting diodes, magnetic materials and sources of fluorescent light.

Through high pressure experiments, the successful syntheses of the novel NiAs-type FeN and  $\varepsilon$ -Fe<sub>2</sub>MnN were made. The NiAs-type FeN was successfully produced, using diamond anvil cells, from both  $\zeta$ -Fe<sub>2</sub>N and elemental Fe, with N<sub>2</sub> used in both as a pressure medium and reactant. This metastable phase was observed only upon heating to 1300 K above 10 GPa and was still present at ambient pressure and temperature, however it slowly changed to ZnS-type FeN. Mössbauer spectroscopy showed that the material has magnetic ordering and this magnetism is stable up to at least 45 GPa.

A high pressure and temperature reaction, using a 10 T press with a Walker-type Multi-anvil module, of  $\zeta$ -Fe<sub>2</sub>N and elemental Mn produced the phase  $\varepsilon$ -Fe<sub>2</sub>MnN, which was confirmed by powder X-ray diffraction to crystallise isostructural to  $\varepsilon$ -Fe<sub>3</sub>N<sub>1±x</sub> and the substituted phases  $\varepsilon$ -Fe<sub>2</sub>MN<sub>x</sub> ( $M = \text{Co}, \text{Ni}$  and  $\text{Ir}$ ). Physical property investigations showed the material to be a soft ferromagnet, which undergoes exothermic decomposition above 900 K to a *fcc*-(Fe,Mn):N phase. Microhardness measurements showed the hardness of  $\varepsilon$ -Fe<sub>2</sub>MnN fits within the range of tool steels and nitrogen hardened steels.

The nitridonickelate series  $\text{Sr}_2[(\text{Li}_{1-x}\text{Ni}_x)\text{Ni}_2\text{N}_2]$  ( $0 \leq x \leq 1$ ) was prepared, using various crystal growing techniques involving metal ampoules. These samples crystallise isostructural to the previously known  $\text{Ba}_2[\text{Ni}_3\text{N}_2]$  and  $\text{Ba}_2[(\text{Ni}_{0.57}\text{Li}_{0.43})\text{Ni}_2\text{N}_2]$ . Each sample produced had crystals measured using energy dispersive spectroscopy to determine the Ni content. Each crystal had several measurements conducted across its surface, which showed a variation in Ni content along the crystal. Since the powder diffraction pattern of every sample did not contain elemental Ni, it was concluded to be caused by a composition gradient within the crystal. To achieve charge balance in this series, either two oxidation states of Ni are needed, Ni(0) and Ni(I), or intermediate valence is present. While magnetic susceptibility measurements were not possible, it is expected to exhibit similar paramagnetic properties as  $\text{Ba}_2[\text{Ni}_3\text{N}_2]$ , with antiferromagnetic exchange interactions dominating.

Employing a crystal growing technique, which involved the heating and controlled cooling of metal ampoules filled with reactants and an alkali metal flux, allowed the production of several new compounds. One of particular interest is the nitridometalate  $\text{SrLi}_2\{\text{Li}[\text{CoN}_2]\}$ , which after analysis of single crystal X-ray diffraction data showed to crystallise in the monoclinic space group  $P2_1/c$  and gave evidence of ordering along the linear infinite chains of  ${}^1_{\infty}[(\text{Li},\text{Co})\text{N}_{2/2}^-]$ . Magnetic susceptibility investigations showed the Co cations to exist as high spin Co(I) cations, which exhibit paramagnetism.

Introduction of C, as a reagent, to this crystal growing technique produced several compounds with anions containing C and N. The fairly well known  $[\text{CN}_2]^{2-}$  anions were observed in the first nitridocuprate carbodiimide compound  $\text{Sr}_6\text{N}[\text{CuN}_2][\text{CN}_2]$ , which exhibited diamagnetic behaviour. When compared with the structurally similar Co containing variant, a very subtle difference in the orientation of the  $[\text{CN}_2]^{2-}$  anions was observed. The more rare and exotic  $[\text{C}_2\text{N}]^{3-}$  anion, which has very seldom been reported, was also observed on two occasions, one in the mixed anion compound  $\text{Sr}_4\text{N}[\text{CN}_2][\text{C}_2\text{N}]$  and the other in  $\text{Sr}_3[\text{C}_2\text{N}]_2$ , the first quasi-binary acetonitriletriide.

Parallel to the main themes of this doctoral work, samples of lead germanate,  $\text{Pb}_5\text{Ge}_3\text{O}_{11}$ , were substituted with either Ba on the Pb position or Si on the Ge position and the effects these substitutions had on the structural and physical properties were investigated. All of the samples crystallised in the low temperature phase, with the space group  $P3$  (No. 143), and were characterised by both single crystal and powder X-ray diffraction. The introduction of Ba into the

system,  $\text{Pb}_{5-x}\text{Ba}_x\text{Ge}_3\text{O}_{11}$ , lead to a general increase of the unit cell parameters, with increasing Ba content. Energy dispersive spectroscopy was used to determine the Pb and Ba content and the obtained values fitted well with the expected values from the ratio of reactants. Investigations into the substituted series,  $\text{Pb}_5\text{Ge}_{3-x}\text{Si}_x\text{O}_{11}$ , showed that with increasing Si content the unit cell parameters decreased and Si had a distinct preference to occupy the isolated  $\text{GeO}_4$  tetrahedra. Wavelength dispersive spectroscopy was conducted on single crystals to determine the extent of Si substitution and lead to the conclusion that a composition gradient was present in each crystal. The average of these values fitted well with what was expected from the ratios of reactants used. The phase transition temperature of each sample was found to be unaffected by the degree of substitution for both the Ba and Si substituted phases.

Through these investigations, a new substituted phase was found,  $\text{Pb}_{3-x}\text{Ba}_x[\text{Ge}_2\text{O}_7]$ . This phase crystallises in the Barysilite structure, which consists of corner sharing tetrahedra,  $[\text{Ge}_2\text{O}_7]$ , and Pb cations, which build up a structure containing channels. Other, crystallographically different, Pb cations are located within the channels of this structure. The Ba cations were found to substitute solely on the Pb positions found along these channels. The degree of substitution was determined by energy dispersive spectroscopy, by measuring along the crystal, and a composition gradient was observed. This resulted in a variation of Ba content for crystals  $\text{Pb}_{3-x}\text{Ba}_x[\text{Ge}_2\text{O}_7]$  ( $0.019 \leq x \leq 0.28$ ), with the average composition fitting well with what was expected from the ratios of the reactants used.





## Zusammenfassung

Diese Arbeit befasst sich mit der Entwicklung und Charakterisierung neuer binärer und höhere Nitride, insbesondere mit der Chemie der späten  $3d$ -Übergangsmetallnitride. Die Untersuchungen führten zur Entdeckung und Charakterisierung neuer Nitridometallat-Verbindungen und später zur Herstellung von Verbindungen mit dem exotischen C und N haltigen Anion  $[C_2N]^{3-}$ .

Aufgrund ihrer elektrischen Leitfähigkeit und deren Eigenschaft als Halbleiter, Isolator und Supraleiter sind viele binäre Nitride momentan von großem Interesse. Außerdem sind sie für ihre katalytische Aktivität, Korrosionsbeständigkeit, magnetische Eigenschaften und Härte bekannt. Die komplexeren Nitridometallat-Verbindungen zeigten potentielle Anwendung als Anodenmaterial in Batterien, Elektrokatalysatoren und Speichermedien. Exotische Verbindungen, die C- und N-Komponenten beinhalten, wie beispielweise Carbodiimide zeigten ebenfalls Korrosionsbeständigkeit sowie andere potentielle Anwendungsbereiche in Photovoltaikzellen, LEDs, magnetischen Materialien und fluoreszierenden Lichtquellen.

Durch Hochdruckexperimente konnte eine neue FeN-Modifikation im NiAs-Strukturtyp und  $\varepsilon$ -Fe<sub>2</sub>MnN erfolgreich synthetisiert werden. Die FeN-Modifikation im NiAs-Strukturtyp wurde durch die Verwendung von Diamantstempelzellen aus  $\zeta$ -Fe<sub>2</sub>N sowie elementarem Fe erfolgreich hergestellt, jeweils mit N<sub>2</sub> fungierend als Reaktant und druckübertragendes Medium. Diese metastabile Phase konnte erst bei einer Temperatur von 1300 K und einem Druck von über 10 GPa beobachtet werden und war dann noch bei Zimmertemperatur und Normaldruck vorhanden, veränderte sich allerdings langsam zur FeN-Modifikation im ZnS-Typ. Mössbauer-Spektroskopie zeigte, dass die Verbindung eine magnetische Ordnung besitzt und dieser Magnetismus bis mindestens 45 GPa beständig bleibt.

Eine Hochdruck- und Hochtemperaturreaktion, bei der eine 10 T Presse mit einem mit  $\zeta$ -Fe<sub>2</sub>N und elementarem Mn gefüllten Walker Multi-Stempelmodul verwendet wurde, lieferte die Phase  $\varepsilon$ -Fe<sub>2</sub>MnN, welche durch röntgenographische Pulverdiffraktometrie-Messungen als isostrukturell zu  $\varepsilon$ -Fe<sub>3</sub>N<sub>1±x</sub> und der substituierten Phase  $\varepsilon$ -Fe<sub>2</sub>MN<sub>x</sub> ( $M = \text{Co, Ni und Ir}$ ) bestimmt wurde. Untersuchungen der physikalischen Eigenschaften zeigten schwachen Ferromagnetismus. Bei Temperaturen über 900 K zersetzt sich das Material exotherm in eine  $fcc$ -(Fe,Mn):N-Phase. Mikrohärt-Messungen zeigten, dass die Härte von  $\varepsilon$ -Fe<sub>2</sub>MnN im Bereich von Werkzeugstahl und stickstoff-gehärtetem Stahl liegt.

Die Nitridonickelat-Verbindungen der Zusammensetzung  $\text{Sr}_2[(\text{Li}_{1-x}\text{Ni}_x)\text{Ni}_2\text{N}_2]$  ( $0 \leq x \leq 1$ ) wurden mithilfe von verschiedenen Kristallwachstumstechniken in unterschiedlichen Metallampullen hergestellt. Die Ansätze kristallisieren isostrukturell zu den bereits bekannten Verbindungen  $\text{Ba}_2[\text{Ni}_3\text{N}_2]$  und  $\text{Ba}_2[(\text{Ni}_{0.57}\text{Li}_{0.43})\text{Ni}_2\text{N}_2]$ . Kristalle aus allen Ansätzen wurden mithilfe von energiedispersiver Röntgenspektroskopie auf ihren Ni-Gehalt untersucht. An der Oberfläche jedes Kristalles wurden mehrere Messungen durchgeführt, welche unterschiedliche Werte für den Ni-Gehalt innerhalb eines Kristalles lieferten. Da die Pulverdiffraktogramme aller Ansätze kein elementares Ni aufwiesen, wurde angenommen, dass ein Zusammensetzungsgradient vorhanden ist. Um die Ladungsneutralität der Verbindungen zu erreichen, muss Ni entweder in den Oxidationsstufen 0 und +1 vorliegen oder eine intermediäre Valenz vorhanden sein. Messungen der magnetischen Suszeptibilität waren nicht möglich, dennoch ist zu erwarten, dass die Verbindungen ähnliche paramagnetische Eigenschaften wie  $\text{Ba}_2[\text{Ni}_3\text{N}_2]$  aufweist, wobei anti-ferromagnetischen Austauschinteraktionen dominieren.

Durch die Anwendung einer Kristallwachstumstechnik, die ein Erhitzen und kontrolliertes Abkühlen von mit Reaktanten und einem Alkalimetall als Flussmittel gefüllten Metallampullen erfordern, war die Herstellung vieler neuer Verbindungen möglich. Ein Nitridometallat von großen Interesse ist  $\text{SrLi}_2\{\text{Li}[\text{CoN}_2]\}$ , welches in der monoklinen Raumgruppe  $P2_1/c$  mit linear unendlichen Ketten entlang  $\frac{1}{\infty}[(\text{Li},\text{Co})\text{N}_{2/2}^{2-}]$  kristallisiert. Untersuchungen der magnetischen Suszeptibilität zeigten, dass die Co-Kationen als high-spin Co(I)-Kationen vorliegen und somit Paramagnetismus aufweisen.

Durch den Einsatz von C als Reaktant in dieser Kristallwachstumstechnik war es möglich einige Verbindungen mit Anionen, die C und N enthalten, herzustellen. Das sehr bekannte  $[\text{CN}_2]^{2-}$ -Anion konnte in der ersten Nitridocuprat-Carbodiimid-Verbindung  $\text{Sr}_6\text{N}[\text{CuN}_2][\text{CN}_2]$  beobachtet werden und weist diamagnetisches Verhalten auf. Im Vergleich zum strukturähnlichen Co-Derivat weisen die  $[\text{CN}_2]^{2-}$ -Anionen eine unterschiedliche Orientierung auf. Das selten dokumentierte und exotische  $[\text{C}_2\text{N}]^{3-}$ -Anion konnte in zwei Fällen beobachtet werden. Zum einen in der Verbindung  $\text{Sr}_4\text{N}[\text{CN}_2][\text{C}_2\text{N}]$  mit gemischten Anionen und zum anderen in der Verbindung  $\text{Sr}_3[\text{C}_2\text{N}]_2$ , dem ersten quasi-binären Acetontriltriid.

Parallel zu den Hauptthemen dieser Doktorarbeit wurde im Blei-Germanat der Zusammensetzung  $\text{Pb}_5\text{Ge}_3\text{O}_{11}$  entweder die Pb-Position mit Ba oder die Ge-Position mit Si substituiert und die Effekte auf die strukturellen und physikalischen Eigenschaften untersucht. Alle Ansätze kristallisierten in der Tieftemperaturphase mit der Raumgruppe  $P3$  (Nr. 143) und wurden mithilfe von Einkristall- und Pulverdiffraktometrie charakterisiert. Das Einführen von Ba in das System  $\text{Pb}_{5-x}\text{Ba}_x\text{Ge}_3\text{O}_{11}$  führte zur Vergrößerung der Zellparameter proportional zum Ba-Gehalt. Mithilfe von energiedispersiver Röntgenspektroskopie-Messungen wurden der Pb- und Ba-Gehalt bestimmt, wobei die erhaltenen Werte gut mit den erwarteten Werten bezüglich des Verhältnisses der Reaktanten übereinstimmten. Untersuchungen der substituierten Verbindungen  $\text{Pb}_5\text{Ge}_{3-x}\text{Si}_x\text{O}_{11}$  zeigten, dass die Zellparameter mit steigendem Si-Gehalt sanken und Si bevorzugt die isolierten  $\text{GeO}_4$ -Tetraeder besetzte. Mithilfe von wellenlängendispersiver Röntgenspektroskopie wurde an den Einkristallen der Grad der Si-Substitution bestimmt, was zu der Annahme führte, dass ein Kompositionsgradient in jedem Einkristall vorhanden ist. Die durchschnittlichen Werte stimmten gut mit den erwarteten Werten bezüglich den verwendeten Reaktantenverhältnisse überein. Die Temperatur des Phasenübergangs der Ansätze war unabhängig vom Substitutionsgrad der Si- und Ba-substituierten Phasen.

Durch diese Untersuchungen wurde die neue substituierte Phase  $\text{Pb}_{3-x}\text{Ba}_x[\text{Ge}_2\text{O}_7]$  entdeckt. Diese Phase kristallisiert in der Barysilit-Struktur, welche aus einem Gerüst aus eckenverbundenen  $[\text{Ge}_2\text{O}_7]$ -Tetraedern und Pb-Kationen besteht und zusätzlich kristallographisch unterschiedliche Pb-Kationen enthält, die in den Tunneln des Gerüsts lokalisiert sind. Die Ba-Kationen substituieren ausschließlich die Pb-Positionen entlang der Tunnel. Der Substitutionsgrad wurde mithilfe von energiedispersiver Röntgenspektroskopie-Messungen bestimmt. Außerdem konnte im Rahmen dieser Messungen entlang eines Kristalls ein Kompositionsgradient beobachtet werden. Daraus folgte eine Variation des Ba-Gehalts in den Kristallen  $\text{Pb}_{3-x}\text{Ba}_x[\text{Ge}_2\text{O}_7]$  ( $0.019 \leq x \leq 0.28$ ). Die durchschnittliche Zusammensetzung stimmte gut mit den erwarteten Werten bezüglich der verwendeten Reaktantenverhältnissen überein.



## 1. Introduction

Molecular nitrogen,  $N_2$ , is the most abundant gas in the earth's atmosphere, ca. 78 %, followed by molecular oxygen,  $O_2$ , ca. 21%. However, regardless of this abundance, reported compounds containing oxide anions,  $O^{2-}$ , outnumber those containing nitride anions,  $N^{3-}$ , by a substantial amount. This is due to the high dissociation energy of  $N_2$  (945 kJ/mol) and unfavourable electron affinity  $E_{ea}(N \rightarrow N^{3-}) = +2300$  kJ/mol, which are both considerably higher than those of  $O_2$  (498 kJ/mol and  $E_{ea}(O \rightarrow O^{2-}) = +844$  kJ/mol).<sup>[1,2]</sup> Overcoming this boundary typically involves reactions at high temperatures without the presence of  $O_2$  and moisture, due to nitrides often having a lower thermodynamic stability than oxides. The affinity of most elements towards O is larger than that of N, which results in there generally being higher bond energies between an element and O (i. e.  $E(\text{Si-O}) = 444$  kJ/mol and  $E(\text{P-O}) = 407$  kJ/mol), than for the corresponding nitrides (i. e.  $E(\text{Si-N}) = 335$  kJ/mol and  $E(\text{P-N}) = 290$  kJ/mol).<sup>[3]</sup> This affinity is the reason why many nitrides are very sensitive towards air and moisture, especially at elevated temperatures.

The extensive interest in nitride compounds is due to their outstanding physical properties and industrial applications. A large amount of nitrides are used for their exceptional hardness and corrosion resistance, such as  $MN$  ( $M = \text{B, Ti, V, Cr, Zr}$  and  $\text{Ta}$ ),<sup>[4-7]</sup>  $\text{Si}_3\text{N}_4$ ,<sup>[3]</sup>  $\gamma\text{-Fe}_4\text{N}$  and  $\epsilon\text{-Fe}_3\text{N}_{1+x}$ .<sup>[8]</sup> The, perhaps, most well-known example of these is BN, which exists in either a cubic, hexagonal or wurzite form and is isoelectronic to C. The cubic phase is isostructural with diamond and exhibits the same structural and physical properties as the C variant. The hexagonal form is colourless and an electrical insulator, but shares the same-layered hexagonal sheets as graphite, which is black and an excellent electrical conductor.<sup>[4,9]</sup> Another non-metal nitride of note is  $\text{Si}_3\text{N}_4$ , which exists in  $\alpha$ -,  $\beta$ - and  $\gamma$ -phases.<sup>[3,10]</sup> These phases have high wear resistance and the  $\alpha$ - and  $\beta$ -phases are used in ceramic components for turbochargers and turbines.<sup>[3]</sup> Electronic conductive properties are something which varies a great deal in nitride chemistry, with some being good electronic conductors (TiN),<sup>[5]</sup> superconductors, with a Curie temperature of up to 30 K for binary nitrides (NbN, MoN and HfN),<sup>[11]</sup> semiconductors ( $\text{Cu}_3\text{N}$ ,  $\text{Zn}_3\text{N}_2$ , GaN and InN)<sup>[12-14]</sup> and electronic insulators (AlN).<sup>[15]</sup> Although there have not been many examples so far, there are some binary nitrides which can function as catalysts, such as  $\text{Ta}_3\text{N}_5$ , which is used as a catalyst for water splitting.<sup>[16]</sup>

For anions containing purely N atoms, the simplest one is the previously mentioned nitride anion, which consists of one trivalent anion of nitrogen. Oligonitride anions are also known, which differ greatly in complexity (*Figure 1.1.*). These oligonitride anions can vary from the simple dumbbell anions, such as diazenide and pernitride, to the 3 atom containing azide anion, to the poly[tetraz-1-ene-1,4-diyl] anion and to the aromatic pentazole anion. Compounds containing oligonitride anions exhibit a wide variety of interesting properties, such as high energy density (e.g.  $\text{LiN}_3$  and  $\text{NaN}_3$ )<sup>[17]</sup> and high hardness (e.g.  $\text{TiN}_2$ ).<sup>[18]</sup>

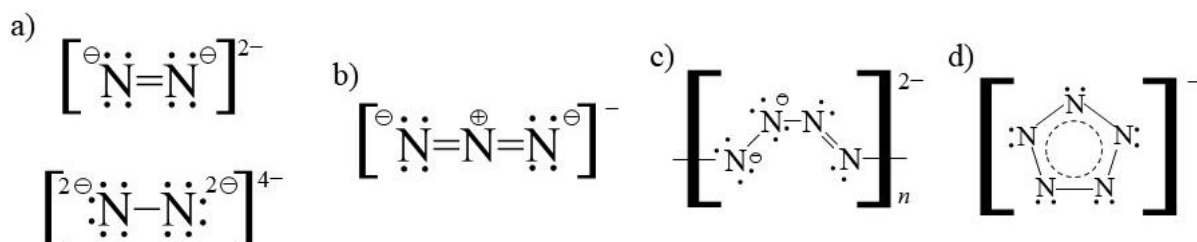


Figure 1.1. Lewis structure of oligonitride anions: a) diazenide (top) and pernitride (bottom); b) azide; c) poly[tetraz-1-ene-1,4-diyl]; d) pentazole.

Binary nitrides show a wide range of compositions, as well as properties and bonding behaviour, which can range from metallic and ionic through to covalent bonding. This wide range of compositions comes from the extremely varied oxidation states of the transition metals found in binary nitrides, all of which require high temperature synthesis conditions and in some cases high pressure as well. These oxidation states can vary from +1 up to +5, which is the highest seen so far for these compounds. A trend is seen for when ionic or covalent bonding dominates. The covalent bonds between a nitride anion and non-metal cation are typically quite strong, which results in compounds with high stability such as BN and  $\text{Si}_3\text{N}_4$ . In the binary 1:1 transition metal nitrides the highest thermodynamic stability is seen for nitrides with elements from groups 4 and 5. In 1:1 metal nitrides, those with a metal from group 3 exhibit more ionic bonding, via metallic phases, whereas covalent bonding is seen to be dominant in binary nitrides containing a group 1 transition metal (i. e.  $\text{Cu}_3\text{N}$ ).<sup>[19]</sup>

Most binary nitrides adopt basic structural prototypes. For transition metal nitrides the  $\text{N}^{3-}$  anions are typically found six fold coordinated by  $M^{n+}$  cations as either octahedra or trigonal prisms. These tend to build up close-packed layers, which can stack in various ways to produce the basic structural prototypes, such as NaCl-type and NiAs-type (*Figure 1.2.*). With metal rich nitrides,  $M_x\text{N}$  ( $x \geq 2$ ), the N atoms occupy the vacancies of a metal *fcc*, *hcp* or *bcc* type packing, such as compounds of Fe, Co and Ni in the  $\gamma'$ - $M_4\text{N}$ ,  $\varepsilon$ - $M_3\text{N}$  and  $\zeta$ - $M_2\text{N}$  type phases.

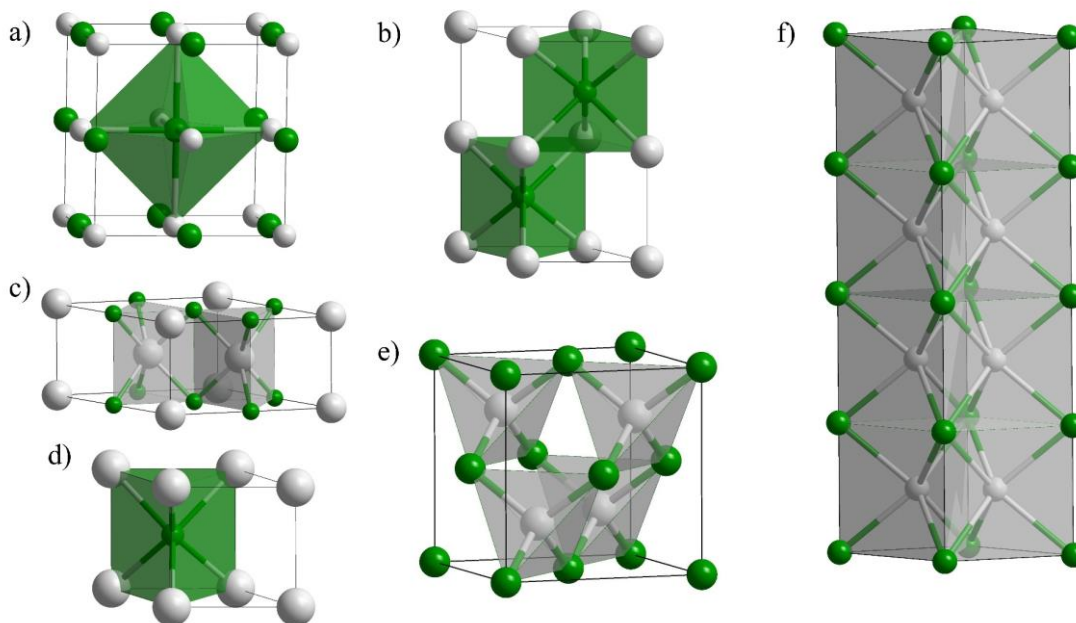


Figure 1.2. Common structure prototypes for binary 1:1 nitrides: a) CrN (NaCl-type);<sup>[5]</sup> b) FeN (NiAs-type); c) TaN (CoSn-type);<sup>[7]</sup> d) WN (WC-type);<sup>[20]</sup> e) *c*-BN (Shalerite-type);<sup>[21]</sup> f)  $\varepsilon$ -NbN (distorted WC-type).<sup>[22]</sup> (*M* is shown in grey and N is shown in green).

The pernitride anion,  $\text{N}_2^{4-}$ , is isoelectronic with both the peroxide anion,  $\text{O}_2^{2-}$ , and molecular fluorine, with both N atoms being connected by one strong covalent N–N single bond. Due to their large range of surprising properties, such as superconductivity, photoluminescence, magnetism and low compressibility,<sup>[23–30]</sup> pernitride compounds have seen a lot of attention in recent years, with a wide range of transition metal pernitrides already being known,  $M\text{N}_2$  ( $M = \text{Ti}, \text{Fe}, \text{Co}, \text{Ru}, \text{Rh}, \text{Pd}, \text{Re}, \text{Os}, \text{Ir}$  and  $\text{Pt}$ ).<sup>[18,25,28,31–35]</sup> All of these compounds require both high temperature and high pressure to allow the formation of the pernitride anion. This is typically achieved using either a multi-anvil press or diamond anvil cells. These pernitride compounds have been seen to adopt either a pyrite- ( $M = \text{Pd}$  and  $\text{Pt}$ ), baddeleyite- ( $M = \text{Ir}$ ), marcasite- ( $M = \text{Fe}, \text{Co}, \text{Ru}, \text{Rh}$  and  $\text{Os}$ ) or  $\text{Al}_2\text{Cu}$ - ( $M = \text{Ti}$ ) type structure (*Figure 1.3.*). Even though several structure types are known for pernitrides, they can all be described as being comprised of  $M\text{N}_6$  octahedra, which are interconnected in all three dimensions by the single N–N bonds.

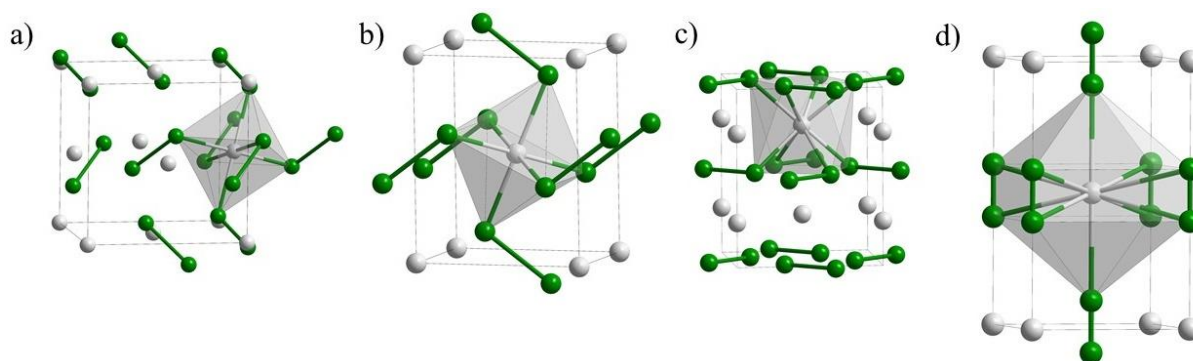


Figure 1.3. Common structures for pernitrides and diazenides: a) Pyrite; b) Marcasite; c)  $\text{Al}_2\text{Cu}$ ; d)  $\text{CaC}_2$  ( $M$  is shown in grey and  $N$  is shown in green).

For cations that cannot have an oxidation state larger than +2, the diazenide compound is formed. The diazenide anion,  $\text{N}_2^{2-}$ , is isoelectronic with molecular oxygen and have been produced for  $M\text{N}_2$  ( $M = \text{Ca} - \text{Ba}$ ),<sup>[36]</sup>  $\text{Li}_2\text{N}_2$ <sup>[37]</sup> and  $\text{Li}_2\text{Ca}_3[\text{N}_2]_3$ ,<sup>[38]</sup> with the latter compound being a metallic diazenide with delocalised electrons to achieve charge balance. Synthesis of these compounds also relies on high temperature and pressure, just like the pernitride compounds. So far, these compounds have been seen to adopt either a tetragonally distorted NaCl-type structure ( $M = \text{Ca}$ ,  $\text{Sr}$  and  $\text{Ba}$ ),<sup>[39]</sup> completely new structure types ( $M = \text{Li}$  and  $\text{Cu}$ )<sup>[40,41]</sup> or a Notwotny phase ( $\text{Li}_2\text{Ca}_3[\text{N}_2]_3$ ).<sup>[38]</sup> A similar coordination tendency for  $M\text{N}_6$  octahedra is also observed for the diazenide compounds.

The azide anion,  $\text{N}_3^-$ , is a linear three atom anion, with the  $N$  atoms being connected through  $\text{N}=\text{N}$  double bonds. Metal azides are known to become unstable under certain conditions, such as increased temperature or pressure, and violently decompose, sometimes explosively, to produce elemental  $\text{N}_2$  and the respective metal. This has led to azides being used as a source of pure  $\text{N}_2$ , explosives and even as photographic materials at low temperatures.<sup>[17]</sup> A substantial amount of metal azides are already known, which involve metals from across the periodic table. These compounds typically have the composition of either  $M(\text{N}_3)$  ( $M = \text{Li} - \text{Cs}$ ,  $\text{Cu}$ ,  $\text{Ag}$  and  $\text{Tl}$ )<sup>[42-45]</sup> or  $M(\text{N}_3)_2$  ( $M = \text{Ca} - \text{Ba}$ ,  $\text{Zn}$ ,  $\text{Hg}$ ,  $\text{Cd}$  and  $\text{Pb}$ ),<sup>[39,46-48]</sup> however compounds that have a very highly charged cation adopt a different composition, such as  $M(\text{N}_3)_6$  ( $M = \text{Mo}$  and  $\text{W}$ ).<sup>[49]</sup>

Isoelectronic to the azide anion are other three atom anions;  $[\text{CN}_2]^{2-}$ ,  $[\text{C}_2\text{N}]^{3-}$ ,  $[\text{C}_3]^{4-}$  and  $[\text{OCN}]^-$  (Figure 1.4). These anions are very difficult to distinguish from one other, due to them being isoelectronic and each atom having very similar electron density. The near identical carbodiimide and cyanamide units contain, like azides, a large range of metals from throughout the periodic table, with compositions like  $M[\text{CN}_2]$  ( $M = \text{Be} - \text{Ba}$ ,  $\text{Mn} - \text{Zn}$ ,  $\text{Cd}$ ,  $\text{Pb}$  and  $\text{Eu}$ )<sup>[50,51,60,52-59]</sup> and



$M_2[CN_2]$  ( $M = \text{Li, Cr, Ag and Hg}$ ).<sup>[61–64]</sup> The cyanate containing compounds,  $M[OCN]$  ( $M = \text{Li – Cs, Ag and Tl}$ ),<sup>[62,65–68]</sup> actually adopt the same structure as their respective azides, with the exception for  $M = \text{Rb, Cs and Tl}$ , which adopt the  $\text{KN}_3$  structure. The only known non-metal cyanate is  $\text{Si}[OCN]_4$ , which is also the only example of a cyanate compound with a non-monovalent cation in a solid state system.<sup>[69]</sup> At the time of writing only two solid state examples of acetonitriletriide containing compounds are known,  $\text{Ba}_5[\text{TaN}_4][\text{C}_2\text{N}]$  and  $\text{Sr}_4\text{N}[\text{C}_2\text{N}][\text{CN}_2]$ ,<sup>[70,71]</sup> and this is also true for allylenide containing compounds:  $\text{Mg}_2[\text{C}_3]$  and  $\text{Ca}_3\text{Cl}_2[\text{C}_3]$ .<sup>[72,73]</sup>

Compounds containing these anions have found possible uses as molecular precursors for the synthesis of new ceramics, 1D-polymerised carbon chains, production of Mg-intercalated graphites, carbon clathrates, negative electrode material for batteries, corrosion protective layers, photovoltaic devices, fluorescent light sources and light-emitting diodes.<sup>[69,74,83–86,75–82]</sup>

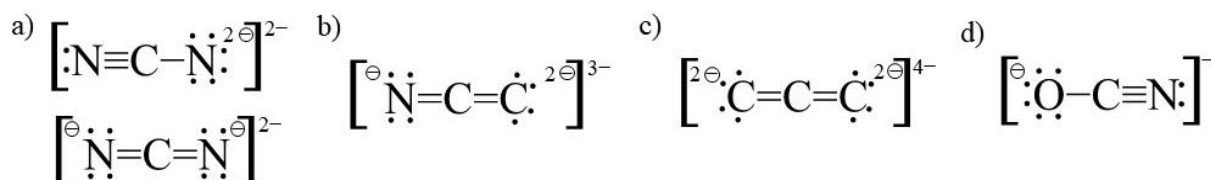


Figure 1.4. Lewis structure of C and N containing three atom complex anions: a) cyanamide (top) and carbodiimide (bottom); b) acetonitriletriide; c) allylenide; d) cyanate.

Nitridometalates of transition metals are defined as compounds with complex anions  $[M_xN_y]^{z-}$ , which have bonding that is more covalent in character. Charge balance of these complex anions is typically achieved from either alkali or alkaline earth metals, which are predominantly ionic in nature. While there is a substantial number of complex anions present, there are several of note, which are of particular interest in this doctoral thesis (*Figure 1.5*).

For these complex anions a wide range of oxidation states are observed for transition metal cations. The higher oxidation states are typically seen for transition metals between groups 3 and 6, such as  $\text{Li}_6[\text{MN}_4]$  ( $M = \text{Cr, Mo and W}$ ).<sup>[87]</sup> Group 7 has the widest range of oxidation states, varying from +1 for nitridomanganates, such as  $\text{Li}_2[(\text{Li}_{1-x}\text{Mn}_x)\text{N}]$ ,<sup>[88]</sup> to +7 for nitridorhenates, such as  $\text{Sr}_2\text{Li}[\text{ReN}_4]$ .<sup>[89]</sup> So far for groups 8–12, only compounds with 3d metals are known. The highest oxidation state seen from these groups is +3 from Fe ( $\text{Sr}_8[\text{FeN}_3]_2[\text{FeN}_2]$ ),<sup>[90]</sup> while the others metals, Co, Ni and Cu, predominantly show very low oxidation states  $\leq +1$ , such as the series  $\text{Li}_2[(\text{Li}_{1-x}M_x)\text{N}]$ .<sup>[91–94]</sup>

The shape of the nitridometalate complex anions is linked with the oxidation state of the transition metal present. For metals with a high, or highest possible, oxidation state tetrahedral complexes are seen, such as in the compound  $\alpha$ -Li<sub>7</sub>[VN<sub>4</sub>].<sup>[95]</sup> Anions which contain a metal in an intermediate oxidation state can exhibit either trigonal planar or T-shaped complexes, such as in the compounds Ca<sub>3</sub>[MN<sub>3</sub>] (*M* = V, Cr and Mn).<sup>[96]</sup> Low valence transition metal cations result in twofold coordination with the nitride anions to produce either linear three atom complex anions, such as those found in Sr<sub>6</sub>N[MN<sub>2</sub>][CN<sub>2</sub>] (*M* = Fe and Co)<sup>[97,98]</sup> or infinite linear chains, such as those found in Li<sub>2</sub>[(Li<sub>1-x</sub>M<sub>x</sub>)N] (*M* = Mn, Fe, Co, Ni, Cu).<sup>[92,99,100]</sup>

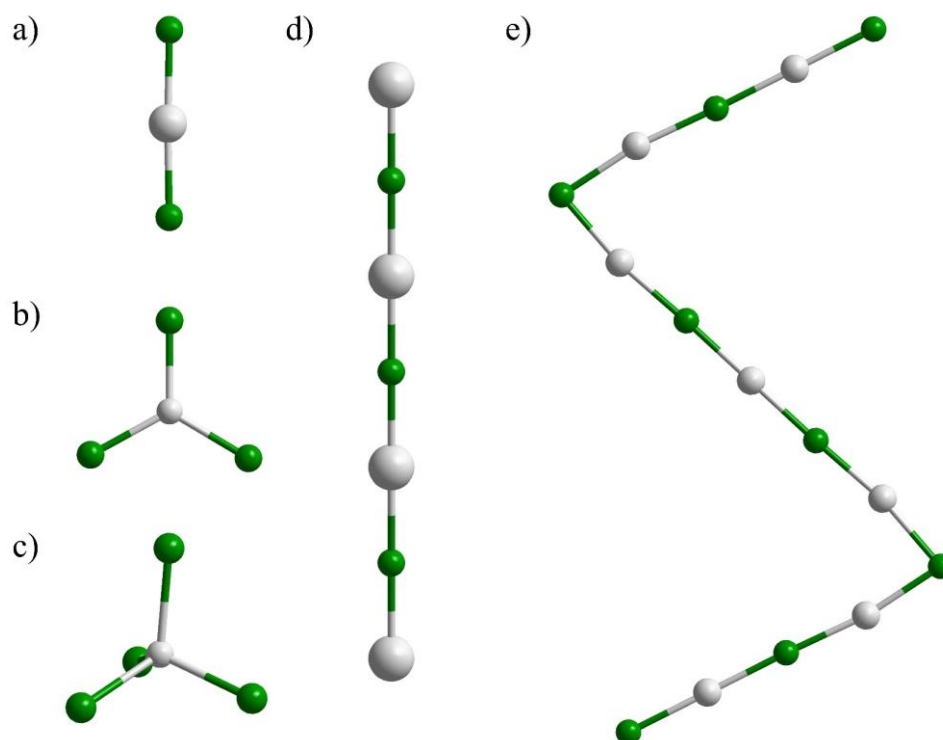


Figure 1.5. Commonly observed nitridometalate complex anions a) linear three atom arrangement; b) trigonal planar; c) tetrahedral arrangement; d) infinite linear chains; e) infinite zig-zag chains. (*M* is shown in grey and N is shown in green).

The aim of this work was to produce and characterise novel binary and higher nitrides, utilising varying synthetic approaches, with a focus on iron nitride compounds. These investigations naturally lead to the exploration of the chemistry of the similar elements Co, Ni and Cu, which expanded this work into the discovery and characterisation of new nitridometalate compounds, containing complex anions with infinite linear chains and linear three atoms complex anions. Further experimental investigations resulted in the production of compounds with exotic C and N containing anions.

## 2. Experimental methods

### 2.1. Chemicals used

A list of the chemicals used during this research, including purities and suppliers, can be found in Table 2.1. A reactant that was used often for the synthesis of compounds was  $\alpha$ -Li<sub>3</sub>N, which was produced in the laboratory. An elemental lithium rod (0.980 g), with the outer layer removed to minimise the presence of any oxides, were cut into pieces with an approximate length of 5 mm. These pieces were placed in a tantalum crucible and inserted into a fused silica tube. The tube was heated under N<sub>2</sub> flow, which was further purified by passing over a molecular sieve (4 Å) and a BTS catalyst, to 443 K for 36 hours, before increasing to 498 K, at 10 K/h, for 2 hours to ensure a complete reaction. The apparatus was allowed to cool naturally to room temperature. The obtained product was confirmed, by powder X-ray diffraction, to be single phase  $\alpha$ -Li<sub>3</sub>N.

Table 2.1. Table of chemicals, purity and supplier used during this research.

Chemical	Purity/%	Supplier
Ar	99.999	Alpha gaz
C (graphite)	99.9995	Alfa Aesar
Co (powder)	>99.8	Fluka
Cu (powder)	99.9	Aber
Cu <sub>3</sub> N (powder)	99.5	Alfa Aesar
Fe (powder)	99.9	Chempur
<sup>57</sup> Fe (powder)	96.28	Certificate of analysis No. 26-01-57-4482
Li	99.9	Sigma Aldrich
N <sub>2</sub>	99.999	Alpha gaz
Na	99	Riedel-de-Haën
Ni (powder)	99.8	Alpha Aesar
NH <sub>3</sub>	99.999	Linde
NaN <sub>3</sub>	>99	Roth
Nb tube	99.9	Sigma Aldrich
Ni tube	99.5	Sigma Aldrich
Sr (dendritic pieces)	99.99	Sigma Aldrich
Sr(N <sub>3</sub> ) <sub>2</sub>	X-ray diffraction single phase	Selfmade <sup>[101]</sup>
Ta tube	99.9	Sigma Aldrich

## 2.2. Glove box

The majority of the materials used during this research were extremely oxygen and moisture sensitive. This meant that the storing of chemicals and set up of experimental apparatus had to be conducted in an air and water free environment. To achieve this a glove box MB 200B (MBraun, Garching, Germany) was used (*Figure 2.1.*), containing an argon atmosphere with less than 0.1 ppm oxygen. The system achieves such a low oxygen and moisture content by circulating the atmosphere in the glove box through two purification towers, which remove any oxygen and moisture present in the atmosphere. The oxygen content within the glove box can be monitored through a touch screen panel, which also controls all other functions of the glove box. To ensure the filter functions efficiently, a regeneration of the filter is conducted at least once a month. This regeneration removes the oxygen and water from the filter, by using a combination of heating under vacuum and heating while flowing a gas containing argon and hydrogen. Inside the glove box there are several pieces of equipment, which were used in this work: analytical balance, modular stereomicroscope (MZ6, Leica, Wetzlar, Germany), arc furnace and hydraulic press. The introduction and removal of items in and out of the glove box is conducted through two antechambers, where the antechamber is evacuated and filled with argon three times before bringing the item into the glovebox. To minimise oxygen and moisture being introduced into the box, all apparatus are stored in a drying oven (353 K) until they are needed.



Figure 2.1. Glove box MB 200B, MBraun.

### 2.3. Arc furnace

The arc furnace (CENTORR Vacuum-Industries, Nashua, USA) is a welding apparatus, with water cooling, that is integrated into the glove box (*Figure 2.2.*). This apparatus is used to melt metals and, in this research, used to weld shut various metal ampoules under argon gas and can reach temperatures of 3500 K.



Figure 2.2. Arc furnace, CENTORR Vacuum-Industries.

### 2.4. High temperature apparatus

Tube furnaces are used for reactions that require elevated temperature and either an inert atmosphere or a particular reactive gas, for a solid-gas reaction. In general, a crucible is inserted into a fused silica tube, which is placed into a furnace and flooded with a desired gas and heated.

#### 2.4.1. Tube furnace

For reactions requiring either an inert atmosphere or  $N_2$  as a nitrogen source, a tube furnace is used. The fused silica tube is fully assembled under inert atmosphere in the glove box. Reactants for the specific reaction are placed into a tantalum crucible. The crucible is then inserted into a steel tube, to ensure homogenous heating, which is then inserted into the fused silica tube on top

## 2. Experimental methods

---

of a corundum tube. This corundum tube prevents the steel tube coming into contact with the glass, which reduces the lifetime of the fused silica tube. The assembled apparatus (*Figure 2.3.*) is inserted into the tube furnace (HTM Reetz GmbH, Berlin, Germany) (*Figure 2.3.*), where it is evacuated and flooded with the desired gas. Each gas is further purified by passing over a molecular sieve (4 Å) and a BTS catalyst. The temperature program is then programmed into the controller (E5CK-T, Omron, Langefeld/Eurotherm 2416, Limburg, Germany).

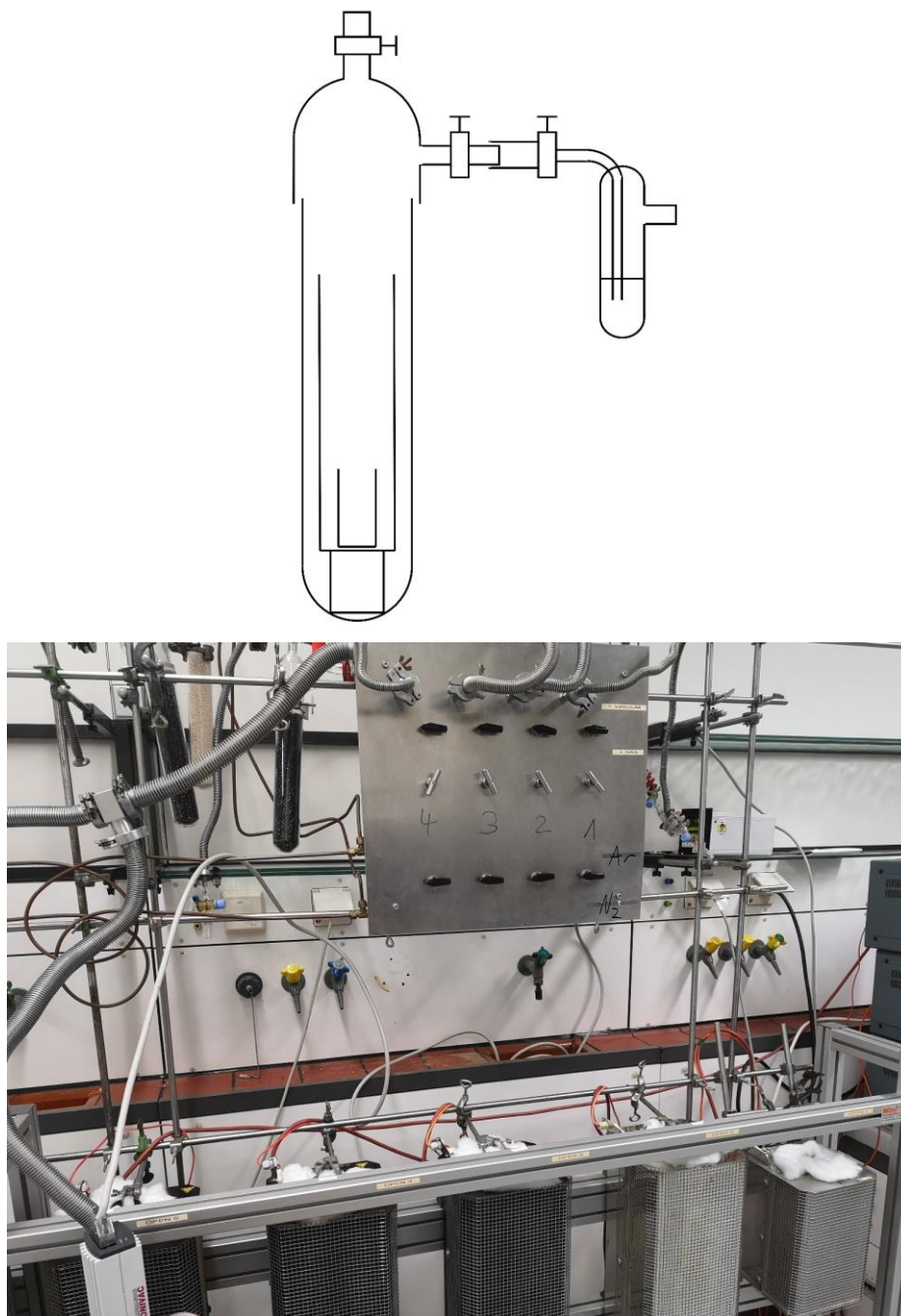


Figure 2.3. Top: Schematic of an assembled glass tube; Bottom: Tube furnaces with gas/vacuum supply.

### 2.4.2. Ammonia flow furnace

Solid-gas reactions that require ammonia and/or hydrogen as a reaction gas have a specific set up and heating apparatus. The glass tube is fully assembled under inert atmosphere in the glove box. Reactants are weighed onto a corundum crucible and inserted horizontally into a fused silica tube. The tube is assembled with a special fused silica cap to ensure a constant flow of gas during the reaction. The assembled apparatus (*Figure 2.4.*) is inserted into the tube furnace (*Figure 2.4.*) and evacuated. The temperature program is then inputted into the controller (E5CK-T, Omron, Langefeld/Eurotherm 2416, Limburg, Germany). Gas flow is controlled via an interface (Type- 179B from MKS Instruments, Munich, Germany) and allows for a specific gas flow, as well as a mixture of ammonia and hydrogen if desired.

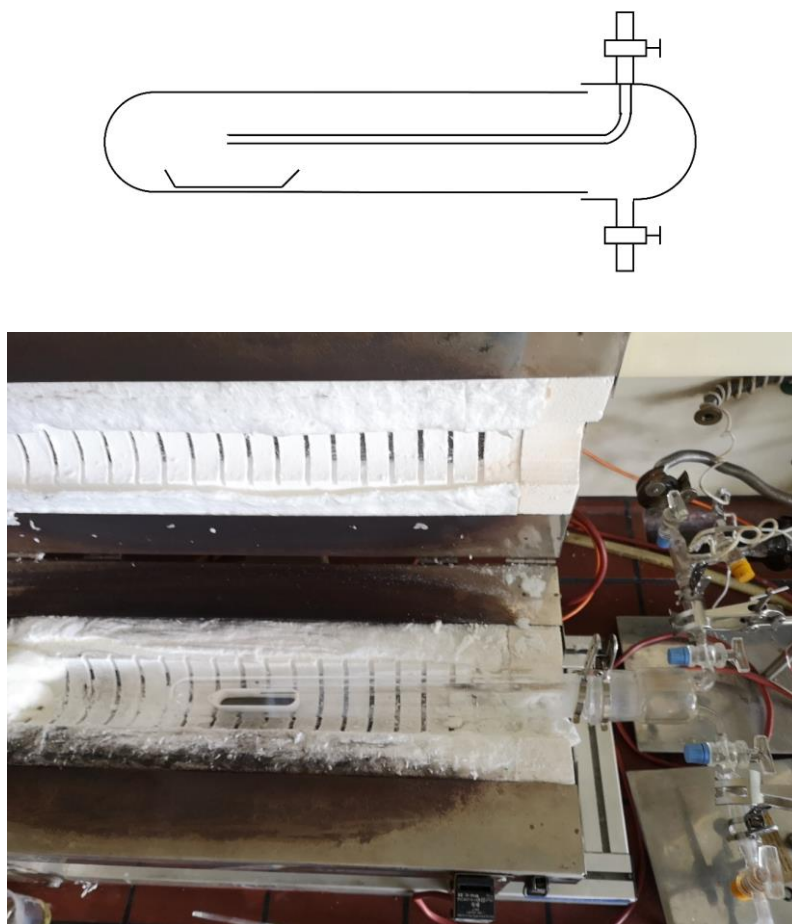


Figure 2.4. Top: Schematic of an assembled glass tube; Bottom: Tube furnace.

### 2.5. Crystal growth with ampoules

All of the single crystal air sensitive products described in this thesis were grown using an alkali metal flux and metal ampoules. The choice of metal used for the ampoule is dependent on the reactants within the ampoule. Typically, niobium is used as a metal, but when nitrogen is included in the reaction, from for example an azide, the niobium readily reacts with the nitrogen to give niobium nitride. This leads to erosion of the ampoule. So in the instance that an azide is used, nickel is chosen as the ampoule material, since it does not react with nitrogen under the conditions used.<sup>[102]</sup>

Both niobium and nickel ampoules are cut from a 50 cm long tube, with a thickness of 0.5 mm and a diameter of 10 mm, of the respective metal. The metal tubes are cut to 5 cm in length and systematically washed in an ultrasonic bath with acetone, distilled water, acetic acid and finally distilled water again, before being dried in a drying oven (353 K). This process cleans the ampoules of any oils and removes any oxide or hydroxide layer on the metal, before transferring them to the glove box. Inside the glove box the ampoules are welded shut on one side using the arc furnace and stored in the glove box to prevent any oxidation of the metal. The ampoule is then filled with the respective reactants and fluxing agent and welded shut. To prevent oxidation of the ampoule during the reaction, the ampoule is placed in a glass tube under argon atmosphere.

As flux, lithium or sodium is used, due to their relatively low melting point, low reactivity under inert conditions and ease of removal after the reaction without damaging the products. Lithium, however, readily reacts with gaseous nitrogen to form lithium nitride, if it is present in the ampoule. Due to this, and the often use of a nitrogen source in the ampoules, sodium became the standard flux in the synthesis of single crystals.

The removal of the flux after the reaction is relatively simple, due to the affinity of alkali metals to dissolve in liquid ammonia. In the glove box, the ampoule is cut open and inserted into a H-shaped tube (*Figure 2.5.*). This H-shaped tube is then transferred to a Tensi-Eudiometer,<sup>[103]</sup> where it is evacuated and filled with roughly 1 bar of ammonia. Since ammonia boils at 240 K, the side of H-shaped tube containing the ampoule has to be cooled in a mixture of dry ice and ethanol. The alkali metal flux in the ampoule dissolves in liquid ammonia and gives a dark blue colour (*Figure 2.5.*). When the level of liquid ammonia is roughly 1 cm above the opened ampoule, the H-shaped tube is removed from the cold bath and the solution is decanted into the



other side of the H-shaped tube. Once complete the solution is slowly heated to evaporate the ammonia, depositing the alkali metal. The side of the H-shaped tube with the ampoule is then again submerged into the cold bath and the process is repeated until the solution is colourless (*Figure 2.5.*), indicating that all of the alkali metal has been removed and deposited on the other side. The H-shaped tube is then heated and evacuated, to remove the liquid and gaseous ammonia, before returning it to the glove box, where the products are removed and analysed.

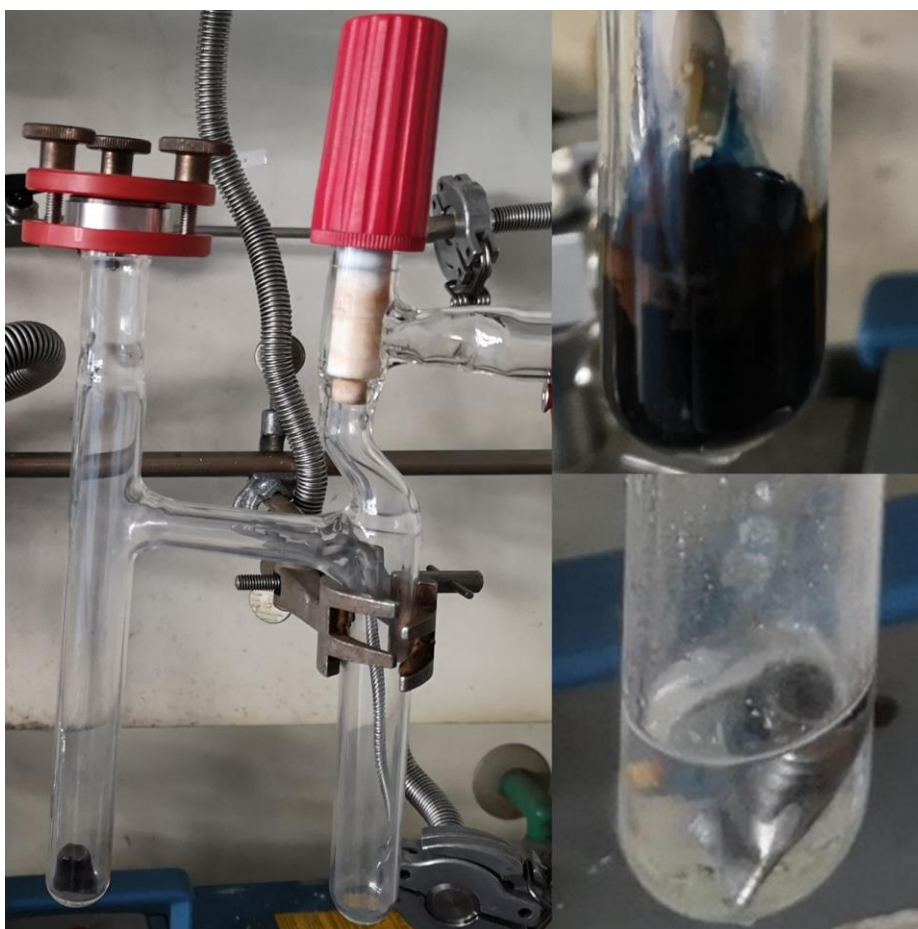


Figure 2.5. Left: Prepared H-shaped tube with an opened metal ampoule on one side. Top right: Dark blue solution containing liquid ammonia and sodium flux from the ampoule. Bottom right: Colourless liquid ammonia indicating no sodium metal is present.

## 2.6. Methods of high pressure and temperature synthesis

Pressure,  $P$ , is defined as the force exerted,  $F$ , over a certain area,  $A$ , (*eq. 2.1*) with the commonly used unit of pressure being the Pascal ( $\text{Pa} = \text{Nm}^{-2}$ ). High pressure reactions are conducted by the application of pressure in the range of 0.1 to 400 GPa and are characterised into two broad groups: static and dynamic. Static pressure is the application of high pressure over a selected length of time, while dynamic pressure is the exertion of high pressure over a very narrow time range. For the research into high pressure iron nitrides the application of static pressure was preferable, since it gives reproducible conditions and allows for hydrostatic conditions with a wide range of pressure.

$$P = \frac{F}{A} \quad (\text{eq. 2.1.})$$

To reach the high static pressures needed, understanding of the equation of pressure is needed (*eq. 2.1.*). Substantially increasing the pressure,  $P$ , exerted on a sample requires a method that either dramatically increases the force exerted,  $F$ , on the sample, for example the Voggenreiter press with a Walker-type multi-anvil module, or that the area of the sample,  $A$ , is extremely small, for example in the diamond anvil cell.

### 2.6.1. Diamond anvil cell

This method was first mentioned over 65 years ago<sup>[104]</sup> and still remains a very popular and reliable method to achieve high pressure and temperature reaction conditions. The diamond anvil cell comprises of essentially four components: anvils, gasket, pressure medium and the sample (*Figure 2.6.*).

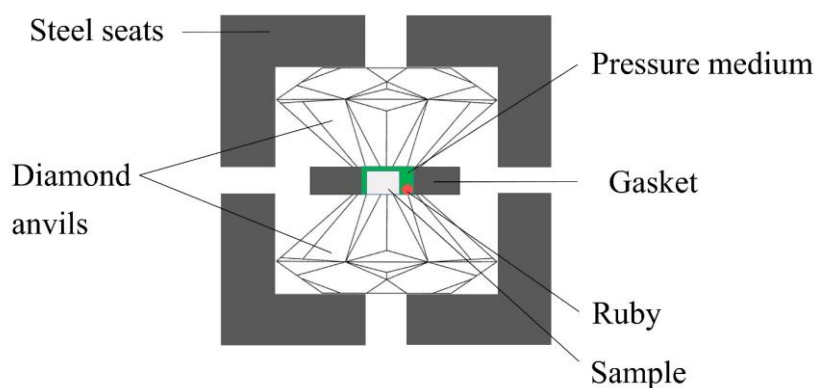


Figure 2.6. Schematic of a diamond anvil cell.

Diamond is used as the anvils, mainly because of its incredible hardness and thermal conductivity. The anvils are specially shaped to have a large base that tapers towards the sample holder, which results in high pressure being subjected to the sample. The exceptional thermal conductivity of diamond allows for a controlled and rapid change in temperature through laser heating of the sample, while under pressure,<sup>[105]</sup> whereas an insulating material would in fact result in higher temperatures than what would be desired. By using diamonds as the material for the anvils, pressures as high as 400 GPa have been achieved<sup>[106,107]</sup> and with reaction temperatures ranging from 0.03 K to 7000 K.<sup>[108,109]</sup>

The gasket is typically made from a high strength metal, such as rhenium, and holds the sample in position, while also acting as containment for the pressure by means of anvil-gasket friction.

Pressure media are used to produce and maintain a constant hydrostatic pressure. This is typically achieved by using an inert gas, such as helium or argon. However, for the purposes of this work the pressure medium, nitrogen, was used as both a pressure medium and reactant. When the nitrogen within the diamond anvil cell is subjected to 0.1 GPa, at room temperature, it becomes fluid, allowing it to produce the constant hydrostatic pressure as the other typical pressure media. Once the pressure exceeds 1 GPa a phase transition occurs, which results in the formation of the disordered hexagonal  $\beta$ -N<sub>2</sub> phase. Further increasing of the pressure above 5 GPa produces the disordered cubic  $\delta$ -N<sub>2</sub> phase, which exists until 16 GPa where it converts to the ordered rhombohedral  $\epsilon$ -N<sub>2</sub> phase.<sup>[110]</sup> Each of these phases are solid forms of nitrogen, which means that above 1 GPa the pressure induced on the sample is no longer hydrostatic pressure and is instead static pressure.

To accurately determine the pressure within the diamond anvil cell is of utmost importance with receiving reliable, good quality results. To this effect, ruby is used to measure the pressure. Ruby exhibits a strong fluorescence spectrum, under pressure, and the ruby fluorescence method<sup>[111]</sup> can accurately determine the pressure within the cell.

Recent breakthroughs with diamond anvil cells,<sup>[112,113]</sup> have allowed *in-* and *ex-situ* analysis and characterisation of samples. X-ray diffraction and Mössbauer spectroscopy experiments can be conducted before, during and after the high pressure and temperature conditions to obtain in depth observations of phase evolution.

### 2.6.2. Voggenreiter press with a Walker-type Multi-anvil module

The Voggenreiter press, with a Walker-type multi-anvil module, (*Figure 2.7.*) is a 1000 t hydraulic press, that can reach reaction conditions of up to 16 GPa and 2500 K. The main principle of the multi-anvil press is that the sample is placed in a particular kind of anvil and pressure is introduced by hydraulic pistons, which drive opposing cylinders towards the anvil. With the Walker press, the special aspect of the design, is the use of steel wedges, which slot together to form the cylindrical piston and a nest for the anvil (*Figure 2.8.*). This allows each wedge to float freely while under high pressure, thus creating a more homogenous and hydrostatic pressure environment.



Figure 2.7. Voggenreiter press with a Walker-type multi-anvil module, located at the Max-Planck-Institut für Chemische Physik fester Stoffe, Dresden, Germany.

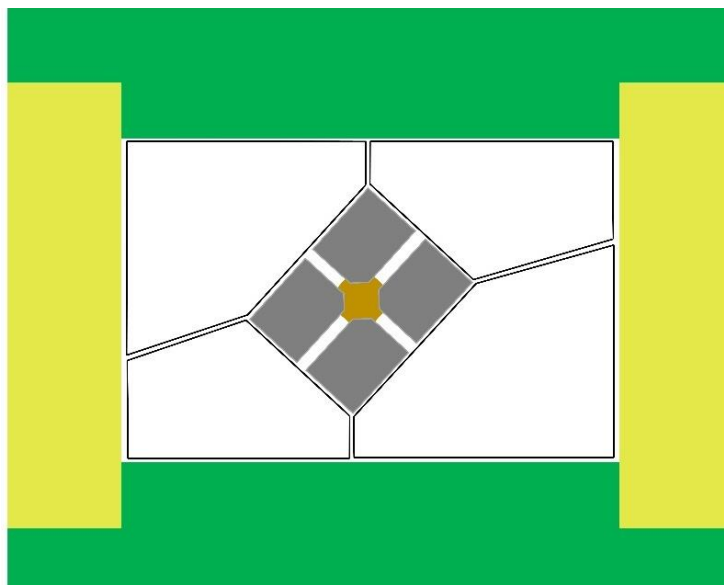


Figure 2.8. Schematic cross section diagram showing the octahedra (bronze) fitted within the anvil (silver), which is in a nest of steel wedges (white) within the Voggenreiter press (green and yellow).

The anvil itself comprises of many specific components and has a very particular assembly process (*Figure 2.9.*). The sample is inserted into a *h*-BN crucible. *h*-BN is taken as a sample holder material, since it remains stable under the extreme temperature and pressure produced by this method.<sup>[114]</sup> The crucible is then covered by a graphite sleeve, to ensure an even thermal conductivity.<sup>[115]</sup> Housing for this sample is a MgO octahedra, which is used to act as a pressure medium. The properties of MgO make it an ideal material for the octahedra, since it has a high melting point and at high temperatures becomes ductile, allowing a more constant hydrostatic pressure during the reaction. To insulate the octahedra from the high temperatures, a ZrO<sub>2</sub> insulating sleeve is introduced between the octahedra and sample. The octahedra are sealed by Mo discs, which act as electric heating conductors, and eight WC cubes are placed around the octahedron to form the anvil.

Decision on what pressure range is needed dictates what size MgO octahedra, and hence which WC cubes are needed. The range of octahedra sizes available range from 12 mm<sup>3</sup> (18/11), resulting in a pressure range of between 4 – 10 GPa, down to 1 mm<sup>3</sup> (7/3), resulting in a pressure range of between 22 – 26 GPa.<sup>[116]</sup> The size of octahedra used for this work was between 5 – 8 mm<sup>3</sup> (14/8), giving a workable pressure range of between 11 and 16 GPa.

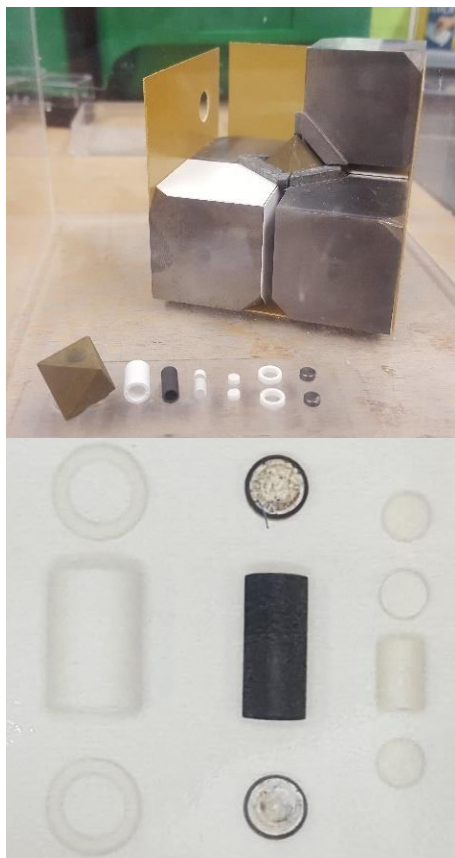


Figure 2.9. Upper: Assembly process of the anvil, Lower: Components for sample holder: Left: Insulating ZrO<sub>2</sub> liner; Middle: Graphite heating sleeve; Right: *h*-BN crucible and lid.

### 3. Analytical techniques

#### 3.1. Structural characterisation by X-ray diffraction

X-rays are an electromagnetic radiation, found between gamma and ultra-violet rays at the high energy end of the electromagnetic spectrum, and have a wavelength in the range of  $1 \cdot 10^{-11}$  and  $1 \cdot 10^{-8}$  m (0.1 – 100 Å).<sup>[117]</sup> The energy ( $E$ ) of a wavelength ( $\lambda$ ) is related by the speed of light ( $c$ ) and Planck's constant ( $h$ ). This wavelength coincides with the rough distance between atoms in a crystalline material, making X-rays the most fitting form of radiation to be used for the analytic analysis of crystalline solids (eq. 3.1.).

$$E = \frac{hc}{\lambda} \quad (\text{eq. 3.1.})$$

##### 3.1.1. Generation and properties of X-rays

In the laboratory, the conventional method of generating X-rays is via an X-ray tube. This tube, under high-vacuum, contains an anode of a very pure metal (typically Mo or Cu) and a tungsten cathode. A high voltage (30 – 60 kV) is applied to the cathode, which produces a focussed beam of high energy electrons that comes into contact with the anode. During this process, two forms of X-rays are produced: the 'white' radiation and the characteristic radiation.

When the high energy electrons approach the anode, some are decelerated by the metal ions and in the process release some of their energy in the form of low energy X-rays, commonly known as 'white' radiation or Bremsstrahlung.

Another situation that can occur is when a high energy electron comes into contact with the anode and ejects an electron from one of the core energy levels. This causes an electron from a higher energy level to compensate and move to the lower energy level and in the process releasing energy, in the form of X-rays (*Figure 3.1.*). This unique energy difference produces characteristic wavelengths, which is determined by the difference in energy of the energy levels ( $E_2 - E_1$ ) (eq. 3.2.). The most intense wavelengths,  $K_{\alpha 1}$  and  $K_{\alpha 2}$ , are produced from the  $L \rightarrow K$  transition (*Figure 3.2.*). These wavelengths are very close to each other, however  $K_{\alpha 1}$  is more intense (*Figure 3.2.*) and so this specific wavelength is selected for crystal structure analysis.

$$\lambda = \frac{hc}{E_2 - E_1} \tag{eq. 3.2.}$$

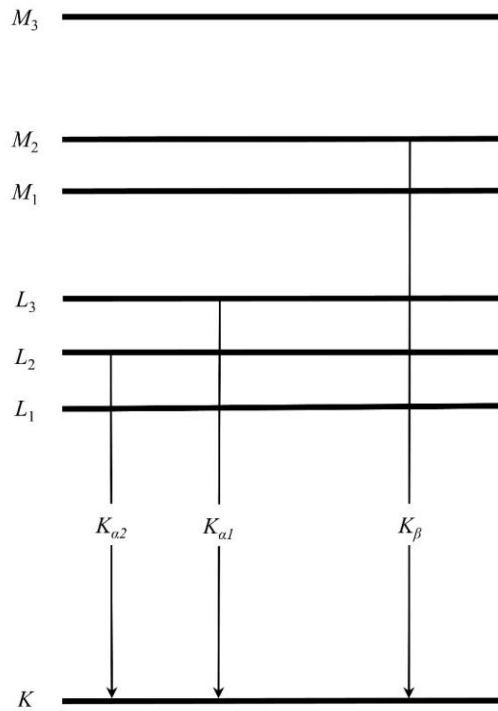


Figure 3.1. Diagram of the origin of K<sub>α1</sub> and K<sub>α2</sub> X-ray generation, depicting the energy levels K, L and M.

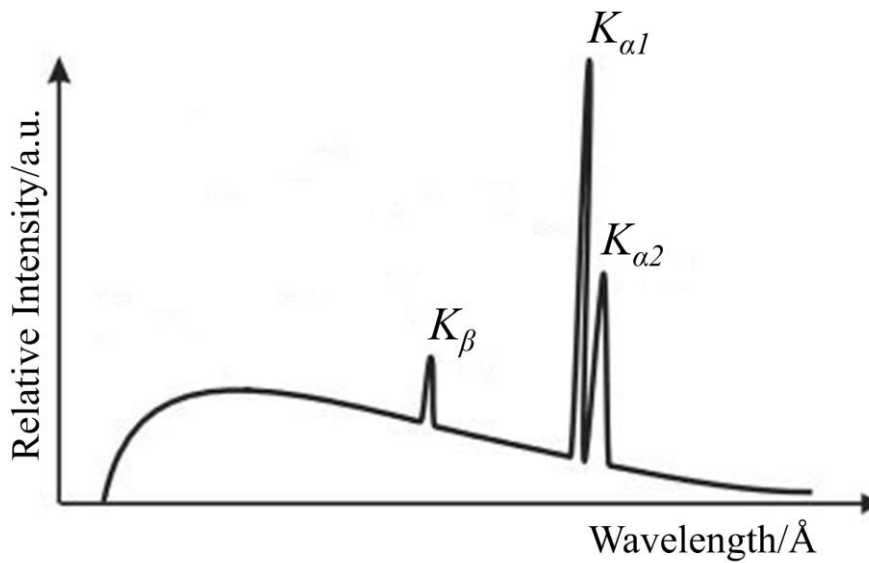


Figure 3.2. Spectrum of relative intensities of X-rays generated, with the Bremsstrahlung at lower wavelengths and the labelled K radiations at relatively higher wavelengths.<sup>[118]</sup> Republished with permission of Springer, from *Moderne Röntgenbeugung*, L. Spieß, G. Teichert, R. Schwarzer, H. Behnken, C. Genzel, Vieweg+Teubner, Wiesbaden, 2009.



Typically, for X-ray diffraction experiments, a monochromatic X-ray is used. This can be achieved by the use of a filter, made of a metal foil, or single crystal monochromator.<sup>[117]</sup> For the method using a metal foil, the metal selected absorbs wavelengths below the ionisation energy of the metal. This removes most of the undesirable wavelengths and results in very little of the desired most intense wavelength,  $K_{\alpha 1}$ , being lost. A single crystal monochromator more effectively removes undesirable radiation by orientating a single crystal, such as Ge, to the beam so that only the desired wavelength,  $K_{\alpha 1}$ , meets the conditions for constructive interference. This also removes unwanted wavelengths, including the very similar  $K_{\alpha 2}$  radiation, giving a monochromatic X-ray beam.

### 3.1.2. Diffraction of X-rays

A crystal is a highly ordered system, comprised of atoms, ions or molecules, that forms a crystal lattice which continues in all directions of three dimensional space. This lattice can be thought of being constructed of parallel lattice planes, which are present in every direction and are identified by Miller indices ( $hkl$ ).

For X-rays to be diffracted within a crystal structure the angle of incidence must equal the angle of reflection and there must be constructive interference, where  $n\lambda = 2x$  when  $n$  is an integer. When these criteria are satisfied, the diffraction of X-rays occurs along each lattice plane ( $hkl$ ) according to Braggs Law (eq. 3.3.). Using parallel lattice planes, both of which diffract parallel X-rays, the exact diffraction angle,  $\theta$ , can be calculated from the distance between the lattice planes,  $d$ , at a particular wavelength,  $\lambda$ , for each order of diffraction,  $n$  (Figure 3.3.).

$$n\lambda = 2d \sin \theta \quad (\text{eq. 3.3.})$$

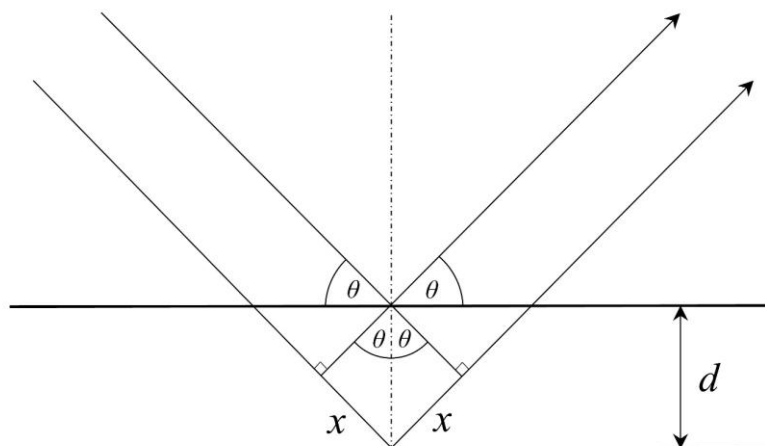


Figure 3.3. Derivation of Bragg's Law.

Visualisation of the plethora of lattice planes of a crystal within real space would quickly become overwhelming. It is much easier to consider each lattice plane as a vector in reciprocal space,  $\mathbf{d}^*$  (eq. 3.4.). This vector is calculated from the reciprocal vectors of their real lattice counterparts,  $\mathbf{a}^*$ ,  $\mathbf{b}^*$  and  $\mathbf{c}^*$ . The relation of lattice planes in real space and axes in reciprocal space, is that they are normal to one another. This means to reach the reciprocal vector, the product of the real space axes normal to the reciprocal vector has to be taken (eq. 3.5.). Simply taking the product of the real space axes would result in a unit of area in normal space, which is corrected by dividing through the volume of the unit cell,  $V$ , to reach a unit of length in reciprocal space.

$$d^* = h^2 a^{*2} + k^2 b^{*2} + l^2 c^{*2} \quad (\text{eq. 3.4.})$$

$$a^* = \frac{bc}{V}, \quad b^* = \frac{ac}{V}, \quad c^* = \frac{ab}{V} \quad (\text{eq. 3.5.})$$

The scattering vector,  $\mathbf{d}^*$ , is used to describe and calculate the diffraction angle of an X-ray in reciprocal space. When an X-ray passes through a crystal,  $K$ , it is diffracted by the scattering vector. By using Bragg's Law, in the form of a Pythagoras equation, it is possible to calculate the diffraction angle,  $2\theta$ , and where in reciprocal space it will end, which must be on a circle with a radius of  $1/\lambda$  from the crystal. This is described by the Ewald construction (Figure 3.4.), which is depicted here as a 2D circle, however in 3D space it is in fact a sphere. So, whenever a reciprocal lattice plane passes through the Ewald construction a reflection is observed at the corresponding diffraction angle.

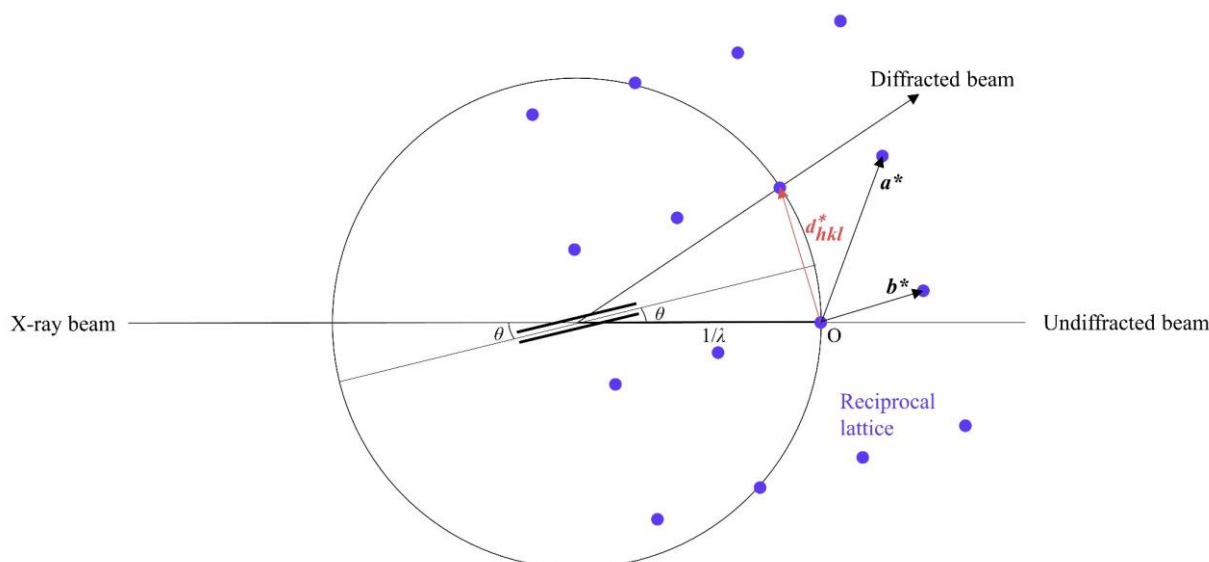


Figure 3.4. Ewald construction.

### 3.1.3. Single crystal X-ray diffraction

For this research, diffraction intensity data of single crystals were collected from either a 4-circle Kappa-CCD single crystal diffractometer (Bruker-Nonius, Karlsruhe) (Figure 3.5.), which uses a charge coupled device as a detector, or an IPDS single crystal diffractometer (STOE & CIE GmbH, Darmstadt) (Figure 3.6.), which used an image plate as a detector. Both of these diffractometers, which utilised Mo- $K_\alpha$  wavelength ( $\lambda = 0.7093 \text{ \AA}$ ), produced the X-rays from a conventional X-ray tube. For samples needing more hard X-rays, a Stadi Vari single crystal diffractometer (STOE & CIE GmbH, Darmstadt) was used (Figure 3.7.), which utilised a graded multilayer mirror monochromator and a fine focus beam, and was able to produce both Ag- $K_\alpha$  ( $\lambda = 0.56083 \text{ \AA}$ ) and Mo- $K_\alpha$  ( $\lambda = 0.7093 \text{ \AA}$ ) wavelengths. Resulting diffraction data was analysed and refined using the ShelX program package.<sup>[119–122]</sup> The information of every lattice plane is collected by the rotation of the crystal in every direction, allowing all reciprocal lattice planes to pass through the Ewald sphere and the corresponding reflections and diffraction angles to be recorded at the detector.

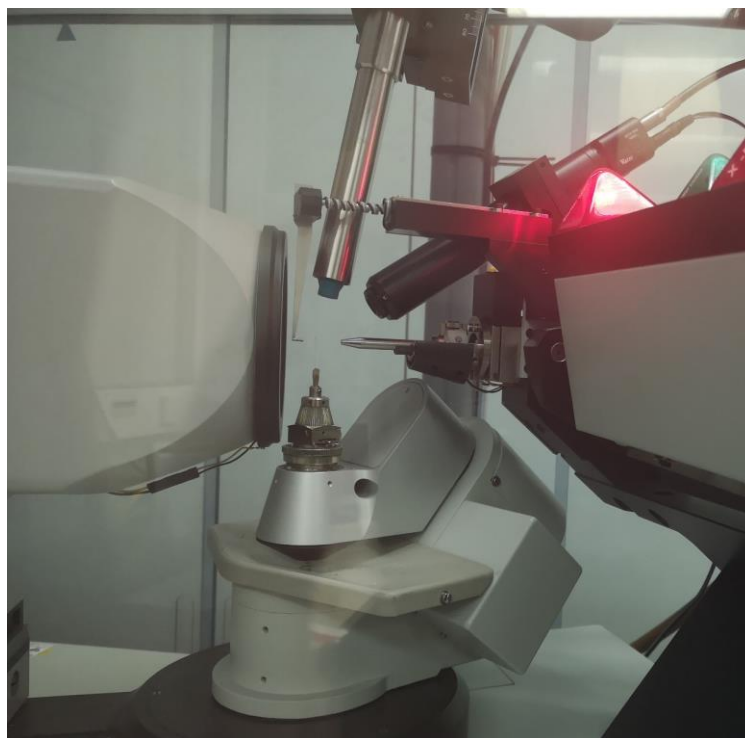


Figure 3.5. 4-circle Kappa-CCD single crystal diffractometer (Bruker-Nonius, Karlsruhe, Germany).

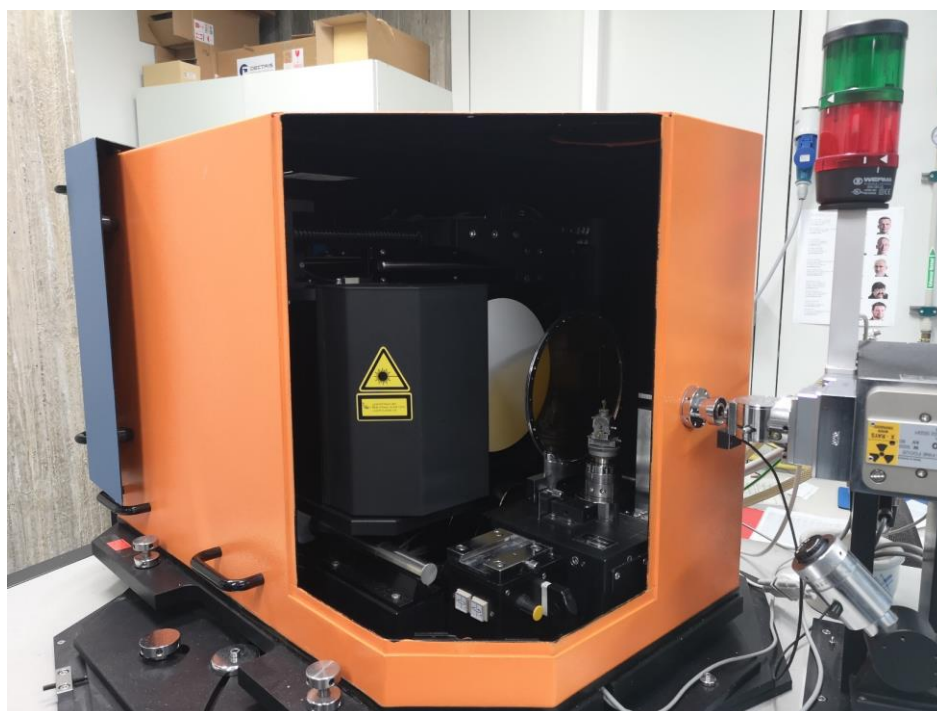


Figure 3.6. IPDS single crystal diffractometer (STOE & CIE GmbH, Darmstadt, Germany).



Figure 3.7. Stadi Vari single crystal diffractometer (STOE & CIE GmbH, Darmstadt, Germany).

The results of a single crystal X-ray diffraction experiment yields the unit cell parameters, the intensity of reflections and possible space groups. The use of a Fourier transformation (eq. 3.6.) allows the accurate determination of structure factors,  $F_c$ , and the atom positions,  $x$ ,  $y$  and  $z$ , from the individual structure factors,  $F_{hkl}$  (eq. 3.6.)

$$F_c = \sum_i f_i [\cos 2\pi (hx_i + ky_i + lz_i) + i \sin 2\pi (hx_i + ky_i + lz_i)] \quad (\text{eq. 3.6.})$$

A refinement of these calculated structure factors,  $F_c$ , with the calculated intensity,  $F_o^2$ , and the observed structure factors,  $F_o$ , result in the description of the crystal structure. However, errors can occur mainly from approximations of the method of refinement, as well as errors from the measured data. This leads to a discrepancy between the calculated and observed structure factors (eq. 3.7., 3.8.).

$$\Delta_1 = ||F_o| - |F_c|| \quad (\text{eq. 3.7.})$$

$$\Delta_2 = |F_o^2 - F_c^2| \quad (\text{eq. 3.8.})$$

For refinement of single crystal data the SHELX program package was used.<sup>[119–122]</sup> To assess the quality of the structural refinement, the conventional  $R$ -factor,  $R_I$ , is used (eq. 3.9).

$$R_I = \frac{\sum_{hkl} |F_o| - |F_c|}{\sum_{hkl} |F_o|} \quad (\text{eq. 3.9.})$$

However, every reflection intensity has a different error associated with it. To compensate for this a weighting function is used. The resulting weighted  $R$ -factor,  $\omega R_2$ , (eq. 3.10.) and goodness of fit, GooF, (eq. 3.11.) give a more sensitive indication of the quality of the refinement by incorporating the number of reflections ( $m$ ) and parameters ( $n$ ) into the calculations.<sup>[123]</sup>

$$\omega R_2 = \sqrt{\frac{\sum_{hkl} \omega (F_o^2 - F_c^2)^2}{\sum_{hkl} \omega (F_o^2)^2}} \quad (\text{eq. 3.10.})$$

$$\text{GooF} = \sqrt{\frac{\sum_{hkl} \omega (F_o^2 - F_c^2)^2}{m - n}} \quad (\text{eq. 3.11.})$$

### 3.1.4. Powder X-ray diffraction

For samples that either did not form single crystals, or crystals of insufficient quality, the powder diffraction method was used. For this research an X-ray diffractometer with Mo- $K_{\alpha 1}$  wavelength ( $\lambda = 0.7093 \text{ \AA}$ , STADI P with Mythen1K micro-strip detector, STOE & CIE GmbH, Darmstadt, Germany) (Figure 3.8.) or with Cu- $K_{\alpha 1}$  wavelength ( $\lambda = 1.5406 \text{ \AA}$ , STADI P with a germanium-monochromator, STOE & CIE GmbH, Darmstadt, Germany) (Figure 3.9.) were used. Analysis of the resulting diffraction patterns were conducted using WinXPow and the Fullprof suite.<sup>[124,125]</sup>

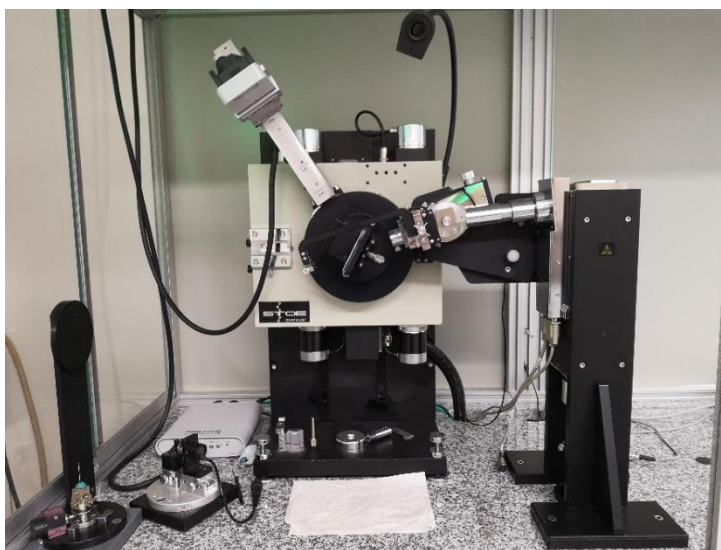


Figure 3.8. Stoe STADI P powder diffractometer with Mythen1K micro-strip detector.

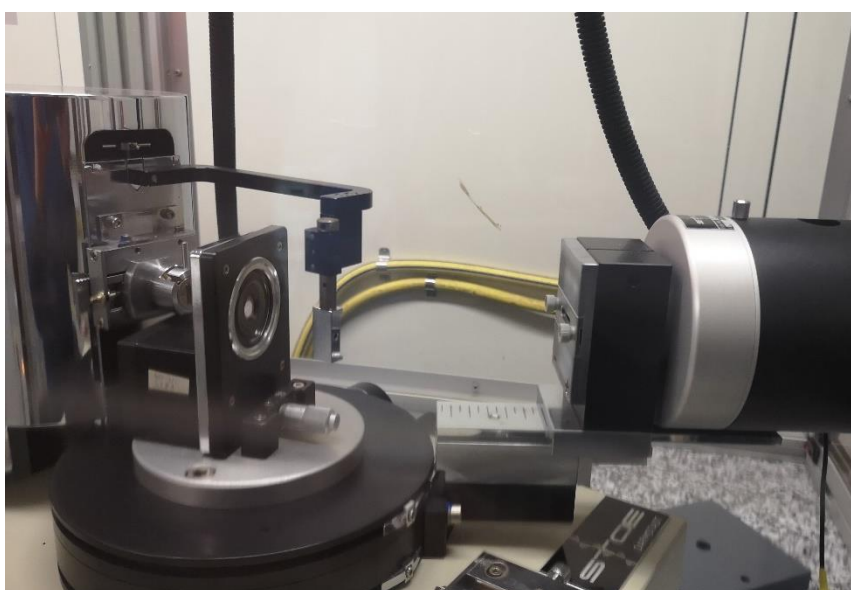


Figure 3.9. Stoe STADI P powder diffractometer.

Powder X-ray diffraction experiments produce a diffraction pattern of diffraction intensities plotted against the diffraction angle,  $2\theta$ . This pattern can then be compared with other diffraction patterns and, when the correct composition and structure is known, refined using the Rietveld method.<sup>[126,127]</sup> Once the refinement is complete, the quality of the refinement can be assessed by using the weighted differences between the observed,  $\gamma_{i(o)}$ , and calculated,  $\gamma_{i(c)}$ , intensity, known as the  $R$ -factor (eq. 3.12.). Another gauge of the quality of the refinement is based on the integrated intensity of reflections,  $n$ , known as the Bragg- $R$ -value (eq. 3.13.).

$$R_{wp} = \sqrt{\frac{\sum \omega_i (\gamma_{i(o)} - \gamma_{i(c)})^2}{\sum \omega_i (\gamma_{i(o)})^2}} \quad (\text{eq. 3.12.})$$

$$R_{Bragg} = \frac{\sum |I_{n(o)} - I_{n(c)}|}{\sum I_{n(o)}} \quad (\text{eq. 3.13.})$$



## 3.2. Magnetism and magnetic measurements

### 3.2.1. Overview

The magnetisation,  $M$ , of a material occurs when the material is placed in a magnetic field,  $H$ . The strength of magnetisation that occurs is directly proportional to the magnetic susceptibility of the substance,  $\chi$ , (eq. 3.14.).

$$M = \chi H \quad (\text{eq. 3.14.})$$

The form of magnetism inherent in all materials is diamagnetism, simply caused by the circulation of electrons in a material. When materials have unpaired electrons, this leads to the rise of paramagnetism. Under a magnetic field the unpaired electrons align, to a certain degree, in a particular orientation, depending on temperature, to increase the magnetic susceptibility. Typically, magnetic properties are described in terms of the magnetic moment,  $\mu$ , which has the unit of Bohr Magneton (BM). A Bohr Magneton is defined in the equation below (eq. 3.15.), where  $e$  is the elemental charge of an electron,  $h$  is Planck's constant,  $m$  is electron mass and  $c$  is the speed of light. The magnetic moment is calculated directly from the sum of the spin quantum numbers,  $S$ , of the unpaired electron in the material (eq. 3.16.).

$$BM = \frac{eh}{4\pi mc} \quad (\text{eq. 3.15.})$$

$$\mu = \sqrt{S(S+1)} \quad (\text{eq. 3.16.})$$

### 3.2.2. Curie-Weiss Law

In paramagnetic materials, arrangements of the unpaired electrons can be either: disordered (Curie-paramagnetism), aligned parallel (ferromagnetism), aligned anti-parallel (anti-ferromagnetism) or a mixture of both parallel and anti-parallel alignment (ferrimagnetism). Under a magnetic field the disordered unpaired electrons of a paramagnetic material prefer to align along the direction of the field, however this is disrupted by thermal energy. Upon cooling, the influence of thermal energy diminishes and the electrons tend more towards alignment. This relationship is governed by the Curie Weiss law (*eq. 3.17.*), where  $\chi$  is the magnetic susceptibility,  $C$  is the Curie constant,  $T$  is absolute temperature and  $\theta$  is the Weiss constant.

$$\chi = \frac{C}{T - \theta} \quad (\text{eq. 3.17.})$$

$$\mu = \sqrt{\frac{3k}{\mu_0 N_A} \chi (T - \theta)} \quad (\text{eq. 3.18.})$$

This paramagnetic relationship between the magnetic susceptibility and temperature creates a characteristic plot (*Figure 3.10a.*), which when the Curie Weiss law is applied the magnetic moment can be calculated (*eq. 3.18.*). By taking the inverse of the magnetic susceptibility against the temperature, the presence of dominating ferro- or antiferro-magnetic interactions can be determined through the fitting of a line, through a temperature range, of the inverse Curie-Weiss law. When this linear extrapolation intercepts the  $x$ -axis at 0 K, then only Curie-paramagnetic interactions are present (*Figure 3.10b*) however, when ferromagnetic interactions, a spontaneous parallel alignment between adjacent spins, dominate the extrapolated value of the  $x$ -axis intercept is higher than 0 K (*Figure 3.10b.*). The opposite is true when antiferromagnetic interactions, a spontaneous anti-parallel alignment between adjacent spins, dominates, where the extrapolated value of the  $x$ -axis intercept shifts to lower than 0 K (*Figure 3.10b*). In reality, at low temperatures a curved deviation from the linear extrapolation is often observed.

Magnetic susceptibility measurements taken for this work were conducted on a SQUID-Magnetometer MPMS3 (Quantum Design, Darmstadt, Germany) (*Figure 3.11.*)

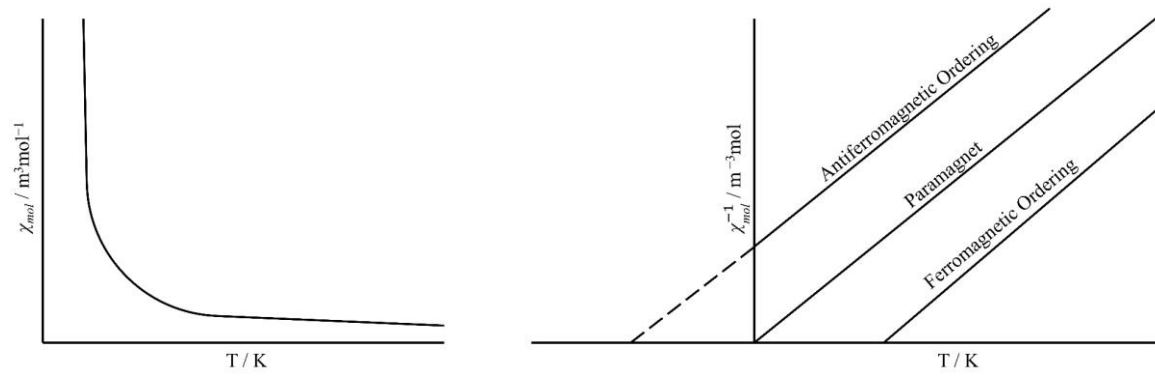


Figure 3.10. a) Magnetic susceptibility against temperature for a Curie-paramagnet; b) Inverse magnetic susceptibility against temperature for a Curie-paramagnet: without, with dominating ferromagnetic and antiferromagnetic interactions.

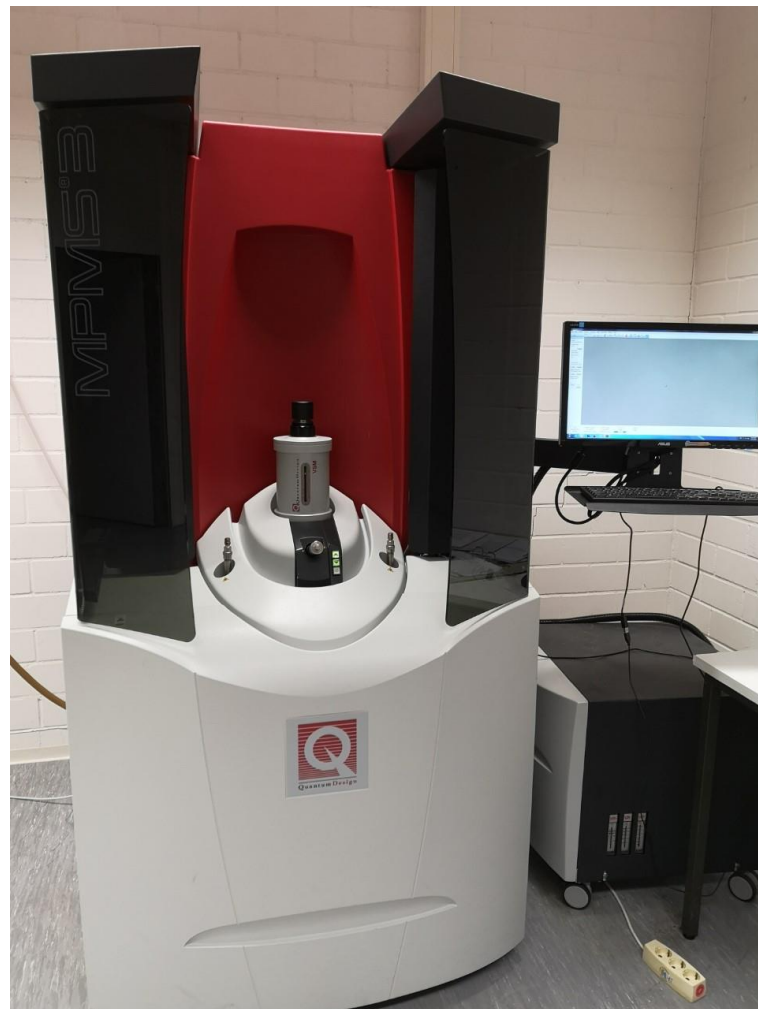


Figure 3.11. SQUID-Magnetometer MPMS3 (Quantum Design, Darmstadt, Germany).

### 3.3. Raman spectroscopy

Raman spectroscopy is an analytical technique, where a monochromatic light, typically a laser, is beamed onto the sample, where the incident photon excites an electron to an excited vibrational state. From here, the electron can decay and emit a scattered photon in three different ways (*Figure 3.12.*). The electron can decay back to the same vibrational energy level from which it started (Rayleigh scattering), or it can decay to a higher (Stokes Raman scattering) or lower (anti-Stokes Raman scattering) vibrational energy level relative to the energy level from which it started. The energy difference between the initial and final vibrational levels are plotted, along with the intensity, into a spectrum. From this spectrum the peaks, which are assigned to vibrational modes, can be used to identify the distortion, stretching and bending frequencies of bonds that have been excited and from this the type of bonding and atoms involved can be determined.

For this research Raman spectroscopy was conducted using a confocal polarisation microscope BX51 (Olympus, Japan). The light sources available were a green laser ( $\lambda = 532$  nm) and a red laser ( $\lambda = 638$  nm).

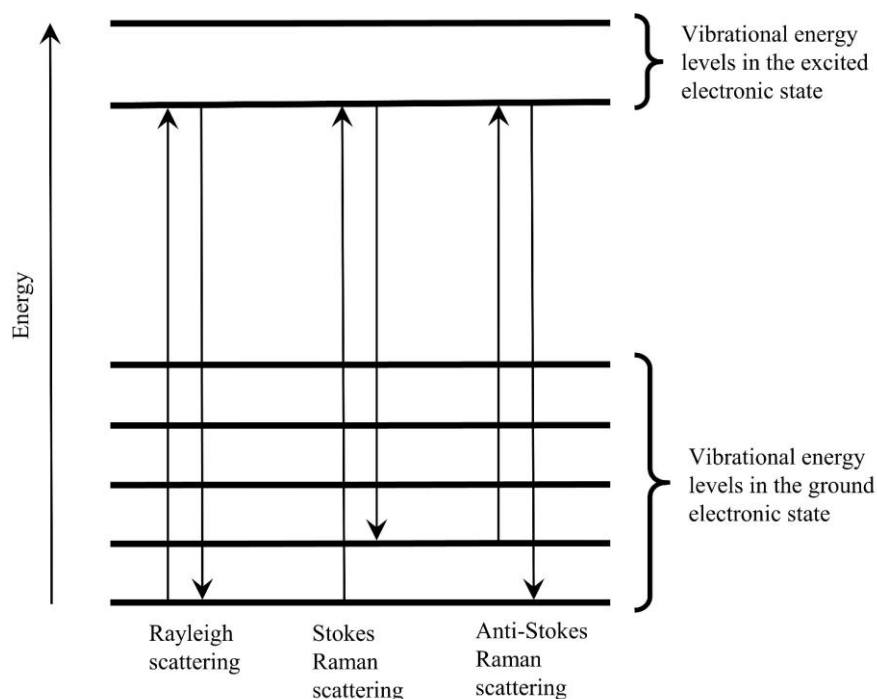


Figure 3.12. Energy diagrams for light scattering: Rayleigh scattering, Stokes and anti-Stokes scattering.

### 3.4. Mössbauer Spectroscopy

Mössbauer spectroscopy observes the transitions between ground and excited states within the nuclei of a sample, using a monochromatic beam of  $\gamma$ -rays from a predetermined source. Typically, the  $\gamma$ -rays are absorbed by a nuclei and released as recoil energy however, in a crystalline solid the  $\gamma$ -rays are absorbed and released, with negligible loss of energy to recoil, by the same isotope in the sample. The recoil energy is instead distributed through the solid. When the source of  $\gamma$ -rays and the nuclei are the same, then the resonant absorption condition of  $\gamma$ -rays is satisfied and the resulting absorption is plotted against a function of energy. From this spectra information regarding oxidation states, coordination numbers and bonding character can be determined.

One of the most used applications of Mössbauer spectroscopy is for the analysis of iron containing species. For this, the radioactive isotope  $^{57}\text{Fe}$  is typically used as the source of the  $\gamma$ -rays, where only  $^{57}\text{Fe}$  atoms in the sample absorb the radiation. The position of the resulting peak or peaks can be compared with a standard, usually  $\alpha$ -Fe, and the variance from the standard, chemical shift, can give valuable information about oxidation state and coordination number. Splitting of the peaks can occur, quadrupole splitting, which is sensitive to the atomic surroundings, such as coordination, and the ligand field splitting of the  $^{57}\text{Fe}$ . A second form of splitting, magnetic hyperfine splitting, can be also present and is evidence of magnetic ordering.

The Mössbauer spectra presented in this work were measured at the Nuclear Resonance beamline (ID18) at the European Synchrotron Radiation Facility (ESRF), Grenoble, France.<sup>[128]</sup>

### **3.5. Elemental Analysis**

#### **3.5.1. Energy dispersive X-ray analysis**

Energy dispersive X-ray analysis is a technique that allows for a chemical analysis of a sample and can identify any element heavier than boron. This is achieved by the bombardment of the sample by a stream of high energy electrons, which produce varying X-rays from the sample. The intensity of these X-rays is plotted in a spectrum against the energy at which the X-ray was produced. Every element produces a characteristic wavelength, which is determined by the difference in energy of the energy levels ( $E_2 - E_1$ ). This characteristic wavelength can be used to identify which elements are present in a sample. This assignment of peaks, along with the ratio of intensities, allows the chemical composition and chemical formula to be calculated.

The results in this work produced by energy dispersive X-ray analysis, were measured using a Cameca SX-100 electron microscope (Cameca, Gennevilliers, France).

#### **3.5.2. Wavelength dispersive X-ray spectroscopy**

This technique operates with the same principle as energy dispersive X-ray analysis. However, it focusses on only one particular wavelength at a time, instead of producing a broad spectrum. This allows for precise quantitative and qualitative measurements of elements that produce similar X-ray wavelengths.

The results in this work produced by wavelength dispersive X-ray analysis, were measured using a Cameca SX-100 electron microscope, with several spectrometer attachments to allow quantitative measurements (Cameca, Gennevilliers, France).

### **3.6. Thermal Analysis**

#### **3.6.1. Differential Thermal Analysis**

Differential thermal analysis investigates the thermodynamic properties of a material. To achieve this, a sample and reference are heated, under the identical heating program, and changes in mass and, to a general extent, the enthalpy can be monitored. The curve that is produced after the measurement can show the percentage mass increase or decrease of the sample during heating, from which the potential liberation, adsorption or reaction with gases can be calculated. Another aspect of the curve is the change in enthalpy, where investigations into chemical reactions and phase transitions can also be conducted.

The differential thermal analysis results presented in this work were produced using a STA 449 C instrument (Netzsch, Selb, Germany).

#### **3.6.2. Differential Scanning Calorimetry**

In many ways similar to differential thermal analysis, differential scanning calorimetry focuses primarily on measuring the amount of heat needed to increase the temperature of the sample, compared to the linear heating of the reference over time. From this, changes in enthalpy can be measured and identified, such as crystallisation or phase transitions.

During this work, differential scanning calorimetry measurements were performed using a DSC-204 Phoenix differential calorimeter (Netzsch, Selb, Germany).





## 4. High pressure synthesis of iron containing nitrides

### 4.1. Overview of iron nitrides

The existence of binary iron nitrides has been known since the mid-19<sup>th</sup> century.<sup>[129,130]</sup> Since then, a large range of iron nitrides have been produced, from more iron rich phases, such as  $\alpha''$ -Fe<sub>16</sub>N<sub>2</sub> or  $\alpha'$ -Fe<sub>8</sub>N, through  $\gamma'$ -Fe<sub>4</sub>N,  $\epsilon$ -Fe<sub>3</sub>N<sub>1±x</sub> and  $\zeta$ -Fe<sub>2</sub>N, to more nitrogen rich phases such as cubic FeN.<sup>[8,131]</sup> The introduction of nitrogen into an iron lattice enhances the materials hardness and resistance to corrosion, making them ideal for industrial coatings, as well as producing interesting magnetic properties.<sup>[8,132–135]</sup> More recent investigations have shown that iron nitrides can be used as catalysts in the production of hydrocarbons<sup>[136]</sup> and as a potential agent in the treatment of cancer cells.<sup>[137]</sup>

Iron nitrides are easily synthesised by direct nitridation, under ammonia, of elemental iron. This method, however, results in several phases of iron nitride. In depth investigations produced a non-equilibrium phase diagram, which for the synthesis of a desired iron nitride careful consideration must be given (*Figure 4.1*).<sup>[8,138–140]</sup> This non-equilibrium phase diagram shows, not only the synthesis temperature range of particular iron nitrides, but also the homogeneity range for the respective iron nitride. The iron nitride to date with the largest homogeneity range is  $\epsilon$ -Fe<sub>3</sub>N<sub>1±x</sub> ( $-0.3 \leq x \leq 0.5$ ), which enjoys a large range of nitrogen content.<sup>[141]</sup> Consideration also has to be taken about the flow rate of ammonia and possible mixture of gases, a good example is the formation of  $\epsilon$ -Fe<sub>3</sub>N<sub>1±x</sub> and  $\gamma'$ -Fe<sub>4</sub>N. To produce single phase  $\epsilon$ -Fe<sub>3</sub>N<sub>1±x</sub>,  $\alpha$ -Fe must be simply heated at 723 K under a constant flow of ammonia. However, the synthesis of  $\gamma'$ -Fe<sub>4</sub>N requires a specific ratio of ammonia and hydrogen to produce the single phase iron nitride. This specific ratio is required to achieve the nitriding-potential needed, as demonstrated by the Lehrer diagram,<sup>[142]</sup> to produce single phase  $\gamma'$ -Fe<sub>4</sub>N, and not  $\epsilon$ -Fe<sub>3</sub>N<sub>1±x</sub>.

The synthesis of the metastable  $\alpha''$ -Fe<sub>16</sub>N<sub>2</sub>/ $\alpha'$ -Fe<sub>8</sub>N has a much more specific reaction program, due to the product decomposing at moderate temperatures and every step of the reaction being kinetically controlled. This means that experimental conditions, such as heating and gas flow rates, have a large impact on the resulting purity of the product.<sup>[143]</sup> This synthesis requires the reduction of  $\gamma$ -Fe<sub>2</sub>O<sub>3</sub> to elemental  $\gamma$ -Fe, before a long reaction period, at a precise temperature, under a specific mix of ammonia and hydrogen.<sup>[143,144]</sup>

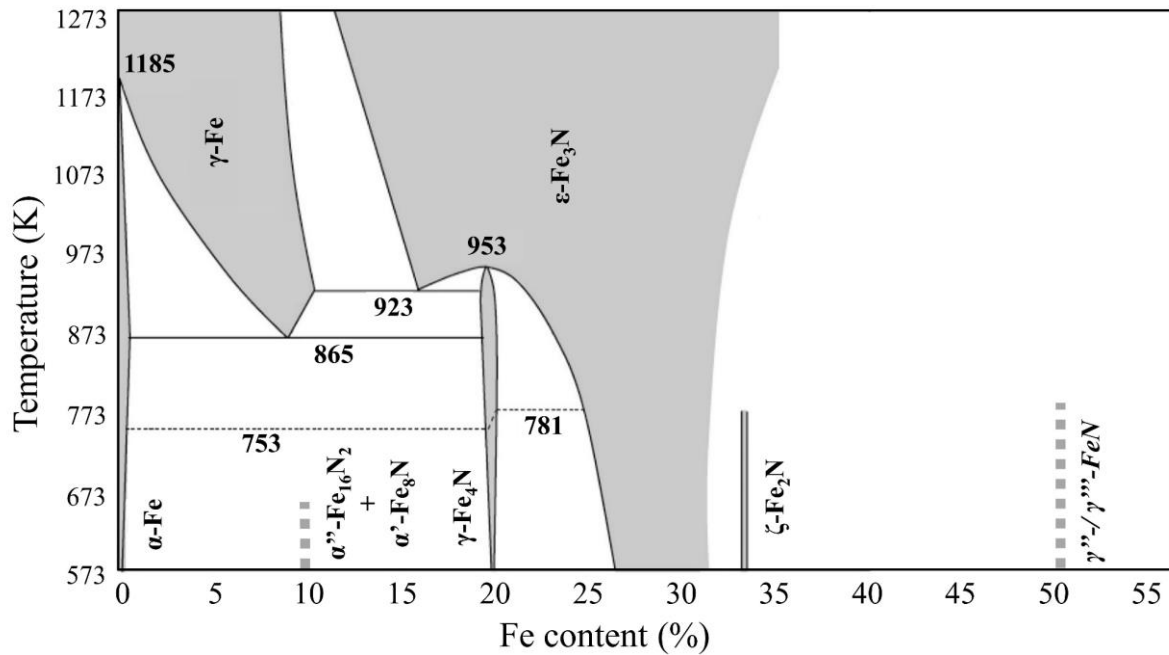


Figure 4.1. Non-equilibrium phase diagram of iron nitride, with metastable phases presented with vertical dashed lines.<sup>[8,145]</sup> Adapted with permission from Springer Nature: Springer, Bull. Alloy Phase Diagr., The Fe-N (Iron-Nitrogen) system, H. A. Wriedt, N. A. Gokcen and R. H. Nafziger, 1987.

Certain iron nitrides are not so easily produced and instead rely on other more elaborate or complicated synthesis techniques. The aforementioned cubic FeN is produced through reactive D.C. sputtering of elemental iron.<sup>[131]</sup> Synthesis of iron-nitrogen phases under high pressure from an excess of  $N_2$ , typically, produce materials with a high nitrogen content. These pressures are achieved using diamond anvil cells and have recently produced materials with interesting compositions such as:  $\beta$ -/ $\epsilon$ - $Fe_7N_3$ ,  $Fe_3N_2$ ,  $FeN_2$  and  $FeN_4$ .<sup>[2,146-148]</sup>

At elevated temperatures, iron nitrides lose nitrogen and thus undergo structural transitions to more iron rich phases. The introduction of high pressure prevents this loss of nitrogen and therefore allows the investigation of iron nitrides under high pressure and temperature, with barely any loss of nitrogen. This experimental procedure was taken with  $\gamma'$ - $Fe_4N$  and resulted in a reconstructive phase transition to a nitrogen deficient  $\epsilon$ - $Fe_3N_{1+x}$  ( $-0.3 \leq x \leq -0.05$ ), which produced the first single crystal of  $\epsilon$ - $Fe_3N_{1+x}$ .<sup>[149,150]</sup> Single crystals of  $\gamma'$ - $Fe_{4-x}Ni_xN$ , which were at first mistakenly described as  $\gamma'$ - $Fe_4N$ , have previously been produced under ammonothermal conditions.<sup>[151,152]</sup> The same pressure induced crystallisation approach was taken with  $\epsilon$ - $Fe_3N$  and produced single crystals of the same composition,<sup>[145]</sup> while  $\zeta$ - $Fe_2N$  recrystallised into a nitrogen rich  $\epsilon$ - $Fe_3N_{1+x}$  ( $x = 0.5$ ).<sup>[153]</sup>

## 4.2. Synthesis and characterisation of NiAs-type FeN

### 4.2.1. Introduction

Recently, there has been a surge in discoveries of iron-nitrogen materials with a high nitrogen content, such as FeN<sub>2</sub> or FeN<sub>4</sub>.<sup>[31,148]</sup> However, at the time of this research the known iron nitride with the highest nitrogen content was cubic FeN.

Since the cubic FeN was reported, there has been much debate with regards to its structure.<sup>[131,154–156]</sup> There is evidence to support it crystallising in the rock salt structure,  $\gamma''$ -FeN,<sup>[157–160]</sup> and also in the zinc blende structure,  $\gamma'''$ -FeN.<sup>[161,162]</sup> A separate publication, suggests that the cubic FeN would prefer the zinc blende structure, while FeN<sub>x</sub> ( $0.5 \leq x \leq 0.7$ ) would prefer the rock salt structure.<sup>[161]</sup> This discussion still remains controversial, however single phase thin films of  $\gamma'''$ -FeN have been shown to adopt the zinc blende structure.<sup>[156]</sup> An independent investigation predicated that FeN could also crystallise in the hexagonal NiAs-type structure.<sup>[163]</sup>

Before the aforementioned FeN<sub>2</sub> had been produced, only the alkali metal diazenides, Li<sub>2</sub>N<sub>2</sub>,<sup>[40]</sup> alkaline earth metal diazenides, MN<sub>2</sub> ( $M = \text{Ca} - \text{Ba}$ ),<sup>[39,164]</sup> Li<sub>2</sub>Ca<sub>3</sub>[N<sub>2</sub>]<sub>3</sub>,<sup>[38]</sup> Sr<sub>4</sub>N<sub>2</sub>[N<sub>2</sub>],<sup>[165]</sup> 4d and 5d metal pernitrides, MN<sub>2</sub> ( $M = \text{Pt}, \text{Ir}, \text{Pd}, \text{Os}$ )<sup>[23,25,35,166]</sup> and 3d metal pernitride TiN<sub>2</sub> were known.<sup>[18]</sup> Electronic structure calculations suggested FeN<sub>2</sub> could be produced above the annealing temperature of elemental iron, 1000 K, at a pressure of 17 GPa and would crystallise in the space group  $R\bar{3}m$  (No. 166).<sup>[27]</sup> The following experiment initially focussed on producing FeN<sub>2</sub> using these conditions.

When high pressures are used, then knowledge about the effect of high pressure on magnetic properties is crucial. The effect of pressure on elemental  $\alpha$ -Fe has been well documented.<sup>[167–170]</sup> Upon increasing pressure the ferromagnetic  $\alpha$ -Fe (*bcc*) undergoes a phase transition to  $\epsilon$ -Fe (*hcp*), which has no permanent magnetic moment. Using Mössbauer spectroscopy this reversible transition can be observed through the reversible degeneration of the ferromagnetism (*Figure 4.2*). The same magnetic behaviour is also observed with regards to increasing temperature instead of pressure.<sup>[171]</sup>

The nitrogen content within an iron nitride also has an influence on the magnetic properties. Iron rich  $\gamma'$ -Fe<sub>4</sub>N actually exhibits, at room temperature, two magnetic sextets (Figure 4.3.). These sextets arise from there being two crystallographically different iron positions, with different electronic situations, within the perovskite type structure.<sup>[171]</sup> The well defined magnetic sextet of  $\epsilon$ -Fe<sub>3</sub>N<sub>x</sub>, displays a clear degradation with increasing nitrogen content, until  $x = 1.25$  at which the sextet disappears and is replaced by a diamagnetic singlet. This singlet continues being observed through to the more nitrogen rich phase  $\zeta$ -Fe<sub>2</sub>N (Figure 4.3.).<sup>[171]</sup>

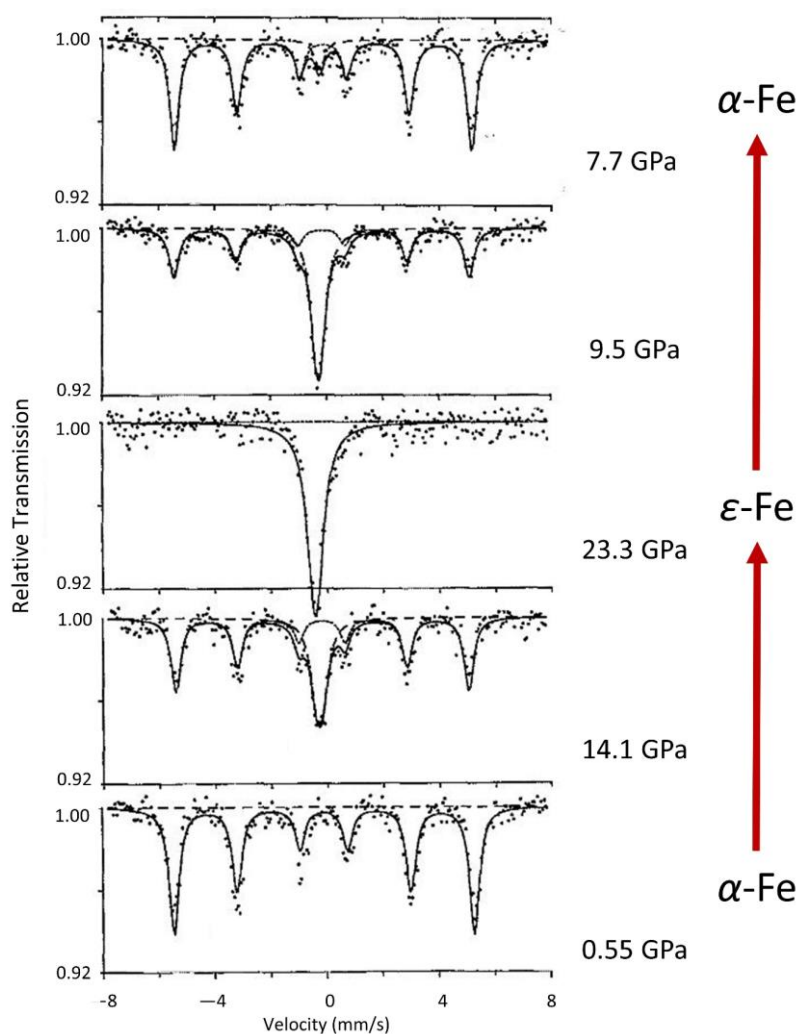


Figure 4.2. Mössbauer spectra of the  $\alpha$ -Fe to  $\epsilon$ -Fe phase transition with pressure.<sup>[167]</sup> Reprinted from R. D. Taylor, M. P. Pasternak, R. Jeanloz, *J. Appl. Phys.* **1991**, *69*, 6126–6128, with the permission of AIP Publishing.

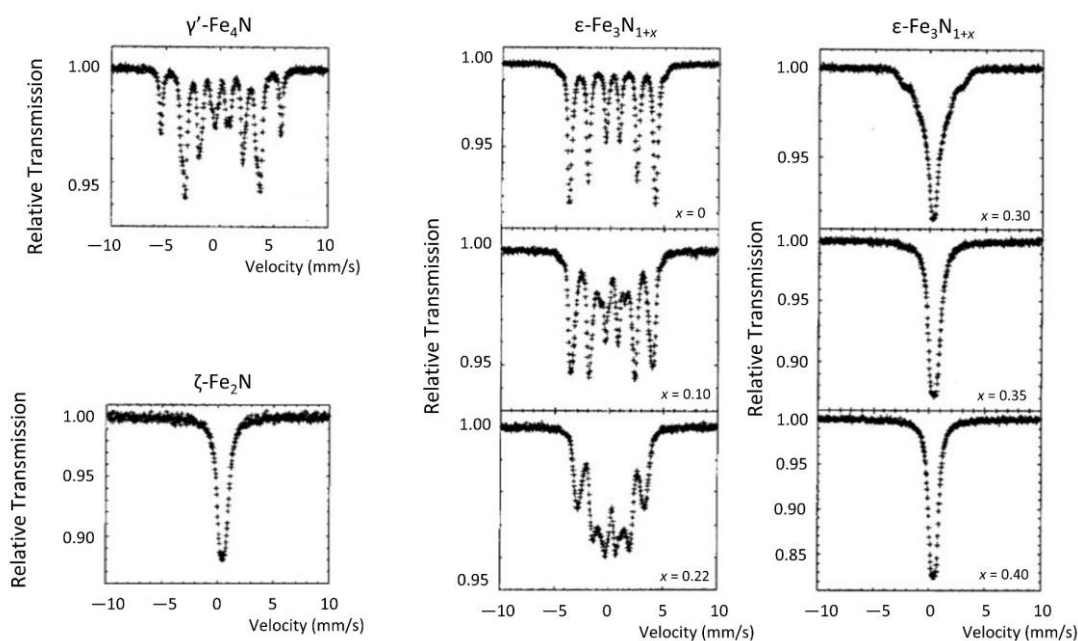


Figure 4.3. Mössbauer spectra, at room temperature, of  $\gamma'$ -Fe<sub>4</sub>N,  $\epsilon$ -Fe<sub>3</sub>N<sub>x</sub> and  $\zeta$ -Fe<sub>2</sub>N magnetic transition with increasing nitrogen content.<sup>[171]</sup> Adapted from V. Ksenofontov, S. Reiman, M. Waldeck, R. Niewa, R. Kniep, P. Gütlich, *Z. Anorg. Allg. Chem.* **2003**, 629, 1787–1794, with permission from WILEY.

The following part of this work was conducted in a collaboration, with several key contributions. Prof. R. Niewa (Institut für Anorganische Chemie, Universität Stuttgart, Germany) and Priv.-Doz. Dr. U. Schwarz (Max-Planck-Institut für Chemische Physik fester Stoffe, Germany) conducted the high pressure experiments at ESRF, Grenoble, France. The diamond anvil cells were provided by Dr. M. Bykov and Prof. L. Dubrovinsky (Bayerisches Geoinstitut, Universität Bayreuth, Germany). Dr. C. McCammon (Bayerisches Geoinstitut, Universität Bayreuth, Germany) performed the refinement of the Mössbauer spectra. Dr. I. Kuppenko (ESRF, Grenoble, France) operated the ID18 beamline at the ESRF, Grenoble, France. Dr. S. Steinberg and Prof. R. Dronskowski (Institut für Anorganische Chemie, RWTH Aachen, Germany) provided electronic structure calculations. Lev Akselrud (Max-Planck-Institut für Chemische Physik fester Stoffe, Germany) gave support in Rietveld structure refinements.

#### 4.2.2. Synthesis of NiAs-type FeN

For the experiment both elemental  $^{57}\text{Fe}$  and  $\zeta\text{-}^{57}\text{Fe}_2\text{N}$  were used. Single phase  $\zeta\text{-}^{57}\text{Fe}_2\text{N}$  was prepared from elemental  $^{57}\text{Fe}$ , heated under  $\text{NH}_3$  flow (60 mL/minute) at 686 K for 60 hours. The temperature was then decreased, over 6 hours, to 386 K, where it stayed for one hour before cooling to room temperature.<sup>[172]</sup> The resulting product was confirmed to be single phase  $\zeta\text{-}^{57}\text{Fe}_2\text{N}$  through powder X-ray diffraction (Figure 4.4.).

Two different kind of experiments were conducted, one diamond anvil cell was filled with  $^{57}\text{Fe}$  and the other diamond anvil cell was filled with  $\zeta\text{-}^{57}\text{Fe}_2\text{N}$ . Both experiments used  $\text{N}_2$  as both a reactant and pressure medium. Samples were repeatedly heated to varying temperatures, as high as 1300 K, with cells being subjected to varying pressures up to 45 GPa. *In-situ* measurements were performed, along with variations in pressure and temperature, before returning to ambient conditions.

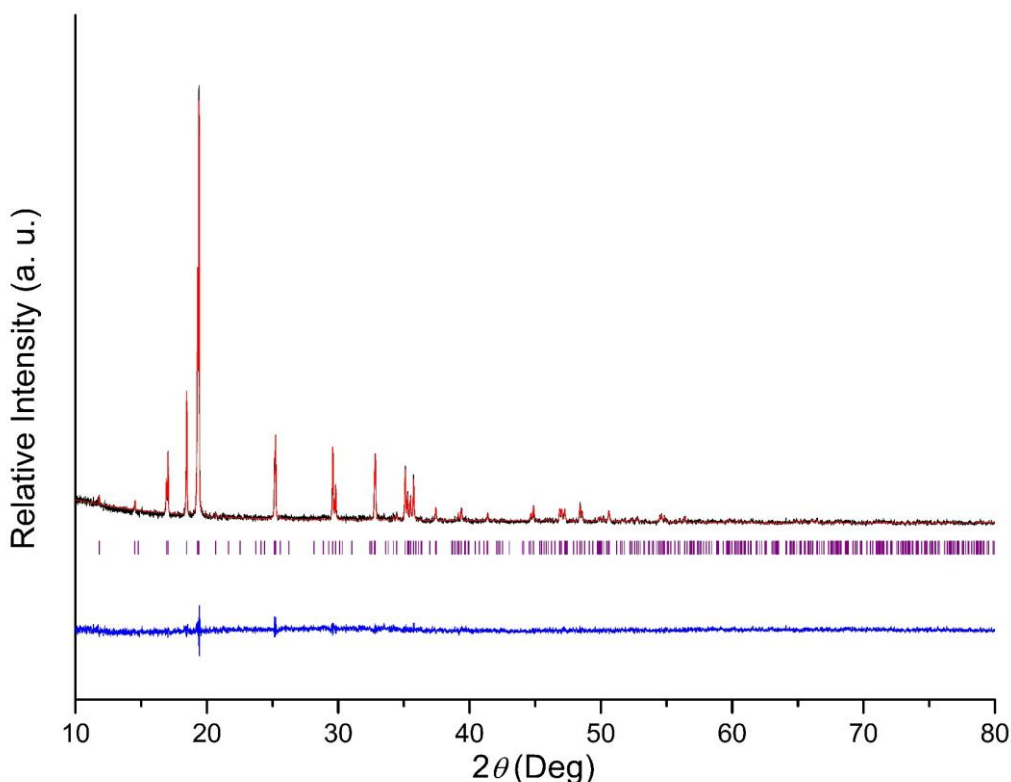


Figure 4.4. Graphical representation of Rietveld structural refinement of  $\zeta\text{-}^{57}\text{Fe}_2\text{N}$ . The observed pattern is shown in black, the calculated one in red, possible Bragg reflection positions are in purple and the difference in blue.

One of the weaknesses of diamond anvil cell reactions, is that different reaction environments are present within the cell. This is in part due to the relatively large sample area in comparison to the heating laser. Each sample is divided into regions for diffraction measurements and the most ‘clean’ patterns are selected, ones not containing reflections of the gasket material, Re, solid N<sub>2</sub> or reagent. X-ray diffraction patterns were measured using synchrotron radiation ( $\lambda = 0.415054 \text{ \AA}$ ) at ID09 beam-line at ESRF, Grenoble, with a beam size of roughly 10  $\mu\text{m}$  FWHM and Mössbauer spectroscopy was conducted using the ID18 beam-line at ESRF, Grenoble.

### 4.2.3. Characterisation

#### 4.2.3.1. Structure determination of NiAs-type FeN

Samples that were heated to 1300 K, at pressures below 10 GPa, formed iron nitrides with the composition of  $\zeta\text{-}^{57}\text{Fe}_2\text{N}/\varepsilon\text{-}^{57}\text{Fe}_3\text{N}_{1.4}$ .<sup>[171]</sup> Determination of which specific phase is rather difficult, since both are structurally very similar (*Figure 4.5*). This similarity is due to both phases having hexagonal close packing of Fe atoms with a different pattern of N in the octahedra holes, which produces diffraction patterns that are very similar. The most notable differences being that  $\zeta\text{-Fe}_2\text{N}$  has a shoulder on the most intense reflection and splitting is observed in certain reflections, due to variations in the unit cell parameters and orthorhombic splitting in  $\zeta\text{-Fe}_2\text{N}$ . However, two samples that were subjected to pressures of over 10 GPa produced a new phase after annealing. One sample had  $\zeta\text{-}^{57}\text{Fe}_2\text{N}$  as a reactant and the other had  $^{57}\text{Fe}$ .

The X-ray diffraction patterns, at ambient temperature, of the first diamond anvil cell, with  $\zeta\text{-}^{57}\text{Fe}_2\text{N}$  as a reagent, were measured at 13.3 GPa and also at ambient pressure, 0.1 MPa. Both patterns contained the new phase, which did not correspond to the predicted FeN<sub>2</sub>.<sup>[27]</sup> The pattern was indexed onto a hexagonal unit cell based on a  $\varepsilon\text{-Fe}$  subcell. Rietveld refinements (*Figure 4.6* and *Table 4.1*.) showed a NiAs-type crystal structure of this new phase, resulting in a composition of FeN. Heating of the product, below 10 GPa, results in the formation of  $\zeta\text{-}^{57}\text{Fe}_2\text{N}/\varepsilon\text{-}^{57}\text{Fe}_3\text{N}_{1.4}$ , which indicates that NiAs-type FeN decomposes upon heating at pressures below 10 GPa. Most patterns contain extra reflections, which were assigned to the presence of Re, N<sub>2</sub> or unreacted  $\zeta\text{-}^{57}\text{Fe}_2\text{N}$ .

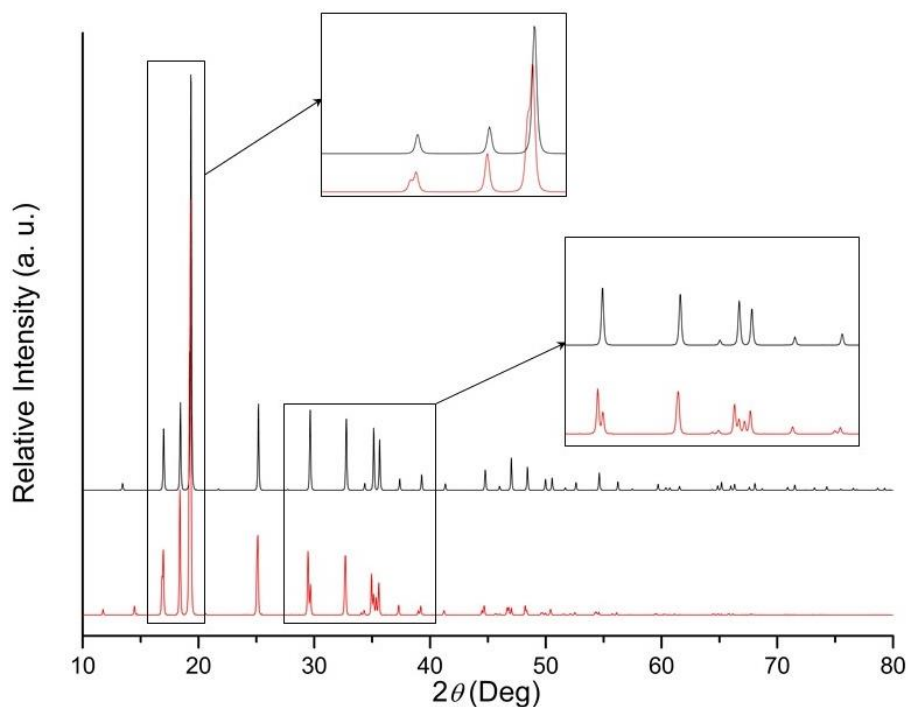


Figure 4.5. Comparison of simulated diffraction patterns of  $\epsilon$ - $\text{Fe}_3\text{N}_{1.47}$  (black)<sup>[153]</sup> and  $\zeta$ - $\text{Fe}_2\text{N}_{0.94}$  (red).<sup>[173]</sup>

X-ray diffraction measurements, at ambient temperature, of the second diamond anvil cell, with  $^{57}\text{Fe}$  as a reagent, were measured at 4.44 GPa, after heating to 1500 K at 13.9 GPa. This sample was indexed onto a hexagonal unit cell and refined using the same NiAs-type FeN configuration (Figure 4.7. and Table 4.1.). This proves that the NiAs-type FeN can be formed from both elemental iron, as well as  $\zeta$ - $\text{Fe}_2\text{N}$ . Reflections which did not belong to NiAs-type FeN were again attributed to the presence of Re,  $\text{N}_2$  or  $\zeta$ - $^{57}\text{Fe}_2\text{N}$ .

Structural refinements of the measured samples, at various pressures and sample positions, suggest a broad homogeneity range for NiAs-type  $\text{Fe}_x\text{N}$ , where  $x$  is estimated to range from 0.60(5) to 1.0(1). This homogeneity range can be caused by either random vacancies in (0, 0, 0) and (0, 0,  $\frac{1}{2}$ ) or (0, 0, 0) being fully occupied and (0, 0,  $\frac{1}{2}$ ) being partially occupied. This homogeneity range is also observed in classic NiAs-type structures, such as  $\text{Fe}_x\text{S}$ ,  $\text{Co}_x\text{Te}$ ,  $\text{Cr}_x\text{S}$  and  $\text{Fe}_x\text{Te}$ .<sup>[174]</sup> For each classic example the homogeneity range varies and outside of this range transitions to different phases occurs. The classic examples with the broadest homogeneity ranges are  $\text{Co}_x\text{Te}$  ( $0.5 \leq x \leq 1$ ) and  $\text{Fe}_x\text{Te}$  ( $0.66 \leq x \leq 1$ ), which fit well with the values observed for  $\text{Fe}_x\text{N}$ . The metal deficient phases of  $\text{Co}_x\text{Te}$  and  $\text{Fe}_x\text{Te}$ , where  $x$  is around 0.5, undergo a transition to the layered  $\text{CdI}_2$  type structure, due to the vacancy at (0, 0,  $\frac{1}{2}$ ). It would be interesting to determine if this characteristic is also possible for  $\text{Fe}_x\text{N}$ .



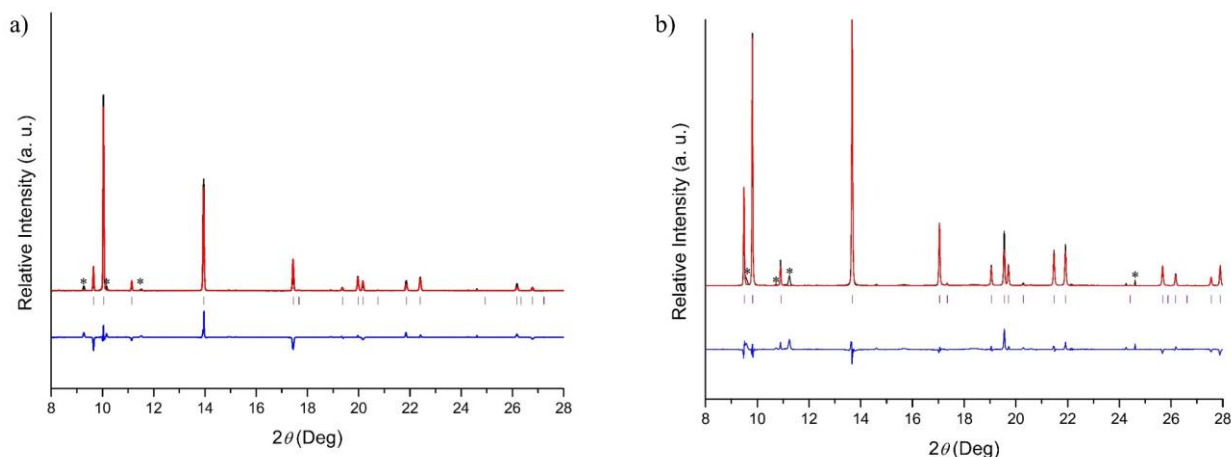


Figure 4.6. Graphical representations of Rietveld structural refinements of NiAs-type FeN from X-ray powder diffraction measurements, using synchrotron radiation ( $\lambda = 0.415054 \text{ \AA}$ ), at a) 13.3 GPa, marked reflections (\*) are assigned to a  $\delta\text{-N}_2$  and b) 0.1 MPa, the origin of the marked reflections (\*) could not be determined. The observed pattern is shown in black, the calculated one in red, possible Bragg reflection positions are in purple and the difference in blue.

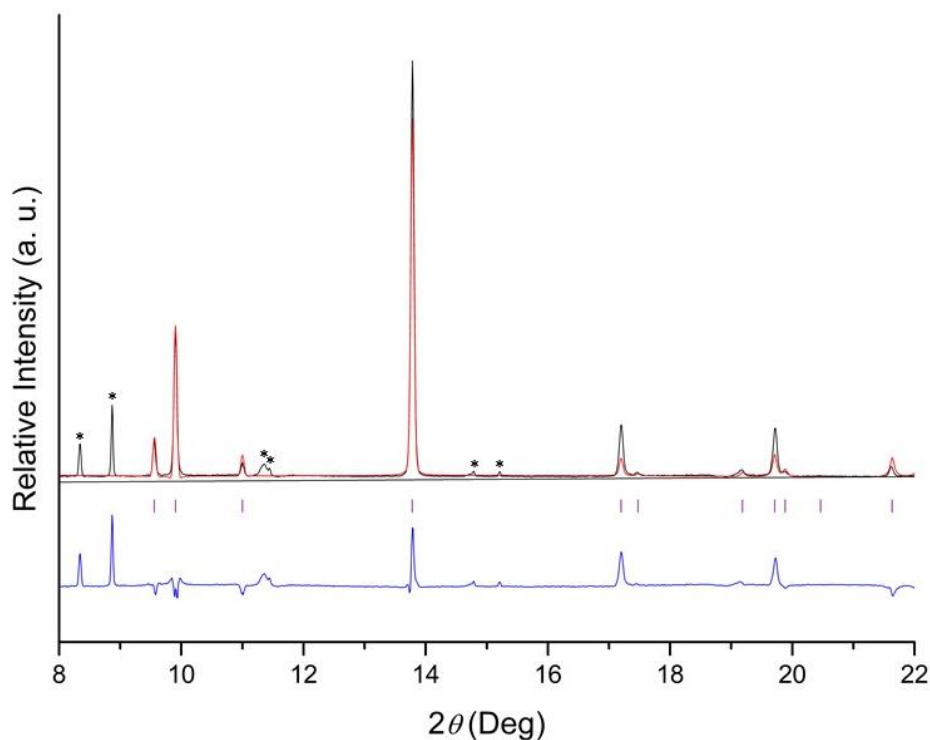


Figure 4.7. Graphical representation of Rietveld structural refinement of NiAs-type FeN from X-Ray powder diffraction measurements, using synchrotron radiation ( $\lambda = 0.415054 \text{ \AA}$ ), at 4.44 GPa. The observed pattern is shown in black, the calculated one in red, possible Bragg reflection positions are in purple and the difference in blue. The marked reflections (\*) are assigned to  $\delta\text{-N}_2$ .

Table 4.1. Unit cell and atomic positions obtained for NiAs-type FeN, with varying pressure, through Rietveld refinement and values for quality of refinement.

	13.3 GPa	4.44 GPa	0.1 MPa
Space Group	$P6_3/mmc$ (No. 194)		
$a/\text{\AA}$	2.737(3)	2.776(7)	2.800(1)
$c/\text{\AA}$	4.933(5)	4.981(1)	5.014(3)
$V/\text{\AA}^3$	32.005	33.236	34.037
$R_{wp}/\%$	14.70	21.30	7.40
$R_{Bragg}/\%$	16.2	20.30	9.10
	Wyckoff site	Atomic Position	
Fe	$2a$	0, 0, 0	
N	$2c$	$1/3, 2/3, 1/4$	

#### 4.2.3.2. Crystal structure

The NiAs-type FeN consists of hexagonal closed packing of nitride anions, with the iron cations occupying all octahedral holes, to form FeN<sub>6</sub> octahedra. These octahedra face share with each other to form infinite chains along the  $c$  direction (*Figure 4.8.*). At the time of writing, this appears to be not only the first observation of this face-sharing arrangement of FeN<sub>6</sub> in a nitride, but also the only NiAs-type 3d transition-metal nitride. Predictions of certain NiAs-type 3d transition-metal nitrides have been suggested, such as VN<sup>[175]</sup> and MoN,<sup>[176]</sup> however they have yet to be produced and only those of heavier atoms have been successfully synthesised, like  $\delta$ -NbN<sup>[177]</sup> and TaN.<sup>[178]</sup>

By comparing the interatomic iron distances of NiAs-type FeN and  $\epsilon$ -Fe, which also contains *hcp* of atoms,<sup>[179]</sup> there is only a slight change in Fe–Fe distance along the  $c$ -axis (2.467 Å versus 2.442 Å). However, along the  $a$ -axis there is a more notable difference in the Fe–Fe distance of the NiAs-type FeN and  $\epsilon$ -Fe (2.737 Å versus 2.473 Å). This difference is believed to be due to the preference of two nitride anions to be further apart than the corresponding iron atoms in  $\epsilon$ -Fe. The interatomic distance between iron and nitrogen is 2.0458(1) Å, which is at the upper limit of what is typically seen for a Fe–N bond (1.8 Å – 2.0 Å).<sup>[152,173]</sup> All interatomic distances in the NiAs-type FeN appear to barely change with increasing pressure.

A detail of note is that NiAs-type FeN, when compared with the NiAs structure itself, has a relatively high  $c/a$  ratio. This is quite common for NiAs-type compounds of transition metals with group V or VI elements as anions, however it does have the smallest ratio of these type of compounds (Table 4.2.).

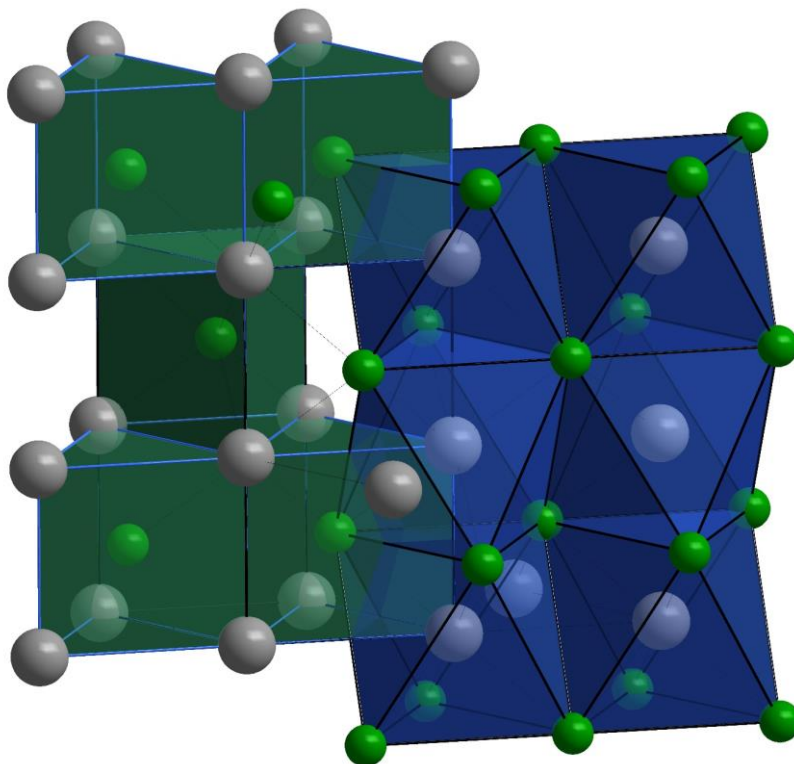


Figure 4.8. Section of the crystal structure of NiAs-type FeN. Depicting the face-sharing of the  $\text{FeN}_6$  octahedra (blue) and the trigonal-prismatic coordination environment of the nitride ions (green).

Table 4.2. Comparison of the  $c/a$  ratios of NiAs-type FeN, under pressure and ambient pressure, with related NiAs-type compounds.

NiAs-Type Compound	$c/a$ ratio
NiAs	1.3920 <sup>[180]</sup>
FeN (0.1 MPa)	1.7911
FeN (13.3 GPa)	1.8015
$\delta$ -NbN	1.8665 <sup>[177]</sup>
TiS	1.9515 <sup>[181]</sup>
VP	1.9560 <sup>[182]</sup>

### 4.2.3.3. Mössbauer Spectroscopy

The starting materials,  $\zeta\text{-}^{57}\text{Fe}_2\text{N}$  and  $^{57}\text{Fe}$ , were measured using Mössbauer spectroscopy as a comparison for any change that would occur during the reaction.  $\zeta\text{-}^{57}\text{Fe}_2\text{N}$  produced the typical diamagnetic singlet, with a characteristic chemical shift value of 0.4 mm/s (*Figure 4.9.*), while  $^{57}\text{Fe}$  produced the well defined magnetic sextet and the expected chemical shift of  $-0.073$  mm/s (*Figure 4.9.*). If no chemical reaction with  $\text{N}_2$  occurred, then the expected behaviour, with increasing pressure and temperature, would be that the singlet of  $\zeta\text{-}^{57}\text{Fe}_2\text{N}$  would remain throughout the experiment and the sextet of  $^{57}\text{Fe}$  would convert to a singlet, corresponding to the conversion to  $\epsilon\text{-}^{57}\text{Fe}$ . However, during the experiment both predicted trends were not observed. Instead, both produced spectra with a major magnetic sextet component and a minor singlet component (*Figures 4.9. and 4.10.*).

After the reaction, both spectra contained a magnetic sextet component and a minor singlet component. The resulting sextet observed in both diamond anvil cells, one with the  $\zeta\text{-}^{57}\text{Fe}_2\text{N}$  as a reactant and the other containing  $\zeta\text{-}^{57}\text{Fe}$  as an reactant, belongs to the same phase. This is evident when the values from each spectra are compared. The chemical shift of the product produced from both  $\zeta\text{-}^{57}\text{Fe}_2\text{N}$  and  $\zeta\text{-}^{57}\text{Fe}$  are 0.356 mm/s and 0.305 mm/s respectively. This near identical chemical shift indicates that both sextets belong to the same phase. Also, the measured values for the quadrupole splitting and the hyperfine field splitting of the product produced from  $\zeta\text{-}^{57}\text{Fe}_2\text{N}$ , 0.015 mm/s and 11.553 T respectively, are very similar to those measured from the product produced from  $\zeta\text{-}^{57}\text{Fe}$ , 0.012 mm/s and 10.814 T respectively. This shows that the atomic environment and spin of this phase are the same, implying that the resultant product is present in both experiments (*Table 4.3.*). The magnetic sextet was stable up to at least 45 GPa, the highest pressure reached during the experiment, suggesting very robust magnetic characteristics. The chemical shift value of the minor diamagnetic singlet component corresponds to  $\zeta\text{-}^{57}\text{Fe}_2\text{N}$  (0.4 mm/s).<sup>[171]</sup>

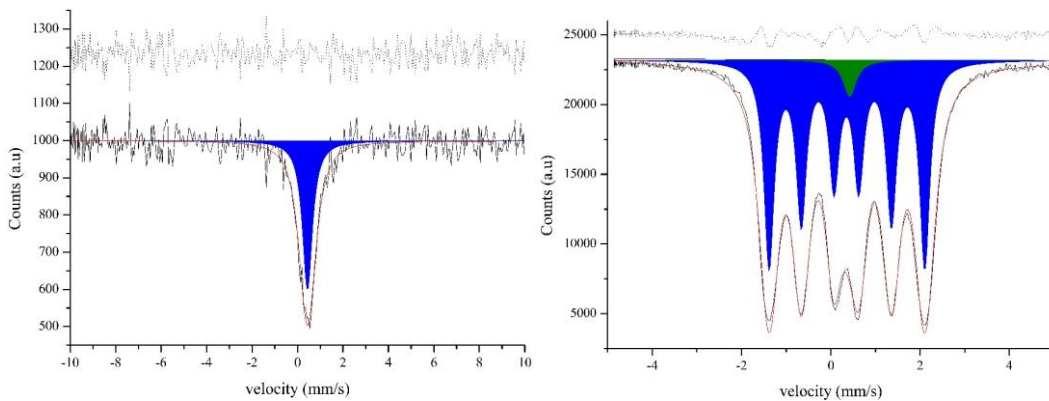


Figure 4.9. Fitted Mössbauer spectra of the diamond anvil cell containing  $\zeta$ - $^{57}\text{Fe}_2\text{N}$  before (left) and after (right) the reaction with  $\text{N}_2$  at 1500 K at 17.7 GPa. Blue belongs to the main reactant/product and the green corresponds to the unreacted  $\zeta$ - $^{57}\text{Fe}_2\text{N}$ .

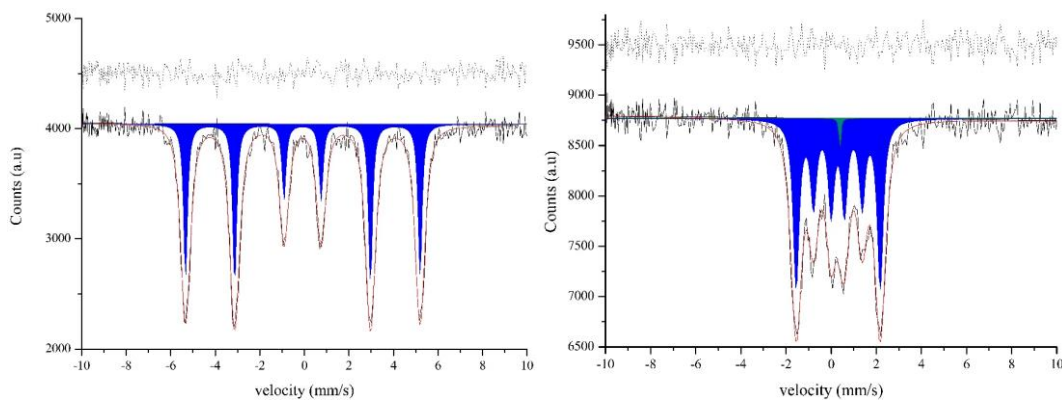


Figure 4.10. Fitted Mössbauer spectra of the diamond anvil cell containing  $^{57}\text{Fe}$  before (left) and after (right) the reaction with  $\text{N}_2$  at 1500 K at 13.9 GPa. Blue belongs to the main reactant/product and the green corresponds to  $\zeta$ - $^{57}\text{Fe}_2\text{N}$  side product.

Table 4.3. Comparison of refined  $^{57}\text{Fe}$ -Mössbauer spectra parameters before and after annealing of the chemical shift,  $\delta$ , quadrupole splitting,  $\Delta E_Q$ , and hyperfine field,  $\Delta E_M$ . The spectra were fit using MossA software.<sup>[183]</sup>

Sample	$\delta$ (mm/s)	$\Delta E_Q$ (mm/s)	$\Delta E_M$ (T)
$^{57}\text{Fe}$ in $\text{N}_2$ (0.1 MPa, not annealed)	$-0.073 \pm 0.005$	$0.011 \pm 0.009$	$32.645 \pm 0.037$
$^{57}\text{Fe}$ in $\text{N}_2$ (11.9 GPa, annealed)	$0.305 \pm 0.012$	$0.015 \pm 0.019$	$11.553 \pm 0.063$
$\zeta\text{-}^{57}\text{Fe}_2\text{N}$ in $\text{N}_2$ (0.1 MPa, not annealed)	$0.441 \pm 0.023$	—	—
$\zeta\text{-}^{57}\text{Fe}_2\text{N}$ in $\text{N}_2$ (17.7 GPa, annealed)	$0.356 \pm 0.002$	$0.012 \pm 0.003$	$10.814 \pm 0.014$

#### 4.2.3.4. Electronic structure calculations

While not a main topic of this doctoral thesis, electronic structure calculations were conducted in collaboration to gain more insight into the electronic structure of NiAs-type FeN, using theoretical density of state calculations and bonding analysis through the projected crystal orbital Hamilton populations technique (*Figure 4.11.*)<sup>[184]</sup> The calculations showed that NiAs-type FeN is in an electronically unfavourable situation, with strong Fe–N antibonding interactions. However, the calculations also suggest that this unfavourable situation is compensated for by adopting a ferromagnetic ground state,<sup>[185]</sup> which is reinforced by the magnetic sextet observed through Mössbauer spectroscopy.

Spin-only magnetic moment calculations produced a value of  $1.62 \mu_B/\text{Fe}$  for low-spin  $\text{Fe}^{3+}$ . The low-spin configuration of iron fits well to the observed Fe–N distance of  $2.0 \text{ \AA}$ , which is expected since the covalent radii of nitrogen and low-spin  $\text{Fe}^{3+}$  are  $0.71 \text{ \AA}$  and  $1.32 \text{ \AA}$  respectively.<sup>[186]</sup> Alternative calculations also produced a similar distance of  $2.09 \text{ \AA}$  by using Shannon’s ionic radii values. However, due to no value being available for a six fold coordinated  $\text{N}^{3-}$  anion being provided, an ionic radius was estimated based on a fourfold coordinated  $\text{N}^{3-}$  anion.<sup>[187,188]</sup>

Further calculations showed the compatibility of the NiAs-type FeN structure and the previously mentioned ZnS-type FeN (*Figure 4.11.*)<sup>[131]</sup> This calculation suggested that the ZnS-type would undergo a phase transition to the NiAs-type above pressures of  $22.6 \text{ GPa}$ , however this has yet to proven experimentally.

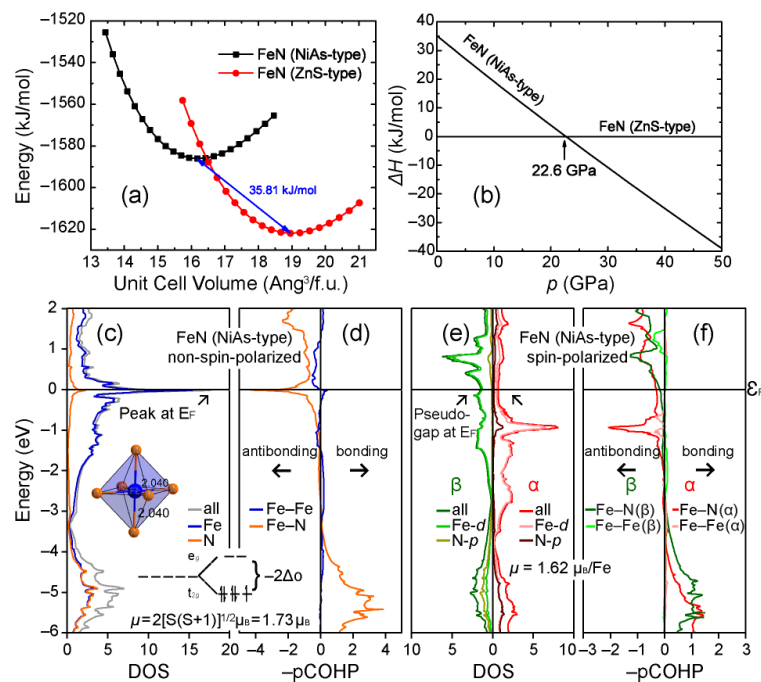


Figure 4.11. Electronic structure calculation diagrams of: a) Energy–volume curves; b) relative enthalpies as functions of pressure for NiAs-type, as well as ZnS-type FeN at 0 K; c), d) non-spin-polarized DOS and  $-p$ COHP curves; e), f): spin-polarized DOS and  $-p$ COHP curves of NiAs-type FeN.

##### 4.2.4. Summary

In this chapter, the attempted synthesis of FeN<sub>2</sub> produced the unexpected NiAs-type FeN. This phase was formed upon the heating of elemental <sup>57</sup>Fe or ζ-<sup>57</sup>Fe<sub>2</sub>N in a N<sub>2</sub> environment, above 1000 K and 10 GPa. If the reactants were reacted below these conditions, then ζ-<sup>57</sup>Fe<sub>2</sub>N/ε-<sup>57</sup>Fe<sub>3</sub>N<sub>1.4</sub> was observed. Upon heating at these conditions, the magnetic sextet of elemental <sup>57</sup>Fe and diamagnetic singlet of ζ-<sup>57</sup>Fe<sub>2</sub>N, from Mössbauer spectroscopy, evolved to very similar magnetic sextets, with the same characteristic chemical shift value. A possible alternative synthetic route could be to subject ZnS-type FeN to pressures of above 22.6 GPa according to bond structure calculations, which is predicted to cause a phase transition to the NiAs-type structure.

This hexagonal FeN adopts the NiAs-type structure, with hexagonal close packing of nitride anions and the iron cations occupying all octahedral holes. This arrangement produces FeN<sub>6</sub> octahedra, with Fe–N interatomic distances at the upper limit seen for an iron nitride. These octahedra are face sharing, which has not been previously seen in an iron nitride. The *c/a* ratio of this compound fits well with the values reported for other NiAs-type compounds comprised of transition metals and group V or VI elements.

The NiAs-type FeN phase exhibits magnetic ordering behaviour up to 45 GPa, where typically some form of degradation of the magnetic behaviour would have commenced at this pressure. The iron cations were calculated to be low-spin Fe<sup>3+</sup>, which corresponds well to the calculated interatomic distances.

A publication, produced at a similar time when the aforementioned research was reported, also produced NiAs-type FeN, under larger pressures of 30 GPa and above, with similar unit cell parameters and theoretical calculations.<sup>[32]</sup> A more recent synthesis produced NiAs-type FeN and went up to pressures of 128 GPa and showed that NiAs-type FeN becomes energetically favourable above 17.7 GPa.<sup>[189]</sup> In addition to these experimental investigations, theoretical calculations have also been produced, which further corroborate the magnetic properties of NiAs-type FeN and the proposed phase transition of ZnS-type to NiAs-type FeN at sufficient pressure.<sup>[190,191]</sup>



### 4.3. High pressure synthesis and characterisation of $\epsilon$ -Fe<sub>2</sub>MnN

#### 4.3.1. Introduction

The high temperature phase of Ferrite,  $\alpha$ -Fe, is Austenite,  $\gamma$ -Fe, and this allotrope has found a large application in the construction industry as carbon steel, due to its ability to dissolve more carbon into its structure than Ferrite and thus produce better mechanical properties. By absorbing carbon into the face-centred cubic structure, it in fact stabilises the Austenite at lower temperatures to produce Martensite steels.

In more recent years, it was discovered that  $\gamma$ -Fe can be also stabilised by Mn, which produces a steel with exceptional mechanical properties of strength and strain.<sup>[192–194]</sup> This has led to investigations into the cause of these properties, which originates from a pressure induced transition from  $\gamma$ -Fe to martensite and can be influenced by Mn and C content.<sup>[195,196]</sup>

As mentioned previously, binary iron nitrides are known for their hardness and magnetic properties. Several investigations into tailoring of the magnetic properties have been attempted, by substitution of iron with another transition metal, mainly producing substituted variants of  $\gamma'$ -Fe<sub>4</sub>N.<sup>[64,197–200]</sup> Substituted variants of  $\epsilon$ -Fe<sub>3</sub>N have been particularly difficult to produce, due to the formation of impurity phases during synthesis, such as intermetallic phases.<sup>[201–204]</sup>

Using a high pressure, high temperature approach metastable ternary nitrides with the composition  $\epsilon$ -Fe<sub>2</sub>MN<sub>x</sub> ( $M = \text{Co, Ni, Ru, Ir}$ ) were synthesised.<sup>[205,206]</sup> These phases were produced by subjecting a 1:1 mixture of  $\zeta$ -Fe<sub>2</sub>N and the respective transition metal to 8–15 GPa at 1373–1523 K. These ternary nitrides are metastable and upon heating above 800 K N<sub>2</sub> is released exothermally, which results in the ternary nitrides  $\epsilon$ -Fe<sub>2</sub>MN<sub>x</sub> ( $M = \text{Co, Ru, Ir}$ ) directly converting into an iron-metal intermetallic phase. However,  $\epsilon$ -Fe<sub>2</sub>NiN first converts to the metal rich nitride,  $\gamma'$ -(Fe, Ni)<sub>4</sub>N, and then converts to Fe<sub>1-x</sub>Ni<sub>x</sub> upon liberation of all of the N<sub>2</sub>.<sup>[205,206]</sup> Interestingly, a recent publication has shown that the intermetallic phase Fe<sub>2</sub>Co can be directly nitrated under NH<sub>3</sub> to produce  $\epsilon$ -Fe<sub>2</sub>CoN.<sup>[207]</sup> This could not only imply a more accessible synthetic route, but also that the  $\epsilon$ -Fe<sub>2</sub>MN phase could be regenerated after thermal decomposition.

These ternary nitrides are soft ferromagnets, which is very similar to the non-substituted  $\epsilon$ -Fe<sub>3</sub>N<sub>1±x</sub>.<sup>[141]</sup> When comparing the magnetic moment per formula unit and Curie temperature of  $\epsilon$ -Fe<sub>3</sub>N, 6  $\mu_B$ /f.u. and 575 K respectively,<sup>[135]</sup> with those of  $\epsilon$ -Fe<sub>2</sub>CoN, 4.3  $\mu_B$ /f.u. and 488 K, and  $\epsilon$ -Fe<sub>2</sub>NiN, 3.1  $\mu_B$ /f.u. and 234 K, there is a trend for both values to decrease with substitution of a metal from further across the row. This loss of ferromagnetism has been attributed to the additional valence electrons from Co and Ni that are brought into the system.<sup>[205]</sup>

The following part of this work was conducted in a collaboration, with several key contributions from the Max-Planck-Institut für Chemische Physik fester Stoffe, Germany. Dr. K. Guo and Priv.-Doz. Dr. U. Schwarz produced the conception and implementation of the experiment. Dr. R. Castillo conducted preliminary work, which contributed to the understanding of the synthetic route. Dr. U. Burkhardt conducted the elemental analysis and Vickers microhardness measurements. Dr. M. Bobnar performed the thermal analysis of the samples. Dr. L. Akselrud gave support with regards to Rietveld refinements.

#### 4.3.2. Synthesis

The reactant,  $\zeta$ -Fe<sub>2</sub>N, was prepared from elemental Fe and heated under NH<sub>3</sub> flow (60 mL/minute) at 686 K for 60 hours. The temperature was then decreased, over 6 hours, to 386 K, where it stayed for one hour before cooling to room temperature.<sup>[172]</sup>  $\zeta$ -Fe<sub>2</sub>N was then mixed with elemental Mn powder, produced by grinding of the bulk metal, in a 1:1.02 ratio, prepared and inserted into a Vöggenreiter press with a Walker-type multi-anvil module. A slight excess of Mn was used to compensate for side reactions with the BN crucible at high temperature and pressure.

The pressure was first increased to 15(2) GPa, in 4.5 hours, where the sample was heated to 1573(200) K for 30 minutes, before being quenched to ambient temperature and the pressure being reduced to ambient pressure over 13 hours. The recovered product showed a metallic luster.

Powder X-ray diffraction measurements used Co-*K*<sub>α1</sub> radiation ( $\lambda = 1.78896$  Å, HUBER G-670 diffractometer, Rimsting, Germany).

### 4.3.3. Characterisation

#### 4.3.3.1. Structure determination and crystal structure of $\epsilon$ -Fe<sub>2</sub>MnN

Powder X-ray diffraction patterns were indexed with a hexagonal unit cell with lattice parameters of  $a = 4.71872(5) \text{ \AA}$  and  $c = 4.41982(7) \text{ \AA}$ . These values were very similar to those of  $\epsilon$ -Fe<sub>3</sub>N,  $a = 4.6982(3) \text{ \AA}$ ,  $c = 4.3789(4) \text{ \AA}$ ,<sup>[152]</sup> and of the recently produced nanoparticle sized  $\epsilon$ -Fe<sub>2.1</sub>Mn<sub>0.9</sub>N,  $a = 4.781 \text{ \AA}$ ,  $c = 4.368 \text{ \AA}$ .<sup>[208]</sup> Rietveld refinement (*Figure 4.12. and Table 4.4.*) showed the material crystallises isostructural to  $\epsilon$ -Fe<sub>3</sub>N, with Mn substituted onto the Fe site. Numerous samples were measured, with varying unit cell parameters. This implies a large homogeneity range for  $\epsilon$ -Fe<sub>3-x</sub>Mn<sub>x</sub>N. However, no information regarding ordering of the Fe and Mn content within the crystal structure can be determined via Rietveld structural refinement, due to both atoms being difficult to distinguish by conventional X-ray diffraction.

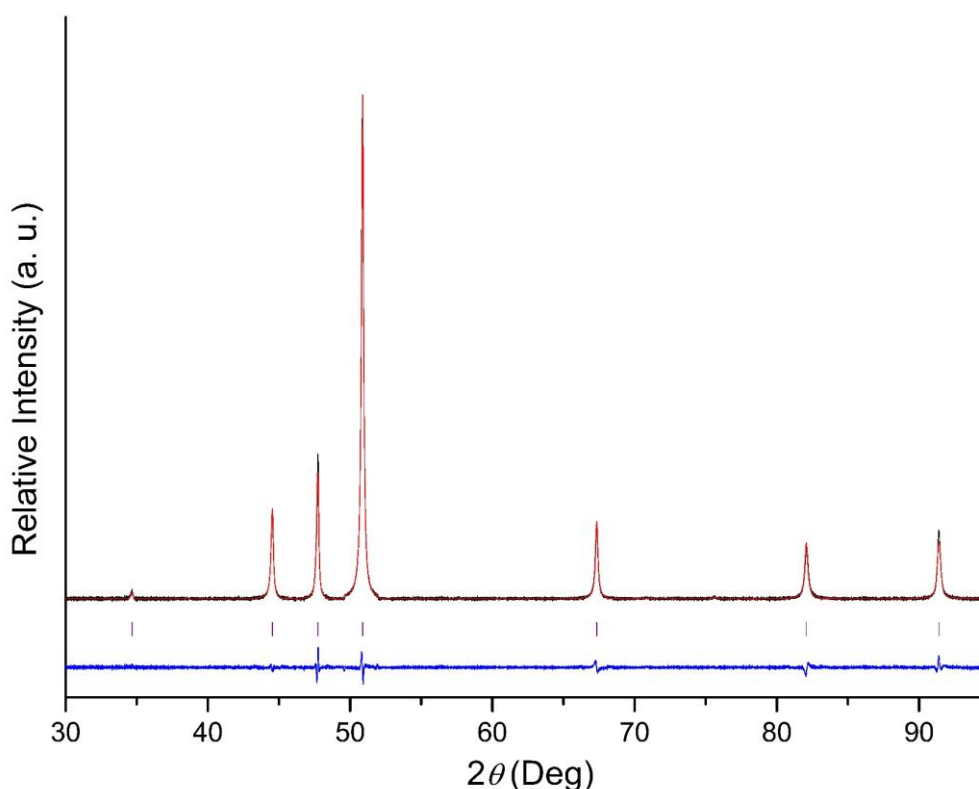


Figure 4.12. Graphical representation of Rietveld structural refinement of  $\epsilon$ -Fe<sub>2</sub>MnN from X-ray powder diffraction measurements. The observed pattern is shown in black, the calculated one in red, possible Bragg reflection positions are in purple and the difference in blue (Performed at Max-Planck-Institut für Chemische Physik fester Stoffe, Germany).

#### 4. High pressure synthesis of iron containing nitrides

Table 4.4. Unit cell and atomic positions of  $\epsilon$ -Fe<sub>2</sub>MnN obtained through Rietveld refinements and values for quality of refinement.

Space Group		$P6_322$ (No. 182)	
$a/\text{\AA}$		4.71872(5)	
$c/\text{\AA}$		4.41982(7)	
$V/\text{\AA}^3$		85.23	
$R_{wp}/\%$		0.0034	
$R_{Bragg}/\%$		0.0051	
Wyckoff site	Atomic Position	Occupation	
Fe(1)/Mn(1)	6g	0.3413(3), 0, $1/2$	$2/3 / 1/3$
N(1)	2c	$2/3, 1/3, 1/4$	0.571(8)
N(2)	2b	0, 0, $1/4$	0.429(8)

Comparison of  $\epsilon$ -Fe<sub>2</sub>MnN with  $\epsilon$ -Fe<sub>3</sub>N and the other known phases, which also contain a 3d transition metal,  $\epsilon$ -Fe<sub>2</sub>MN ( $M = \text{Co}$  and  $\text{Ni}$ ), shows a slow decrease in unit cell parameters as the metal  $M$  progresses later in the series (Figure 4.13.). This decrease can be attributed to the gradual shortening of the interatomic distances between  $M(\text{I})$  and N,  $d(\text{Mn-N}) = 1.93 \text{ \AA} - 2.13 \text{ \AA}$ ,<sup>[209,210]</sup>  $d(\text{Fe-N}) = 1.8 \text{ \AA} - 2.0 \text{ \AA}$ ,<sup>[152,173]</sup>  $d(\text{Co-N}) = 1.824 \text{ \AA}$ <sup>[211]</sup> and  $d(\text{Ni-N}) = 1.77 \text{ \AA}$ .<sup>[102]</sup>

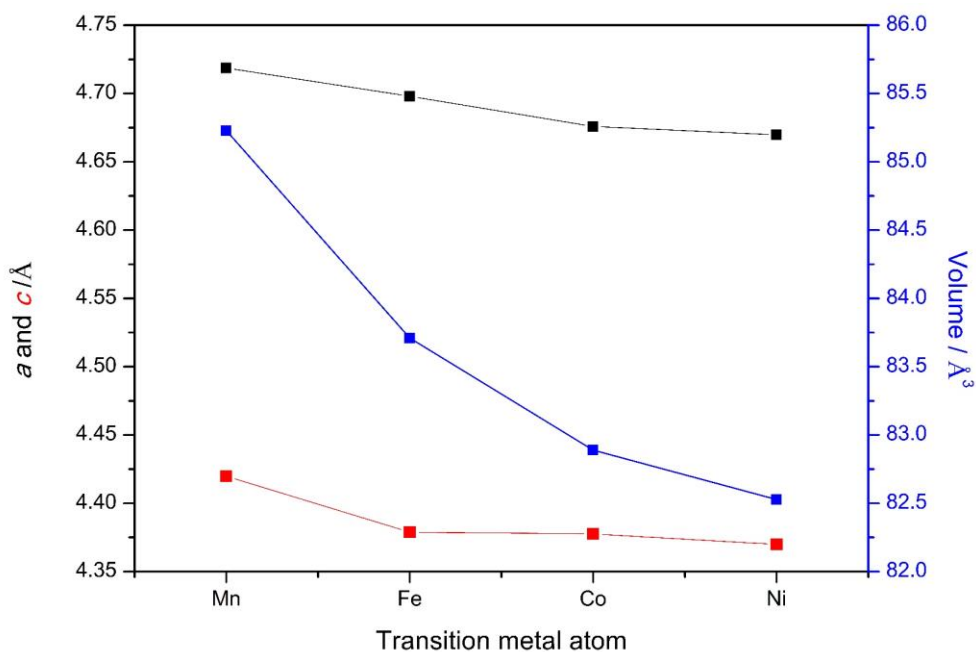


Figure 4.13. Relationship between the transition metal in  $\epsilon$ -Fe<sub>2</sub>MN ( $M = \text{Mn} - \text{Ni}$ ) and unit cell parameters ( $a$  is shown in black,  $c$  is shown in red and volume is shown in blue).

The structure of  $\varepsilon$ -Fe<sub>2</sub>MnN, like  $\varepsilon$ -Fe<sub>3</sub>N and the substituted variants mentioned earlier, is constructed from *hcp* Fe and Mn atoms with the nitrogen occupying a third of the octahedral holes. The nitrogen centred Fe<sub>6</sub>N octahedra are linked to other octahedra via corner sharing (*Figure 4.14*). The slight difference in the unit cell, compared to  $\varepsilon$ -Fe<sub>3</sub>N, is attributed to the slight difference in atomic radii of Mn and Fe, 0.62 Å and 0.56 Å respectively.

Since no value for the ionic radii of two fold coordinated Mn(I) and Fe(I) cations are given in the literature, a value was approximated based on six fold Mn(II) and Fe(II) (*eq. 4.1*). The increase in the ionic radius from an oxidation state of +2 to +1 was estimated from the relative change in ionic radius of Cu(II) to Cu(I).<sup>[187]</sup>

$$[2]_r = [6]_r \left(\frac{2}{6}\right)^{\frac{1}{8}} \quad (\text{eq. 4.1})$$

In an idealised  $\varepsilon$ -Fe<sub>3</sub>N type structure, all of the N atoms occupy the *2c* Wyckoff position to produce vertex sharing Fe<sub>6</sub>N octahedra. However, in reality the *2b* position can also be occupied by N atoms, leading to rods of face-sharing octahedra along [001], which are edge sharing with the octahedra of the *2c* position. To minimise the amount of face-sharing between octahedra, the N atoms have a disordered arrangement along [001], if occupation is less than 50 %. If an ordered occupation of the *2b* site, with occupation being 50 %, is seen, then a symmetry reduction to *P312* (No. 149) is observed, which is likely for phases with high N content.<sup>[145]</sup>

The influence of the substitution of Mn for Fe can be seen in the interatomic distances. The Fe/Mn–N interatomic distances range from 1.907(1) Å to 1.953(1) Å. When compared with the typical interatomic distance range for  $d(\text{Fe–N}) = 1.8 \text{ \AA} - 2.0 \text{ \AA}$ ,<sup>[152,173]</sup> and  $d(\text{Mn–N}) = 1.93 \text{ \AA} - 2.13 \text{ \AA}$ ,<sup>[209,210]</sup> there is an elongation of the interatomic distance between Fe/Mn and N due to the influence of Mn having a longer distance, which is caused by Mn having a larger ionic radii than that of Fe.

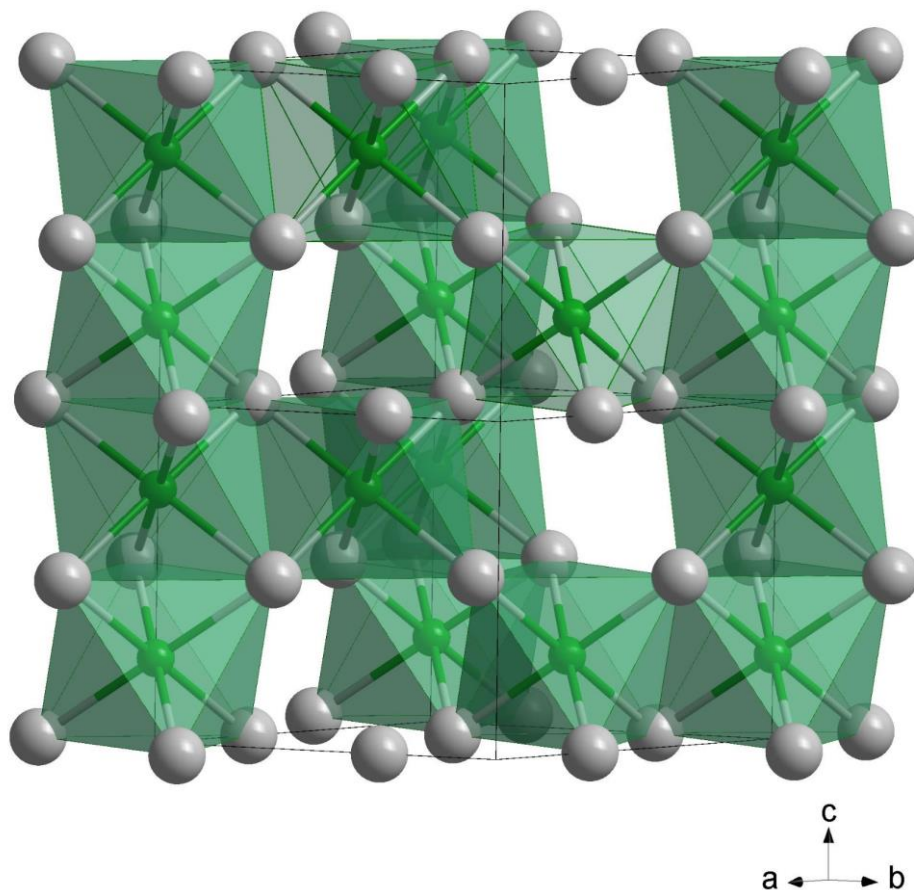


Figure 4.14. Section of the idealised crystal structure of  $\epsilon$ -Fe<sub>2</sub>MnN. Fe/Mn atoms are depicted in silver and N is depicted in green. Unit cell edges are shown in black.

#### 4.3.3.2. Energy dispersive X-ray analysis

Elemental analysis was performed using a scanning electron microscope, with integrated EDXS-system (Quantax, Bruker), located at the Max-Planck-Institut für Chemische Physik fester Stoffe, Germany.

Three independent elemental analysis measurements showed a homogeneous distribution of Fe, Mn and N, with the average ratio of the metals being 2.06(1) : 0.94(1). This results in a chemical composition of Fe<sub>2.06(1)</sub>Mn<sub>0.94(1)</sub>N, which was close to the expected composition, and complies with previously produced substituted  $\epsilon$ -Fe<sub>3</sub>N phases.

### 4.3.3.3. Magnetic susceptibility

Magnetic characteristics were measured using a SQUID magnetometer (MPMS XL-7, Quantum Design), located at the Max-Planck-Institut für Chemische Physik fester Stoffe, Germany.

The magnetic properties of  $\varepsilon$ -Fe<sub>2</sub>MnN were investigated as a function of temperature, in the range of 1.8 K to 650 K in applied magnetic fields of 0.1 T and 3.5 T, as well as a function of applied magnetic field, up to 7.0 T at 1.8 K (Figure 4.15.).

Above the Curie temperature,  $402 \pm 5$  K,  $\varepsilon$ -Fe<sub>2</sub>MnN is paramagnetic, which undergoes a magnetic phase transition to a ferromagnet below the Curie temperature. Fitting of the inverse susceptibility against temperature, between 550 K and 650 K, with a Curie-Weiss law, results in an effective magnetic moment per formula unit of  $5.0 \mu_B$ , with a rather large ferromagnetic ordering,  $\theta = 448$  K (Figure 4.15. Lower inset). Below the Curie temperature, soft ferromagnetic behaviour is observed (Figure 4.15. Upper inset). From the plotted hysteresis the spontaneous magnetic moment was calculated to be  $3.88 \mu_B$ .

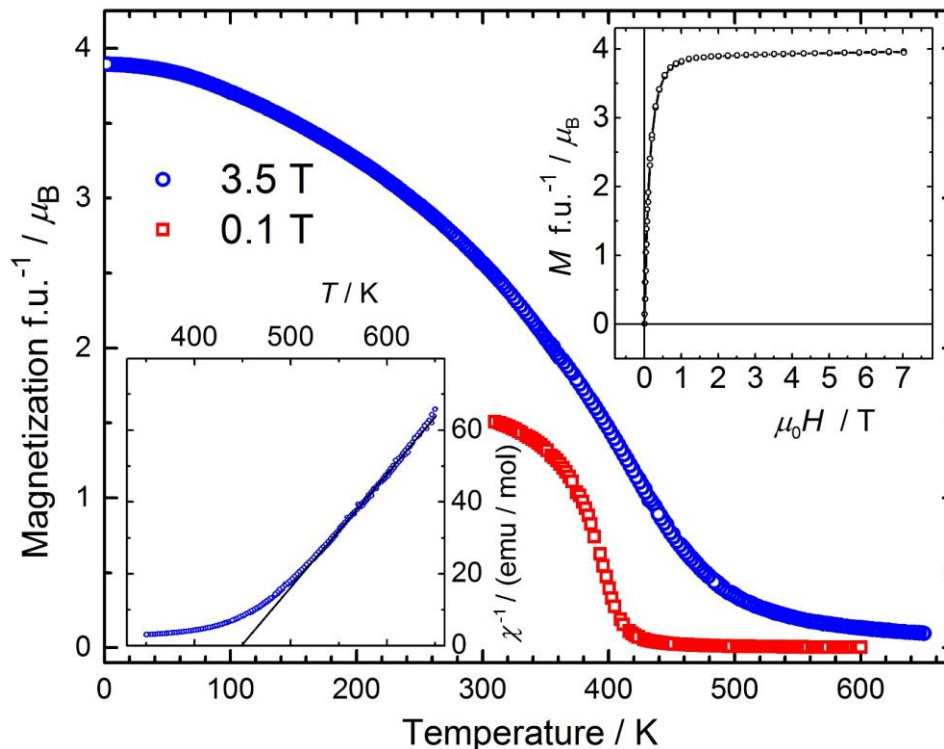


Figure 4.15. Magnetisation against temperature for  $\varepsilon$ -Fe<sub>2</sub>MnN, measured at 3.5 T and 0.1 T. Upper inset: Magnetisation against magnetic field at  $T = 1.8$  K. Lower inset: Inverse susceptibility against temperature measured at 3.5 T, fitted with a Curie-Weiss law (black line).

Both the spontaneous magnetic moment and Curie temperature of  $\epsilon$ -Fe<sub>2</sub>MnN are lower than those seen for  $\epsilon$ -Fe<sub>3</sub>N (6.0  $\mu_B$  and 575 K) and the other substituted phase (*Table 4.5.*), with the observed values fitting between those of  $\epsilon$ -Fe<sub>2</sub>CoN (4.3  $\mu_B$  and 488 K) and  $\epsilon$ -Fe<sub>2</sub>NiN (3.1  $\mu_B$  and 234 K).<sup>[205]</sup> The magnetic moment of  $\epsilon$ -Fe<sub>2</sub>MnN is significantly lower than the expected value from the Slater-Pauling curve,<sup>[212,213]</sup> which predicts an average magnetic moment of roughly 1.8  $\mu_B$  per 3d metal and thus a magnetic moment of 5.4  $\mu_B$  for  $\epsilon$ -Fe<sub>2</sub>MnN. Such a surprising difference between the observed and expected values could be an indication of ferrimagnetism, which would cause a lower magnetic moment due to the opposing magnetic moments.

Table 4.5. Comparison of the magnetic moments and Curie temperatures for  $\epsilon$ -Fe<sub>2</sub>MN ( $M = \text{Mn} - \text{Ni}$ ).

$M$	Magnetic moment/ $\mu_B$	Curie temperature/K
Mn	3.88	402
Fe <sup>[145]</sup>	6.0	575
Co <sup>[205]</sup>	4.3	488
Ni <sup>[205]</sup>	3.1	234



#### 4.3.3.4. Differential thermal analysis and thermogravimetry

Differential thermal analytical paired with thermogravimetry were performed for  $\epsilon$ -Fe<sub>2</sub>MnN to observe its thermal stability (Figure 4.16). The sample was measured under Ar flow between 300 and 1270 K, with a heating rate of 10 K/min, using a NETZSCH STA 449C.

The resultant data showed the  $\epsilon$ -phase to be stable up to roughly 800 K. At this temperature an exothermic signal is observed, which is attributed to the loss of N<sub>2</sub> and the formation of cubic  $\gamma'$ -(Fe,Mn)<sub>4</sub>N phase. After 900 K a mass loss of roughly 7.32 wt.% is observed, finishing at around 1270 K. The mass loss correlates well with the mass of nitrogen in  $\epsilon$ -Fe<sub>2</sub>MnN, 7.75 wt.%. This, combined with the observed endothermic signal at 1030 K, implies the loss of nitrogen which causes a transition to a (Fe,Mn):N phase, which was confirmed to be *fcc* by indexing of a powder X-ray diffraction pattern of the thermally degraded product.

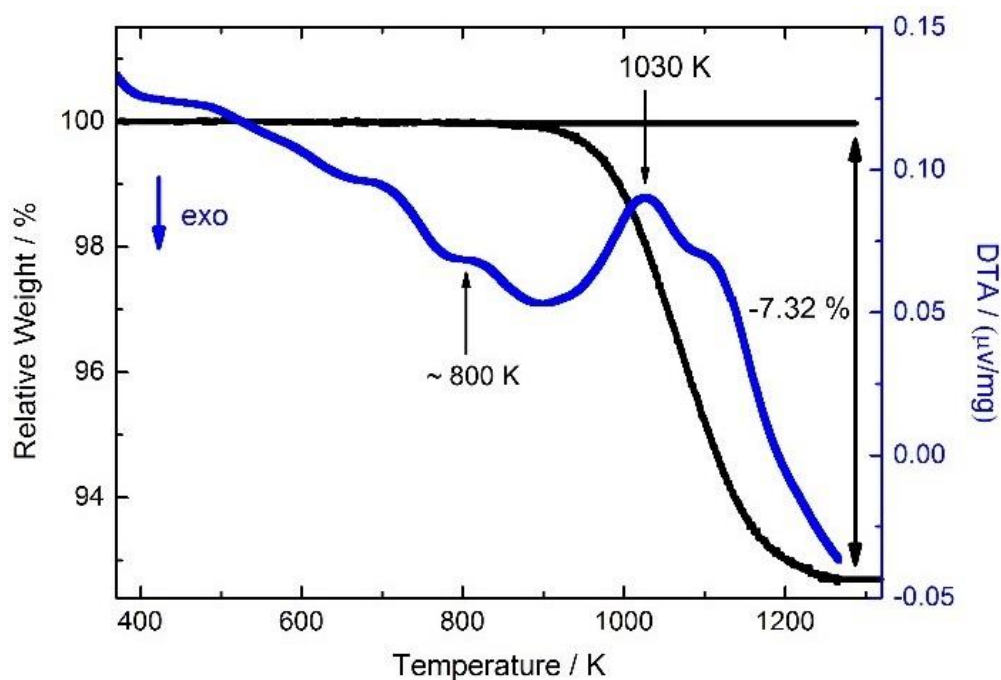


Figure 4.16. DTA-TG data of  $\epsilon$ -Fe<sub>2</sub>MnN, under Ar flow between 300 and 1270 K.

For the non-substituted  $\epsilon$ -Fe<sub>3</sub>N phase, thermal decomposition is also observed. Upon heating above 516 K at ambient pressure, the phase loses N content and transforms into the thermodynamically stable  $\gamma'$ -Fe<sub>4</sub>N.<sup>[150]</sup> The substituted phases,  $\epsilon$ -Fe<sub>2</sub>MN (*M* = Co and Ni), also undergo similar decompositions, with both compounds being metastable up to 750 K at ambient pressure. For  $\epsilon$ -Fe<sub>2</sub>CoN, the phase decomposes starts at 820 K at ambient pressure, and transforms into the cubic  $\gamma'$ -(Fe,Co)<sub>4</sub>N phase, similar to  $\epsilon$ -Fe<sub>2</sub>MnN, but the cubic phase directly decomposes

to Fe-Co intermetallic phase, which results in a single phase intermetallic phase at 920 K.<sup>[205]</sup> The  $\epsilon$ -Fe<sub>2</sub>NiN phase decomposes in a very similar way as  $\epsilon$ -Fe<sub>2</sub>MnN, but at lower temperatures, with thermal decomposition beginning at 809 K at ambient pressure. At 820 K the  $\epsilon$ -Fe<sub>2</sub>NiN completely transforms to the cubic  $\gamma'$ -(Fe,Ni)<sub>4</sub>N, which decomposes further into a Fe-Ni alloy above 920 K.<sup>[205]</sup>

From the phases discussed, the non-substituted  $\epsilon$ -Fe<sub>3</sub>N phase appears to have the lowest thermal stability. This would imply that the introduction of another 3d transition metal element increases the thermal stability of the  $\epsilon$ -phase. Both the Co and Ni containing phases have a similar thermal stability, up to 750 K, and the Mn has an even higher thermal stability, up to 800 K.

##### 4.3.3.5. Microhardness

To assess the effect of Mn substitution on the hardness of  $\epsilon$ -Fe<sub>3</sub>N, microhardness measurements, via Vickers indentation, were conducted (*Figure 4.17.*). Six independent indentations produced an average value of  $636 \pm 21$  HV, which correlates to 6.2(2) GPa. Around the indentation, cracks were observed. This indicates that the pressure given to the sample was too high, meaning that the measured hardness is at the upper limit of hardness for this material and gives a larger value than that of the actual hardness of the material. However, the values measured are slightly lower than that of  $\epsilon$ -Fe<sub>3</sub>N, 7(1) GPa,<sup>[145]</sup> but still within the range of tool steels, up to 9 GPa, and nitrogen hardened steels, 5 – 15 GPa.<sup>[214–217]</sup>

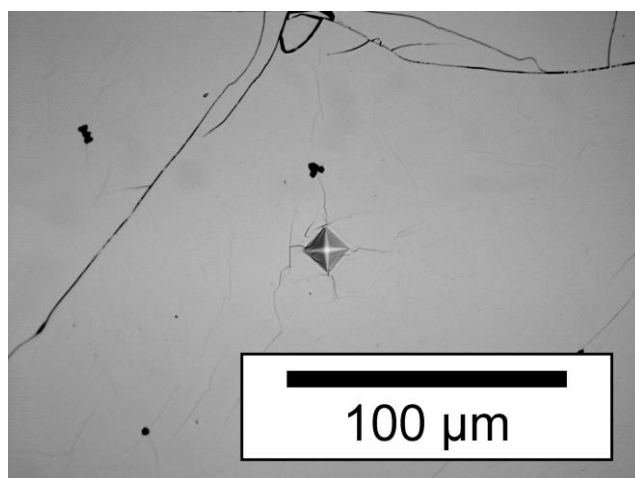


Figure 4.17. Vickers microhardness measurement of  $\epsilon$ -Fe<sub>2</sub>MnN, by indentation in a polished sample.

#### 4.3.4. Summary

In this chapter the successful synthesis and characterisation of Mn substituted  $\epsilon$ -Fe<sub>3</sub>N had been conducted. The synthesis, under high pressure and temperature, produced  $\epsilon$ -Fe<sub>2</sub>MnN, along with an indication of a broad homogeneity range for  $\epsilon$ -Fe<sub>3-x</sub>Mn<sub>x</sub>N.

The material crystallises isostructural to other known substituted ternary iron nitride phases,  $\epsilon$ -Fe<sub>2</sub>MN<sub>x</sub> ( $M = \text{Co, Ni, Ir}$ ) and also exhibits similar properties.  $\epsilon$ -Fe<sub>2</sub>MnN is also a soft ferromagnet, below the Curie temperature, with a magnetic moment of  $3.88 \mu_B/\text{f.u.}$  Both the Curie temperature and magnetic moment are lower than the non-substituted  $\epsilon$ -Fe<sub>3</sub>N, however these values are in between those seen for  $\epsilon$ -Fe<sub>2</sub>CoN and  $\epsilon$ -Fe<sub>2</sub>NiN. The lower magnetic moment was unexpected since the sum of the magnetic moments of Fe and Mn, assuming pure ferromagnetic coupling, produces a higher magnetic moment than that seen for  $\epsilon$ -Fe<sub>2</sub>MnN. This might indicate the presence of ferrimagnetism, which would account for a lower magnetic moment being observed.

Thermal decomposition of  $\epsilon$ -Fe<sub>2</sub>MnN is very similar to that observed for  $\epsilon$ -Fe<sub>2</sub>CoN and  $\epsilon$ -Fe<sub>2</sub>NiN. At temperatures of 800 K the phase converts to the cubic  $\gamma'$ -(Fe,Mn)<sub>4</sub>N, and loss of N<sub>2</sub> occurs above 900 K to yield the intermetallic phase (Fe,Mn):N. The same decomposition, via the cubic phase, is observed for  $\epsilon$ -Fe<sub>2</sub>NiN, however at lower temperatures than that of  $\epsilon$ -Fe<sub>2</sub>MnN. Investigations into the hardness of  $\epsilon$ -Fe<sub>2</sub>MnN has shown it to possess a hardness lower than that of  $\epsilon$ -Fe<sub>3</sub>N, however the hardness is still within the range of nitrided steels and tool steels.



## 5. Transition metal nitridometalates containing infinite linear chains

### 5.1. Overview of nitridometalates

Binary nitrides, which exhibit bonding that can vary between ionic, covalent to metallic, have been relatively well investigated. However, nitridometalates have seen less attention. These materials are described as containing covalent complex anions,  $[M_xN_y]^{z-}$ , with the ternary and higher lithium-containing nitridometalates being a topic of interest for both solid state chemists and industry. A contributing factor to this interest is the potential applications of these nitrides as anode materials for batteries.<sup>[218,219]</sup>

In recent decades, nitridometalates have seen a substantial boost in attention, producing various compounds, which exhibit a wide range of interesting crystal structures.<sup>[220–222]</sup> Nitridometalates can allow atoms to exist in low oxidation states, with low coordination numbers, resulting in structures that are not often observed outside of nitride chemistry. These compounds, unlike other nitrides, also show multiple types of bonding, such as a combination of covalent, ionic and metallic being present within the same system.

Nitridometalates can be also characterised by having complex anions, which have the general formula  $[M_xN_y]^{z-}$ , and tend to have an alkali or alkaline earth cation as a counter ion.<sup>[220,221]</sup> These complex anions can vary from simple two-fold coordination of the metal cation, such as three atom units or chains, to more complex arrangements, such as six-fold coordination.<sup>[223]</sup>

A common arrangement observed with late 3*d*-transition metals, in a low oxidation state, is that the complex anion is comprised of infinite linear chains  ${}^1_{\infty}[MN_{2/2}]^{2-}$ , which are interconnected to each other by crystallographically different metal cations to produce condensed chains. The position of the metal cation within this complex anion can be occupied by one metal cation, such as for  $\alpha$ -Li<sub>3</sub>N,<sup>[224]</sup> Li<sub>4</sub>SrN<sub>2</sub><sup>[225]</sup> and Ba<sub>2</sub>[Ni<sub>3</sub>N<sub>2</sub>],<sup>[226]</sup> or they can have a mixed occupation, such as Li<sub>2</sub>[(Li<sub>1-x</sub>M<sub>x</sub>)N] (*M* = Mn, Fe, Co, Ni and Cu)<sup>[227–232]</sup> and SrLi<sub>2</sub>[(Li<sub>1-x</sub>M<sub>x</sub>)N]<sub>2</sub> (*M* = Fe, Ni and Cu).<sup>[225,233,234]</sup>

## 5.2. Synthesis and characterisation of $\text{SrLi}_2\{\text{Li}[\text{CoN}_2]\}$

### 5.2.1. Introduction

The ternary nitride  $\text{Li}_4\text{SrN}_2$  is structurally very similar to  $\alpha\text{-Li}_3\text{N}$ .<sup>[219,225]</sup>  $\alpha\text{-Li}_3\text{N}$  is constructed of hexagonal bipyramids of lithium cations, with a nitride anion in the centre,  ${}^0\left\{\left[\text{NLi}_{6/3}\text{Li}_{2/2}\right]^{5+}\right\}$ . In the case of  $\text{Li}_4\text{SrN}_2$ , these polyhedra are in fact distorted pentagonal bipyramids, which are built up of three lithium and two strontium cations on the equatorial positions and two lithium cations on the axial positions,  ${}^0\left\{\left[\text{NLi}_{3/3}\text{Sr}_{2/4}\text{Li}_{2/2}\right]^{6+}\right\}$ . The axial lithium cations are linearly bonded to two nitride anions, which leads to the formation of one-dimensional infinite linear  ${}^1\left[\text{LiN}_{2/2}^{2-}\right]$  chains. Each strontium cation is coordinated by four nitrogen anions to produce distorted tetrahedra, which makes the  ${}^1\left[\text{LiN}_{2/2}^{2-}\right]$  chains run parallel in the [100] and [010] directions of the tetragonal unit cell. This results in blocks of parallel chains, which are perpendicular to each other (Figure 5.1.).

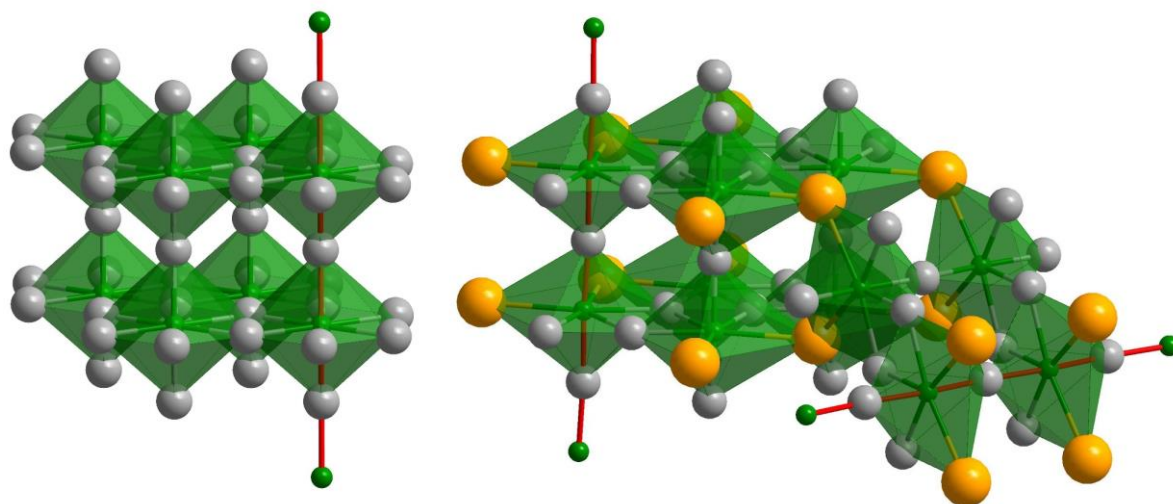


Figure 5.1. Comparison of the coordination environments in  $\alpha\text{-Li}_3\text{N}$ <sup>[224]</sup> and  $\text{Li}_4\text{SrN}_2$ <sup>[225]</sup> showing the infinite linear  ${}^1\left[\text{LiN}_{2/2}^{2-}\right]$  chains (red). Sr–orange, N–green and Li–silver.

Numerous examples of substitution of the lithium positions for a transition metal have been successfully achieved for  $\text{Li}_4\text{SrN}_2$ .<sup>[225,233–237]</sup> Some of these substitutions resulted in quaternary compounds, which are isotopic to  $\text{Li}_4\text{SrN}_2$ , with the compositions  $\text{SrLi}_2\left[(\text{Li}_{1-x}\text{M}_x)\text{N}\right]_2$  ( $M = \text{Fe}$ ,  $x = 0.46$ ,  $\text{Ni}$ ,  $x = 0.05$ , and  $\text{Cu}$ ,  $0.22 \leq x \leq 0.39$ ).<sup>[225,233,234]</sup> The substitution of a transition metal for lithium occurs solely on the lithium position located in the infinite linear chains. This behaviour is also observed for the substituted variants of the aforementioned  $\alpha\text{-Li}_3\text{N}$ .<sup>[91,238–240]</sup> So far, there

has been no reported evidence or investigation into the possibility of ordering within the partially substituted chains of the quaternary nitridometalates, with the exception of the fully substituted  $[-\text{Li}-\text{N}-\text{Co}-\text{N}-]^{4-}$  chains in  $\text{Sr}_2[\text{LiCoN}_2]$ .<sup>[236]</sup>

### 5.2.2. Synthesis

To synthesise the reagent  $\text{Li}_{2.773}\text{Co}_{0.227}\text{N}$ , a mixture of  $\alpha\text{-Li}_3\text{N}$ , prepared using the method seen in Chapter 2.1., and elemental Co, with a 3:1 molar ratio, was pressed into a tablet with a diameter of 8 mm weighing 1.003 g. This tablet was placed into a tantalum crucible and inserted into a fused silica tube. The apparatus was heated, under  $\text{N}_2$  flow, to 573 K for 2 h, before increasing the temperature to 973 K, at 50 K/h, for 8 h and then allowed to naturally cool to room temperature.<sup>[229]</sup> This produced  $\text{Li}_2[(\text{Li},\text{Co})\text{N}]$ , which was confirmed to be single phase by powder X-ray diffraction. The degree of Co substitution was determined via correlation between the unit cell parameters and amount of Co. For refined unit cell parameters,  $a = 3.6951(3)$  Å,  $c = 3.7581(3)$  Å and  $V = 44.445$  Å<sup>3</sup>, the correlating  $x$  values from the literature were 0.28, 0.22 and 0.18 respectively.<sup>[241]</sup> This lead to an averaged chemical formula of  $\text{Li}_{2.773}\text{Co}_{0.227}\text{N}$ .

Strontium pieces were reacted with  $\text{N}_2$  at 823 K for 8 h and cooled to room temperature. The sample was ground and reacted under the same conditions several times to ensure a complete reaction to  $\text{Sr}_2\text{N}$ . The resultant product was confirmed to be single phase  $\text{Sr}_2\text{N}$  by powder X-ray diffraction.

$\text{Li}_{2.725}\text{Co}_{0.275}\text{N}$  (0.127 g, 2.762 mmol) and  $\text{Sr}_2\text{N}$  (0.128 g, 0.690 mmol) were mixed and filled in a tantalum ampoule, along with elemental Li (0.25 g) as a fluxing agent. This would produce a product with the composition of  $\text{SrLi}_2\{\text{Li}[\text{CoN}_2]\}$ . The ampoule was then sealed by an arc welder and inserted into a fused silica tube, which was then heated, under Ar flow, to 973 K and allowed to cool at a controlled rate of 1.5 K/h. After opening the ampoule, the Li flux was removed using liquid ammonia leaving a sample containing a mixture of black crystal shards and metallic silver crystals. A black single crystal was selected and all characterisation was conducted on this one crystal, whereas characterisation of the metallic silver crystals has proven difficult. Powder X-ray diffraction experiments were unable to produce a diffraction pattern of use with both available X-ray wavelengths ( $\text{Mo-}K_\alpha$ ,  $\text{Cu-}K_\alpha$ ). This is due to strong fluorescence between the  $\text{Mo-}K_\alpha$  wavelength and the Sr within the sample and between the  $\text{Cu-}K_\alpha$  wavelength Co within the sample.

### 5.2.3. Characterisation

#### 5.2.3.1. Structure Determination

Reflections from single crystal X-ray diffraction experiments were initially assigned to a body centred tetragonal crystal lattice and refined in the space group  $I4_1/amd$  (No. 141), with the substituted Co atoms being located exclusively on the infinite chains, which would be expected. The unit cell parameters were in agreement with other known substitutions of the isostructural  $\text{SrLi}_2[(\text{Li}_{1-x}\text{M}_x)\text{N}]_2$  ( $M = \text{Fe}, \text{Ni}$  and  $\text{Cu}$ ),<sup>[100,234,235]</sup> as well as the unsubstituted  $\text{Li}_4\text{SrN}_2$  ( $a = 3.822(2) \text{ \AA}$ ,  $c = 27.042(9) \text{ \AA}$ )<sup>[225]</sup> (Table 5.1.). All substituted phases of  $\text{Li}_4\text{SrN}_2$  show a decrease of the  $a$  unit cell parameter. This is a result of the, in general, shorter interatomic distances between the transition metal and N,  $d(\text{Fe-N}) = 1.896 \text{ \AA}$ ,<sup>[233]</sup>  $d(\text{Ni-N}) = 1.912 \text{ \AA}$ <sup>[234]</sup> and  $d(\text{Cu-N}) = 1.885 \text{ \AA}$ ,<sup>[235]</sup> than those seen between Li and N in the non-substituted  $\text{Li}_4\text{SrN}_2$  ( $1.913 \text{ \AA}$ )<sup>[225]</sup> which causes an overall shortening of the Li – N interatomic distances that build up the pentagonal bipyramids. An increase in the  $c$  unit cell parameter and volume is observed for the substituted phases, compared to  $\text{Li}_4\text{SrN}_2$ , however the cause for this has proven difficult to identify, with no discernible structural reason being identified. Structural refinements (Table 5.2.) agreed well for the  $\text{Li}_4\text{SrN}_2$  structure type, however the refinement produced a high  $R_{int} = 0.2109$ , suggesting that the chosen symmetry could be incorrect.

Table 5.1. Unit cell parameters of  $\text{SrLi}_2[\text{Li}[\text{CoN}_2]]$ ,  $\text{Li}_4\text{SrN}_2$ <sup>[225]</sup> and  $\text{SrLi}_2[(\text{Li}_{1-x}\text{M}_x)\text{N}]_2$  ( $M = \text{Fe}, \text{Ni}$  and  $\text{Cu}$ ).<sup>[225,233,234]</sup>

Composition	$\text{SrLi}_2[\text{Li}[\text{CoN}_2]]$	$\text{Li}_4\text{SrN}_2$	$\text{SrLi}_2[(\text{Li}_{0.54}\text{Fe}_{0.46})\text{N}_2]$	$\text{SrLi}_2[(\text{Li}_{1.9}\text{Ni}_{0.1})\text{N}_2]$	$\text{SrLi}_2[(\text{Li}_{1.22}\text{Cu}_{0.78})\text{N}_2]$
$Z$	4	4	4	4	4
$a/\text{\AA}$	3.7414(2)	3.822(2)	3.7909(2)	3.822(2)	3.770(1)
$c/\text{\AA}$	27.931(2)	27.0472(2)	27.719(3)	27.042(2)	27.368(6)
$c/a$	7.465	7.077	7.312	7.075	7.259
$\rho_{\text{calc}}/\text{gcm}^{-3}$	3.319	2.41	3.14	2.50	3.20
Volume $V/\text{\AA}^3$	390.98	395.02	398.35	395.02	388.98

A closer inspection of the diffraction data, through reconstructed diffraction patterns, showed diffuse streaks superimposed with reflections, except for  $hkl$  where  $l = 2n$  (Figure 5.2.). Overlaying the allowed reflections for a tetragonal lattice onto the reconstructed diffraction patterns showed that all reflections were described, except for the diffuse reflections (Figure 5.2e.). Also in the images, splitting of reflections at higher angles could be observed. These two factors, along with the high  $R_{int}$  value, gave significant evidence that the assumed tetragonal symmetry was incorrect and a monoclinic lattice would be the correct lattice.



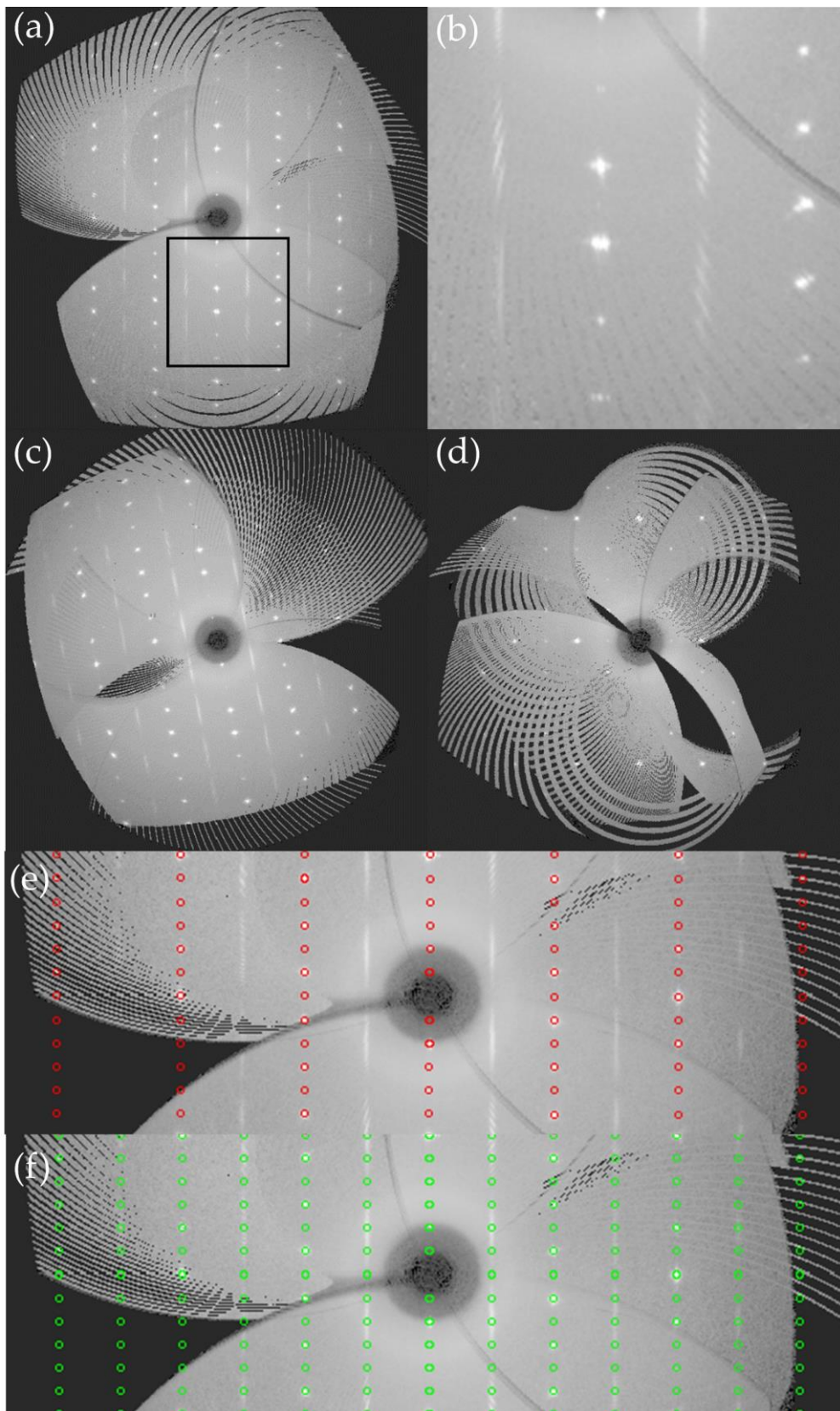


Figure 5.2. Reconstructed diffraction patterns of  $\text{SrLi}_2\{\text{Li}_{0.65}\text{Co}_{0.35}[\text{Co}_{0.65}\text{Li}_{0.35}\text{N}_2]\}$  (a)  $0kl$ ; (b) Magnified section from Figure 5.1a.; (c)  $h0l$ ; (d)  $hk0$ ; (e)  $0kl$  with superimposed reflections for a tetragonal lattice (red); (f)  $0kl$  with superimposed reflections for a monoclinic lattice (green).

A tetragonal space group was deemed insufficient to describe the crystal structure properly. Therefore, a monoclinic subcell, with the space group  $P2_1/c$  (No. 14), was derived from the original tetragonal space group,  $I4_1/amd$  (No. 141), through a Bärnighausen symmetry tree diagram (Figure 5.3.). The symmetry was first reduced to a face-centred orthorhombic unit cell (Figure 5.4.), which then allows the reduction in symmetry needed to free the  $\beta$  angle of the unit cell to create a  $C$ -centred monoclinic unit cell (Figure 5.4.). Finally, a loss of the  $C$ -centring allows the mixed Li/Co position along the infinite chains to be split into two crystallographically independent positions in a primitive monoclinic unit cell.

The previously mentioned splitting of reflections at high angles was a characteristic indication of the presence of crystal twinning. To determine the presence of twinning, the program PLATON<sup>[242]</sup> was used and the following twinning matrix was proposed.

$$\begin{pmatrix} -1 & 0 & 1 \\ 0 & -1 & 0 \\ 0 & 0 & 1 \end{pmatrix}$$

This twinning matrix would mean that the crystal twins are related to each other through a two-fold rotation axis. This axis, in fact, belongs to the  $c$ -axis of the orthorhombic unit cell and lies parallel to  $[102]$  (Figure 5.5.) in the monoclinic setting. This can explain why the structure was at first misinterpreted as a tetragonal unit cell, due to the pseudo-orthorhombic reflections mimicking higher symmetry, resulting from the crystal twinning. Since this unit cell translates very well into the orthorhombic, as well as the tetragonal system, the twin shows merohedral characteristics however, due to the symmetry reduction to the monoclinic unit cell, the twinning present is pseudo-merohedral.

This pseudo-merohedral twinned monoclinic lattice correctly describes the splitting of reflections at high angles (Figure 5.2f.). The splitting of the crystallographic unique mixed occupied Li/Co position in the tetragonal system produced two crystallographically independent positions in the monoclinic crystal system. One position occupied with mainly Li (Li(1)/Co(1)) and the other occupied with mainly Co (Li(2)/Co(2)). These positions show a strong indication of ordering however, there are no definitive positions on these chains which are solely occupied by either Li or Co. This produces an overall disorder, which appears on the reconstructed diffraction patterns as diffuse scattering. The monoclinic indexing of the reflections led to the space group of  $P2_1/c$  (No. 14), with the new unit cell ( $a = 5.2958(3)$  Å,  $b = 5.2898(4)$  Å,  $c = 14.2164(5)$  Å,

$\beta = 100.728(1)^\circ$ ). The new monoclinic unit cell can be derived from the tetragonal unit cell by multiplying the lengths  $a$  and  $b$  by  $\sqrt{2}$  and a near halving of the length of the  $c$  axis. The crystallographic relationship is shown in Figures 5.2 and 5.3.

A refinement of the monoclinic unit cell reduced the  $R_{int}$  and  $wR_2$  values from 0.2109 and 0.1611, to 0.0985 and 0.1470 respectively, indicating that this monoclinic space group describes the crystal structure better and produces a more accurate refinement, when compared with the refinement of the tetragonal unit cell. The splitting of the mixed Li/Co position on the  ${}^1_{\infty}[(\text{Li,Co})\text{N}_{2/2}^-]$  chains, allowed independent refinement of the occupation along these chains, resulting in different amounts for Li and Co on both positions (*Figure 5.6.*), leading to a composition of  $\text{SrLi}_2\{\text{Li}_{0.753(7)}\text{Co}_{0.246(7)}[\text{Co}_{0.748(6)}\text{Li}_{0.252(6)}\text{N}_2]\}$ . This showed a clear preference for ordering along the chains. With this occupation, the atomic displacements were refined isotropically. Attempts to refine anisotropically proved problematic for the mixed valence Li/Co and N positions. An attempt to fix the occupation and refine anisotropically still proved difficult. A different approach was to take the refined occupation from the tetragonal unit cell and apply it to the twinned monoclinic unit cell. After applying this fixed occupation, the anisotropic displacements parameters for each atomic position were able to be refined successfully. This gave the most accurate refinement (*Tables 5.2., 5.3. and 5.4.*), and described the diffuse reflections (*Figure 5.2f.*), producing a final composition of  $\text{SrLi}_2\{\text{Li}_{0.65}\text{Co}_{0.35}[\text{Co}_{0.65}\text{Li}_{0.35}\text{N}_2]\}$ .

5. Transition metal nitridometalates containing infinite linear chains

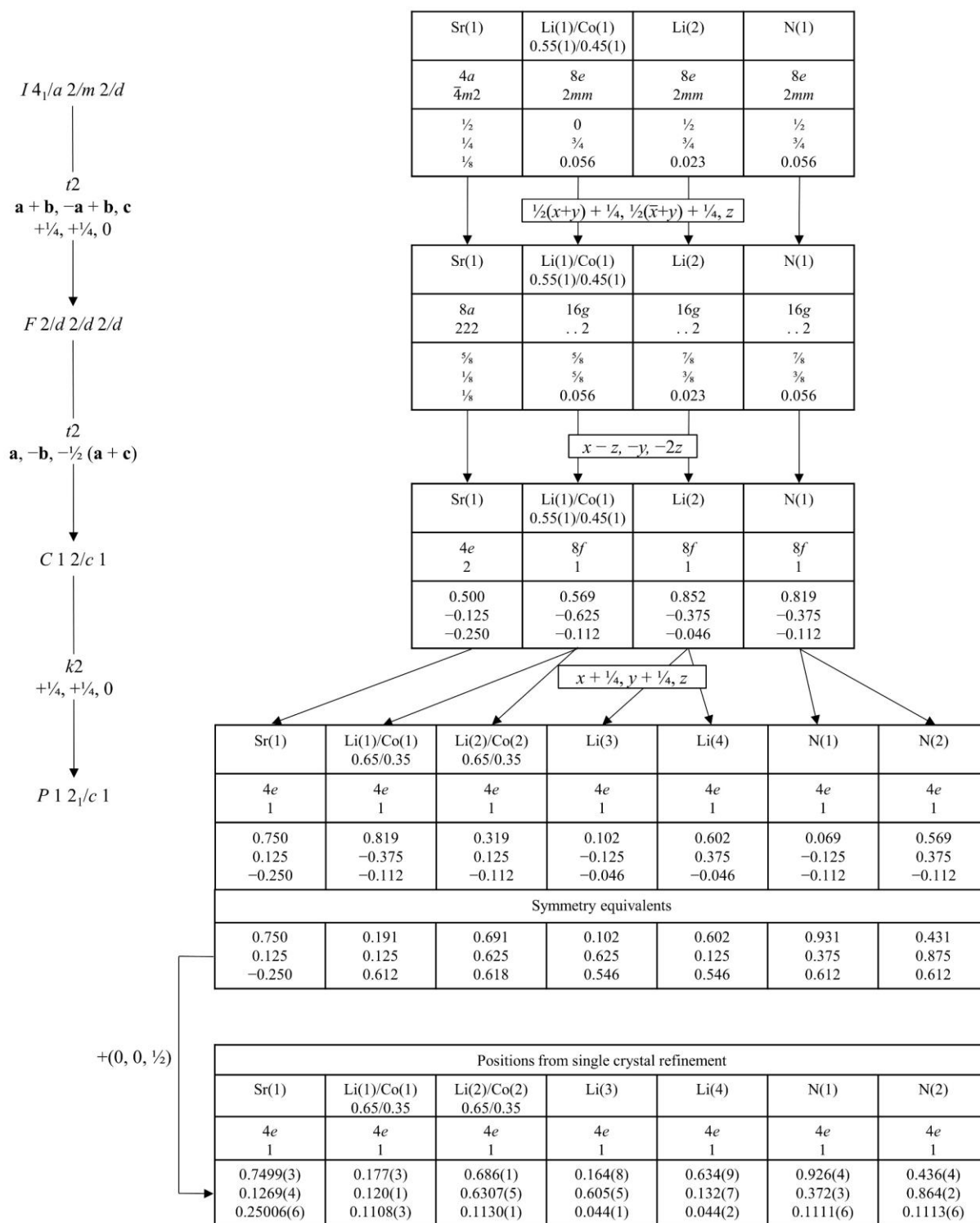


Figure 5.3. Bärnighausen symmetry tree diagram<sup>[243]</sup> describing the relation from  $I4_1/amd$  to  $P2_1/c$  for  $SrLi_2\{Li_{0.65}Co_{0.35}[Co_{0.65}Li_{0.35}N_2]\}$ .

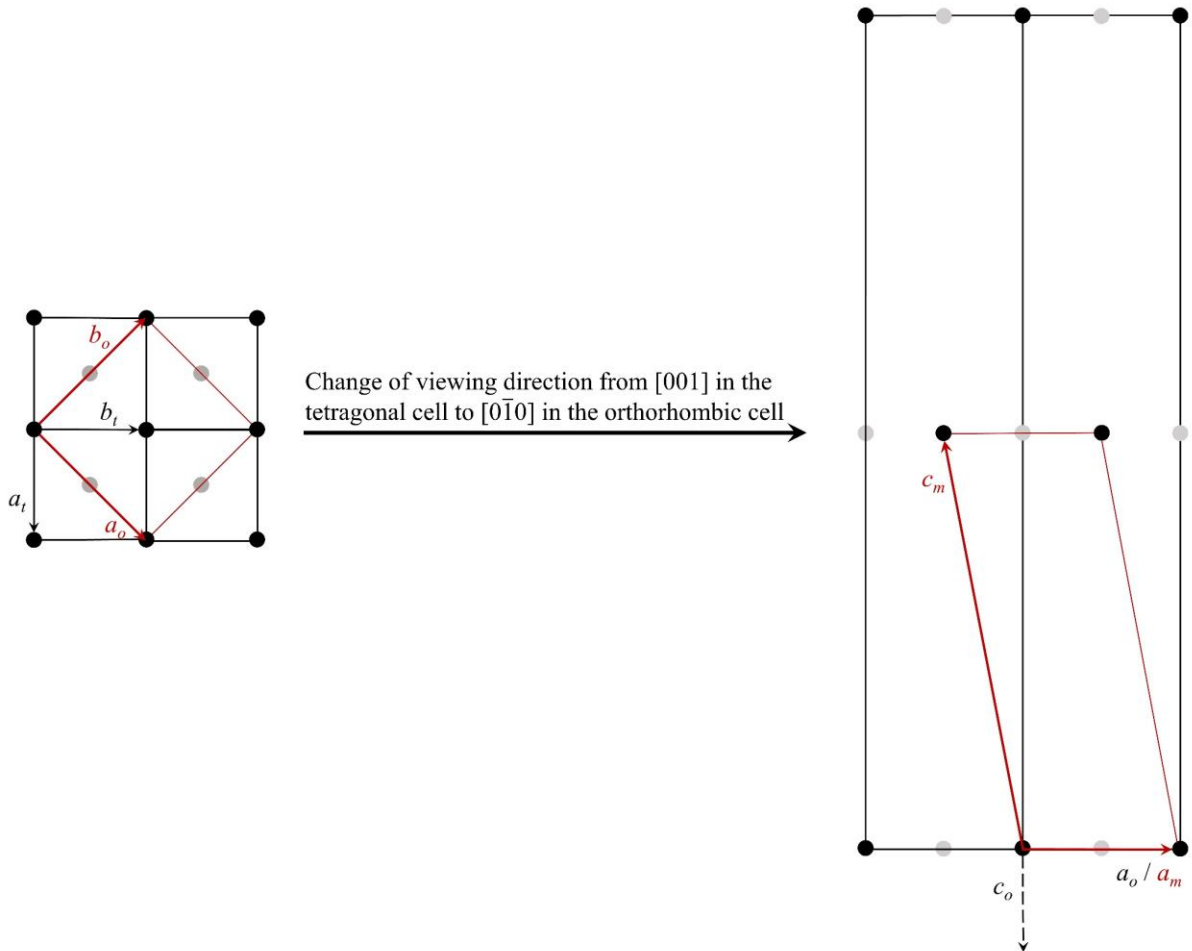


Figure 5.4. Symmetry reduction from a body-centred tetragonal unit cell to a face-centred orthorhombic unit cell, which is then reduced to a C-centred monoclinic unit cell. Black spheres are in plane and grey spheres are half the length of the projection direction above the plane. Red lines indicate the unit cell of lower symmetry.

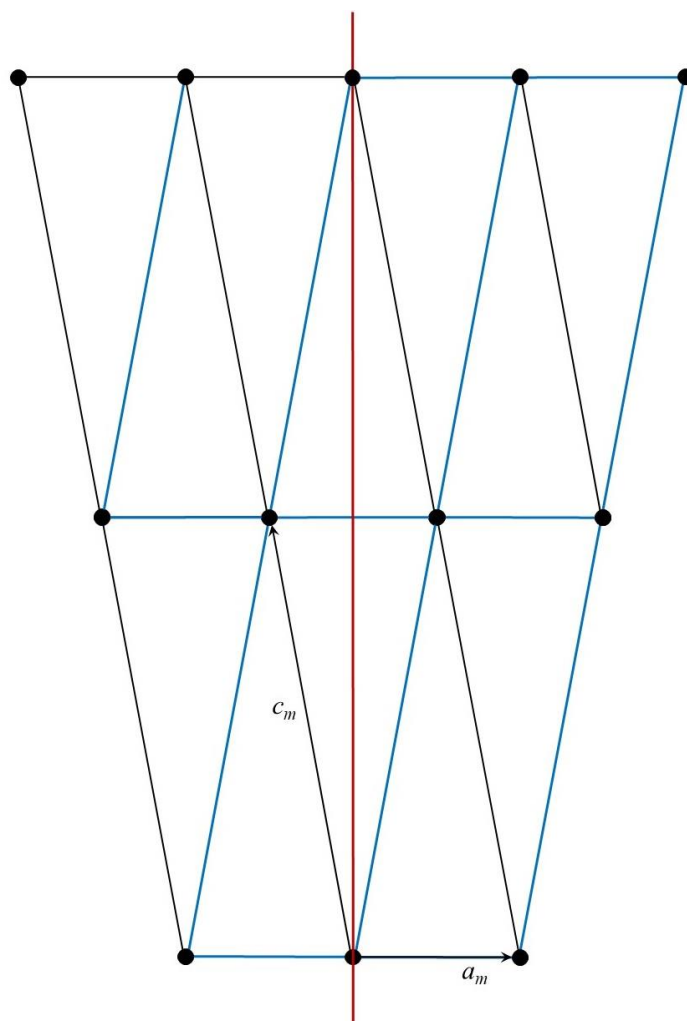


Figure 5.5. Twinning of the primitive monoclinic unit cell, viewed along  $[0\bar{1}0]$ , with the twinning axis  $[102]$  (red) and the resulting twinned unit cell (blue).

Table 5.2. Single crystal structural refinement of  $\text{SrLi}_2\{\text{Li}[\text{CoN}_2]\}$  in the space groups  $I4_1/amd$  (subcell) and  $P2_1/c$  (supercell).

Composition	$\text{SrLi}_2\{\text{Li}_{0.55(1)}\text{Co}_{0.45(1)}[\text{Co}_{0.55(1)}\text{Li}_{0.45(1)}\text{N}_2]\}$	$\text{SrLi}_2\{\text{Li}_{0.65}\text{Co}_{0.35}[\text{Co}_{0.65}\text{Li}_{0.35}\text{N}_2]\}$
Crystal System	Tetragonal	Monoclinic
Space Group	$I4_1/amd$ (No. 141)	$P2_1/c$ (No. 14)
$Z$	4	4
$a/\text{\AA}$	3.741(2)	5.2958(3)
$b/\text{\AA}$		5.2898(4)
$c/\text{\AA}$	27.93(2)	14.2164(5)
$\beta/^\circ$	90	100.728(1)
$\rho_{\text{calc}}/\text{gcm}^{-3}$	3.319	3.317
Volume $V/\text{\AA}^3$	390.98	391.29
Measurement temperature/K	293(2)	293(2)
Index range	$-4 \leq h \leq 4$ $-4 \leq k \leq 4$ $-36 \leq l \leq 36$	$-6 \leq h \leq 6$ $-6 \leq k \leq 6$ $-18 \leq l \leq 18$
Max. $2\theta/\text{deg}$	54.85	54.98
$F(000)$	360.8	352.0
$\mu/\text{mm}^{-1}$	18.03	17.64
Observed reflections	4373	7168
Unique reflections	148	878
Refined parameters	17	56
$R_{\text{int}}/R_\sigma$	0.2109/0.0515	0.0985/0.0473
$R_1/wR_2$	0.0636/0.1611	0.0640/0.1470
$GooF$	1.136	1.133
Remaining electron density (max/min)/ $\text{\AA}^{-3}$	1.55/-3.63	1.60/-1.20
BASF		0.49(1)
Twin matrix		-1 0 0 0 -1 0 1 0 1

Table 5.3. Atomic positions and occupations for the refinement of  $\text{SrLi}_2\{\text{Li}_{0.65}\text{Co}_{0.35}[\text{Co}_{0.65}\text{Li}_{0.35}\text{N}_2]\}$  in the space group  $P2_1/c$ .

	Wyckoff Position	$x/a$	$y/b$	$z/c$	Occupation	$U_{eq}$
Sr(1)	$4e$	0.7499(3)	0.1269(4)	0.25006(6)	1	0.0221(5)
Li(1)/Co(1)	$4e$	0.177(3)	0.120(1)	0.1108(3)	0.65/0.35	0.041(1)
Li(2)/Co(2)	$4e$	0.686(1)	0.6307(5)	0.1130(1)	0.35/0.65	0.0145(5)
Li(3)	$4e$	0.164(8)	0.605(5)	0.044(1)	1	0.032(5) <sup>1</sup>
Li(4)	$4e$	0.634(9)	0.132(7)	0.044(2)	1	0.037(5) <sup>1</sup>
N(1)	$4e$	0.926(4)	0.372(3)	0.1111(6)	1	0.023(2)
N(2)	$4e$	0.436(4)	0.864(2)	0.1113(6)	1	0.020(2)

<sup>1</sup> Value was treated isotropically during refinement.



Table 5.4. Anisotropic displacement parameters from the refinement of  $\text{SrLi}_2\{\text{Li}_{10.65}\text{Co}_{0.35}[\text{Co}_{0.65}\text{Li}_{0.35}\text{N}_2]\}$  in the space group  $P2_1/c$ .

	$U_{11}$	$U_{22}$	$U_{33}$	$U_{23}$	$U_{13}$	$U_{12}$	$U_{eq}$
Sr(1)	0.0246(9)	0.0221(6)	0.0198(6)	-0.0001(4)	0.005(2)	0.000(1)	0.0221(5)
Li(1)/Co(1)	0.059(4)	0.045(3)	0.032(2)	0.003(3)	0.038(4)	0.017(4)	0.041(1)
Li(2)/Co(2)	0.017(1)	0.0099(9)	0.020(1)	-0.001(1)	0.014(2)	0.001(1)	0.0145(5)
N(1)	0.023(6)	0.028(5)	0.019(4)	0.004(6)	0.011(9)	0.011(7)	0.023(2)
N(2)	0.019(5)	0.019(4)	0.025(4)	-0.007(6)	0.012(8)	-0.004(6)	0.020(2)

### 5.2.3.2. Crystal Structure

$\text{SrLi}_2\{\text{Li}_{0.65}\text{Co}_{0.35}[\text{Co}_{0.65}\text{Li}_{0.35}\text{N}_2]\}$  crystallises in a structure very similar to  $\text{Li}_4\text{SrN}_2$  (Figure 5.6.). The splitting of the mixed valence Li/Co position along the infinite chains, shows that there is a strong indication of ordering, which results in Li and Co almost alternating along the chains. Since Co is larger than Li, this alternating probably allows structural stability and prevents the distortion of the surroundings of the chains.

The influence of Co in the structure can be seen in the interatomic distances along the  ${}^1_{\infty}[(\text{Li},\text{Co})\text{N}_{2/2}^-]$  chains (Table 5.5.). When comparing the interatomic distances from this compound with the  $\text{Li}_4\text{SrN}_2$  structure, the Li(1)/Co(1)–N(1)/(2) interatomic distances (1.89(2) Å/1.92(2) Å), which are occupied with mainly Li, are in clear agreement with the distances found in  $\text{Li}_4\text{SrN}_2$  (1.913 Å).<sup>[225]</sup> In comparison, the position occupied with mainly Co, Li(2)/Co(2)–N(1)/(2) interatomic distances (1.87(2) Å/1.81(2) Å), exhibit shorter interatomic distances that tend more towards a typical Co–N interatomic distance, similar to those found in  $\text{Li}_2[\text{Li}_{0.57}\text{Co}_{0.43}\text{N}]$  (1.824 Å).<sup>[211]</sup> This interatomic distance is in fact shorter than the distances already known for  $M$ –N in the series  $\text{SrLi}_2[(\text{Li}_{1-x}\text{M}_x)\text{N}]_2$ ,  $d(\text{Fe}–\text{N}) = 1.896$  Å,<sup>[233]</sup>  $d(\text{Ni}–\text{N}) = 1.912$  Å<sup>[234]</sup> and  $d(\text{Cu}–\text{N}) = 1.885$  Å<sup>[235]</sup>.

Table 5.5. Interatomic distances (Å) and angles (°) of selected interatomic distances for  $\text{SrLi}_2\{\text{Li}_{0.65}\text{Co}_{0.35}[\text{Co}_{0.65}\text{Li}_{0.35}\text{N}_2]\}$ .

	Sr(1)	Li(1)/Co(1)	Li(2)/Co(2)	Li(3)	Li(4)
$M$ –N(1)	2.67(1)	1.89(2)	1.87(2)	2.11(4)	2.09(4)
$M$ –N(2)	2.71(1)	1.92(2)	1.81(2)	2.09(4)	2.09(4)
N(1)– $M$ –N(1)	121.1(3)	—	—	117(1)	—
N(1)– $M$ –N(2)	87.8(3)	179.4(9)	175.8(7)	126(2)	115(1)
N(2)– $M$ –N(2)	121.1(3)	—	—	—	117(1)

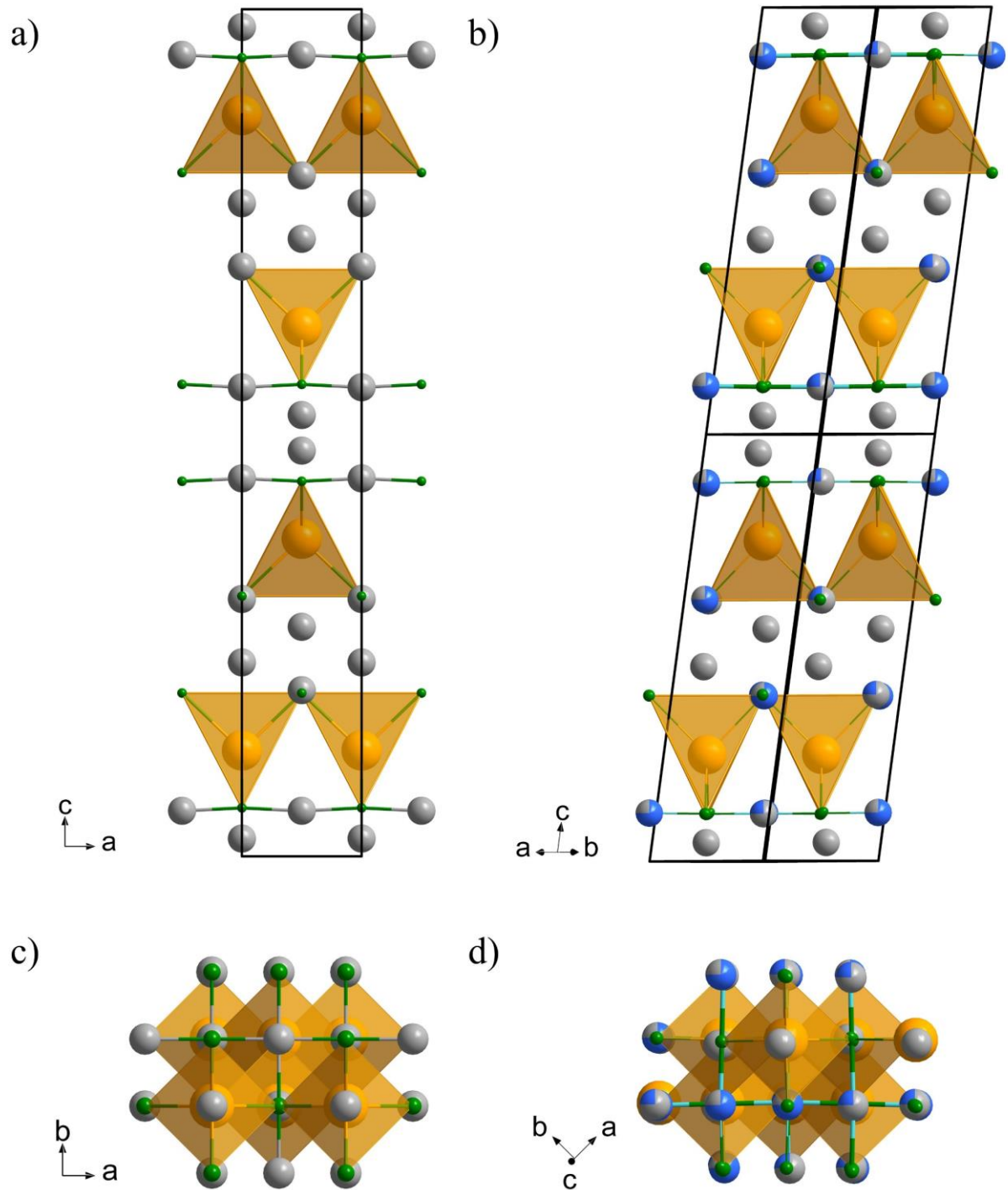


Figure 5.6. Crystal structure comparisons of: a)  $\text{Li}_4\text{SrN}_2$ ;<sup>[225]</sup> b)  $\text{SrLi}_2\{\text{Li}[\text{CoN}_2]\}$ ; c)  $\text{Li}_4\text{SrN}_2$  viewed along the *c*-axis;<sup>[225]</sup> d)  $\text{SrLi}_2\{\text{Li}[\text{CoN}_2]\}$  viewed along the *c*-axis. Sr–orange, N–green, Li–silver and Co–blue. Unit cells edges are shown by black lines.

### 5.2.4. Magnetic Susceptibility

The substitution of Li cations with Co(I) cations in the  ${}^1_{\infty}[(\text{Li},\text{Co})\text{N}_{2/2}^-]$  chains gave rise to the question of possible magnetic ordering and the spin-state of Co(I) present in this compound. Magnetic susceptibility measurements were conducted using the same black crystal, approximately 0.05 mm in diameter, from the diffraction experiments. This sample was sealed in a glass capillary, with 0.1 mm diameter, and fixed to a plastic tube that is typically used for magnetic measurements. The sample was subjected to magnetic fields between  $-50$  kOe and  $50$  kOe (*Figure 5.7a.*) and temperatures between  $5$  K and  $300$  K (*Figure 5.7b.*), which showed a hysteresis and temperature dependence corresponding to Curie-Weiss paramagnetic behaviour, with no long-range ordering at temperatures down to  $2$  K.

From the measurement of magnetic susceptibility against temperature, an experimental magnetic moment, using a modified Curie-Weiss law (*eq. 5.1.*), was calculated. This produced an experimental magnetic moment for Co(I) of  $\mu_{exp} = 2.62 \mu_B$  however, due to the small mass of the crystal measured, the calculated value has a high uncertainty, but is still in close agreement with a spin-only magnetic moment calculation,  $\mu_{cal} = 2.83 \mu_B$  for  $S = 1$ . This indicates the linearly coordinated Co(I) along the chains exists in a high-spin configuration.

$$\chi = \frac{C}{T - \theta} + \chi_0 \quad (\text{eq. 5.1.})$$

A rather high temperature-independent susceptibility ( $\chi_0$ ) is present,  $\chi_0 = 0.109 \text{ cm}^3/\text{mol}$ , which could be an indication of a small amount of elemental ferromagnetic Co impurity being on the surface of the crystal. However, this is difficult to confirm by magnetic susceptibility measurements, since the ferromagnetic transition temperature of Co occurs around  $1300$  K.<sup>[244]</sup>

Fitting of the inverse magnetic susceptibility against temperature, between  $40$  K and  $150$  K, showed that the Weiss constant from the measurement is negative ( $\theta = -1.87$  K), meaning a negative intercept of the  $x$ -axis of the inverse susceptibility against temperature. This suggests antiferromagnetic exchange interactions dominate among the moments of the Co(I) cations. This interaction has been previously observed for  $\text{Li}_2[(\text{Li}_{1-x}\text{Ni}_x)\text{N}]$  ( $0.06 \leq x \leq 0.85$ ),<sup>[245]</sup> which also contain infinite chains with mixed valence Li and transition metal. When a minimal amount of Ni was substituted ( $x = 0.06$ ), the Weiss constant and magnetic moment were  $-24$  K and  $2.33 \mu_B$

respectively however, at the highest amount of Ni content ( $x = 0.85$ ) the Weiss constant and magnetic moment had decreased to  $-85$  K and  $0.76 \mu_B$  respectively.

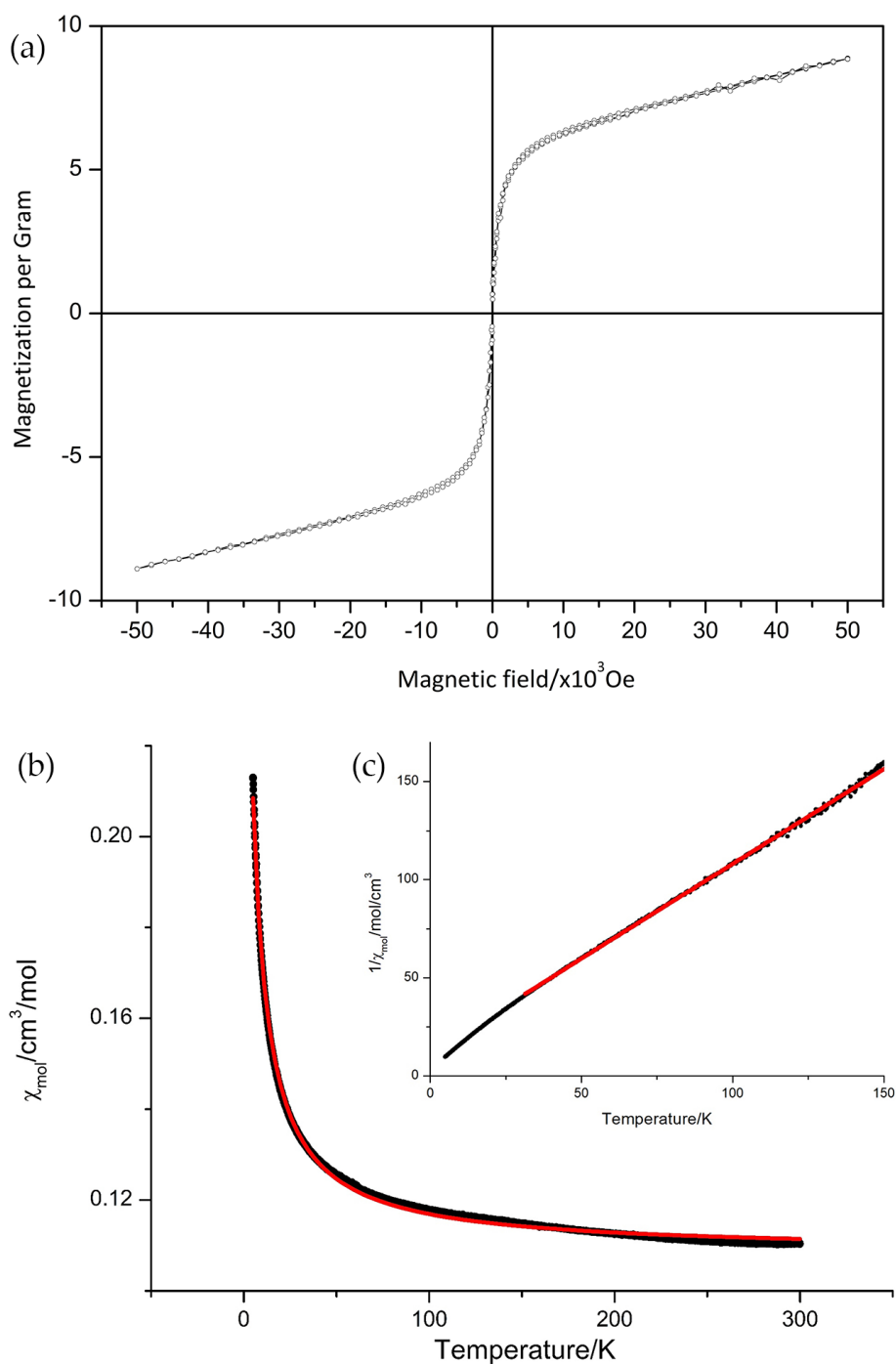


Figure 5.7. Magnetic measurements of  $\text{SrLi}_2\{\text{Li}_{0.65}\text{Co}_{0.35}[\text{Co}_{0.65}\text{Li}_{0.35}\text{N}_2]\}$ . a) Hysteresis of the magnetization per Co(I) cation against varying magnetic field at 300 K; b) Magnetic susceptibility per mol, with varying temperature at 10 kOe (black) and a fitted Curie-Weiss law curve (red); c) Inverse magnetic susceptibility per mol with varying temperature at 10 kOe (black) and a fitted inverse Curie-Weiss law line between 40 and 150 K (red).

### 5.2.5. Summary

In this chapter,  $\text{SrLi}_2\{\text{Li}_{0.65}\text{Co}_{0.35}[\text{Co}_{0.65}\text{Li}_{0.35}\text{N}_2]\}$  has been produced, which is the first member of  $\text{SrLi}_2[(\text{Li},M)\text{N}]_2$  ( $M =$  transition metal) to contain Co. This compound was first thought to crystallise in a body-centred tetragonal unit cell. However, upon close inspection of the structural refinement and reconstructed diffraction images, the correct structure was in fact described in a primitive monoclinic unit cell, with the space group  $P2_1/c$ . The lower symmetry allowed independent refinement of the Li and Co content along the infinite chains. This led to the first evidence of ordering along infinite chains in such a nitride system.

Magnetic susceptibility measurements showed the material to be a paramagnet, exhibiting Curie-Weiss behaviour, and no indication of magnetic ordering at low temperatures, down to 2 K. The linearly coordinated Co(I) cations are in a high-spin state, with the experimental and calculated magnetic moments being in close agreement. Between the moments of the Co(I) antiferromagnetic exchange interactions dominate. This behaviour has been seen in other compounds with infinite nitride chains, with varying substitution of transition metal for Li. Although no evidence of ordering was found in these compounds, it would be of interest to explore whether the increase of antiferromagnetic interactions and decrease of magnetic moment observed with these compounds, with increasing transition metal content, is observed for  $\text{SrLi}_2\{\text{Li}_{0.65}\text{Co}_{0.35}[\text{Co}_{0.65}\text{Li}_{0.35}\text{N}_2]\}$ , with varying Co content.

### 5.3. Synthesis and characterisation of $\text{Sr}_2[(\text{Li}_{1-x}\text{Ni}_x)\text{Ni}_2\text{N}_2]$

#### 5.3.1. Introduction

A particular group of nitridometalates that have been thoroughly investigated are the lithium and transition metal containing nitridonickelates. These are comprised of two-fold coordinated chains with low valence nickel and nitrogen in a nearly linear arrangement  ${}^1_{\infty}[\text{NiN}_{2/2}^-]$ . These chains can be interconnected to a neighbouring chain by a separate cation to form puckered layers. The interconnecting cations can be either solely Ni cations<sup>[226]</sup> or a mixed occupation of  $\text{Ni}_{1-x}\text{Li}_x$ .<sup>[246]</sup>

The nitridonickelate  $\text{Ba}_2[\text{Ni}_3\text{N}_2]$  was the first low-valence nitridonickelate to be produced, with the aforementioned two-fold coordinated chains of nickel and nitrogen, which are connected through interlinking nickel cations.<sup>[226]</sup> Partial substitution of the interconnecting nickel cation with lithium has been observed, producing the mixed occupied  $\text{Ba}_2[(\text{Ni}_{0.57}\text{Li}_{0.43})\text{Ni}_2\text{N}_2]$ .<sup>[246]</sup> The Ba cations are coordinated by N anions to form a distorted trigonal planar arrangement. The overall structure is closely related to the  $\alpha\text{-Li}_3\text{N}$  structure, where the vertex sharing hexagonal bipyramids around N seen in  $\alpha\text{-Li}_3\text{N}$  are closely replicated in the  $\text{Ba}_2[\text{Ni}_3\text{N}_2]$  and  $\text{Ba}_2[(\text{Ni}_{0.57}\text{Li}_{0.43})\text{Ni}_2\text{N}_2]$  structures. The equatorial positions consist of two Ba cations, two Li/Ni cations and two vacancies, producing a hexagonal sheet, while the axial positions consist of Ni, which are bonded to nitride anions producing infinite chains, as also seen in  $\alpha\text{-Li}_3\text{N}$  with lithium cations and nitride anions. The Ni cations in this compound are proposed as being mixed valent, with both Ni(I) and Ni(0) being present within the compound, although to date no investigation into the exact valence states of the Ni cations and their positions within the structure have been reported.

The following part of this work was conducted in a collaboration with Max-Planck-Institut für Chemische Physik fester Stoffe, Germany and the Technische Universität Dresden. Dr. P. Höhn and Ms K. Zechel synthesised several of the samples analysed. Mr. S. Hückmann conducted the powder X-ray diffraction measurements of the aforementioned samples.

### 5.3.2. Synthesis

Overall five samples were produced however, due to the collaborative nature of this project, the samples were not produced under the same conditions. For the ease of comprehension, each sample will be referred to by the label A, B, C, D or E.

Samples labelled A, B, D and E were prepared at the Max-Planck-Institut für Chemische Physik fester Stoffe, Germany and the Technische Universität Dresden. Single crystals were grown by filling a tantalum ampoule with the respective reagents, using Li metal as a fluxing agent (*Table 5.6.*). The ampoules were heated to 1023 K at 100 K/h and allowed to cool to 673 K at a controlled rate of 1 K/h, before being allowed to cool to ambient temperature. After opening the ampoule, the Li flux was removed, using high temperature centrifugation aided filtration, giving a final sample of black powder, which contained large crystals. The crystals produced from samples A and B had a dark metallic brass colour and crystals from samples D and E had a blue metallic colour.

Table 5.6. Reactants and masses used for the synthesis of  $\text{Sr}_2[(\text{Li}, \text{Ni})\text{Ni}_2\text{N}_2]$ .

	Sample A	Sample B	Sample D	Sample E
$\alpha\text{-Li}_3\text{N}$	0.050 g, 1.436 mmol	0.349 g, 10.022 mmol	–	0.142 g, 4.078 mmol
$\text{Sr}_2\text{N}$	0.402 g, 2.124 mmol	0.248 g, 1.311 mmol	0.300 g, 1.585 mmol	0.502 g, 2.653 mmol
Ni	0.053 g, 0.903 mmol	0.197 g, 3.356 mmol	0.200 g, 3.408 mmol	0.203 g, 3.459 mmol
$\text{NaN}_3$	–	–	0.071 g, 1.092 mmol	–
Li	0.260 g, 37.459 mmol	0.349 g, 50.281 mmol	0.244 g, 35.153 mmol	0.190 g, 27.374 mmol

Another sample, sample C, was prepared using an alternate method. A mixture of  $\alpha\text{-Li}_3\text{N}$ , prepared using the method described in Chapter 2.1., and elemental Ni, with a 2 : 1 molar ratio, were pressed into a tablet with a diameter of 8 mm weighing 0.6478 g. This tablet was placed into a tantalum crucible and inserted into a fused silica tube. The apparatus was heated, under  $\text{N}_2$  flow, to 925 K, at 100 K/h, for 168 h and then naturally cooling to room temperature.<sup>[231]</sup> This produced  $\text{Li}_2[(\text{Li},\text{Ni})\text{N}]$ , which was confirmed to be single phase by powder X-ray diffraction. The amount of Ni substitution was determined via correlation between the unit cell parameters and amount of Ni.<sup>[92]</sup> The refined unit cell parameters ( $a = 3.72098(8)$  Å and  $c = 3.6457(1)$  Å) confirmed the actual chemical formula to be  $\text{Li}_{2.4}\text{Ni}_{0.6}\text{N}$ , which is in close agreement to the expected composition of  $\text{Li}_{2.5}\text{Ni}_{0.5}\text{N}$ .



$\text{Li}_{2.4}\text{Ni}_{0.6}\text{N}$  (0.517 g, 7.848 mmol) and filed elemental Sr pieces (0.370 g, 4.223 mmol), were mixed in a 1 : 2 molar ratio and pressed into a tablet of 8 mm. This tablet was placed into a tantalum crucible and inserted into a silica tube. The apparatus was heated, under  $\text{N}_2$  flow, to 973 K, at 100 K/h, for 20 h and then allowed to naturally cool to room temperature. The obtained product was then ground, repressed into a tablet and reheated with the same heating program to encourage a complete reaction.

Single crystals of the product were grown by filling a tantalum ampoule with the product (0.211 g), along with elemental Li (0.393 g) as a fluxing agent. The ampoule was then sealed by an arc welder and inserted into a fused silica tube, which was then heated, under Ar flow, to 973 K at 100 K/h and allowed to cool at a controlled rate of 1.5 K/h. After opening the ampoule, the Li flux was removed using liquid ammonia leaving a sample containing a metallic dark blue powder and small metallic blue crystals.

### 5.3.3. Characterisation

#### 5.3.3.1. Structure determination and crystal structure of $\text{Sr}_2[(\text{Li}_{1-x}\text{Ni}_x)\text{Ni}_2\text{N}_2]$

Single crystals of each sample were measured using single crystal X-ray diffraction and indexed with an orthorhombic unit cell, with only slight variation in unit cells ( $a = 7.1531(3) - 7.1580(3) \text{ \AA}$ ,  $b = 9.7018(5) - 9.72380(5) \text{ \AA}$  and  $c = 7.3606(3) - 7.3959(4) \text{ \AA}$ ). This agrees well with the unit cell seen for the isostructural  $\text{Ba}_2[\text{Ni}_3\text{N}_2]$  ( $a = 7.152 \text{ \AA}$ ,  $b = 10.323 \text{ \AA}$  and  $c = 7.401 \text{ \AA}$ ).<sup>[226]</sup> The  $a$  and  $c$  lengths are close to those seen for  $\text{Ba}_2[\text{Ni}_3\text{N}_2]$  however, the  $b$  length is noticeably shorter, which would be expected, since Sr cations have a smaller ionic radii than Ba cations and forms a smaller distorted trigonal planar arrangement with N, which leads to decreasing the distance between the puckered layers along [010] (*Figure 5.8*).

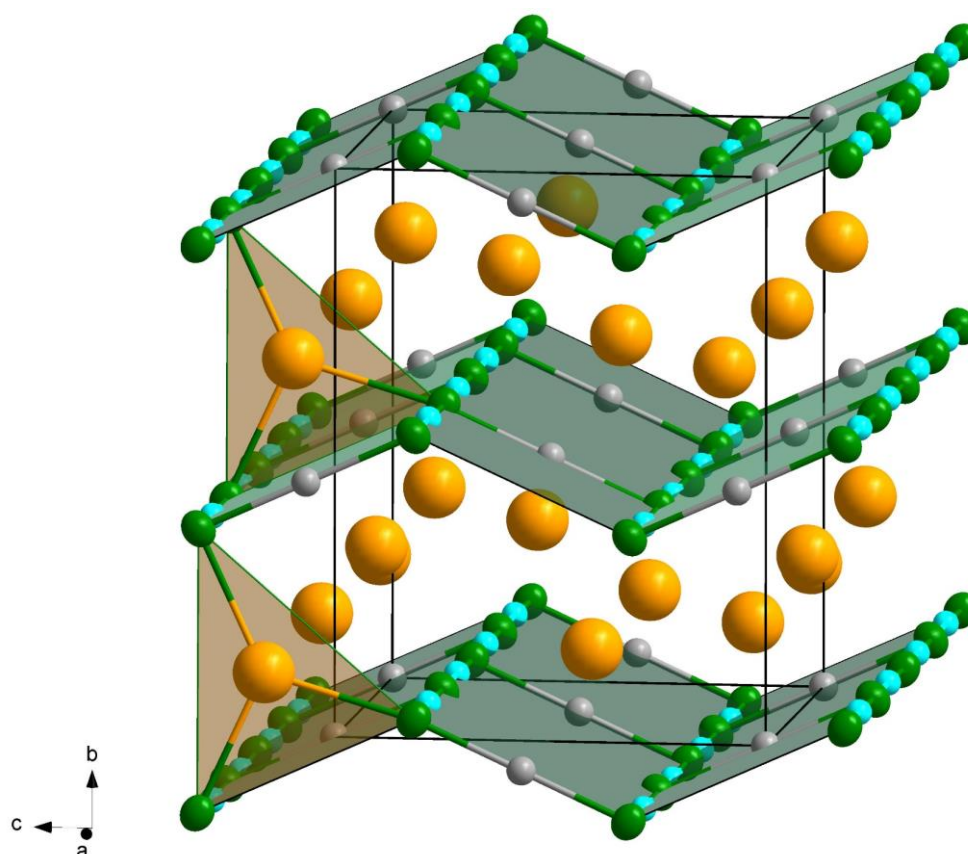


Figure 5.8. Section of the crystal structure of  $\text{Sr}_2[(\text{Li}_{1-x}\text{Ni}_x)\text{Ni}_2\text{N}_2]$ . Sr—orange, N—green, Ni—blue and Li/Ni—silver. Unit cell edges are shown by black lines.

Refinements of the single crystal X-ray diffraction data proved that each sample was  $\text{Sr}_2[(\text{Li}_{1-x}\text{Ni}_x)\text{Ni}_2\text{N}_2]$  and had crystallised isostructural to  $\text{Ba}_2[\text{Ni}_3\text{N}_2]$  (Tables 5.7., A.1. and A.2.), except for the Ni cations that interconnect the linear chains are partially replaced with Li cations. Refining the occupation of the Li position, by introducing Ni substitution, gave a better refinement and produced an estimated degree of substitution on the interconnecting position for the respective crystal. Attempts at substituting Li cations into the Ni cations found in the infinite near linear chains proved unsuccessful, implying that substitution exclusively occurs at the interconnecting position, resulting in a final composition of  $\text{Sr}_2[(\text{Li}_{1-x}\text{Ni}_x)\text{Ni}_2\text{N}_2]$ . The unit cell and volume appear to, with increasing Ni content, slowly increase however, a sudden decrease is seen in the unit cell and volume for sample D. The following sample, sample E, shows the same tendency to increase the unit cell and volume with increasing Ni (Figure 5.9.).

Powder X-ray diffraction measurements and refinements were conducted on every sample and crystal structure data for  $\text{Sr}_2[(\text{Li}_{1-x}\text{Ni}_x)\text{Ni}_2\text{N}_2]$ , obtained from single crystal refinement, was used as a structural template (Tables 5.1., 5.8. and A.3.). The values for the unit cells calculated from

the powder diffraction measurements agree well with those calculated from a single crystal (*Table 5.9*). However, the volumes from powder diffraction data have no correlation with Ni content. This is likely due to the microcrystalline powder samples having a more overall varied Ni content, resulting in there being no observable trend between the volume and Ni content. Samples B and D were found to primarily contain  $\text{Sr}_2[(\text{Li}_{1-x}\text{Ni}_x)\text{Ni}_2\text{N}_2]$ , except for a small number of reflections which could not be assigned. The other samples contained side products of either  $\text{SrLi}_{4-x}\text{Ni}_x\text{N}_2$ ,  $\text{Sr}_2\text{N}$  or an unidentifiable phase.<sup>[225,247]</sup> An exception to this is sample A, which appeared to contain, as a side product, the previously unknown compound  $\text{Sr}_{2-x}\text{Ni}_x\text{N}$  (*See Appendix C*).

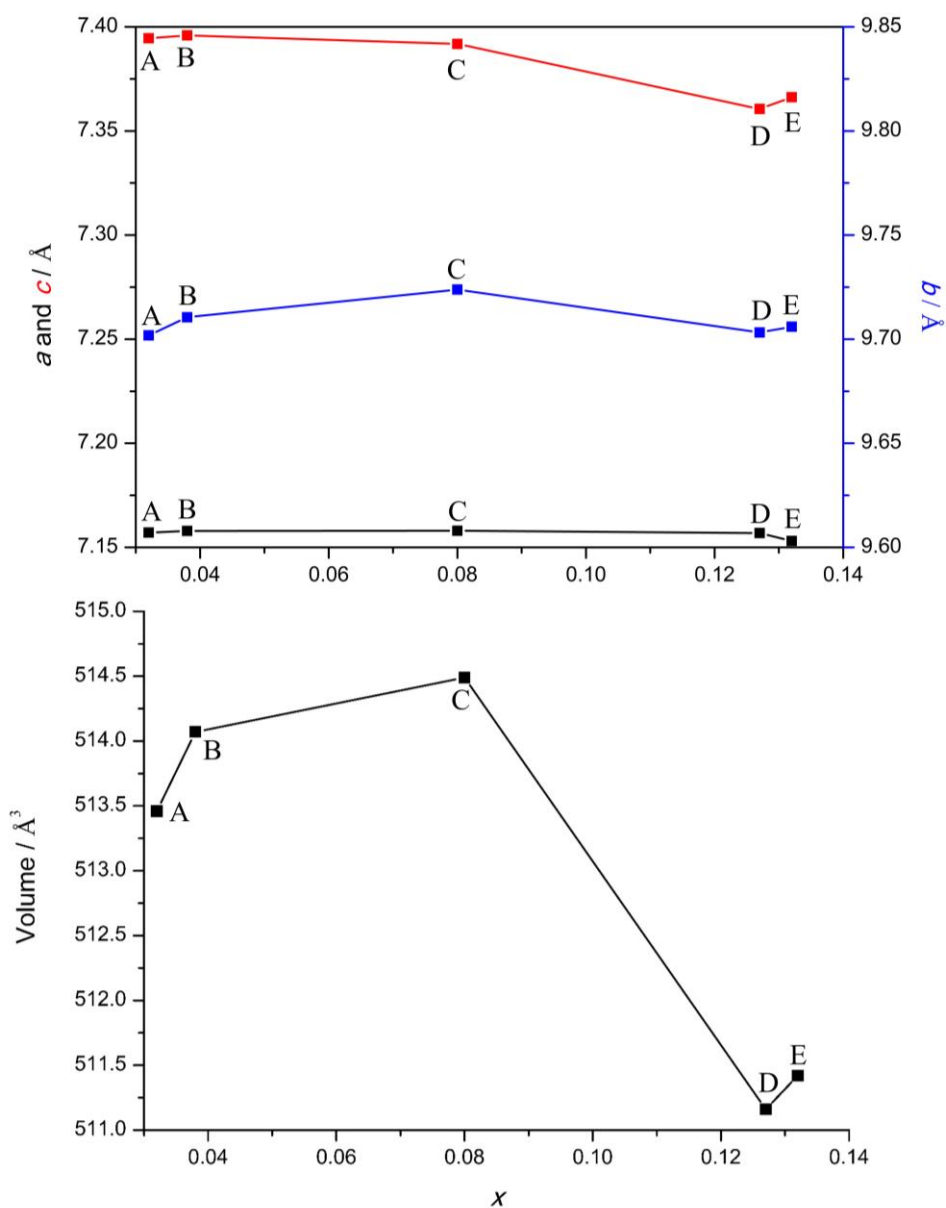


Figure 5.9. Relationship between values of  $x$  for  $\text{Sr}_2[(\text{Li}_{1-x}\text{Ni}_x)\text{Ni}_2\text{N}_2]$  and unit cell parameters (upper) and volume (lower).  $a$  is shown in black,  $b$  is shown in blue and  $c$  is shown in red.

Comparison of the unit cell parameters of each sample, from single crystal refinement and Rietveld refinement, shows very slight variation in unit cell parameters, with no correlation to expected Ni content, resulting in no simple method to determine related Ni content between samples. Since no value for the ionic radii of two fold coordinated Li(I) and Ni(I) cations are given in the literature, a value was approximated based on a six-fold Li(I) and Ni(II) (eq. 5.2). For estimation of the change in ionic radius from Ni(II) to Ni(I), the relative increase in ionic radius of Cu(II) to Cu(I) was used as an example.<sup>[187]</sup> This resulted in the ionic radius of Li(I) and Ni(I) cations, in two fold coordination, having very similar ionic radii, 0.65 Å and 0.64 Å respectively. Since there is not a significant difference between the ionic radii, this would explain why no discernible correlation between Ni content and unit cell is observed.

$$[2]_r = [6]_r \left(\frac{2}{6}\right)^{\frac{1}{8}} \quad (\text{eq. 5.2})$$

Table 5.7. Single crystal refinement data of  $\text{Sr}_2[(\text{Li}_{1-x}\text{Ni}_x)\text{Ni}_2\text{N}_2]$ .

	Sample A $x = 0.032(2)$	Sample B $x = 0.038(2)$	Sample C $x = 0.080(1)$	Sample D $x = 0.127(1)$	Sample E $x = 0.132(2)$
Crystal System	Orthorhombic	Orthorhombic	Orthorhombic	Orthorhombic	Orthorhombic
Space Group	<i>Cmca</i> (No. 64)	<i>Cmca</i> (No. 64)	<i>Cmca</i> (No. 64)	<i>Cmca</i> (No. 64)	<i>Cmca</i> (No. 64)
<i>Z</i>	4	4	4	4	4
<i>a</i> /Å	7.1571(3)	7.1579(5)	7.1580(3)	7.1569(3)	7.1531(3)
<i>b</i> /Å	9.7018(5)	9.7105(7)	9.72380(5)	9.7032(4)	9.7060(5)
<i>c</i> /Å	7.3945(3)	7.3959(4)	7.3918(4)	7.3606(3)	7.3662(4)
$\rho_{\text{calc}}/\text{gcm}^{-3}$	4.238	4.233	4.230	4.257	4.255
Volume <i>V</i> /Å <sup>3</sup>	513.45	514.07	514.49	511.16	511.42
Measurement temperature/K	293(2)	293(2)	293(2)	293(2)	293(2)
Index range	$-9 \leq h \leq 8$ $-12 \leq k \leq 12$ $-9 \leq l \leq 9$	$-8 \leq h \leq 9$ $-12 \leq k \leq 12$ $-9 \leq l \leq 9$	$-9 \leq h \leq 8$ $-12 \leq k \leq 12$ $-9 \leq l \leq 9$	$-9 \leq h \leq 9$ $-12 \leq k \leq 11$ $-9 \leq l \leq 9$	$-8 \leq h \leq 9$ $-12 \leq k \leq 12$ $-9 \leq l \leq 9$
Max. $2\theta$ /deg	54.87	54.83	54.82	54.92	54.92
<i>F</i> (000)	596	596	596	596.0	596.0
$\mu/\text{mm}^{-1}$	27.72	27.69	27.66	27.84	27.83
Observed reflections	4846	3642	4287	4889	4401
Unique reflections	323	323	323	323	323
Refined parameters	24	24	24	24	24
$R_{\text{int}}/R_{\sigma}$	0.0597/0.0232	0.0778/0.0322	0.0487/0.0203	0.0551/0.0204	0.0901/0.0308
$R_1/wR_2$	0.0249/0.0552	0.0311/0.0686	0.0199/0.0460	0.0215/0.0513	0.0292/0.0758
<i>Goof</i>	1.113	1.054	1.157	1.171	1.223
Remaining electron density (max/min)/Å <sup>-3</sup>	1.37/-0.54	1.57/-0.76	0.93/-0.44	0.89/-0.72	1.57/-0.71

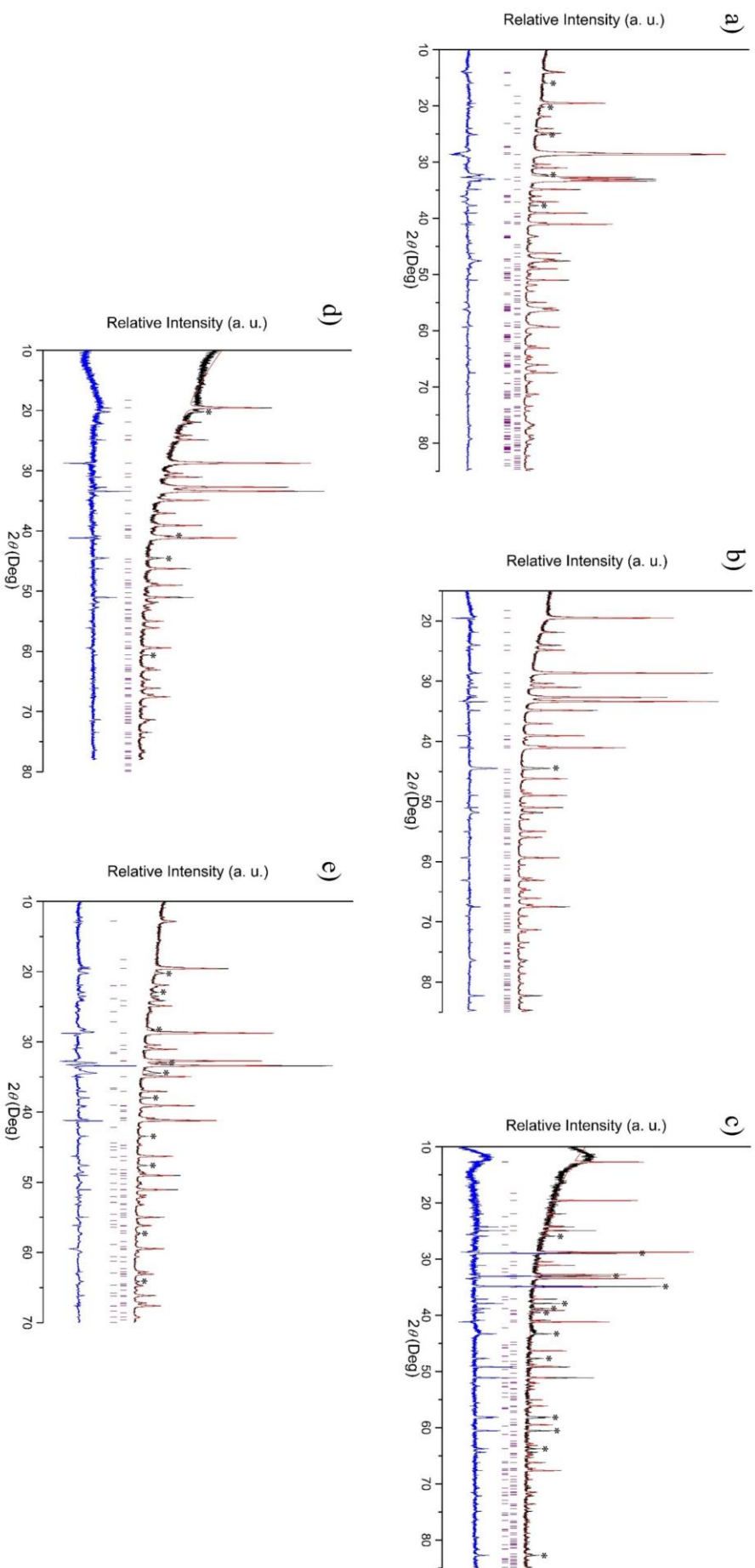


Figure 5.10. Graphical representations of Rietveld structural refinements of  $\text{Sr}_2[(\text{Li}_{1-x}\text{Ni}_x)\text{Ni}_2\text{N}_2]$  from X-ray powder diffraction measurements of a) sample A –  $\text{Sr}_2[(\text{Li}_{1-x}\text{Ni}_x)\text{Ni}_2\text{N}_2]$  and  $\text{Sr}_{2-x}\text{Ni}_x\text{N}$ ; b) sample B –  $\text{Sr}_2[(\text{Li}_{1-x}\text{Ni}_x)\text{Ni}_2\text{N}_2]$ ; c) sample C –  $\text{Sr}_2[(\text{Li}_{1-x}\text{Ni}_x)\text{Ni}_2\text{N}_2]$  and  $\text{SrLi}_{4-x}\text{Ni}_x\text{N}_2$ ; d) sample D –  $\text{Sr}_2[(\text{Li}_{1-x}\text{Ni}_x)\text{Ni}_2\text{N}_2]$  and  $\text{SrLi}_{4-x}\text{Ni}_x\text{N}_2$ . The observed pattern is shown in black, the calculated one in red, possible Bragg reflection positions are in purple and the difference in blue. Marked reflections (\*) were unable to be identified.

Table 5.8. Unit cell from the powder X-ray diffraction refinement of  $\text{Sr}_2[(\text{Li}_{1-x}\text{Ni}_x)\text{Ni}_2\text{N}_2]$ .

	Sample A	Sample B	Sample C	Sample D	Sample E
	$x = 0.032(2)$	$x = 0.038(2)$	$x = 0.080(1)$	$x = 0.127(1)$	$x = 0.132(2)$
Space Group	<i>Cmca</i> (No. 64)				
$a/\text{\AA}$	7.1546(2)	7.1546(2)	7.1416(7)	7.1530(2)	7.1496(3)
$b/\text{\AA}$	9.6910(3)	9.6928(3)	9.681(1)	9.6936(3)	9.6954(5)
$c/\text{\AA}$	7.3894(2)	7.3911(2)	7.3690(7)	7.3700(3)	7.3625(3)
$V/\text{\AA}^3$	512.345	512.557	509.478	511.024	510.352
$R_{wp}/\%$	11.8	13.6	30.1	9.18	12.2
$R_{Bragg}/\%$	13.1	13.7	33.4	13.2	12.9

 Table 5.9. Comparison between unit cell parameters from powder X-ray diffraction refinement and single crystal X-ray diffraction refinement of  $\text{Sr}_2[(\text{Li}_{1-x}\text{Ni}_x)\text{Ni}_2\text{N}_2]$ .

	Single crystal				Powder			
	$a/\text{\AA}$	$b/\text{\AA}$	$c/\text{\AA}$	$V/\text{\AA}^3$	$a/\text{\AA}$	$b/\text{\AA}$	$c/\text{\AA}$	$V/\text{\AA}^3$
Sample A $x = 0.032(2)$	7.1571(3)	9.7018(5)	7.3945(3)	513.45	7.1546(2)	9.6910(3)	7.3894(2)	512.345
Sample B $x = 0.038(2)$	7.1579(5)	9.7105(7)	7.3959(4)	514.07	7.1546(2)	9.6928(3)	7.3911(2)	512.557
Sample C $x = 0.080(1)$	7.1580(3)	9.72380(5)	7.3918(4)	514.49	7.1416(7)	9.681(1)	7.3690(7)	509.478
Sample D $x = 0.127(1)$	7.1569(3)	9.7032(4)	7.3606(3)	511.16	7.1530(2)	9.6936(3)	7.3700(3)	511.024
Sample E $x = 0.132(2)$	7.1531(3)	9.7060(5)	7.3662(4)	511.42	7.1496(3)	9.6954(5)	7.3625(3)	510.352

Examination of the complex anion,  $[(\text{Ni}_{1-x}\text{Li}_x)\text{Ni}_2\text{N}_2]^{4-}$ , shows that it consists of near linear infinite chains of  ${}^1_\infty[\text{NiN}_{2/2}^{2-}]$ , identical to those found in  $\text{Ba}_2[\text{Ni}_3\text{N}_2]$ .<sup>[226]</sup> However, the interconnecting cations, which bridge the infinite chains, are Li cations substituted with varying amounts of Ni (*Figure 5.8*). While puckered complex anions, such as these, have been observed before,<sup>[226,246]</sup> it appears to be the first observation of a dominant presence of Li cations on this singular position. The resulting interatomic distance between the substituted interconnecting atom Li(1)/Ni(1) and N(1) along the linear chain,  $\sim 2.0$  Å, is in agreement with the interatomic distances previously seen in  $\alpha\text{-Li}_3\text{N}$ , 1.938 Å,<sup>[224]</sup> and ternary  $\text{Li}_{3-x}\text{Ni}_x\text{N}$ , between 1.923 and 1.761 Å, (*Table 5.10*).<sup>[231,245]</sup> However, it is slightly longer than what has been previously observed in  $\text{Ba}_2[(\text{Ni}_{0.57}\text{Li}_{0.43})\text{Ni}_2\text{N}_2]$ , 1.913 Å.<sup>[246]</sup> Typically, the influence of Ni content on this mixed position could be observed through observation of the interatomic distances between the mixed Li(1)/Ni(1) position and N(1) position (*Table 5.11*). It would be expected that with increasing Ni content, the interatomic distance would decrease, due to Ni and N having a shorter interatomic distance, 1.89 Å, as observed in  $\text{Ni}_3\text{N}$ .<sup>[102]</sup> This kind of decrease of interatomic distance has been observed for the isotypic phase  $\text{Ba}_2[(\text{Ni}_{0.57}\text{Li}_{0.43})\text{Ni}_2\text{N}_2]$ , which contains a majority of Ni content on this position and exhibits a lower Li/Ni–N interatomic distance, 1.9 Å.<sup>[246]</sup> However, the amount of Ni on the interconnecting cation of the titular compounds is relatively small and the difference in interatomic distances between each sample falls within the margin of error. The Sr(1)–N(1) interatomic distance and angles seem unaffected by the content of Ni (*Table 5.11*).

Table 5.10. Comparison of interatomic distances between Ni and N, including coordination number, for selected metal nitrides.

	CN(N)	M–N/Å
$\alpha\text{-Li}_3\text{N}$ <sup>[224]</sup>	8	1.938
$\text{Li}_{2.93}\text{Ni}_{0.07}\text{N}$ <sup>[245]</sup>	8	1.923
$\text{Li}_{2.435}\text{Ni}_{0.565}\text{N}$ <sup>[231]</sup>	8	1.807
$\text{Li}_{2.15}\text{Ni}_{0.85}\text{N}$ <sup>[245]</sup>	8	1.761
$\text{Ni}_3\text{N}$ <sup>[102]</sup>	6	1.770



Table 5.11. Interatomic distances (Å) and angles (°) of selected interatomic distances for Sr<sub>2</sub>[(Li<sub>1-x</sub>Ni<sub>x</sub>)Ni<sub>2</sub>N<sub>2</sub>].

	Sample A <i>x</i> = 0.032(2)	Sample B <i>x</i> = 0.038(2)	Sample C <i>x</i> = 0.080(1)	Sample D <i>x</i> = 0.127(1)	Sample E <i>x</i> = 0.132(2)
Li(1)/Ni(1)–N(1)	2.031(5)	2.034(6)	2.027(4)	2.014(4)	2.016(5)
Ni(2)–N(1)	1.7895(1)	1.7897(2)	1.7897(1)	1.7894(1)	1.7885(1)
Sr(1)–N(1)	2.672(5)	2.6706(6)	2.676(4)	2.667(4)	2.670(5)
N(1)–Li(1)/Ni(1)–N(1)	180	180	180	180	180
N(1)–Ni(2)–N(1)	178.4(3)	178.2(4)	178.3(2)	178.5(2)	178.2(3)
N(1)–Sr(1)–N(1)	131.1(1)	131.2(2)	131.3(2)	131.2(1)	131.2(1)

### 5.3.3.2. Energy dispersive spectroscopy

Single crystals of every sample were measured using energy dispersive spectroscopy. This technique was used to analyse the Ni content of each sample by determining the ratio between Sr and Ni content. The content of Li cations in each sample was not possible to determine, due to energy dispersive spectroscopy not being able to detect elements lighter than B atoms. Mounting of samples onto the measurement apparatus exposed each crystal to air for a short duration. Since the samples are sensitive to air and moisture, the accurate determination of N content was not possible.

Multiple crystals from every sample were selected for measurement. Since the majority of the bulk products were not single phase, samples which did not correspond to the expected ratio of Sr to Ni (2:2+*x*, where 0 ≤ *x* ≤ 1) were not used. Multiple measurements were conducted on each crystal at different points across the selected surface, which showed a fluctuation in the value of *x*, amount of Ni substituted onto the Li position, indicating that a composition gradient could be present along the crystal (*Table 5.12.*). Since the measurements are sensitive to any impurity on the surface of the crystal, this variation in Ni content could be also caused by elemental Ni on the surface of the crystal. Due to the uncertainty for the origin of the variation in Ni content, the lowest value of Ni content for each respective sample was selected to reduce the impact of false data for Ni content (*Table 5.13.*).

The largest range for  $x$  in  $\text{Sr}_2[(\text{Li}_{1-x}\text{Ni}_x)\text{Ni}_2\text{N}_2]$  is seen in sample C ( $0.23 \leq x \leq 1$ ), which was synthesised under different conditions to the other samples. The difference in synthesis method could be responsible for this broad composition gradient however, the presence of Ni impurities on the crystal surface could produce misleading values.

Table 5.12. Relative values from energy dispersive spectroscopy of Sr and Ni for samples of  $\text{Sr}_2[(\text{Li}_{1-x}\text{Ni}_x)\text{Ni}_2\text{N}_2]$ .

Sample A	<i>at</i> (Sr)/%	<i>at</i> (Ni)/%	$x$
1	20.05±0.09	22.11±0.09	0.21±0.01
2	20.94±0.09	22.02±0.09	0.10±0.01
3	22.96±0.10	25.91±0.10	0.26±0.01
4	22.97±0.10	24.66±0.11	0.15±0.01
5	20.46±0.09	23.37±0.09	0.28±0.01
6	21.77±0.13	22.40±0.16	0.06±0.01
Sample B	<i>at</i> (Sr)/%	<i>at</i> (Ni)/%	$x$
1	16.47±0.07	19.01±0.08	0.31±0.01
2	19.42±0.09	20.24±0.10	0.08±0.01
3	20.09±0.09	20.94±0.10	0.08±0.01
4	20.17±0.09	20.60±0.10	0.04±0.01
5	19.47±0.09	20.36±0.10	0.09±0.01
Sample C	<i>at</i> (Sr)/%	<i>at</i> (Ni)/%	$x$
1	32.33±0.15	36.06±0.16	0.23±0.01
2	22.99±0.11	30.03±0.13	0.61±0.01
3	14.85±0.09	20.34±0.13	0.74±0.02
4	13.79±0.09	20.78±0.13	1.01±0.02
5	24.49±0.12	28.46±0.13	0.32±0.01
Sample D	<i>at</i> (Sr)/%	<i>at</i> (Ni)/%	$x$
1	24.98±0.11	27.09±0.12	0.17±0.01
2	25.02±0.12	26.77±0.12	0.14±0.01
3	24.86±0.12	28.22±0.14	0.27±0.02
4	25.12±0.12	27.25±0.12	0.17±0.02
5	26.21±0.12	27.25±0.12	0.08±0.01
Sample E	<i>at</i> (Sr)/%	<i>at</i> (Ni)/%	$x$
1	18.67±0.10	19.93±0.12	0.13±0.01
2	18.18±0.09	19.58±0.11	0.15±0.01

### 5.3.4. Discussion and conclusion

In this chapter several samples of  $\text{Sr}_2[(\text{Li}_{1-x}\text{Ni}_x)\text{Ni}_2\text{N}_2]$  ( $0 \leq x \leq 1$ ) were prepared, which crystallises isostructural to the previously known  $\text{Ba}_2[\text{Ni}_3\text{N}_2]$ <sup>[226]</sup> and  $\text{Ba}_2[(\text{Ni}_{0.57}\text{Li}_{0.43})\text{Ni}_2\text{N}_2]$ .<sup>[246]</sup> This structure is built from parallel infinite linear chains,  $\frac{1}{\infty}[\text{NiN}_{2/2}^{2-}]$ , which are interconnected by a mixed Li/Ni position. Since Li and Ni cations have similar ionic radii, there are very little changes in unit cell parameters with increasing Ni content.

X-ray diffraction experiments were conducted on both isolated single crystals and microcrystalline powder sample. These measurements confirmed the existence of the titular compound, as well as side products of  $\text{SrLi}_{4-x}\text{Ni}_x\text{N}_2$ ,<sup>[225]</sup>  $\text{Sr}_2\text{N}$ <sup>[248]</sup> and  $\text{Sr}_{2-x}\text{Ni}_x\text{N}$ . Determination of the amount of Ni on the mixed Li/Ni position through X-ray diffraction techniques is not very reliable, with the error associated to it being in fact three times higher than what is calculated.

Energy dispersive spectroscopy was utilised to obtain a precise value of Ni on the mixed position. These measured values vary quite a bit from those calculated by single crystal refinement (*Table 5.13.*). An exception to this are samples B and C, which both have single crystal refinements that fit very well with the values obtained by energy dispersive spectroscopy. While a large error is attributed to refinement of a mixed occupied position, this error does not account for the large difference seen between the values from energy dispersive spectroscopy and single crystal refinement. Instead, it is more likely that every crystal within a sample has varying Ni content.

Table 5.13. Comparison of calculated chemical formula of each sample from energy dispersive spectroscopy and single crystal refinement.

Sample	Energy dispersive spectroscopy	Single crystal
A	$\text{Sr}_{2.00(1)}[(\text{Li}_{0.94}\text{Ni}_{0.06(1)})\text{Ni}_{2.00(1)}\text{N}_2]$	$\text{Sr}_2[(\text{Li}_{0.968(2)}\text{Ni}_{0.032(2)})\text{Ni}_2\text{N}_2]$
B	$\text{Sr}_{2.000(9)}[(\text{Li}_{0.96}\text{Ni}_{0.04(1)})\text{Ni}_{2.00(1)}\text{N}_2]$	$\text{Sr}_2[(\text{Li}_{0.962(2)}\text{Ni}_{0.038(2)})\text{Ni}_2\text{N}_2]$
C	$\text{Sr}_{2.000(9)}[(\text{Li}_{0.77}\text{Ni}_{0.23(1)})\text{Ni}_{2.00(1)}\text{N}_2]$	$\text{Sr}_2[(\text{Li}_{0.920(1)}\text{Ni}_{0.080(1)})\text{Ni}_2\text{N}_2]$
D	$\text{Sr}_{2.000(9)}[(\text{Li}_{0.92}\text{Ni}_{0.08(1)})\text{Ni}_{2.00(1)}\text{N}_2]$	$\text{Sr}_2[(\text{Li}_{0.873(1)}\text{Ni}_{0.127(1)})\text{Ni}_2\text{N}_2]$
E	$\text{Sr}_{2.00(1)}[(\text{Li}_{0.87}\text{Ni}_{0.13(1)})\text{Ni}_{2.00(1)}\text{N}_2]$	$\text{Sr}_2[(\text{Li}_{0.868(2)}\text{Ni}_{0.132(2)})\text{Ni}_2\text{N}_2]$

Each crystal had several measurements across the selective surface, which showed a variation in Ni content along the crystal. This variation was first thought to be caused by elemental Ni impurities on the surface. However, since the powder diffraction pattern of every sample did not contain elemental Ni, it is more likely that the variation is caused by a composition gradient within the crystal. This gradient can not be characterised via powder X-ray diffraction, since this method results in the average occupation of the sample. This composition gradient is present for every sample analysed, some with a broader gradient than others. The common occurrence of this composition gradient can be explained as subtle variations in synthesis conditions, such as temperature fluctuations. As mentioned previously, Li and Ni cations having relatively similar ionic radii, which means both cations can equally occupy the interconnecting position of the complex anion. Since the atomic environment surrounding of this position is not affected by which of these cations are present, there is no chemical reason for Li and Ni cations to be ordered along this position and thus a statistical distribution is more likely.

The sample that, through energy dispersive spectroscopy, resulted in the largest composition gradient, including highest content, of Ni was sample C ( $0.23 \leq x \leq 1$ ). This result is particularly interesting since the single crystal analysed by X-ray diffraction showed a much lower Ni content ( $x = 0.08$ ). Even with the large error taken into account, the Ni content calculated by refinement of the single crystal is still lower than the lowest value determined via energy dispersive spectroscopy. This would imply that this particular sample has a variety of crystals containing very different amounts of Ni, which was not seen for the other samples. This is the only sample to have been produced using a different experimental procedure and is perhaps the reason why such a diverse gradient of Ni content, both along a single crystal and between crystals in the sample, is observed.

To achieve charge balance in this compound either two oxidation states of Ni are needed, Ni(0) and Ni(I), or a mixed valence intermediate. Investigations into mixed valence intermediates have been limited, but the effect of having two different valencies of an ion on equivalent positions are known to produce unusual properties. The presence of mixed valence intermediates can drastically change the electrical conductivity, magnetic properties, electronic structure and colour, compared to when the material does not have a mixed valence component.<sup>[249]</sup> An example of this effect with Ni cations has been observed in NiO and Li doped NiO.<sup>[250]</sup> Stoichiometric NiO is a green compound, but upon doping of Li to produce  $\text{Li}_x\text{Ni}_{1-x}\text{O}$  a mixed valence intermediate is formed, Ni(II) and Ni(III), which varies from grey to black, depending on Li content.<sup>[250]</sup> Mixed valence

of Ni has been observed before in  $\text{Ba}_2[\text{Ni}_3\text{N}_2]$ , suggesting an average Ni oxidation state of +0.67,<sup>[226]</sup> with a combination of X-ray absorption spectroscopy and magnetic susceptibility measurements confirming that Ni exists in a low oxidation state. Attempts at measuring magnetic susceptibility for crystals of  $\text{Sr}_2[(\text{Li}_{1-x}\text{Ni}_x)\text{Ni}_2\text{N}_2]$  were performed. However, after numerous measurements of different crystals, no presentable data was able to be produced, which is attributed to impurities along the surface as well as not being able to determine the orientation of the crystal relative to the sample holder. It would be expected that the material would exhibit similar Curie-paramagnetic properties as  $\text{Ba}_2[\text{Ni}_3\text{N}_2]$ , with antiferromagnetic exchange interactions dominating.



## 6. Synthesis and characterisation of $\text{Sr}_6\text{N}[\text{CuN}_2][\text{CN}_2]_2$

### 6.1. Overview

A branch of compounds that has been intensely studied are those containing the pseudo-chalcogenide anion  $[\text{CN}_2]^{2-}$ , which was first discovered in the compound  $\text{Ca}[\text{CN}_2]$ .<sup>[56]</sup> The  $[\text{CN}_2]^{2-}$  anion can exist in both the symmetric carbodiimide anion,  $[\text{N}=\text{C}=\text{N}]^{2-}$ , and the asymmetric cyanamide,  $[\text{N}\equiv\text{C}-\text{N}]^{2-}$ , both of which have been included into a diverse range of compounds with varying properties.

The determining factor of which of the two forms, cyanamide or carbodiimide, is favoured by the cations present. Hard cations result in the linear  $[\text{N}=\text{C}=\text{N}]^{2-}$  anion, due to the preferred ionic character which results in a symmetrical anion. Binary carbodiimides, which have been previously reported, include  $\text{Ca}[\text{CN}_2]$ ,<sup>[56]</sup>  $\text{Cr}_2[\text{CN}_2]_3$ <sup>[64]</sup> and  $M[\text{CN}_2]$  ( $M = \text{Mn} - \text{Cu}$ ).<sup>[57-60]</sup> The crystal structure types of these carbodiimides include: NaCl-type like structure,  $\beta$ - $\text{NaN}_3$ -type structure and NiAs-type like structure.

The near linear cyanamide anion,  $[\text{N}\equiv\text{C}-\text{N}]^{2-}$ , arises from the presence of soft cations. These cations have a stronger preference to covalent bond to one side of the anion, this results in the asymmetric cyanamide unit. The known binary cyanamides mainly have the same composition of  $M[\text{CN}_2]$  ( $M = \text{Be}, \text{Mg}, \text{Sr}, \text{Ba}, \text{Zn}, \text{Cd}, \text{Pb}$  and  $\text{Eu}$ ),<sup>[50-55]</sup> but compounds with monovalent cations are also known in the form  $M_2[\text{CN}_2]$  ( $M = \text{Li}, \text{Ag}, \text{Hg}$ ).<sup>[61-63]</sup> Interestingly,  $\text{Hg}_2[\text{CN}_2]$  has been produced as both a cyanamide and a carbodiimide, depending on reaction conditions.<sup>[251]</sup> This indicates that the synthetic approach can actually influence which  $[\text{CN}_2]^{2-}$  anion is produced within compounds containing cations that are between the typical soft and hard cation characteristics.

Property investigations of binary transition metal carbodiimides have, in recent years, seen a sudden increase of attention. This has led, not only to reports of varying synthesis methods,<sup>[57,59,252]</sup> but also a surprisingly diverse range of properties. The most promising application of transition metal carbodiimides is as a negative electrode material for lithium and sodium ion batteries.<sup>[82-86]</sup> Other possible applications are as corrosion protective layers,<sup>[78]</sup> photovoltaic devices,<sup>[81]</sup> fluorescent light sources<sup>[79,80]</sup> and light-emitting diodes.<sup>[76,77]</sup>

The  $[\text{CN}_2]^{2-}$  unit has also been observed to exist alongside other species of anions within a compound. These units can co-exist with the pseudo-halide anion  $\text{CN}^-$ , in  $M_2[\text{CN}_2][\text{CN}]_2$  ( $M = \text{Sr}$  and  $\text{Ba}$ ),<sup>[253]</sup> the nitride anion in  $M_4\text{N}_2[\text{CN}_2]$  ( $M = \text{Ca}$  and  $\text{Sr}$ )<sup>[254,255]</sup> and  $\text{Ca}_{11}\text{N}_6[\text{CN}_2]_2$ ,<sup>[254]</sup> hydrogencyanamide anion in  $M_5[\text{HCN}_2][\text{CN}_2]_2$  ( $M = \text{Na}$  and  $\text{K}$ )<sup>[256,257]</sup> and even the hydride anion, as observed in  $\text{K}_5\text{H}[\text{CN}_2]_2$ .<sup>[258]</sup>

Due to the near identical nature of the cyanamide and carbodiimide anions, distinguishing one from the other can prove quite problematic. This is partly due to the mesomeric effect of carbodiimides to convert to cyanamides. Investigative analysis showed that both anions can be distinguished from one another by Raman and infrared spectroscopy.<sup>[53,55,63,251,259–261]</sup> The resulting spectra are still very similar however, the asymmetry of the cyanamide anion causes the IR peak at roughly  $1220\text{ cm}^{-1}$  to be noticeably stronger (*Figure 6.1.*). In both anions vibrational frequencies are observed at around  $655\text{ cm}^{-1}$ , which correlates to the deformation vibration frequency of C–N single bond, and  $2000\text{ cm}^{-1}$ , which arises from symmetric stretching of the  $\text{C}\equiv\text{N}$  triple bond. Splitting of the asymmetric stretching frequency at roughly  $2000\text{ cm}^{-1}$  arises from the C atom being coordinated to two crystallographically independent N atoms.<sup>[51]</sup> This splitting is more pronounced for cyanamides, due to there being a preference in the mesomeric structure to adopt a triple and single bonding environment, unlike the carbodiimide counterpart (*Figure 6.1.*). Raman investigations of alkaline earth metal cyanamides and carbodiimides showed a strong correlation between C–N interatomic distances and coordination environments.<sup>[53]</sup>

The carbodiimide anion is considered a pseudo-chalcogenide anion. This characteristic allows it to act as a bridging ligand to allow effective magnetic super exchange between the bridged paramagnetic cations. The resulting structures of these compounds, containing  $3d$  transition metals such as  $\text{Cr}_2[\text{CN}_2]_3$  and  $M[\text{CN}_2]$  ( $M = \text{Mn} - \text{Cu}$ ), are isostructural to their respective oxide variants and also have the same colours.<sup>[57–60,64]</sup> Not only are these compounds isostructural to their oxide counterparts, but they also exhibit the same magnetic ordering, typically antiferromagnetic. This ability of the carbodiimide anion has made it an interesting field of investigation for new magnetic materials.



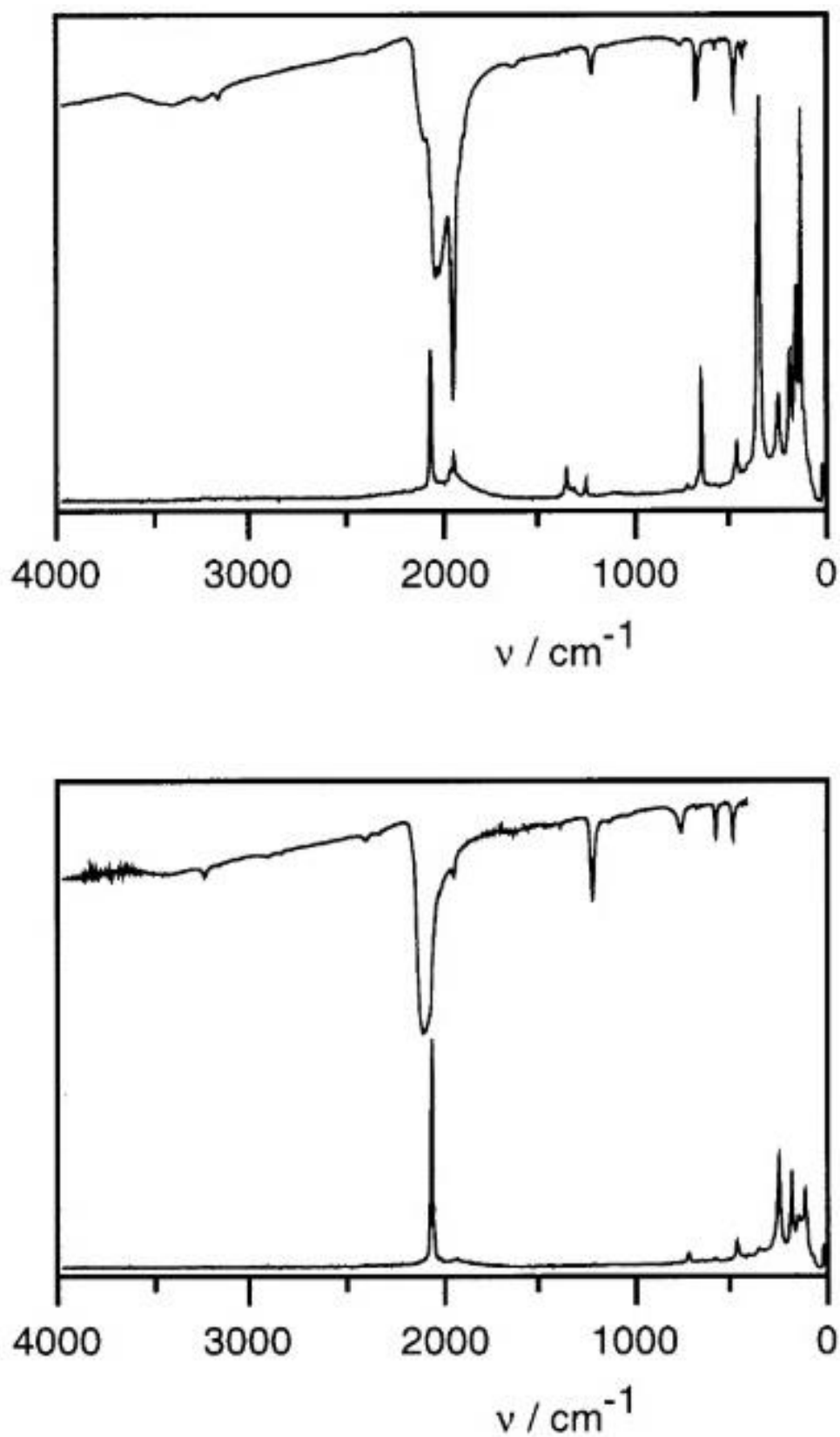


Figure 6.1. Raman and Infrared spectra from  $\text{Hg}[\text{N}=\text{C}=\text{N}]$  (top) and  $\text{Hg}[\text{N}\equiv\text{C}-\text{N}]$  (bottom).<sup>[251]</sup> Adapted with permission from X. Liu, P. Müller, P. Kroll, R. Dronskowski, *Inorg. Chem* **2002**, *41*, 4259–4265. Copyright 2002 American Chemical Society.

As mentioned previously, transition metal cations can function as the counter cation for the  $[\text{CN}_2]^{2-}$  anion. However, the transition metal can also act as part of a complex anion alongside the  $[\text{CN}_2]^{2-}$  anion. The formation of nitridometalate anions, with the form  $[\text{MN}_x]^{y-}$ , has been reported for several 4*d* and 5*d* transition metals with the form  $\text{Ba}_8[\text{MN}_4][\text{CN}_2]_5$  ( $M = \text{Mo}$  and  $\text{W}$ ),  $\text{Ba}_9[\text{MN}_4][\text{CN}_2]_6$  ( $M = \text{Mo}$  and  $\text{W}$ ) and  $\text{Ba}_9[\text{NbN}_4]\text{O}[\text{CN}_2]$ .<sup>[262,263]</sup>

Recently, the first row transition metal nitridometalate carbodiimides were produced, containing three different anionic species: carbodiimide anions, linear nitridometalate three atom anions and isolated nitride anions, resulting in a general formula of  $\text{Sr}_6\text{N}[\text{MN}_2][\text{CN}_2]_2$  ( $M = \text{Fe}$  and  $\text{Co}$ ).<sup>[97,259]</sup> To date in depth characterisation has only been conducted for  $\text{Sr}_6\text{N}[\text{CoN}_2][\text{CN}_2]_2$ . This characterisation showed that the linear coordinated Co cations exists in a +1 oxidation state and obeys the Curie-Weiss law.

## 6.2. Synthesis

A mixture of  $\alpha\text{-Li}_3\text{N}$ , prepared using the method seen in Chapter 2.1, and elemental Cu, with a 5:2 molar ratio, was pressed into a tablet with a diameter of 8 mm weighing 1.686 g. This tablet was placed into a tantalum crucible and inserted into a silica tube. The apparatus was heated, under  $\text{N}_2$  flow, to 773 K for 120 h and then allowed to naturally cool to room temperature.<sup>[92]</sup> This produced  $\text{Li}_2[(\text{Li,Cu})\text{N}]$ , which confirmed to be single phase by powder X-ray diffraction. Determination of the amount of Cu substitution was determined via correlation between the unit cell parameters and amount of Cu.<sup>[92]</sup> The refined unit cell parameters ( $a = 3.6626(3)$  Å and  $c = 3.7928(3)$  Å) confirmed the actual chemical formula to be  $\text{Li}_{2.6}\text{Cu}_{0.4}\text{N}$ .

$\text{Li}_{2.6}\text{Cu}_{0.4}\text{N}$  (0.070 g, 1.16 mmol), elemental Sr (0.114 g, 1.16 mmol) and C powder (0.0058 g, 0.48 mmol) were mixed and filled in a Nb ampoule, along with elemental Na (0.120 g) as a fluxing agent. The ampoule was then sealed by an arc welder and inserted into a fused silica tube, which was then heated, under Ar flow, to 1073 K and allowed to cool at a controlled rate of 2 K/h. After opening the ampoule, the Na flux was removed using liquid ammonia leaving a sample containing a mixture black powder and large rectangular red crystals.

### 6.3. Structure determination and characterisation of $\text{Sr}_6\text{N}[\text{CuN}_2][\text{CN}_2]_2$

#### 6.3.1. Structure Determination

A rectangular red single crystal was measured using single crystal X-ray diffraction and was indexed in a monoclinic unit cell ( $a = 3.8454(1) \text{ \AA}$ ,  $b = 9.9244(3) \text{ \AA}$ ,  $c = 14.6528(5) \text{ \AA}$ ,  $\beta = 92.280(2)^\circ$ ). Refinement single crystal structural data showed the structure crystallises in the space group  $P2_1/c$  (No. 14) and resulted in the suspected composition of  $\text{Sr}_6\text{N}[\text{CuN}_2][\text{CN}_2]_2$  (Tables 6.1. and 6.2. and Figure 6.2.).

While confirming the identity of the proposed  $[\text{CN}_2]^{2-}$  unit is not possible through the use of X-ray diffraction alone, the resultant structure was found to crystallise nearly identical to the previously reported carbodiimide  $\text{Sr}_6\text{N}[\text{MN}_2][\text{CN}_2]_2$  ( $M = \text{Fe}, \text{Co}$ ).<sup>[97,259]</sup> When the interatomic distances of C–N from  $\text{Sr}_6\text{N}[\text{FeN}_2][\text{CN}_2]_2$  (1.23 and 1.24  $\text{\AA}$ )<sup>[97]</sup> and  $\text{Sr}_6\text{N}[\text{CoN}_2][\text{CN}_2]_2$  (1.23 and 1.24  $\text{\AA}$ )<sup>[259]</sup> are compared with the distances found for the proposed  $[\text{CN}_2]^{2-}$  anion in the produced compound (1.225(9) and 1.242(9)  $\text{\AA}$ ), they are observed to be near identical. This observation is a reasonable first indication that the three atom anions present in the structure are the  $[\text{CN}_2]^{2-}$  units.

The crystal structure can be described as being constructed of face sharing corrugated layers (Figure 6.2.). The first layer is comprised of edge and corner sharing bidisphenoid polyhedra. The proposed C cation is nearly linearly coordinated by two crystallographically different N positions, which are in total coordinated by eight Sr cations. This results in a bidisphenoid polyhedron,  $\text{Sr}_8[\text{CN}_2]$  (Figure 6.3.). The second layer contains  $[\text{CuN}_2]^{5-}$  units, which construct two corner sharing octahedra of  $\text{Sr}_5\text{CuN}$ , with N at the centre (Figure 6.3.). These octahedra are linked into a corrugated layer by edge sharing with  $\text{Sr}_6\text{N}$  units. Both of these structural motifs are also observed in the aforementioned  $\text{Sr}_6\text{N}[\text{MN}_2][\text{CN}_2]_2$  ( $M = \text{Fe}, \text{Co}$ ).<sup>[97,259]</sup> However, the N-centred  $\text{Sr}_5\text{CuN}$  octahedra formed from the  $[\text{MN}_2]^{5-}$  anions, for the produced compound, are in fact regular octahedra.

The linearly coordinated [CuN<sub>2</sub>]<sup>5-</sup> anion has a Cu–N interatomic distance of 1.899(5) Å, which when compared with the interatomic distances of the [MN<sub>2</sub>]<sup>5-</sup> anions for Sr<sub>6</sub>N[MN<sub>2</sub>][CN<sub>2</sub>]<sub>2</sub> (*M* = Fe, Co), 1.85 Å and 1.84 Å respectively,<sup>[97,259]</sup> can be seen to be slightly longer than what has previously been seen. However, this interatomic distance appears to be normal for a Cu–N distances in [CuN<sub>2</sub>]<sup>5-</sup> anions when compared with the distances seen in Ca<sub>4</sub>Ba[CuN<sub>2</sub>]<sub>2</sub> (1.865 Å).<sup>[264]</sup> Comparison with the Cu–N distances for Cu<sub>3</sub>N (1.908 Å)<sup>[19]</sup> shows that the distances observed are typical for Cu–N interatomic distances.

Table 6.1. Single crystal structural refinement of Sr<sub>6</sub>N[CuN<sub>2</sub>][CN<sub>2</sub>]<sub>2</sub>.

Crystal system	Monoclinic
Space group	<i>P</i> 2 <sub>1</sub> / <i>c</i> (No. 14)
<i>Z</i>	2
<i>a</i> /Å	3.8454(1)
<i>b</i> /Å	9.9244(3)
<i>c</i> /Å	14.6528(5)
<i>β</i> /°	92.280(2)
$\rho_{\text{calc}}/\text{gcm}^{-3}$	4.228
Volume <i>V</i> /Å <sup>3</sup>	558.76
Measurement temperature/K	293(2)
Index range	–4 ≤ <i>h</i> ≤ 4 –12 ≤ <i>k</i> ≤ 12 –18 ≤ <i>l</i> ≤ 18
Max. 2 $\theta$ /deg	54.99
<i>F</i> (000)	636.0
$\mu/\text{mm}^{-1}$	30.26
Observed reflections	13782
Unique reflections	1265
Refined parameters	77
<i>R</i> <sub>int</sub> / <i>R</i> <sub>σ</sub>	0.0747/0.0309
<i>R</i> <sub>1</sub> / <i>wR</i> <sub>2</sub>	0.0300/0.0683
<i>Goof</i>	1.110
Remaining electron density (max/min)/Å <sup>-3</sup>	1.07/–1.32

Table 6.2. Atomic positions for the refinement of Sr<sub>6</sub>N[CuN<sub>2</sub>][CN<sub>2</sub>]<sub>2</sub>.

	Wyckoff Position	<i>x/a</i>	<i>y/b</i>	<i>z/c</i>	<i>U<sub>eq</sub></i>
Sr(1)	4 <i>e</i>	0.4881(2)	0.0713(6)	0.39014(4)	0.0136(2)
Sr(2)	4 <i>e</i>	0.0280(2)	0.10371(6)	0.83282(4)	0.0143(2)
Sr(3)	4 <i>e</i>	0.0332(1)	0.24551(6)	0.55485(4)	0.0132(2)
Cu(1)	2 <i>b</i>	1/2	0	0	0.0168(3)
C(1)	4 <i>e</i>	0.669(2)	0.2261(7)	0.2156(4)	0.016(1)
N(1)	2 <i>c</i>	0	0	1/2	0.014(2)
N(2)	4 <i>e</i>	0.522(1)	0.1719(5)	0.9436(4)	0.015(1)
N(3)	4 <i>e</i>	0.517(1)	0.1706(6)	0.6919(4)	0.021(1)
N(4)	4 <i>e</i>	0.853(2)	0.1293(6)	0.2412(4)	0.025(1)

Table 6.3. Anisotropic displacement parameters from the refinement of the crystal structure data of Sr<sub>6</sub>N[CuN<sub>2</sub>][CN<sub>2</sub>]<sub>2</sub>.

	$U_{11}$	$U_{22}$	$U_{33}$	$U_{23}$	$U_{13}$	$U_{12}$	$U_{eq}$
Sr(1)	0.0140(3)	0.0118(3)	0.0152(3)	-0.0003(2)	0.0020(2)	-0.0008(2)	0.0136(2)
Sr(2)	0.0141(3)	0.0133(3)	0.0155(3)	-0.0010(2)	-0.0006(2)	0.0011(2)	0.0143(2)
Sr(3)	0.129(3)	0.0125(3)	0.0143(3)	0.0000(2)	0.0008(2)	0.0004(2)	0.132(2)
Cu(1)	0.0171(6)	0.0142(6)	0.0189(6)	0.0013(4)	0.0003(4)	0.0007(4)	0.0168(3)
C(1)	0.019(3)	0.018(3)	0.012(3)	-0.004(3)	0.002(2)	-0.003(3)	0.016(1)
N(1)	0.012(4)	0.011(4)	0.018(4)	0.001(3)	0.005(3)	0.003(3)	0.014(2)
N(2)	0.018(3)	0.012(2)	0.014(3)	0.002(2)	0.000(2)	0.003(2)	0.015(1)
N(3)	0.024(3)	0.018(3)	0.022(3)	-0.001(2)	-0.003(2)	0.003(2)	0.021(1)
N(4)	0.029(3)	0.016(3)	0.032(4)	0.002(3)	0.012(3)	0.005(2)	0.025(1)

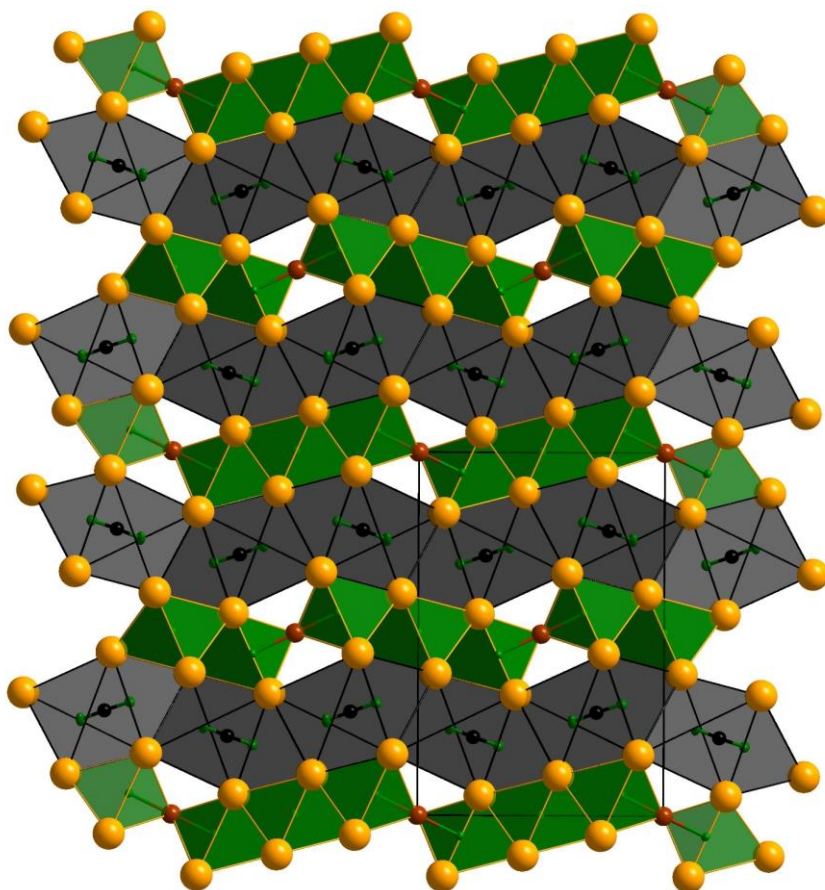


Figure 6.2. Section of the crystal structure of  $\text{Sr}_6\text{N}[\text{CuN}_2][\text{CN}_2]_2$  viewed along [100]. Sr–orange, N–green, Cu–brown and C–black. Unit cell edges are shown by black lines.

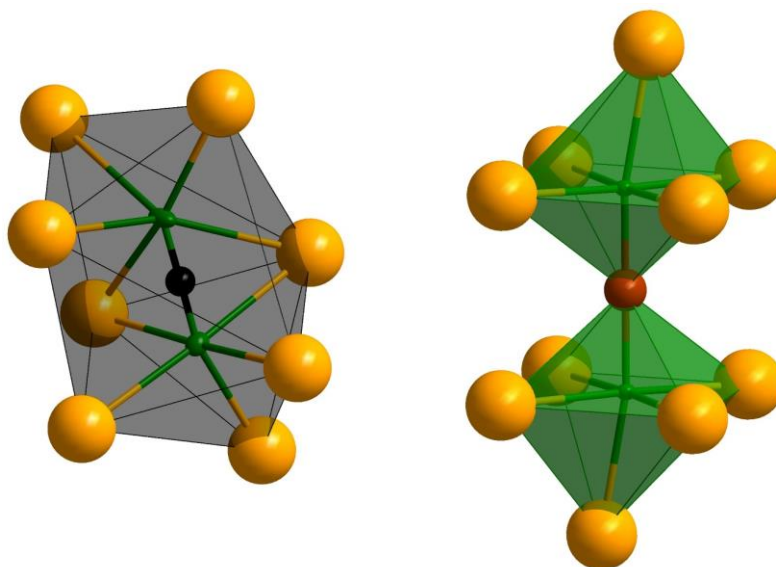


Figure 6.3. Coordination environments of  $[\text{CuN}_2]^{5-}$  units (left) and  $[\text{CN}_2]^{2-}$  units (right). Sr–orange, N–green, Cu–brown and C–black.

While crystal structures of  $\text{Sr}_6\text{N}[\text{MN}_2][\text{CN}_2]_2$  ( $M = \text{Fe}, \text{Co}$ ) and the titular compound are extremely similar, they are not isostructural. The first indication of this was that the Fe and Co variants crystallise in the orthorhombic space group  $P2_12_12$  (No. 18), while  $\text{Sr}_6\text{N}[\text{CuN}_2][\text{CN}_2]_2$  crystallises in the monoclinic space group  $P2_1/c$  (No. 14). Upon closer inspection of the crystal structures, the only discerning difference was that for  $\text{Sr}_6\text{N}[\text{MN}_2][\text{CN}_2]_2$  ( $M = \text{Fe}, \text{Co}$ ) the  $[\text{CN}_2]^{2-}$  anions are aligned, when viewed along  $[010]$ . However, for  $\text{Sr}_6\text{N}[\text{CuN}_2][\text{CN}_2]_2$  the  $[\text{CN}_2]^{2-}$  anions can be seen to ‘criss-cross’ along the equivalent viewing direction  $[001]$  (Figure 6.4.).

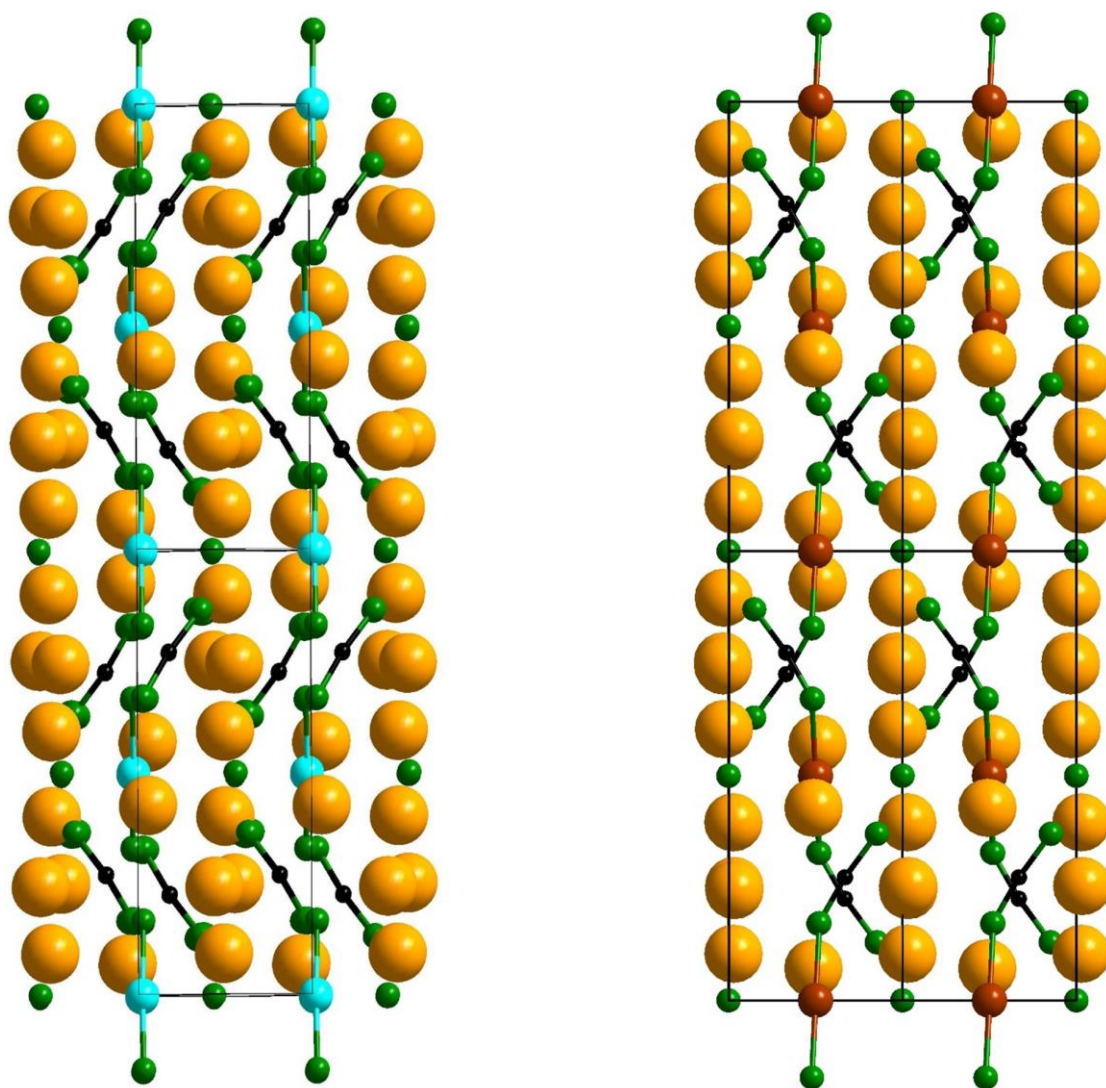


Figure 6.4. Comparison of sections of the crystal structures of  $\text{Sr}_6\text{N}[\text{CoN}_2][\text{CN}_2]_2$  (left),<sup>[259]</sup> viewed along  $[010]$  and  $\text{Sr}_6\text{N}[\text{CuN}_2][\text{CN}_2]_2$  (right), viewed along  $[001]$ . Sr—orange, N—green, Co—blue and Cu—brown. Unit cell edges are shown by black lines.



### 6.3.2. Magnetic susceptibility

Magnetic susceptibility measurements were conducted on a red single crystal of  $\text{Sr}_6\text{N}[\text{CuN}_2][\text{CN}_2]_2$ , approximately 0.5 mm in diameter. This sample was sealed in a glass capillary, with 0.1 mm diameter, and fixed to a plastic tube that is typically used for magnetic measurements and subjected to varying temperatures (*Figure 6.5.*).

The measurement showed the sample exhibits diamagnetic behaviour. This fits with what would be expected for a sample containing Cu(I) cations. However, a slight paramagnetic behaviour is also observed, which results in a  $\mu_{exp} = 1.16 \mu_B$ . This behaviour is clearly not an intrinsic part of  $\text{Sr}_6\text{N}[\text{CuN}_2][\text{CN}_2]_2$  and is attributed to the presence of paramagnetic impurities introduced into the glass capillary during sample preparation.

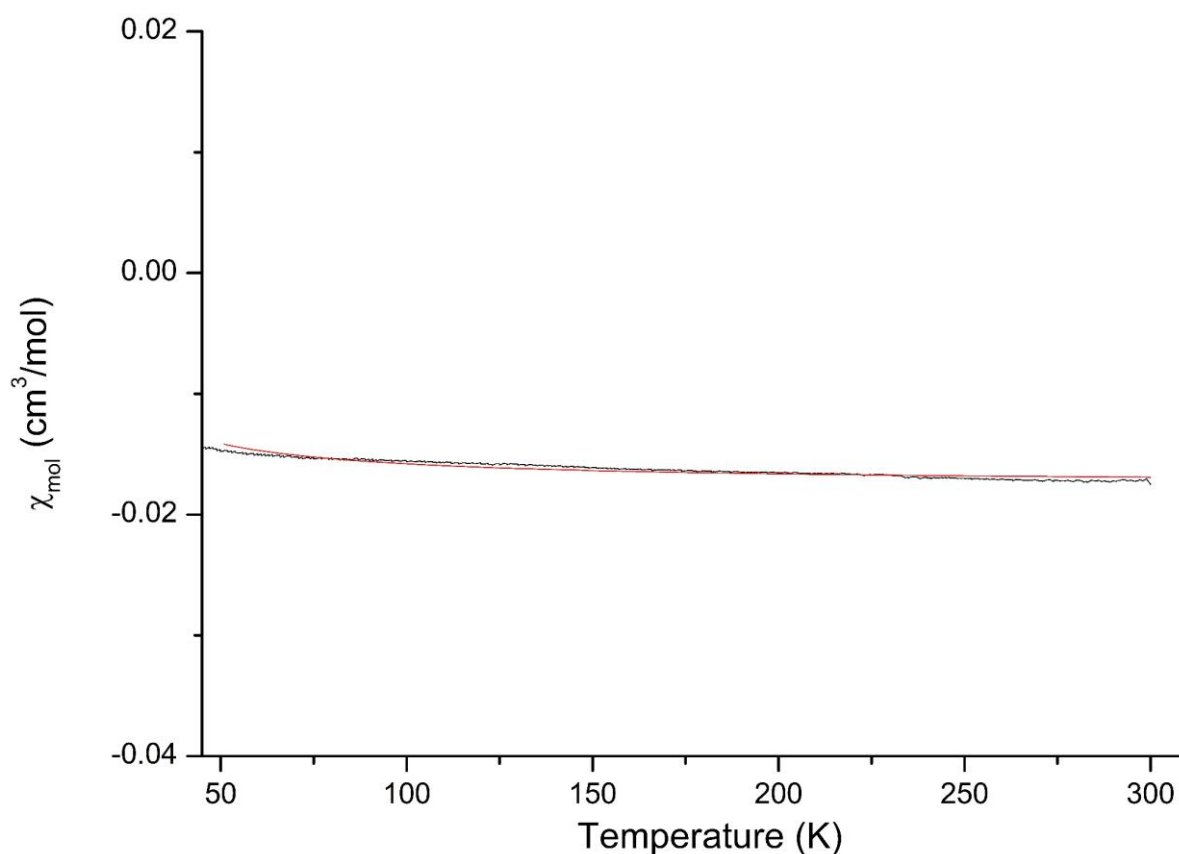


Figure 6.5. Magnetic susceptibility of  $\text{Sr}_6\text{N}[\text{CuN}_2][\text{CN}_2]_2$  with varying temperature at 50 kOe and a fitted Curie-Weiss law line between 50 and 300 K (red).

### 6.3.3. Raman spectroscopy

Due to the impossible task of discriminating between C and N by standard X-ray diffraction, single crystal Raman spectroscopy was employed to confirm the identity of the assumed  $[\text{CN}_2]^{2-}$  three atom anion. A red crystal was selected for this technique and spectroscopic data was collected, between 92 and  $4000\text{ cm}^{-1}$ , using the red laser ( $\lambda = 638\text{ nm}$ ).

For the resultant spectrum (Figure 6.6.), characteristic vibrational frequencies for the  $[\text{CN}_2]^{2-}$  anion were observed (Table 6.4.). The observed symmetric ( $\nu_1 = 1232$  and  $1245\text{ cm}^{-1}$ ) and asymmetric ( $\nu_3 = 1949$  and  $1993\text{ cm}^{-1}$ ) stretching frequencies, as well as the deformation vibration frequencies ( $\delta = 605$  and  $661\text{ cm}^{-1}$ ), are in agreement with those observed for  $\text{Sr}_6\text{N}[\text{CoN}_2][\text{CN}_2]_2$  ( $\nu_1 = 1240\text{ cm}^{-1}$ ,  $\nu_2 = 1950$  and  $1978\text{ cm}^{-1}$  and  $\delta = 663$  and  $676\text{ cm}^{-1}$ ).<sup>[259]</sup>

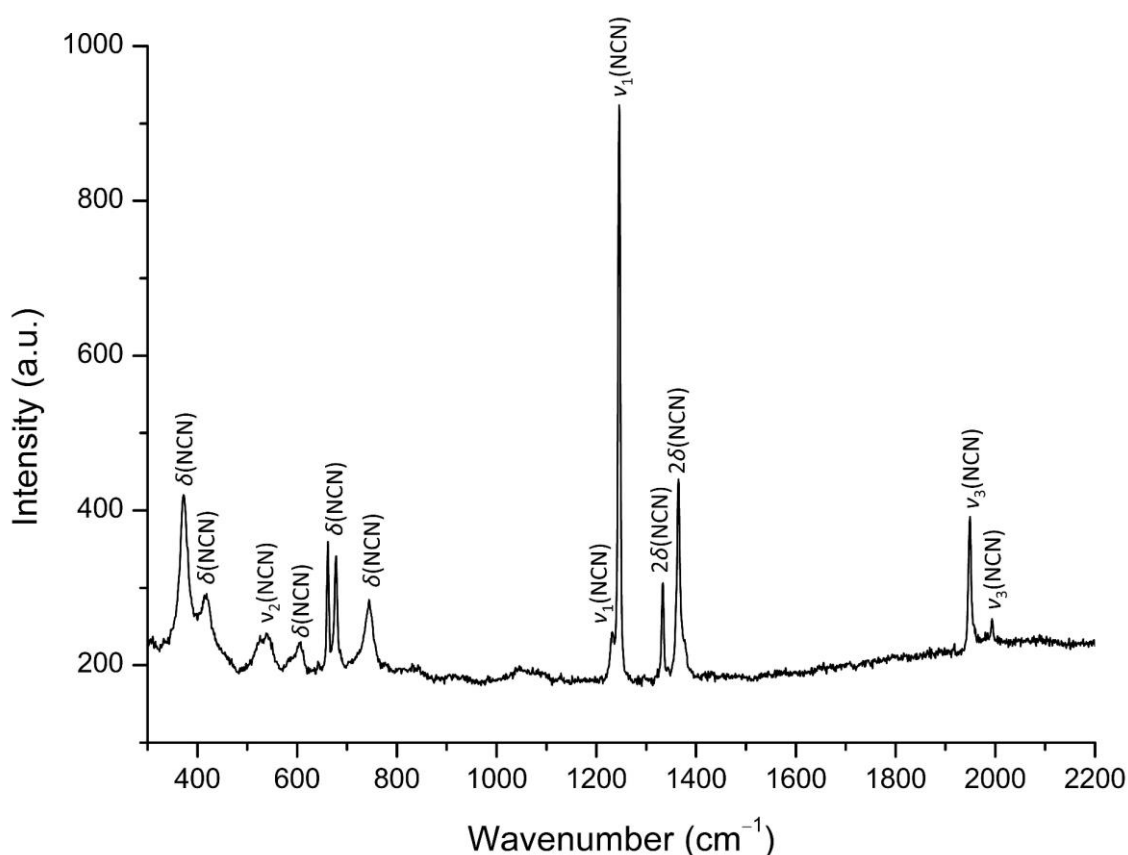


Figure 6.6. Raman spectrum of a single crystal of  $\text{Sr}_6\text{N}[\text{CuN}_2][\text{CN}_2]_2$ . Measured using red laser ( $\lambda = 638\text{ nm}$ ).

Table 6.4. Vibrational frequencies from the Raman spectrum of Sr<sub>6</sub>N[CuN<sub>2</sub>][CN<sub>2</sub>]<sub>2</sub>. Relative intensity is denoted by the following descriptions: very strong (vs) ≥ 90 %, medium (m) 70 – 30 %, weak (w) 30 – 10 % and very weak (vw) ≤ 10 %.

Raman/cm <sup>-1</sup>		Assignment
372	m	δ(C≡N)
418	m	δ(C≡N)
525	w	ν <sub>2</sub> (NCN)
537	w	ν <sub>2</sub> (NCN)
605	w	δ(NCN)
661	m	δ(NCN)
678	m	δ(NCN)
743	m	δ(C=N)
1232	w	ν <sub>1</sub> (NCN)
1245	vs	ν <sub>1</sub> (NCN)
1332	m	2δ(NCN)
1364	m	2δ(NCN)
1949	m	ν <sub>3</sub> (NCN)
1993	w	ν <sub>3</sub> (NCN)

The measured vibrational frequencies were further confirmed to be [CN<sub>2</sub>]<sup>2-</sup> through comparison with several cyanamides and carbodiimides (*Table 6.5.*). Asymmetric and deformation vibrational frequencies correspond well with what has been previously observed however, the symmetric vibrational frequencies could only be compared with samples measured via Raman spectroscopy. This is due to the symmetrical breathing mode being IR forbidden, but the value does fit well with those measured using Raman spectroscopy. While splitting at roughly 2000 cm<sup>-1</sup> is typically observed for cyanamides, it is also seen in multi-cationic carbodiimides. A vibrational frequency is observed at 743 cm<sup>-1</sup>, which belongs to a C=N double bond, and would suggest the presence of carbodiimides is more probable.

Table 6.5. Comparison of vibrational frequencies from the Raman spectrum of Sr<sub>6</sub>N[CuN<sub>2</sub>][CN<sub>2</sub>]<sub>2</sub> and selected Raman/IR frequencies from certain cyanamides and carbodiimides.

Measured vibrational frequencies/cm <sup>-1</sup>	Cyanamide		Carbodiimide	
	HgCN <sub>2</sub> <sup>[63]</sup>	CdCN <sub>2</sub> <sup>[53]</sup>	MnCN <sub>2</sub> <sup>[57]</sup>	SrZn[CN <sub>2</sub> ] <sub>2</sub> <sup>[260]</sup>
	Raman/cm <sup>-1</sup>	IR/cm <sup>-1</sup>	IR/cm <sup>-1</sup>	Raman/cm <sup>-1</sup>
661	653	655	650	633
678	666	–	–	687
1232	1214	–	–	1211
1245	–	–	–	1269
1949	1942	2071	2049	1990
1993	2036	2113	–	2048

#### 6.4. Discussion and conclusion

Through Raman spectroscopy the three atom anions, which are not [CuN<sub>2</sub>]<sup>5-</sup> anions, can be identified as being the [CN<sub>2</sub>]<sup>2-</sup> anions. The precise identity of this anion, cyanamide or carbodiimides, requires close observation of all collected structural data. Within the Raman spectrum are deformation vibrational frequencies (372 and 418 cm<sup>-1</sup>), which are caused by a C≡N triple bond. This is observed in both types of [CN<sub>2</sub>]<sup>2-</sup> anions, due to the mesomeric effect of carbodiimides. However, a vibrational frequency is seen at 743 cm<sup>-1</sup>, belonging to a C=N double bond. This combined with the interatomic distances between C and both N atoms being nearly the same (1.225(9) and 1.242(9) Å), compared to a noticeable difference for the cyanamide anion (1.16 and 1.30 Å),<sup>[251]</sup> gives a good indication that the anions are in fact [CN<sub>2</sub>]<sup>2-</sup>. Also, the small anisotropic displacement parameter of C, showing a symmetrical coordination environment for C, gives very strong reasoning to classify the [CN<sub>2</sub>]<sup>2-</sup> anions as being carbodiimides.

The structural difference between the produced Sr<sub>6</sub>N[CuN<sub>2</sub>][CN<sub>2</sub>]<sub>2</sub> and Sr<sub>6</sub>N[MN<sub>2</sub>][CN<sub>2</sub>]<sub>2</sub> (M = Fe, Co), as mentioned previously, is the orientation of the [CN<sub>2</sub>]<sup>2-</sup> anions. For the monoclinic Sr<sub>6</sub>N[CuN<sub>2</sub>][CN<sub>2</sub>]<sub>2</sub> the [CN<sub>2</sub>]<sup>2-</sup> units adopt a ‘criss-crossing’ arrangement, whereas the [CN<sub>2</sub>]<sup>2-</sup> units of the orthorhombic Sr<sub>6</sub>N[MN<sub>2</sub>][CN<sub>2</sub>]<sub>2</sub> (M = Fe, Co) are aligned.<sup>[97,259]</sup> The only difference between the synthesis methods used, which should result in a difference in the crystal structure, was the cooling rate. During fast synthetic processes, such as spontaneous crystallisation

at non-equilibrium conditions, the thermodynamically unstable phase can at first be preferred, producing metastable phases which are structurally simpler than the more complex thermodynamically stable counterpart.<sup>[265]</sup> The titular compound was cooled at a far slower rate, 1 K/h, than the compounds  $\text{Sr}_6\text{N}[\text{MN}_2][\text{CN}_2]_2$  ( $M = \text{Fe}, \text{Co}$ ), 10 K/h.<sup>[97,259]</sup> This led to the initial theory that the monoclinic structure could in fact be the thermodynamic product and the orthorhombic structure was the kinetic product. To confirm this hypothesis  $\text{Sr}_6\text{N}[\text{CuN}_2][\text{CN}_2]_2$  was produced with the faster cooling rate used to obtain the orthorhombic structure. The obtained product was  $\text{Sr}_6\text{N}[\text{CuN}_2][\text{CN}_2]_2$  and again crystallised in the monoclinic crystal system, with the same orientation of the  $[\text{CN}_2]^{2-}$  units, showing that a different synthetic approach does not affect the resulting structure.

Due to the presence of paramagnetic transition metal cations in  $\text{Sr}_6\text{N}[\text{MN}_2][\text{CN}_2]_2$  ( $M = \text{Fe}, \text{Co}$ ) and a diamagnetic transition metal cation in  $\text{Sr}_6\text{N}[\text{CuN}_2][\text{CN}_2]_2$ , the possibility of magnetostriction had to be considered as a possible cause for the structural difference between the otherwise very similar structures. If this effect was indeed present for the compounds containing paramagnetic transition metal cations, then a clear difference would be observed in the unit cell and axis ratios between  $\text{Sr}_6\text{N}[\text{CuN}_2][\text{CN}_2]_2$  and  $\text{Sr}_6\text{N}[\text{MN}_2][\text{CN}_2]_2$  ( $M = \text{Fe}, \text{Co}$ ) (Table 6.6.). This, however, is not the case, with the axis ratios of the monoclinic  $\text{Sr}_6\text{N}[\text{CuN}_2][\text{CN}_2]_2$  ( $a/b = 0.3874$ ,  $b/c = 0.6773$  and  $c/a = 3.8105$ ) being practically identical to the equivalent axis ratios of the orthorhombic  $\text{Sr}_6\text{N}[\text{FeN}_2][\text{CN}_2]_2$  ( $c/a = 0.3880$ ,  $a/b = 0.6753$  and  $b/c = 3.8167$ ) and  $\text{Sr}_6\text{N}[\text{CoN}_2][\text{CN}_2]_2$  ( $c/a = 0.3903$ ,  $a/b = 0.6746$  and  $b/c = 3.7977$ ).

Table 6.6. Comparison of unit cell parameter and axis ratios for  $\text{Sr}_6\text{N}[\text{MN}_2][\text{CN}_2]_2$  ( $M = \text{Fe}, \text{Co}, \text{Cu}$ ).

	$\text{Sr}_6\text{N}[\text{FeN}_2][\text{CN}_2]_2$ <sup>[97]</sup>	$\text{Sr}_6\text{N}[\text{CoN}_2][\text{CN}_2]_2$ <sup>[259]</sup>	$\text{Sr}_6\text{N}[\text{CuN}_2][\text{CN}_2]_2$
Space group	$P2_12_12$ (No. 18)	$P2_12_12$ (No. 18)	$P2_1/c$ (No. 14)
$Z$	2	2	2
$a/\text{\AA}$	9.938(2)	9.8807(6)	3.8454(1)
$b/\text{\AA}$	14.717(3)	14.6474(9)	9.9244(3)
$c/\text{\AA}$	3.856(1)	3.8569(3)	14.6528(5)
Volume $V/\text{\AA}^3$	564.0	558.2	558.76
$a/b$	0.6753	0.6746	0.3874
$b/c$	3.8167	3.7977	0.6773
$c/a$	0.3880	0.3903	3.8105

A close inspection of the symmetry elements of both structures was also conducted, in an attempt to identify which was in fact higher in symmetry. Both the space groups of  $\text{Sr}_6\text{N}[\text{CuN}_2][\text{CN}_2]_2$ ,  $P2_1/c$  (No. 14), and  $\text{Sr}_6\text{N}[\text{MN}_2][\text{CN}_2]_2$  ( $M = \text{Fe}, \text{Co}$ ),  $P2_12_12$  (No. 18),<sup>[97,259]</sup> are subgroups of the space group  $Pbam$  (No. 55). The symmetry reduction required to go from this supergroup to either of the resultant space groups is a translationengleiche,  $t2$ , meaning the same type of symmetry reduction is needed to reach either of the space groups discussed (Figure 6.7.). While both undergo the same symmetry reduction, the resultant monoclinic space group,  $P2_1/c$  (No. 14), remains centrosymmetric, with a screw axis and glide plane of the supergroup. The orthorhombic subgroup,  $P2_12_12$  (No. 18), maintains the orthorhombic crystal system, as well as all screw and rotational axes. This shows both subgroups, while possessing different kinds of symmetry operations, have the same symmetry density, due to the near identical cell volumes.

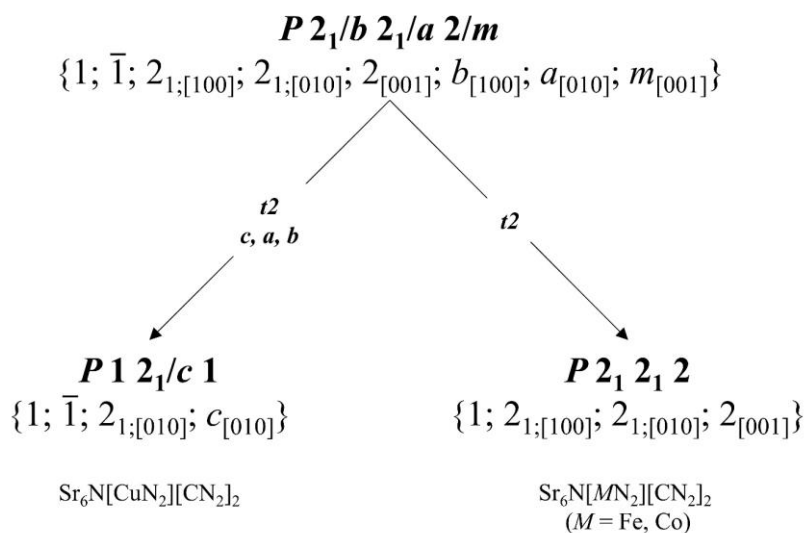


Figure 6.7. Supergroup subgroup relations for  $\text{Sr}_6\text{N}[\text{CuN}_2][\text{CN}_2]_2$  and  $\text{Sr}_6\text{N}[\text{MN}_2][\text{CN}_2]_2$  ( $M = \text{Fe}, \text{Co}$ ).

Since no chemical or crystallographic reason could be found to explain this difference in the crystal structure, a look into the complexity of each structure could determine if one of the structures were more complex, hence lower in symmetry, than the other. Using a series of equations, based on the Shannon information theory, the complex structures of  $\text{Sr}_6\text{N}[\text{CuN}_2][\text{CN}_2]_2$  and  $\text{Sr}_6\text{N}[\text{MN}_2][\text{CN}_2]_2$  ( $M = \text{Fe}, \text{Co}$ ) could be quantitatively evaluated (eq. 6.1. and 6.2.), where  $\rho_{inf}$  is the information density,  $v$  number of atoms in the unit cell,  $k$  is the number of Wyckoff positions,  $\rho_i$  is the probability of occurrence of an atom of the  $i$ th crystallographic multiplicity,  $m_i$  multiplicity symmetry element of the unit cell.<sup>[266,267]</sup> For structures that have very similar unit

cells, but different space groups, the one with the highest information density, and hence complexity, is the one with the lowest symmetry.

$$\rho_{inf} = \frac{-v \sum_{i=1}^k p_i \log_2 p_i}{V} \quad (\text{eq. 6.1.})$$

$$\rho_i = \frac{m_i}{v} \quad (\text{eq. 6.2.})$$

For Sr<sub>6</sub>N[CuN<sub>2</sub>][CN<sub>2</sub>]<sub>2</sub> the density of information was calculated to be 0.1503 bits/Å<sup>3</sup>, which when compared with the values calculated for Sr<sub>6</sub>N[MN<sub>2</sub>][CN<sub>2</sub>]<sub>2</sub> ( $M = \text{Fe, Co}$ ) (0.1489 bits/Å<sup>3</sup> and 0.1505 bits/Å<sup>3</sup> respectively) is higher than Sr<sub>6</sub>N[FeN<sub>2</sub>][CN<sub>2</sub>]<sub>2</sub>, but marginally lower than Sr<sub>6</sub>N[CoN<sub>2</sub>][CN<sub>2</sub>]<sub>2</sub>. This marginally smaller density of information value for the monoclinic Sr<sub>6</sub>N[CuN<sub>2</sub>][CN<sub>2</sub>]<sub>2</sub> would imply that this material is marginally lower in symmetry than the orthorhombic phases. However, it should be taken into account that all compounds have the same number of atoms and Wyckoff positions, which means the only variable between each compound is the volume. Since there is such an extremely small variance between Sr<sub>6</sub>N[CuN<sub>2</sub>][CN<sub>2</sub>]<sub>2</sub> and Sr<sub>6</sub>N[CoN<sub>2</sub>][CN<sub>2</sub>]<sub>2</sub>, the difference between them arises from the standard deviation in the volume. While there is not a large difference between the calculated density of information values, a general increase can be seen as the transition elements move across the periodic table. It would be of interest to see if a Ni containing phase would adopt the orthorhombic or monoclinic structure, or even be able to transition between both phases.

In this chapter, red rectangular crystals of Sr<sub>6</sub>N[CuN<sub>2</sub>][CN<sub>2</sub>]<sub>2</sub> were produced, which crystallised in the monoclinic space group  $P2_1/c$ . Combination of single crystal refinement and Raman spectroscopy described the crystal structure and confirmed that the [CN<sub>2</sub>]<sup>2-</sup> anions were actually present. Magnetic susceptibility measurements showed that the material was diamagnetic, which was expected since Cu(I) has a filled  $3d^{10}$  orbital. The crystal structure is very similar to the other transition metal containing orthorhombic phase Sr<sub>6</sub>N[MN<sub>2</sub>][CN<sub>2</sub>]<sub>2</sub> ( $M = \text{Fe, Co}$ ), however the titular product is monoclinic and has a noticeably different arrangement of the [CN<sub>2</sub>]<sup>2-</sup> anions. No chemical, structural or magnetic effect could explain this difference however, comparison of density of information for each compound suggests a slight decrease in symmetry across the row, which could mean the difference in structure is an intrinsic trait.





## 7. Synthesis and characterisation of strontium acetonitriletriiides

### 7.1. Introduction

The fully deprotonated acetonitrile, the acetonitriletriiide anion  $[\text{C}_2\text{N}]^{3-}$ , is a linear three atom anion, with both terminal atoms being connected to the central C atom by double bonds, isoelectronic to the  $\text{CO}_2$  molecule and  $[\text{CN}_2]^{2-}$  anion. Very few reports of compounds containing the  $[\text{C}_2\text{N}]^{3-}$  anion have been published.<sup>[70,71,268–271]</sup> The more stable anions of acetonitrile,  $[\text{H}_2\text{CCN}]^-$  and  $[\text{HCCN}]^{2-}$ , have been reported more frequently and are primarily used in C–C bond forming reactions in organic synthesis.<sup>[270,271]</sup>

Discrimination between the  $[\text{C}_2\text{N}]^{3-}$  anion and other three atom anions is extremely difficult, due to several other similar three atom anions existing such as,  $[\text{N}_3]^-$ ,  $[\text{CN}_2]^{2-}$ ,  $[\text{C}_3]^{4-}$ ,  $[\text{BN}_2]^{3-}$ ,  $[\text{OCN}]^-$  and  $[\text{CBN}]^{4-}$ . Standard X-ray diffraction techniques cannot distinguish between B, C, N and O, due to their very similar electron density. The interatomic distances between the atoms in these anions are also very similar,  $d(\text{N}=\text{N}) = 1.17 \text{ \AA}$ ,<sup>[42]</sup>  $d(\text{C}=\text{N}) = 1.23 \text{ \AA}$ ,<sup>[251]</sup>  $d(\text{B}-\text{N}) = 1.35 \text{ \AA}$ ,<sup>[272]</sup>  $d(\text{C}=\text{C}) = 1.35 \text{ \AA}$ ,<sup>[73]</sup>  $d(\text{C}=\text{B}) = 1.35 \text{ \AA}$ ,<sup>[273]</sup>  $d(\text{C}=\text{O}) = 1.16 \text{ \AA}$ <sup>[274]</sup>, which makes determination of the three atom anions even more challenging, especially when the orientation of these units in the structure may vary (i.e.  $[\text{C}=\text{C}=\text{N}]^{3-}$  or  $[\text{N}=\text{C}=\text{C}]^{3-}$ ). The best available methods to determine the identity of these kind of anions are Raman and infrared spectroscopy. With these methods, the identity of these three atom anions can be determined by careful comparison of the resultant vibrational frequencies with those already reported (*Table 7.1*).

At the time of writing only two solid state compounds containing the acetonitriletriiide anion have been reported,  $\text{Ba}_5[\text{TaN}_4][\text{C}_2\text{N}]$ <sup>[70]</sup> and  $\text{Sr}_4\text{N}[\text{C}_2\text{N}][\text{CN}_2]$ .<sup>[71]</sup> The compound  $\text{Ba}_5[\text{TaN}_4][\text{C}_2\text{N}]$  consists of layers of nitridometalate ions with alternating  $[\text{C}_2\text{N}]^{3-}$  and  $\text{Ba}^{2+}$  located between the layers.<sup>[70]</sup> The compound  $\text{Sr}_4\text{N}[\text{C}_2\text{N}][\text{CN}_2]$  is discussed in more detail in chapter 7.2.

## 7. Synthesis and characterisation of strontium acetonitriletriides

Table 7.1. Comparison of the Raman vibrational frequencies ( $\text{cm}^{-1}$ ) for the  $[\text{N}_3]^-$ ,  $[\text{CN}_2]^{2-}$ ,  $[\text{C}_2\text{N}]^{3-}$ ,  $[\text{C}_3]^{4-}$ ,  $[\text{BN}_2]^{3-}$ ,  $[\text{OCN}]^-$  and  $[\text{CBN}]^{4-}$  anions.

Vibration mode	N=N=N <sup>[275]</sup>	N=C=N <sup>[251,259]</sup>	C=C=N <sup>[70,71]</sup>	C=C=C <sup>[73,276]</sup>	N-B-N <sup>[277]</sup>	O=C=N <sup>[278]</sup>	C=B-N <sup>[279]</sup>
$\delta$	~ 100	~ 650	460/503	~600	–	~ 100	~590
$\nu_1$	1360	1240	1118/1124/1127	1171/1192	1034	2229/2238/2245	997
$\nu_2$	1268	–	–	–	–	1760/1770	–
$\nu_3$	–	2097/1949	1720/1724/1734	1683/1711	–	1430	1525/1576

The existence of  $[\text{C}_2\text{N}]^{3-}$  anions being stabilised in a solid state system,  $\text{Ba}_5[\text{TaN}_4][\text{C}_2\text{N}]$ ,<sup>[70]</sup> posed the question if it could also be stabilised in a more ‘simplistic’ system, such as in the presence of only one cation. Similar three atom anions, such as  $[\text{CN}_2]^{2-}$  and  $[\text{BN}_2]^{2-}$  have been shown to form binary and ternary compounds with alkaline earth metals, as well as compounds with more than one anion.<sup>[253,272]</sup> Ternary compounds in the system Sr–C–N, primarily, contain only one carbon containing anion, as seen for  $\text{Sr}[\text{CN}_2]^{[51]}$  and  $\text{Sr}[\text{N}(\text{CN})_2]_2$ .<sup>[280]</sup>

Interestingly, the pressure of  $\text{N}_2$  plays a crucial role in determining the presence of  $[\text{CN}_2]^{2-}$  and  $[\text{C}_2\text{N}]^{3-}$  during the synthesis. In the presence of an excess of  $\text{N}_2$  during the reaction, a preference for the formation of nitridometalate carbodiimides is observed, such as  $\text{Sr}_6\text{N}[\text{CoN}_2][\text{CN}_2]_2$ .<sup>[259]</sup> At lower pressures of  $\text{N}_2$ , highly reduced cyanometalates are formed, like  $\text{Ba}_3[\text{Co}(\text{CN})_3]$ <sup>[281]</sup> and  $\text{Sr}_2[\text{NNi}(\text{CN})]$ ,<sup>[282]</sup> as well as the acetonitriletriide containing compounds,  $\text{Ba}_5[\text{TaN}_4][\text{C}_2\text{N}]$ .<sup>[70]</sup> This sensitive relationship between pressure of  $\text{N}_2$  and the identity of the resultant three atom anion can be demonstrated by the reported synthesis of  $\text{Ba}_5[\text{TaN}_4][\text{C}_2\text{N}]$ .<sup>[70]</sup> When this reaction was attempted with an increased  $\text{N}_2$  content, the formation of the carbodiimide phase,  $\text{Ba}_6\text{N}_{5/6}[\text{TaN}_4][\text{CN}_2]_6$ , was preferred.<sup>[70]</sup>

Since reports of solid state systems containing the  $[\text{C}_2\text{N}]^{3-}$  anions still are in the very early stages, it is extremely surprising that in parallel to the work presented here an independent investigation also produced and reported  $\text{Sr}_4\text{N}[\text{C}_2\text{N}][\text{CN}_2]$ .<sup>[71]</sup> This parallel research served as an extremely useful reference point for confirming the identity of the produced phases.

## 7.2. Synthesis and characterisation of $\text{Sr}_4\text{N}[\text{C}_2\text{N}][\text{CN}_2]$

### 7.2.1. Synthesis

A mixture of Sr (0.112 g, 1.28 mmol), C (0.006 g, 0.51 mmol) and  $\text{NaN}_3$  (0.032 g, 0.49 mmol) were filled into a Ni ampoule, along with elemental Na (0.123 g) as a fluxing agent. The ampoule was then sealed by an arc welder and inserted into a fused silica tube, which was then heated, under Ar flow, to 1073 K and allowed to cool at a controlled rate of 1 K/h. After opening the ampoule, the Na flux was removed using liquid ammonia leaving a sample with primarily small yellow crystals and an unidentifiable microcrystalline powder.

### 7.2.2. Structure determination and characterisation

A yellow single crystal was measured using single crystal X-ray diffraction and indexed with a monoclinic unit cell ( $a = 3.9742(1) \text{ \AA}$ ,  $b = 14.1222(5) \text{ \AA}$ ,  $c = 6.9212(2) \text{ \AA}$ ,  $\beta = 103.637(2)^\circ$ ) in the space group  $P2_1/c$  (No. 14). This agrees well with what was parallel established,  $\text{Sr}_4\text{N}[\text{C}_2\text{N}][\text{CN}_2]$  ( $a = 3.9774 \text{ \AA}$ ,  $b = 14.1172 \text{ \AA}$ ,  $c = 6.9257 \text{ \AA}$ ,  $\beta = 103.57^\circ$ ).<sup>[71]</sup> Refinement of the single crystal structural data showed it to be identical to the parallel reported  $\text{Sr}_4\text{N}[\text{C}_2\text{N}][\text{CN}_2]$ <sup>[71]</sup> (Tables 7.2., 7.3. and 7.4.).

At the time this structural characterisation was being conducted, the compound  $\text{Sr}_4\text{N}[\text{C}_2\text{N}][\text{CN}_2]$  had not yet been reported. Therefore, direct identification of the anionic component was difficult. While the Sr atoms were easily identified, the refinement of the single crystal structural data showed the existence of a linear three atom arrangement of atoms and isolated atoms located in octahedra of Sr, which were challenging to classify. Identification of these atoms via standard X-ray diffraction techniques proved difficult, due to each atom having the very similar electron density. Since C and N were part of the reaction, it was likely that one or both of these atoms were present in these environments, meaning the possible three atom anions were  $[\text{N}_3]^-$ ,  $[\text{CN}_2]^{2-}$ ,  $[\text{C}_3]^{4-}$  and  $[\text{C}_2\text{N}]^{3-}$ . As mentioned previously, each of these isoelectric anions also share very similar interatomic distances, which means identification by this method is near impossible. Due to the typical sensitivity of these reactions to air, it was also possible that O atoms were also present, which have very similar electron density as C and N. This extended the possible identity of the three atom anions to include  $[\text{OCN}]^-$ , which also shares similar interatomic distances, as well as raising the question if the isolated anion is  $\text{N}^{3-}$  or  $\text{O}^{2-}$ .

The near linear three atom anions ( $176.2(5)^\circ$ ) have equidistant interatomic distances, within error, ( $1.256(7)$  and  $1.262(7)$  Å), which are similar to each of the potential interatomic distances,  $d(\text{N}=\text{N}) = 1.17$  Å,<sup>[42]</sup>  $d(\text{C}=\text{N}) = 1.23$  Å,<sup>[251]</sup>  $d(\text{C}=\text{C}) = 1.35$  Å,<sup>[73]</sup> and  $d(\text{C}=\text{O}) = 1.16$  Å,<sup>[274]</sup> and are identical to those reported for  $\text{Sr}_4\text{N}[\text{C}_2\text{N}][\text{CN}_2]$  ( $1.256$  and  $1.260$  Å).<sup>[71]</sup> Due to the orientation of these units within the structure not being known, it is extremely difficult to determine the identity of the atoms from their interatomic distance alone, since the observed distances could in fact be an average of the distances present.

Raman spectroscopy (*See part 7.2.3.*) confirmed that the three atom anions are in fact  $[\text{C}_2\text{N}]$  and  $[\text{CN}_2]$ , occupying the same positions. This would mean that the isolated anion has to be a nitride anion,  $\text{N}^{3-}$ , to achieve charge balance, which leads to the composition  $\text{Sr}_4\text{N}[\text{C}_2\text{N}][\text{CN}_2]$ . Each of these units are located inside a bidisphenoid polyhedron of Sr cations (*Figure 7.1.*). The interatomic distances between the Sr cations and the terminal C/N atoms of the three atom anions are between  $2.607(4)$  and  $3.109(4)$  Å, which fits with the values previously reported ( $2.679 - 2.956$  Å).<sup>[71]</sup> These bidisphenoids are edge and corner sharing with other bidisphenoid polyhedra and distorted  $\text{Sr}_6\text{N}$  octahedra (*Figure 7.1.*) to form chains running along  $[100]$ , which are also connected by edge and corner sharing to give the crystal structure (*Figure 7.2.*). The interatomic distances of the distorted  $\text{Sr}_6\text{N}$  octahedra ( $2.5151(4) - 2.7912(5)$  Å) agree very well with what is typically observed for these octahedra, for example  $\text{Sr}_6\text{N}[\text{CuN}_2][\text{CN}_2]_2$  ( $2.5912(6) - 2.704(6)$  Å), and are near identical to those observed for  $\text{Sr}_4\text{N}[\text{C}_2\text{N}][\text{CN}_2]$  ( $2.5124 - 2.7920$  Å).

Table 7.2. Single crystal structural refinement of  $\text{Sr}_4\text{N}[\text{C}_2\text{N}][\text{CN}_2]$ .

Crystal System	Monoclinic
Space Group	$P2_1/c$ (No. 14)
$Z$	2
$a/\text{\AA}$	3.9742(1)
$b/\text{\AA}$	14.1222(5)
$c/\text{\AA}$	6.9212(2)
$\beta/^\circ$	103.637(2)
$\rho_{\text{calc}}/\text{gcm}^{-3}$	3.911
Volume $V/\text{\AA}^3$	377.50
Measurement temperature/K	293(2)
Index range	$-5 \leq h \leq 5$ $-18 \leq k \leq 18$ $-8 \leq l \leq 8$
Max. $2\theta$ /deg	54.99
$F(000)$	398.0
$\mu/\text{mm}^{-1}$	28.04
Observed reflections	9442
Unique reflections	865
Refined parameters	53
$R_{\text{int}}/R_{\sigma}$	0.0630/0.0269
$R_1/wR_2$	0.0291/0.0755
$\text{Goof}$	1.055
Remaining electron density (max/min)/ $\text{\AA}^{-3}$	1.49/-1.02

Table 7.3. Atomic positions and occupations for the refinement of Sr<sub>4</sub>N[C<sub>2</sub>N][CN]<sub>2</sub>].

Wyckoff Position	<i>x/a</i>	<i>y/b</i>	<i>z/c</i>	Occupation	<i>U<sub>eq</sub></i>	
Sr(1)	4e	0.0530(1)	0.033765(3)	0.65367(6)	1	0.0170(2)
Sr(2)	4e	0.3746(1)	0.03607(3)	0.74874(7)	1	0.0171(2)
N(1)	2a	0	0	0	1	0.016(1)
C(1)	4e	0.611(1)	0.1959(3)	0.4515(7)	1	0.0160(9)
C(2)/N(2)	4e	0.740(1)	0.1140(3)	0.4597(6)	0.50/0.50	0.020(1)
N(3)	4e	0.5740(1)	0.2238(3)	0.9332(6)	1	0.0203(9)

Table 7.4. Anisotropic displacement parameters from the refinement of Sr<sub>4</sub>N[C<sub>2</sub>N][CN]<sub>2</sub>].

	<i>U<sub>11</sub></i>	<i>U<sub>22</sub></i>	<i>U<sub>33</sub></i>	<i>U<sub>23</sub></i>	<i>U<sub>13</sub></i>	<i>U<sub>12</sub></i>	<i>U<sub>eq</sub></i>
Sr(1)	0.0165(3)	0.0186(3)	0.0164(3)	0.0020(2)	0.0046(2)	0.0023(2)	0.0170(2)
Sr(2)	0.0208(3)	0.0157(3)	0.0159(3)	0.0011(2)	0.0068(2)	0.0009(2)	0.0171(2)
N(1)	0.023(3)	0.012(3)	0.015(3)	0.001(2)	0.006(2)	0.002(2)	0.016(1)
C(1)	0.017(2)	0.021(2)	0.011(2)	-0.001(2)	0.003(2)	-0.008(2)	0.0160(9)
C(2)/N(2)	0.024(3)	0.018(3)	0.022(3)	-0.001(2)	0.009(2)	0.002(2)	0.020(1)
N(3)	0.022(2)	0.020(2)	0.018(2)	-0.002(2)	0.004(2)	-0.005(2)	0.0203(9)

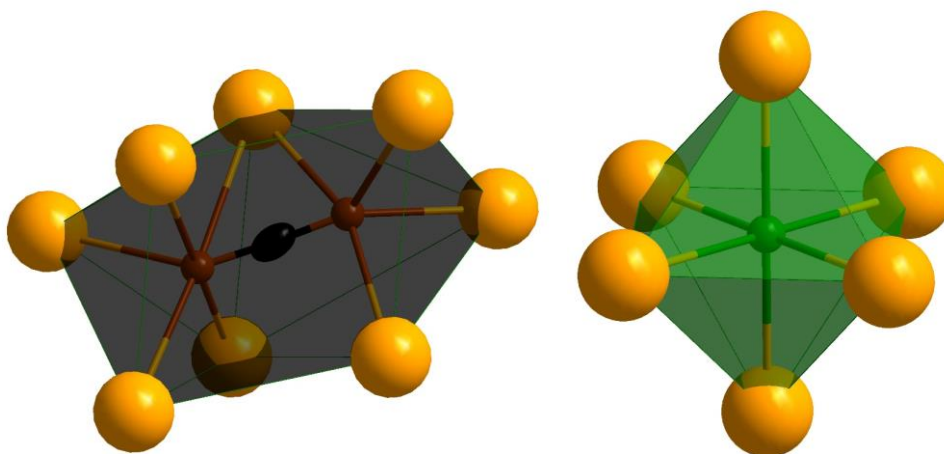


Figure 7.1. Coordination environments of  $[\text{C}_2\text{N}]^{3-}$  (left) and  $\text{N}^{3-}$  (right). Sr–orange, N–green, C/N–brown and C–black.

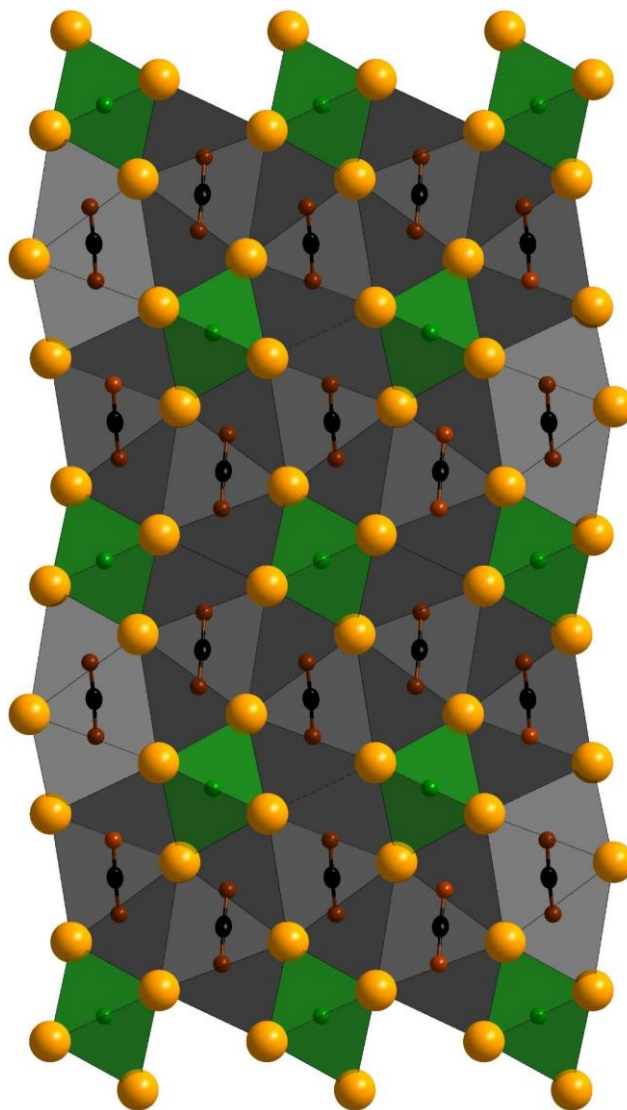


Figure 7.2. Crystal structure of  $\text{Sr}_4\text{N}[\text{C}_2\text{N}][\text{CN}_2]$ , viewed along  $[001]$ . Sr–orange, N–green, C/N–brown and C–black.

### 7.2.3. Raman spectroscopy

Due to the difficult task of determining the identity of the three atom anions by standard X-ray diffraction, single crystal Raman spectroscopy was employed to confirm the identity of the three atom anions. A yellow crystal was selected for this technique and spectroscopic data was collected, between 92 and 4000  $\text{cm}^{-1}$ , using a red laser ( $\lambda = 638 \text{ nm}$ ). For the resultant spectrum (*Figure 7.3.*), vibrational frequencies were compared with the frequencies observed for the potential three atom anion compositions (*Table 7.1.*). The assignment of vibrational frequencies (*Table 7.5.*) showed the existence of both  $[\text{C}_2\text{N}]^{3-}$  and  $[\text{CN}_2]^{2-}$  anions.

While the acetonitriletriiide anion has not been often reported, the observed symmetric ( $\nu_1 = 1154 \text{ cm}^{-1}$ ) and asymmetric ( $\nu_3 = 1773$  and  $1811 \text{ cm}^{-1}$ ) stretching frequencies, as well as the deformation vibration frequencies ( $\delta = 440 \text{ cm}^{-1}$ ), fit well with what has been previously seen, such as for  $\text{Ba}_5[\text{TaN}_4][\text{C}_2\text{N}]$  ( $\nu_1 = 1118$  and  $1127 \text{ cm}^{-1}$ ,  $\nu_3 = 1724$  and  $1734 \text{ cm}^{-1}$  and  $\delta = 460$  and  $503 \text{ cm}^{-1}$ ).<sup>[70]</sup>

For vibrational frequencies assigned to the carbodiimide anion, the observed symmetric ( $\nu_1 = 1238$  and  $1317 \text{ cm}^{-1}$ ) and asymmetric ( $\nu_3 = 1966$  and  $2002 \text{ cm}^{-1}$ ) stretching frequencies, as well as the deformation vibration frequencies ( $\delta = 617, 673$  and  $692 \text{ cm}^{-1}$ ), are in agreement with those observed for  $\text{Sr}_6\text{N}[\text{CuN}_2][\text{CN}_2]_2$  ( $\nu_1 = 1232$  and  $1245 \text{ cm}^{-1}$ ,  $\nu_3 = 1949$  and  $1993 \text{ cm}^{-1}$  and  $\delta = 605$  and  $661 \text{ cm}^{-1}$ ), which was discussed in chapter 6.

Further confirmation that the anions were indeed  $[\text{C}_2\text{N}]^{3-}$  and  $[\text{CN}_2]^{2-}$  was possible after the publication of  $\text{Sr}_4\text{N}[\text{C}_2\text{N}][\text{CN}_2]$ . The observed vibrational frequencies fitted well with those reported for the  $[\text{C}_2\text{N}]^{3-}$  anion and  $[\text{CN}_2]^{2-}$  anion (*Table 7.5.*).



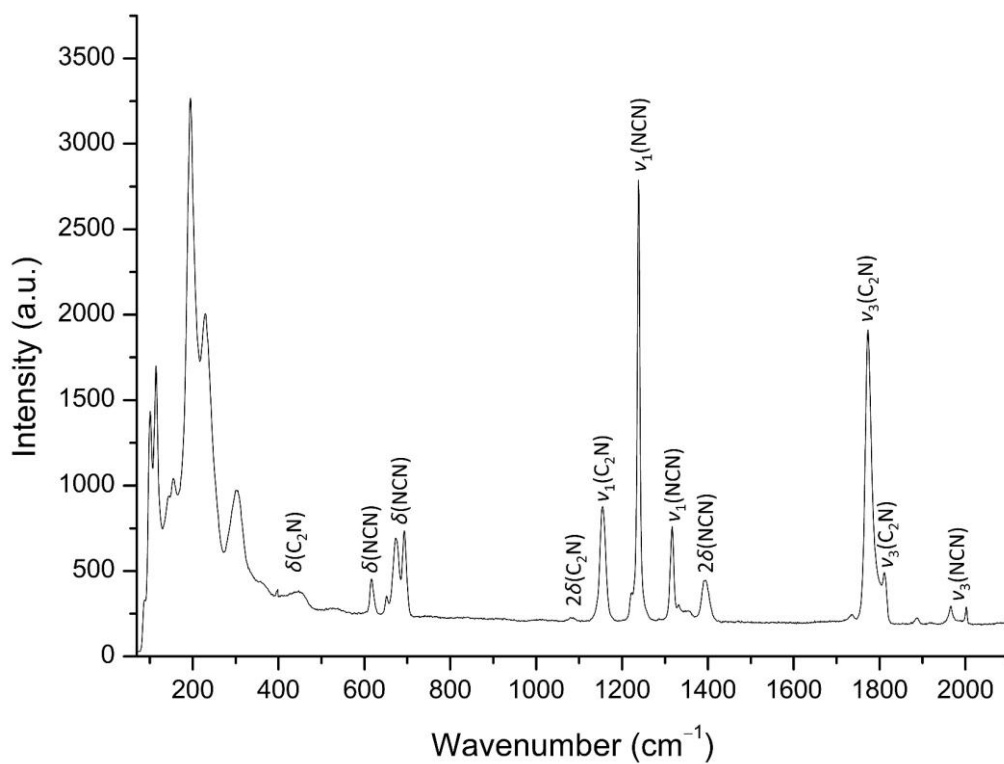


Figure 7.3. Raman spectrum of a single crystal of  $\text{Sr}_4\text{N}[\text{C}_2\text{N}][\text{CN}_2]$ , measured using red laser ( $\lambda = 638 \text{ nm}$ ).

Table 7.5. Comparison of vibrational frequencies from the Raman spectrum of  $\text{Sr}_4\text{N}[\text{C}_2\text{N}][\text{CN}_2]$  and those reported in literature. Relative intensity is denoted by the following descriptions: medium (m) 70 – 30 % and weak (w) 30 – 10 %.

$\text{Sr}_4\text{N}[\text{C}_2\text{N}][\text{CN}_2]$			$\text{Sr}_4\text{N}[\text{C}_2\text{N}][\text{CN}_2]^{[71]}$	
Raman/ $\text{cm}^{-1}$		Assignment	Raman/ $\text{cm}^{-1}$	Assignment
440	w	$\delta(\text{C}_2\text{N})$	–	$\delta(\text{C}_2\text{N})$
617	w	$\delta(\text{NCN})$	615	$\delta(\text{NCN})$
673	w	$\delta(\text{NCN})$	–	$\delta(\text{NCN})$
692	w	$\delta(\text{NCN})$	715	$\delta(\text{NCN})$
1082	m	$2\delta(\text{CCN})$	–	$2\delta(\text{CCN})$
1154	m	$\nu_1(\text{CCN})$	1152	$\nu_1(\text{CCN})$
1238	m	$\nu_1(\text{NCN})$	1221	$\nu_1(\text{NCN})$
1317	m	$\nu_1(\text{NCN})$	1236	$\nu_1(\text{NCN})$
1393	m	$2\delta(\text{NCN})$	–	$2\delta(\text{NCN})$
1773	m	$\nu_3(\text{CCN})$	1767	$\nu_3(\text{CCN})$
1811	m	$\nu_3(\text{CCN})$	1809	$\nu_3(\text{CCN})$
1966	m	$\nu_3(\text{NCN})$	1964	$\nu_3(\text{NCN})$
2002	m	$\nu_3(\text{NCN})$	1993	$\nu_3(\text{NCN})$

### 7.3. Structure determination and crystal structure of Sr<sub>3</sub>[C<sub>2</sub>N]<sub>2</sub>

#### 7.3.1. Synthesis

A mixture of Sr (0.092 g, 1.05 mmol), C (0.005 g, 0.42 mmol) and Sr(N<sub>3</sub>)<sub>2</sub> (0.0038 g, 0.02 mmol) was filled into a Ni ampoule, along with elemental Na (0.130 g) as a fluxing agent. The ampoule was then sealed by an arc welder and inserted into a fused silica tube, which was then heated, under Ar flow, to 1073 K and allowed to cool at a controlled rate of 1 K/h. After opening the ampoule, the Na flux was removed using liquid ammonia leaving a sample, which contained near colourless, with a hint of green, single crystal shards and unreacted Sr.

#### 7.3.2. Structure determination and characterisation

A single crystal was measured using single crystal X-ray diffraction and indexed in a monoclinic unit cell ( $a = 4.0745(1)$  Å,  $b = 10.7254(5)$  Å,  $c = 7.0254(3)$  Å,  $\beta = 102.700(2)$  °). Refinement of the single crystal structural data showed that the compound crystallises in the space group  $P2_1/c$  (No. 14) and consists of Sr cations and an anion composed of three atoms (*Tables 7.6., 7.7. and 7.8.*). The identity of these atoms proved elusive, due to them having very similar electron density, making it difficult to determine by standard X-ray diffraction techniques.

These three atoms anions ( $177.9(7)$  °) have nearly equal interatomic distances ( $1.271(9)$  Å and  $1.291(9)$  Å) and since only C and N, and possibly O, were involved in the reaction, the possible three atom anions were narrowed down to [N<sub>3</sub>]<sup>-</sup>, [CN<sub>2</sub>]<sup>2-</sup>, [C<sub>3</sub>]<sup>4-</sup> and [C<sub>2</sub>N]<sup>3-</sup> and [OCN]<sup>-</sup>. Each of these potential three atom anions have very similar interatomic distances, according to values from the literature,  $d(\text{N}=\text{N}) = 1.17$  Å,<sup>[42]</sup>  $d(\text{C}=\text{N}) = 1.23$  Å,<sup>[251]</sup>  $d(\text{C}=\text{C}) = 1.35$  Å,<sup>[73]</sup>  $d(\text{C}=\text{O}) = 1.16$  Å<sup>[274]</sup>), and since the orientation of these units within the structure are not known, it is impossible to determine the identity of the atoms from their interatomic distance alone, since the observed distances would in fact be an average of the distances present.

The three atom anions were identified, by Raman spectroscopy (*see part 7.3.3.*), to only consist of [C<sub>2</sub>N]<sup>3-</sup> anions. Initially, this would seem to not be the case, since the interatomic distances observed ( $1.271(9)$  Å and  $1.291(9)$  Å) do not match those of the C=N and C=C bonds present in this anion ( $1.23$  Å and  $1.35$  Å respectively).<sup>[73,251]</sup> However, the orientation of the [C<sub>2</sub>N]<sup>3-</sup> anions within the structure are not known and when these anions are randomly orientated (i.e. [C=C=N]<sup>3-</sup> or [N=C=C]<sup>3-</sup>) then an average of these interatomic distances would be

observed. This average distance (1.29 Å) does fit well with the distances observed by single crystal structural data.

Within the crystal structure the  $[\text{C}_2\text{N}]^{3-}$  anions are located inside bidisphenoid polyhedra of Sr cations (*Figure 7.4.*). The interatomic distances between the Sr cations and the terminal C/N atoms of the units are between 2.615(6) Å and 2.895(7) Å, which fits well with the values seen previously for these bidisphenoids in  $\text{Sr}_4\text{N}[\text{C}_2\text{N}][\text{CN}_2]$  (2.607(4) – 3.109(4) Å) (*see part 7.2.2.*) and the recently published  $\text{Sr}_4\text{N}[\text{C}_2\text{N}][\text{CN}_2]$  (2.679 – 2.956 Å).<sup>[71]</sup> Each bidisphenoid is connected to 18 other bidisphenoid to build up the crystal structure (*Figure 7.5.*), from which 9 are connected via edge sharing, 4 are face sharing and 5 are corner sharing.

Table 7.6. Single crystal structural refinement of  $\text{Sr}_3[\text{C}_2\text{N}]_2$ .

Crystal System	Monoclinic
Space Group	$P2_1/c$ (No. 14)
$Z$	2
$a/\text{Å}$	4.0745(1)
$b/\text{Å}$	10.7254(5)
$c/\text{Å}$	7.0254(3)
$\beta/^\circ$	102.700(2)
$\rho_{\text{calc}}/\text{gcm}^{-3}$	1.879
Volume $V/\text{Å}^3$	299.50
Measurement temperature/K	293(2)
Index range	$-6 \leq h \leq 5$ $-13 \leq k \leq 13$ $-4 \leq l \leq 9$
Max. $2\theta/\text{deg}$	55.03
$F(000)$	152.0
$\mu/\text{mm}^{-1}$	13.25
Observed reflections	6116
Unique reflections	690
Refined parameters	45
$R_{\text{int}}/R_\sigma$	–/0.0209
$R_1/wR_2$	0.0323/0.0998
$\text{Goof}$	1.132
Remaining electron density (max/min)/ $\text{Å}^{-3}$	1.44/–0.83
BASF	0.126(4)
Twin Matrix	1 0 0 0 –1 0 – $\frac{3}{4}$ 0 1

Table 7.7. Atomic positions and occupations for the refinement of Sr<sub>3</sub>[C<sub>2</sub>N]<sub>2</sub>.

Wyckoff Position	<i>x/a</i>	<i>y/b</i>	<i>z/c</i>	Occupation	<i>U<sub>eq</sub></i>
Sr(1)	2a	0	0	1	0.0141(3)
Sr(2)	4e	0.6722(2)	0.15470(6)	1	0.0141(3)
C(1)/N(1)	4e	0.086(1)	0.2108(6)	0.5/0.5	0.013(1)
C(2)/N(2)	4e	0.385(2)	0.0777(6)	0.5/0.5	0.022(1)
C(3)	4e	0.231(2)	0.1835(6)	1	0.013(1)

Table 7.8. Anisotropic displacement parameters from the refinement of Sr<sub>3</sub>[C<sub>2</sub>N]<sub>2</sub>.

	<i>U<sub>11</sub></i>	<i>U<sub>22</sub></i>	<i>U<sub>33</sub></i>	<i>U<sub>23</sub></i>	<i>U<sub>13</sub></i>	<i>U<sub>12</sub></i>	<i>U<sub>eq</sub></i>
Sr(1)	0.0136(5)	0.0158(5)	0.0130(5)	-0.0015(3)	0.0034(3)	-0.0007(3)	0.0141(3)
Sr(2)	0.0129(4)	0.0168(4)	0.0122(4)	0.0003(2)	0.0018(2)	0.0010(2)	0.0141(3)
C(1)/N(1)	0.010(3)	0.015(3)	0.014(3)	-0.002(2)	0.001(2)	-0.002(2)	0.013(1)
C(2)/N(2)	0.026(3)	0.020(3)	0.023(3)	0.000(3)	0.009(3)	0.002(3)	0.022(1)
C(3)	0.012(3)	0.016(3)	0.011(3)	-0.000(2)	0.005(2)	0.007(2)	0.013(1)

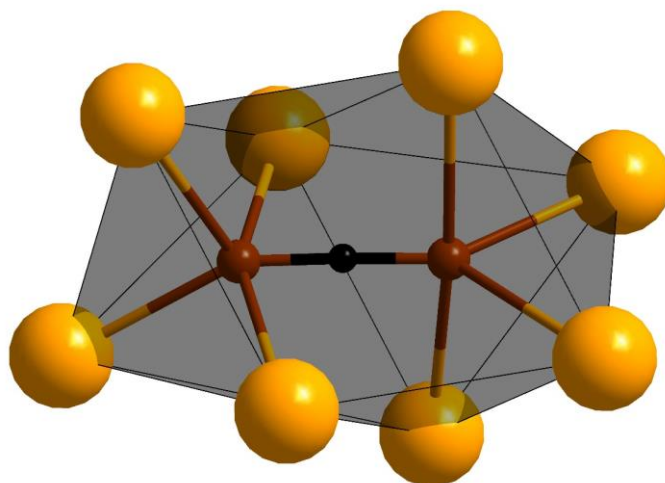


Figure 7.4. Coordination environment of the  $[\text{C}_2\text{N}]^{3-}$  anions. Sr–orange, C/N–brown and C–black.

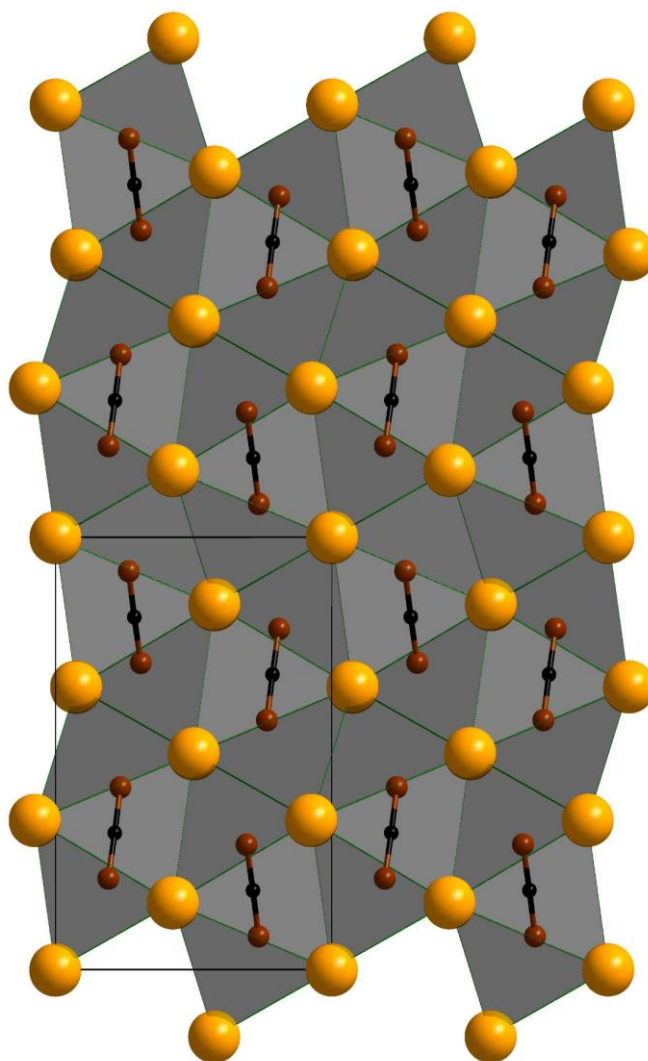


Figure 7.5. Section of the crystal structure of  $\text{Sr}_3[\text{C}_2\text{N}]_2$ , viewed along  $[001]$ . Sr–orange, C/N–brown and C–black. Unit cell edges are shown by black lines.

To determine the presence of twinning within the single crystals analysed, the program PLATON<sup>[242]</sup> was used and the following twinning matrix was proposed.

$$\begin{pmatrix} 1 & 0 & -3/4 \\ 0 & -1 & 0 \\ 0 & 0 & 1 \end{pmatrix}$$

Due to the sample having an unconventional twinning matrix, the program PLATON<sup>[242]</sup> generated a HKL5 file, which separates the  $hkl$  values of each crystal twin. This splitting meant that, due to how the programs function, the SHELX program package<sup>[119–122]</sup> could not calculate the  $R_{int}$  value for the sample. This twinning matrix would mean that the crystal twins are related to each other through a two-fold rotation axis parallel to  $[100]$  (Figure 7.6.). Since the resulting atom positions of the twinned unit cell do not overlap the original unit cell, the twinning present is classed as being non-merohedral.

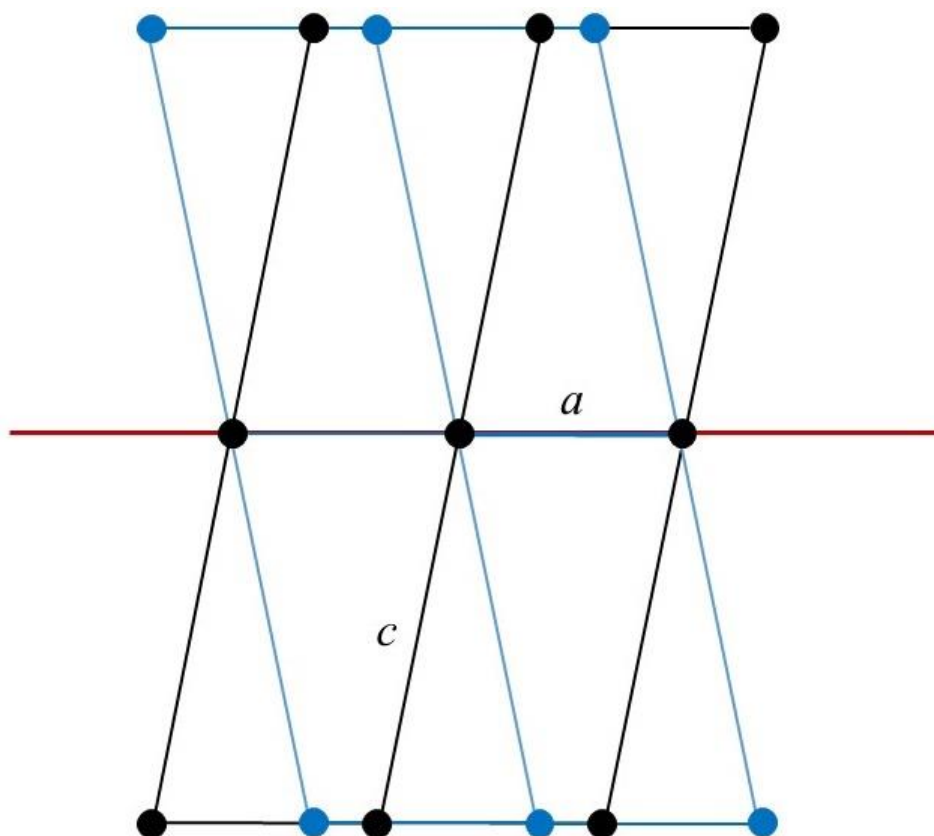


Figure 7.6. Twinning of the primitive monoclinic unit cell, viewed along  $[0\bar{1}0]$ , with the twinning axis  $[100]$  (red) and the resulting twinned unit cell (blue).

### 7.3.3. Raman Spectroscopy

Raman spectroscopy was used to confirm the identity of the three atom anions. A single crystal of the sample was selected and data was collected between 92 and 4000  $\text{cm}^{-1}$ , using a green laser ( $\lambda = 532 \text{ nm}$ ). The vibrational frequencies obtained from the spectrum (*Figure 7.7. and Table 7.9.*) were compared with the frequencies observed for the potential three atom anions compositions (*Table 7.1.*).

The observed symmetric ( $\nu_1 = 1146 \text{ cm}^{-1}$ ) and asymmetric ( $\nu_3 = 1744$  and  $1826 \text{ cm}^{-1}$ ) stretching frequencies, as well as the deformation vibration frequencies ( $\delta = 508 - 651 \text{ cm}^{-1}$ ), fit well with what has been previously seen for  $[\text{C}_2\text{N}]^{3-}$  in  $\text{Ba}_5[\text{TaN}_4][\text{C}_2\text{N}]^{[70]}$  and both reports of  $\text{Sr}_4\text{N}[\text{C}_2\text{N}][\text{CN}_2]$  ( $\nu_1 = 1152 \text{ cm}^{-1}$  and  $\nu_3 = 1767$  and  $1809 \text{ cm}^{-1}$ )<sup>[71]</sup> and ( $\nu_1 = 1154 \text{ cm}^{-1}$ ,  $\nu_3 = 1773$  and  $1811 \text{ cm}^{-1}$  and  $\delta = 440 \text{ cm}^{-1}$ ), as seen in chapter 7.2.

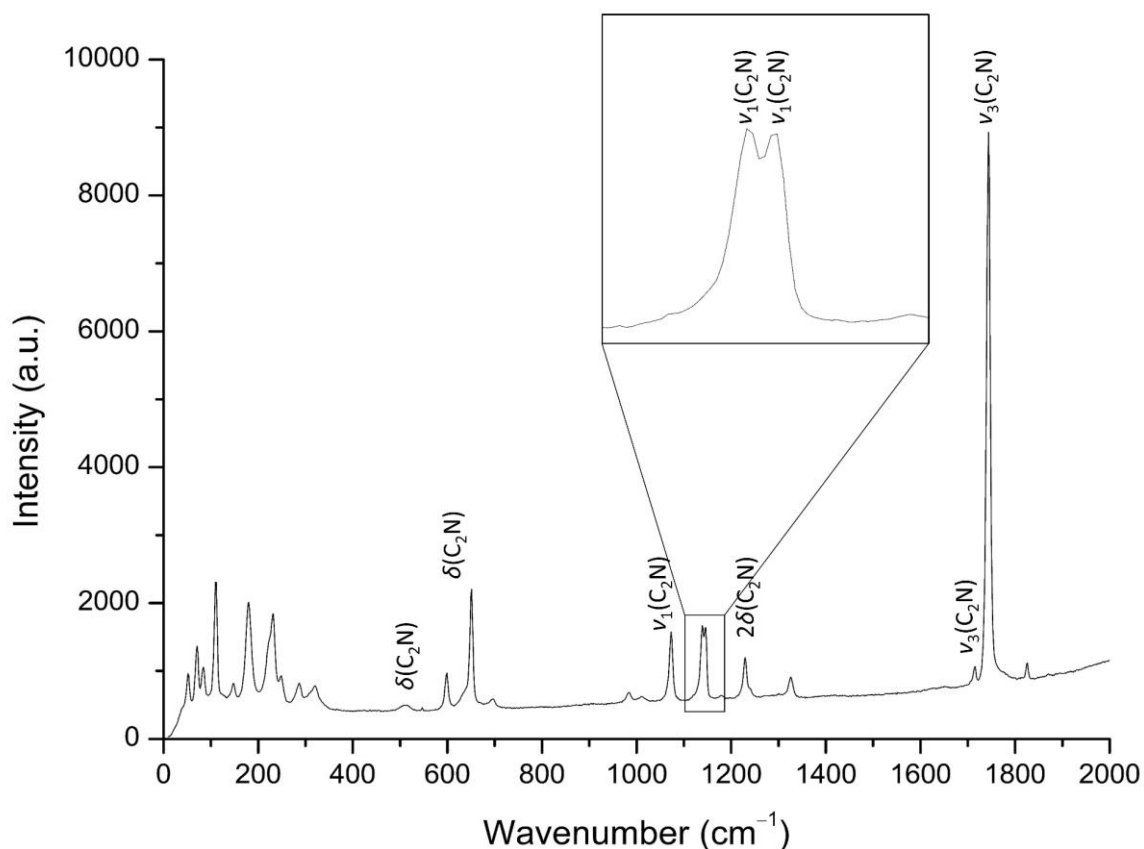


Figure 7.7. Raman spectrum of a single crystal of  $\text{Sr}_3[\text{C}_2\text{N}]_2$  measured using a green laser ( $\lambda = 532 \text{ nm}$ ).



Table 7.9. Comparison of vibrational frequencies from the Raman spectrum of  $\text{Sr}_3[\text{C}_2\text{N}]_2$ ,  $\text{Ba}_5[\text{TaN}_4][\text{C}_2\text{N}]^{[70]}$  and  $\text{Sr}_4\text{N}[\text{C}_2\text{N}][\text{CN}_2]$ , see chapter 7.2. Relative intensity is denoted by the following descriptions: very strong (vs)  $\geq 90\%$ , weak (w)  $30 - 10\%$  and very weak (vw)  $\leq 10\%$ .

$\text{Sr}_3[\text{C}_2\text{N}]_2$			$\text{Ba}_5[\text{TaN}_4][\text{C}_2\text{N}]^{[70]}$		$\text{Sr}_4\text{N}[\text{C}_2\text{N}][\text{CN}_2]$	
Raman/ $\text{cm}^{-1}$		Assignment	Raman/ $\text{cm}^{-1}$	Assignment	Raman/ $\text{cm}^{-1}$	Assignment
508	vw	$\delta(\text{C}_2\text{N})$	460	$\delta(\text{C}_2\text{N})$	440 – 692	$\delta(\text{C}_2\text{N})$
599	vw	$\delta(\text{C}_2\text{N})$	503	$\delta(\text{C}_2\text{N})$	1082	$2\delta(\text{CCN})$
651	vw	$\delta(\text{C}_2\text{N})$	–	$\delta(\text{C}_2\text{N})$	1154	$\nu_1(\text{CCN})$
1073	w	$\nu_1(\text{CCN})$	–	$\nu_1(\text{CCN})$	1238	$\nu_1(\text{NCN})$
1139	w	$\nu_1(\text{CCN})$	1118	$\nu_1(\text{CCN})$	1317	$\nu_1(\text{NCN})$
1146	w	$\nu_1(\text{CCN})$	1127	$\nu_1(\text{CCN})$	1393	$2\delta(\text{NCN})$
1230	w	$2\delta(\text{CCN})$	–	$2\delta(\text{CCN})$	1773	$\nu_3(\text{CCN})$
1715	w	$\nu_3(\text{CCN})$	1724	$\nu_3(\text{CCN})$	1811	$\nu_3(\text{CCN})$
1744	vs	$\nu_3(\text{CCN})$	1734	$\nu_3(\text{CCN})$	1966	$\nu_3(\text{NCN})$
1826	w	$\nu_3(\text{CCN})$	–	$\nu_3(\text{CCN})$	2002	$\nu_3(\text{NCN})$

### 7.3.4. Energy dispersive spectroscopy

A single crystal was selected and measured using energy dispersive spectroscopy. This technique was used to determine the elemental components of the sample and if Sr is the sole cation in the sample. Sample preparation involved a thin coating of C being applied to the surface of the sample, this meant that detection of C within the sample was not possible. Mounting of samples onto the measurement apparatus exposed the sample to air for a short duration. Since the samples are sensitive to air and moisture, the accurate determination of N content was also not possible. Due to these limitations, only a qualitative analysis could be conducted to determine if the sample contained only Sr and not any other elements. The results showed that Sr is the only other detectable element present, apart from C, N and O (*Table 7.10.*). This confirms that the  $[\text{C}_2\text{N}]^{3-}$  anions are found in a mono-cationic environment.

Table 7.10. Relative values from energy dispersive spectroscopy for  $\text{Sr}_3[\text{C}_2\text{N}]_2$ .

	w(Sr)/%	w(C)/%	w(N)/%	w(O)/%
1	71.30 $\pm$ 0.30	4.56 $\pm$ 0.09	4.24 $\pm$ 0.32	19.91 $\pm$ 0.18
2	71.24 $\pm$ 0.30	5.33 $\pm$ 0.09	3.89 $\pm$ 0.32	19.53 $\pm$ 0.14

## 7.4. Discussion and Conclusion

In this chapter a strontium acetonitriletride carbodiimide,  $\text{Sr}_4\text{N}[\text{C}_2\text{N}][\text{CN}_2]$ , and the first quasi-binary strontium acetonitriletride,  $\text{Sr}_3[\text{C}_2\text{N}]_2$ , were produced. Both of these compounds crystallise in the space group  $P2_1/c$  (No. 14) and have similar unit cell parameters (*Table 7.11.*), except for the noticeable difference in the  $b$  axis, which is a result of the  $\text{Sr}_6\text{N}$  octahedra in  $\text{Sr}_4\text{N}[\text{C}_2\text{N}][\text{CN}_2]$  (*Figure 7.8.*). For both compounds, the  $[\text{C}_2\text{N}]^{3-}$  anions are located inside bidisphenoid polyhedra of Sr cations. With these compounds being some of the first to show  $[\text{C}_2\text{N}]^{3-}$  in a mono-cationic environment, this could be an indication that the acetonitriletride anions prefer being situated in bidisphenoid polyhedra of Sr cations. This preference might be key to stabilising them within a solid state system.

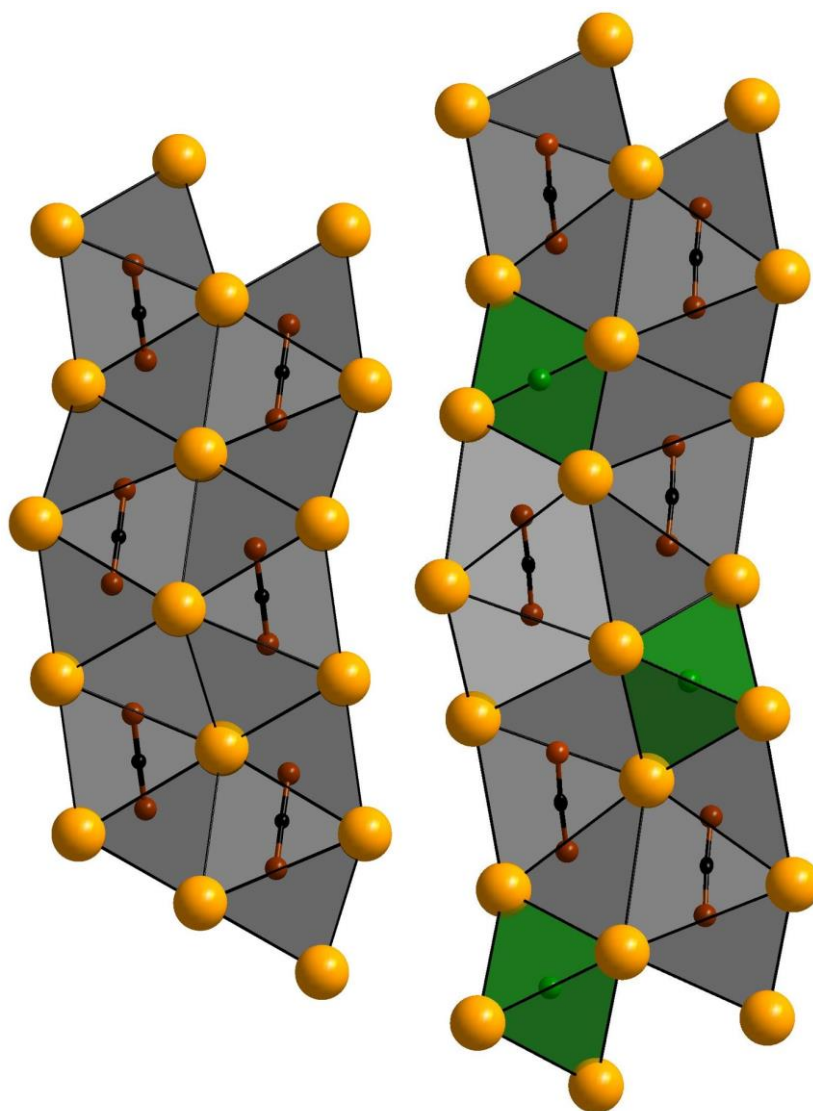


Figure 7.8. Section of crystal structure of  $\text{Sr}_3[\text{C}_2\text{N}]_2$  (left) and  $\text{Sr}_4\text{N}[\text{C}_2\text{N}][\text{CN}_2]$  (right), viewed along  $[001]$ . Sr–orange, N–green, C/N–brown and C–black.

Table 7.11. Comparison of unit cell parameters for Sr<sub>4</sub>N[C<sub>2</sub>N][CN<sub>2</sub>] and Sr<sub>3</sub>[C<sub>2</sub>N]<sub>2</sub>.

	Sr <sub>4</sub> N[C <sub>2</sub> N][CN <sub>2</sub> ]	Sr <sub>3</sub> [C <sub>2</sub> N] <sub>2</sub>
<i>a</i> /Å	3.9742(1)	4.0745(1)
<i>b</i> /Å	14.1222(5)	10.7254(5)
<i>c</i> /Å	6.9212(2)	7.0254(3)
<i>β</i> /°	103.637(2)	102.700(2)

The synthesis methods for both Sr<sub>4</sub>N[C<sub>2</sub>N][CN<sub>2</sub>] and Sr<sub>3</sub>[C<sub>2</sub>N]<sub>2</sub> are nearly identical, except for the amount of azide that was used. For Sr<sub>4</sub>N[C<sub>2</sub>N][CN<sub>2</sub>] a larger amount of N<sub>2</sub> (0.074 mmol, 1.67 MPa) was produced from the azide and thus a larger estimated pressure, assuming for comparison that all N<sub>2</sub> gas is present at the reaction temperature (1073 K), when compared to the amount of N<sub>2</sub> produced during the synthesis of Sr<sub>3</sub>[C<sub>2</sub>N]<sub>2</sub> (0.06 mmol, 0.15 MPa). This sensitivity of the reaction to the N<sub>2</sub> pressure has been also previously observed during the synthesis of Ba<sub>5</sub>[TaN<sub>4</sub>][C<sub>2</sub>N], where at higher N<sub>2</sub> pressures the formation of the carbodiimide phase, Ba<sub>6</sub>N<sub>5/6</sub>[TaN<sub>4</sub>][CN<sub>2</sub>]<sub>6</sub>, was preferred.<sup>[70]</sup> However, the simultaneous investigations of Sr<sub>4</sub>N[C<sub>2</sub>N][CN<sub>2</sub>] reported producing this phase both with a Na flux and NaN<sub>3</sub>, but also without Na and azide. For that particular investigation, the use of Sr<sub>2</sub>N, C and NaCN produced samples of better quality.<sup>[71]</sup> This would imply that the N<sub>2</sub> pressure is not the only factor affecting formation of these compounds.

The interatomic distances observed for the [C<sub>2</sub>N]<sup>3-</sup> anions did not match the numbers that would have been expected. Instead, they are the average of both C=N and C=C distances. This indicates that the units are not aligned within the structure. Since standard X-ray diffraction techniques cannot distinguish between C and N atoms, finding the orientation, and possibly ordering, of these units was not possible. To determine the orientation of these three atom anions neutron diffraction measurements would be required, which would require a bulk single phase sample.



## 8. Substitution and property investigations of lead germanates

### 8.1. Overview

The lead germanate  $\text{Pb}_5\text{Ge}_3\text{O}_{11}$  has experienced a lot of intense characterisation and investigation, due to its ferroelectric and electro-optical properties. Crystals of  $\text{Pb}_5\text{Ge}_3\text{O}_{11}$  and substituted phases show potential for use as ferroelectric memory elements, polarisation switching, refractometric effects and pyroelectric sensors, as well as a material for recording and reading holograms.<sup>[283–288]</sup>

The crystal structure of lead germanate,  $\text{Pb}_5\text{Ge}_3\text{O}_{11}$ , can be described as alternating layers of isolated  $[\text{GeO}_4]^{4-}$  and  $[\text{Ge}_2\text{O}_7]^{6-}$  anions, which are interconnected through  $\text{Pb}^{2+}$  cations (*Figure 8.1.*). Two modifications of  $\text{Pb}_5\text{Ge}_3\text{O}_{11}$  exist, with both looking identical at a first glance. Above 450 K,  $\text{Pb}_5\text{Ge}_3\text{O}_{11}$  crystallises in the space group  $P\bar{6}$  (No. 174), below this temperature a phase transition is observed. This transition causes a translationengleiche,  $t2$ , symmetry reduction to the maximal non-isomorphic subgroup  $P3$  (No. 143).<sup>[283]</sup> Structurally, the phase transition causes a change in the bond lengths between the two germanium cations and the bridging oxygen anion in the  $[\text{Ge}_2\text{O}_7]^{6-}$  unit. In the high temperature phase the Ge–O–Ge distances are identical, due to symmetry restriction (1.81 Å)<sup>[289]</sup> however, upon the transition to the low temperature phase, a distortion of the germanate tetrahedra is observed resulting in distances which are no longer equivalent (1.80 Å and 1.84 Å).<sup>[289]</sup> This change in the interatomic distances results in a loss of the mirror plane perpendicular to [001] and the two-fold rotational axis parallel to [001], which removes the inversion centre and produces two crystallographically different Ge positions in the  $[\text{Ge}_2\text{O}_7]^{6-}$  unit in the space group of lower symmetry.

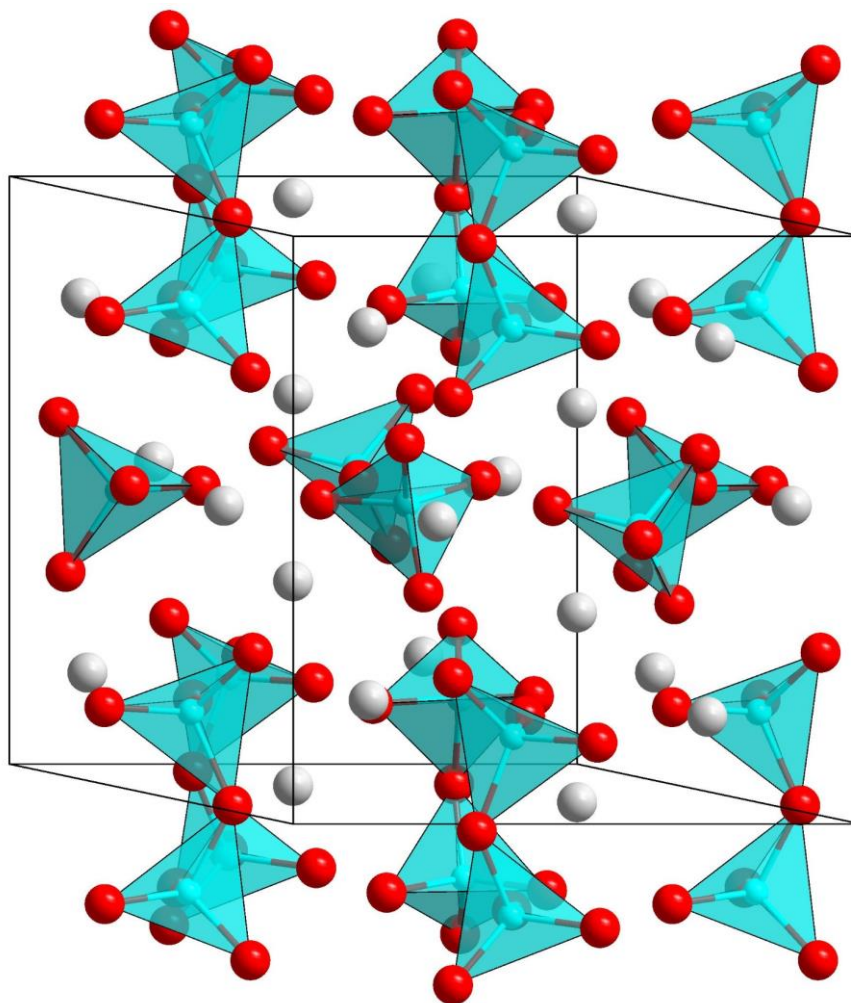


Figure 8.1. Section of the crystal structure of  $\text{Pb}_5\text{Ge}_3\text{O}_{11}$  in the space group  $P3$  (No. 143). Pb—grey, Ge—blue and O—red. Unit cell edges are shown with black lines.

Loss of the two-fold rotation axis during the phase transition from  $P\bar{6}$  (No. 174) to  $P3$  (No. 143) can lead to crystal twins forming. The resulting twins are related to each other through a two-fold rotation axis, which runs along  $[001]$ , and correspond to the same two-fold rotation axis that is lost during the phase transition (*Figure 8.2.*). This crystal twinning occurred often with the compounds discussed in the following chapter and was described with the following twinning matrix.

$$\begin{pmatrix} -1 & 0 & 0 \\ 0 & -1 & 0 \\ 0 & 0 & 1 \end{pmatrix}$$

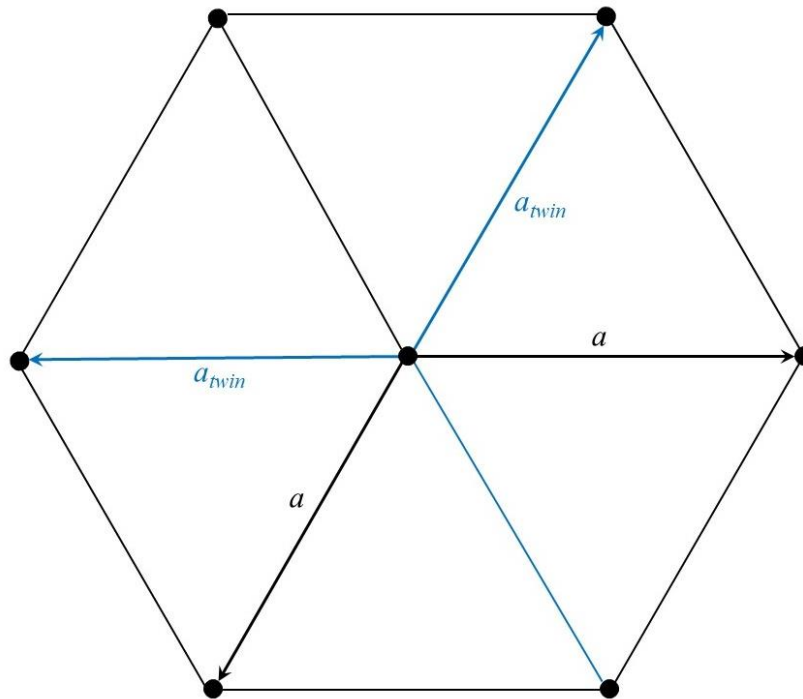


Figure 8.2. Twinning of the primitive trigonal unit cell, viewed along [001], and the resulting twinned unit cells (blue).

Investigations into the ferroelectric properties of  $\text{Pb}_5\text{Ge}_3\text{O}_{11}$ , showed that the phase transition temperature is also the Curie temperature for this compound and results in the evolution of ferroelectric characteristics.<sup>[290,291]</sup> This was the first ferroelectric material in the space group  $P3$  (No. 143) to be discovered and the first uniaxial ferroelectric material to be studied.<sup>[290,292]</sup> The ferroelectric and electro-optical properties are temperature dependent and exhibit similar temperature-refractive index relationship as other ferroelectrics, such as the well-known  $\text{LiTaO}_3$  and  $\text{Ba}_2\text{NaNb}_5\text{O}_{15}$ .<sup>[290,293,294]</sup>

As mentioned previously, there has been a large number of studies into the ferroelectric and electro-optic properties of  $\text{Pb}_5\text{Ge}_3\text{O}_{11}$ . However, there have been relatively few publications regarding the photorefractive properties of this material.<sup>[295–297]</sup> An in depth investigation showed  $\text{Pb}_5\text{Ge}_3\text{O}_{11}$  to be a promising holographic material. This property was determined to be caused by the presence of paramagnetic  $\text{Pb}^{3+}$  cations, which were generated by simple illumination of the crystals.<sup>[288]</sup>

The crystals analysed in the following sections were produced by filling a 40 mL Pt crucible with a finely ground mixture of reagents, which were heated to 1123 K and held at this temperature for 3 hours to allow the mixtures to melt and homogenise. To initialise crystal growth, a Pt wire, with a diameter of 1 mm, was lowered into the melt and the melt was cooled at a rate of 10 K/h. As the melt cooled, the Pt wire was pulled at a rate of 1 mm/day. This produced large amber coloured crystals for each sample (*Figure 8.3.*). From each sample, a small shard of the crystal was broken off and measured using single crystal X-ray diffraction. Due to the strong X-ray absorbing nature of Pb atoms, a harder X-ray source was used (Ag- $K\alpha_1$ ,  $\lambda = 0.56083 \text{ \AA}$ ). A part of each sample was also ground to a fine powder and analysed using powder X-ray diffraction. For each subsequent analytical measurement, a different crystal was used.

Since all of the samples in the following sections were prepared under the same reaction conditions, the non-substituted  $\text{Pb}_5\text{Ge}_3\text{O}_{11}$  produced in sections 8.2. and 8.3. should be identical. However, due to slight variations between each experiment, which are unavoidable, differences in the unit cell parameters were present, as well as a variance in crystal quality. This variation in crystal quality lead to the decision to select the crystal structural data from the crystal of highest quality, the sample of  $\text{Pb}_5\text{Ge}_3\text{O}_{11}$  produced for section 8.2., as the standard for the following sections to observe the effects substitution has on the crystal structure.

The following part of this work was conducted in a collaboration with Dr. Denis Vinnik (South Ural State University, Russia), who grew and provided the samples.

Due to the relatively large number of samples in the following sections, each one is labelled and ordered in increasing amounts of the respective substituted atom. For consistency and ease of comprehension, a constant value shall be given for the degree of substitution for each sample. This value was obtained by either energy dispersive spectroscopy or wavelength dispersive spectroscopy, which is the most reliable technique, from the ones used in this chapter, for determining the overall composition.





Figure 8.3. Large crystals of  $\text{Pb}_5\text{Ge}_3\text{O}_{11}$  produced by flux crystal growth.

## 8.2. Synthesis and characterisation of $\text{Pb}_{5-x}\text{Ba}_x\text{Ge}_3\text{O}_{11}$

### 8.2.1. Introduction

Several attempts have been made to substitute the Pb cations in  $\text{Pb}_5\text{Ge}_3\text{O}_{11}$  with Ba cations and investigate the effect of the substitution on the structural and physical properties.<sup>[296,298]</sup> With increasing Ba content the unit cell was seen to grow gradually,<sup>[298]</sup> which is due to  $\text{Ba}^{2+}$  cations being larger than  $\text{Pb}^{2+}$  cations (1.36 and 1.18 Å respectively, CN = 6).<sup>[187]</sup>

The influence of Ba cations was shown to have detrimental effects on the physical properties of  $\text{Pb}_5\text{Ge}_3\text{O}_{11}$ . While a minute amount of Ba content ( $0.06 \leq x \leq 0.08$ ) actually increases dielectric permittivity, partial substitution of Ba decreases the Curie temperature and peak dielectric permittivity to the point where these characteristics are no longer seen. Decreases in the Curie temperature and dielectric permittivity were also found to be linked with increasing Ba content.<sup>[298]</sup>

### 8.2.2. Synthesis of $\text{Pb}_{5-x}\text{Ba}_x\text{Ge}_3\text{O}_{11}$

Three charge mixtures were produced from weighing out a stoichiometric mixture of  $\text{PbO}$ ,  $\text{BaCO}_3$  and  $\text{GeO}_2$  (Table 8.1.) and treated using the method described earlier (see part 8.1.).

Table 8.1. Mixture composition used to grow single crystals of  $\text{Pb}_{5-x}\text{Ba}_x\text{Ge}_3\text{O}_{11}$ .

	Reactant composition					
	wt%			mol%		
	PbO	BaCO <sub>3</sub>	GeO <sub>2</sub>	PbO	BaCO <sub>3</sub>	GeO <sub>2</sub>
Sample A $x = 0$	78.046	–	21.954	62.511	–	37.489
Sample B $x = 0.15(2)$	76.267	1.729	22.004	60.926	1.562	37.512
Sample C $x = 0.29(2)$	74.838	3.118	22.044	59.676	2.812	37.512

### 8.2.3. Characterisation

#### 8.2.3.1. Structure determination and crystal structure of $\text{Pb}_{5-x}\text{Ba}_x\text{Ge}_3\text{O}_{11}$

Single crystals of each sample were measured using single crystal X-ray diffraction and were indexed in the trigonal space group  $P3$  (No. 143), with varying unit cell parameters ( $a = 10.2056(1) \text{ \AA} - 10.2145(2) \text{ \AA}$  and  $c = 10.6496(2) \text{ \AA} - 10.7070(1) \text{ \AA}$ ). This is in agreement with the unit cell parameters seen for  $\text{Pb}_5\text{Ge}_3\text{O}_{11}$  ( $a = 10.190 \text{ \AA}$  and  $c = 10.624 \text{ \AA}$ ).<sup>[289]</sup> The variation in unit cells, in comparison with  $\text{Pb}_5\text{Ge}_3\text{O}_{11}$ , can be seen to increase in relation to increasing predicted Ba content, which is caused by the larger ionic radii of Ba cations. However, sample B appears to have a slightly smaller  $a$  value unit cell than what would be expected. This difference in the expected trend in unit cell parameters can be attributed to how the crystals were grown, with the Ba content depending on the duration of growth, resulting in a composition gradient, and the temperature of the melt.

Refinement of the single crystal X-ray diffraction data confirmed each sample to be  $\text{Pb}_{5-x}\text{Ba}_x\text{Ge}_3\text{O}_{11}$  (Table 8.2.), with certain Pb crystallographic positions being substituted with Ba (Tables B.1.1. and B.1.2.). To determine the purity of the bulk sample, powdered samples of each product were analysed using powder X-ray diffraction and refined using the structural data obtained by single crystal refinement as a template.

The powder diffraction refinements showed that the bulk sample of each measured product is single phase (Figure 8.4. and Table 8.3.). However, Pb and Ba cations are such large absorbers of X-rays, that refinement of the atomic positions of the lighter O anions was not possible. To compensate for this the refined atomic positions of O from the respective samples were used and fixed as the positions of O for the refinements (Table B.1.3.). Due to program limitation, the occupation of the mixed Pb/Ba positions had to be refined manually, using values from single crystal refinement as a reference. This was achieved by gradual increasing and decreasing of the occupation until the best refinement values were obtained.

While the refined structures are isostructural to  $\text{Pb}_5\text{Ge}_3\text{O}_{11}$ , there is a noticeable change in the interatomic distances between Pb/Ba and O positions with increasing Ba content (Table 8.4.). The interatomic distance range, between Pb and O, for the non-substituted phase,  $\text{Pb}_5\text{Ge}_3\text{O}_{11}$ , is between 2.09(5) and 2.84(4) Å, which is in agreement with the range found in literature (2.17 – 3.20 Å).<sup>[289]</sup> By substitution of the Pb with Ba, the range of the interatomic distances, in general, gets larger with a tendency for the distance overall to increase. The non-substituted Pb positions appear to be relatively unaffected by the amount of Ba in the compound. Due to a lack of reported data regarding the interatomic distances between Pb/Ba and O, no comparison with values from the literature could be made.

Table 8.2. Single crystal structural refinements of  $\text{Pb}_{5-x}\text{Ba}_x\text{Ge}_3\text{O}_{11}$ .

	Sample A	Sample B	Sample C
Composition	$x = 0$	$x = 0.15(2)$	$x = 0.29(2)$
Crystal system	Trigonal	Trigonal	Trigonal
Space group	$P3$ (No. 143)	$P3$ (No. 143)	$P3$ (No. 143)
$Z$	3	3	3
$a/\text{\AA}$	10.2131(1)	10.2056(1)	10.2145(2)
$c/\text{\AA}$	10.6496(2)	10.6712(1)	10.7070(2)
$\rho_{\text{calc}}/\text{gcm}^{-3}$	7.404	7.038	7.002
Volume $V/\text{\AA}^3$	962.01	962.54	967.46
Measurement	293(2)	293(2)	293(2)
Temperature/K			
	$-9 \leq h \leq 18$	$-18 \leq h \leq 18$	$-9 \leq h \leq 18$
Index range	$-18 \leq k \leq 18$	$-10 \leq k \leq 18$	$-18 \leq k \leq 18$
	$-19 \leq l \leq 19$	$-19 \leq l \leq 19$	$-19 \leq l \leq 19$
Max. $2\theta/\text{deg}$	61.29	61.30	61.28
$F(000)$	1782.0	1762.6	1757.8
$\mu/\text{mm}^{-1}$	39.39	33.82	33.65
Observed reflections	124791	139244	146130
Unique reflections	8106	8106	8142
Refined parameters	174	178	178
$R_{\text{int}}/R_{\sigma}$	0.0599/0.0202	0.0792/0.0282	0.0744/0.0288
$R_1/wR_2$	0.0346/0.0942	0.0487/0.1286	0.0483/0.1232
$\text{Goof}$	1.026	1.038	1.059
Remaining electron	4.07/-3.11	4.75/-4.79	3.48/-5.81
Density (max/min)/ $\text{\AA}^{-3}$			
BASF	0.494(2)		
Twin matrix	-100 0-10 001		

Table 8.3. Unit cell parameters from the powder X-ray diffraction refinement of  $\text{Pb}_{5-x}\text{Ba}_x\text{Ge}_3\text{O}_{11}$ .

	Sample A	Sample B	Sample C
	$x = 0$	$x = 0.15(2)$	$x = 0.29(2)$
Space Group	$P3$	$P3$	$P3$
$a/\text{\AA}$	10.2323(4)	10.1926(3)	10.2028(3)
$c/\text{\AA}$	10.6673(4)	10.6448(4)	10.6699(4)
$V/\text{\AA}^3$	967.364	957.711	961.913
$R_{\text{wp}}/\%$	7.71	6.72	7.89
$R_{\text{Bragg}}/\%$	9.41	7.62	8.08

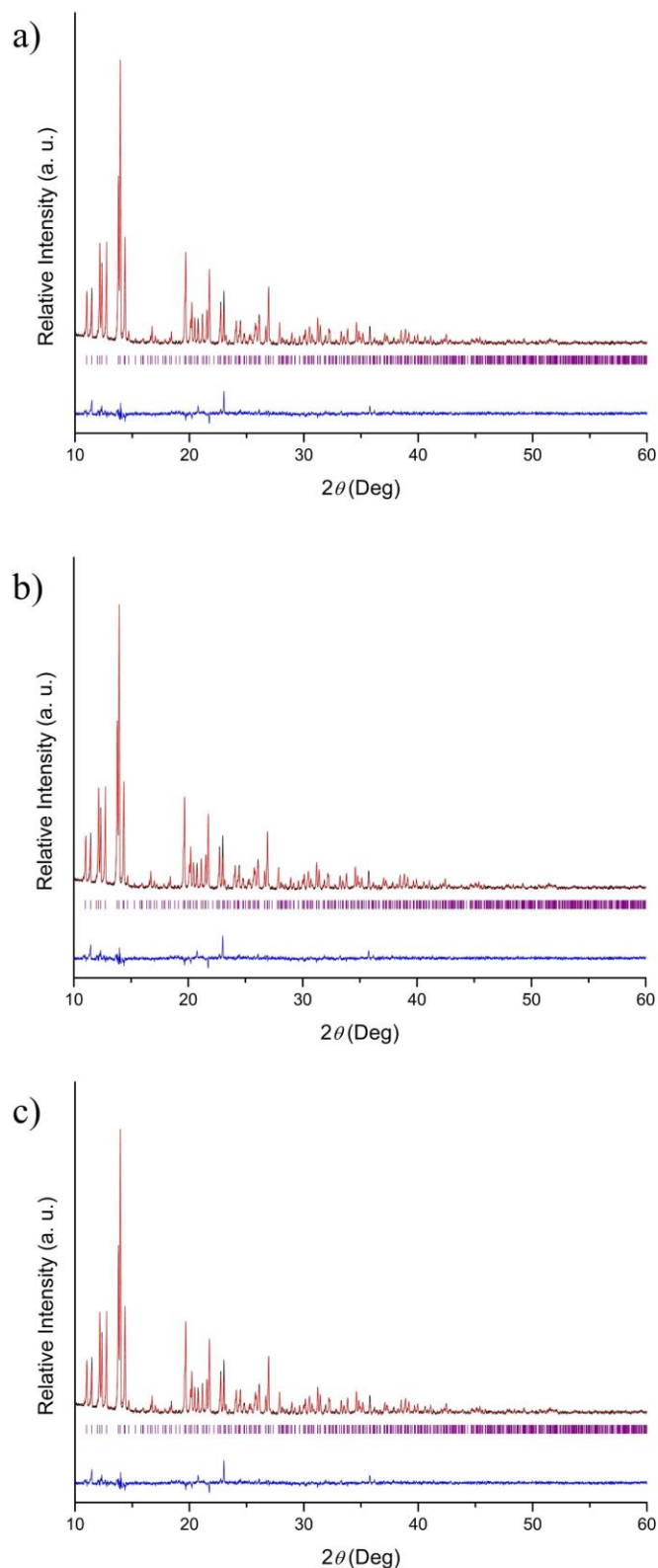


Figure 8.4. Graphical representations of Rietveld structural refinements of  $\text{Pb}_{5-x}\text{Ba}_x\text{Ge}_3\text{O}_{11}$  from powder X-ray diffraction measurements, using  $\text{Mo-K}_{\alpha 1}$  radiation, for: a) Sample A,  $x = 0$ ; b) Sample B,  $x = 0.15(2)$ ; c) Sample C,  $x = 0.29(2)$ . The observed pattern is shown in black, the calculated one in red, possible Bragg reflection positions are in purple and the difference in blue. ( $\text{Mo-K}_{\alpha 1}$ -wavelength,  $\lambda = 0.7093 \text{ \AA}$ ).

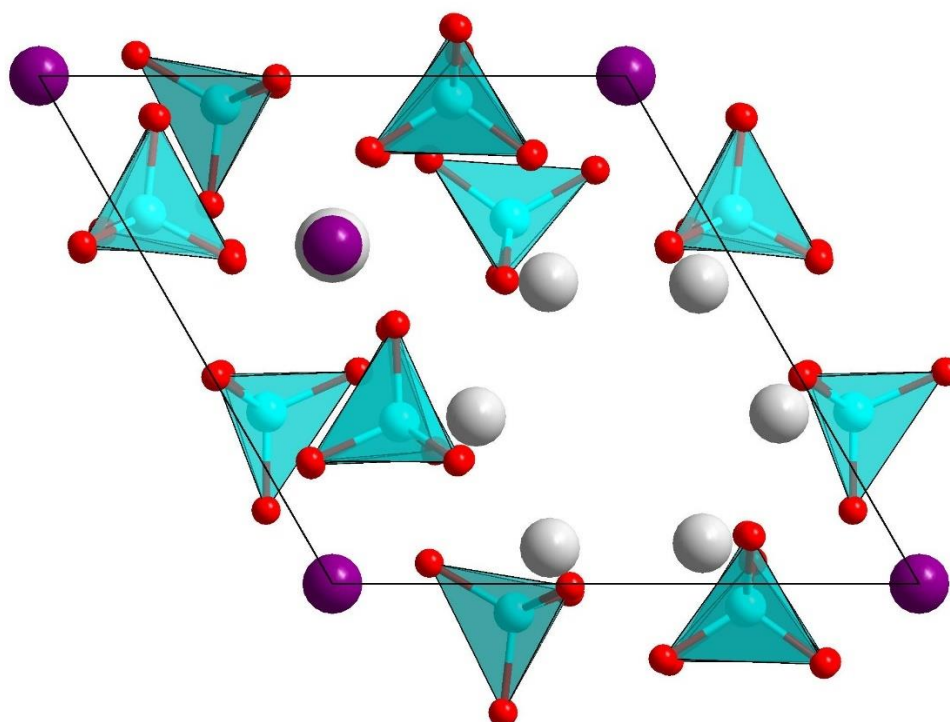
The Pb cations can be found in one of two positions: either as part of hexagonal channels of Pb cations, or surrounded by the GeO<sub>4</sub> tetrahedra (*Figure 8.5.*). Substitution of the Pb cations does not happen randomly and in fact, an order can be observed. Only the Pb cations surrounded by germanium tetrahedra are substituted with Ba, leaving the hexagonal channels to consist solely of Pb cations. A possible explanation for this preference could be that Pb<sup>2+</sup> cations possess a stereochemically active lone pair of electrons. These lone pairs would possibly prefer to be localised in the channels, which would make these Pb<sup>2+</sup> cations relatively more stable against substitution than the Pb<sup>2+</sup> cations found outside of these hexagonal channels.

For the Pb cations that are substituted with Ba cations (samples B and C), a larger value for the anisotropic displacement value  $U_{33}$  can be seen when compared with the non-substituted Pb cations (*Table B.1.2.*). This difference in the value of  $U_{33}$  arises from the substituted Ba<sup>2+</sup> cations being situated in the centre of the coordination polyhedra, while the Pb<sup>2+</sup> cations, with its lone pair, is situated slightly off-centre to accommodate the lone pair. Both the Pb<sup>2+</sup> and Ba<sup>2+</sup> cations are described as occupying the same atomic position, whereas in reality they are in close proximity to each other. This produces an atom shape that is an elongated ellipsoid, which results in the larger anisotropic displacement parameter. For the Pb cation positions that are substituted, an ordering is observed. This ordering occurs along the direction [001] and results in the Pb and mixed occupied Pb/Ba positions alternating along this direction. This would minimise the distortion of the structure from the introduction of cations with larger ionic radii.

Interestingly, the samples which contain Ba (samples B and C) are not twinned. This absence of twinning must be due to the influence of Ba in the system however, there are no obvious structural reactions why twinning would not be present in the Ba substituted phases. To date, no reports have investigated or commented on the effects of substitution on the degree of twinning for Pb<sub>5</sub>Ge<sub>3</sub>O<sub>11</sub> and so it is not known if this is a common effect of Ba substitution or due to the synthesis route taken.

Table 8.4. Interatomic distance range (Å) of Pb/Ba positions for  $\text{Pb}_{5-x}\text{Ba}_x\text{Ge}_3\text{O}_{11}$ .

	Sample A $x = 0$	Sample B $x = 0.15(2)$	Sample C $x = 0.29(2)$
Pb(1)/Ba(1) – O	2.41(2) — 3.04(4)	2.43(2) — 3.04(2)	2.47(1) — 3.05(1)
Pb(2) – O	2.43(1) — 2.74(4)	2.43(1) — 2.78(1)	2.44(1) — 2.80(1)
Pb(3)/Ba(3) – O	2.50(1) — 2.79(2)	2.65(2) — 2.965(2)	2.68(2) — 2.97(2)
Pb(4) – O	2.22(2) — 2.35(1)	2.17(1) — 2.78(1)	2.20(1) — 2.78(1)
Pb(5)/Ba(5) – O	2.44(2) — 3.23(4)	2.41(2) — 3.05(2)	2.44(1) — 3.04(1)
Pb(6) – O	2.42(2) — 2.78(4)	2.43(1) — 2.79(1)	2.45(1) — 2.81(1)
Pb(7)/Ba(7) – O	2.43(2) — 2.49(2)	2.468(2) — 2.47(2)	2.46(1) — 2.47(1)
Pb(8) – O	2.17(2) — 2.30(1)	2.19(1) — 2.78(1)	2.19(1) — 2.76(1)
Pb(9) – O	2.18(1) — 2.65(1)	2.17(2) — 2.76(1)	2.17(2) — 2.78(1)

Figure 8.5. Crystal structure of  $\text{Pb}_{5-x}\text{Ba}_x\text{Ge}_3\text{O}_{11}$  viewed along  $[001]$ . Pb—grey, Pb/Ba—purple, Ge—blue and O—red. Unit cell edges are shown by black lines.

### 8.2.3.2. Energy dispersive spectroscopy

A single crystal of samples B and C were each measured using energy dispersive spectroscopy to determine the ratio between Pb and Ba to calculate the value of  $x$  for  $\text{Pb}_{5-x}\text{Ba}_x\text{Ge}_3\text{O}_{11}$ . For both measurements the O content was unreliable, this is a common occurrence in energy dispersive spectroscopy methods, since all excess atomic weight is automatically assigned to be O.

For sample B, a chemical formula of  $\text{Pb}_{4.9(1)}\text{Ba}_{0.15(2)}\text{Ge}_{3.3(1)}\text{O}_{11.6(3)}$  was calculated (*Table 8.5*). This fits well with the expected composition from the ratio of reactants used,  $\text{Pb}_{4.875}\text{Ba}_{0.125}\text{Ge}_3\text{O}_{11}$ , and those calculated through X-ray diffraction measurements (*Table 8.8*). The measured formula for sample C,  $\text{Pb}_{4.7(1)}\text{Ba}_{0.29(2)}\text{Ge}_{3.5(1)}\text{O}_{11.9(2)}$ , also fitted well with what was predicted from the ratio of reactants used,  $\text{Pb}_{4.775}\text{Ba}_{0.225}\text{Ge}_3\text{O}_{11}$  (*Table 8.5*), and those calculated through X-ray diffraction measurements (*Table 8.8*). However, there is a slightly higher Ba content than what was predicted from the ratio of reagents, which is likely due to the crystal fragment that was measured originating from a more Ba rich region of the bulk crystal.

Table 8.5. Relative values from energy dispersive spectroscopy of for  $\text{Pb}_{5-x}\text{Ba}_x\text{Ge}_3\text{O}_{11}$ .

	w(Pb)/%	w(Ba)/%	w(Ge)/%	$x$
Sample B	24.35±0.62	0.73±0.11	16.61±0.56	0.15±0.02
Sample C	23.08±0.59	1.43±0.12	16.99±0.54	0.29±0.02

### 8.2.3.3. Differential scanning calorimetry

A differential scanning calorimetry measurement of each powdered sample was conducted to track the effect of Ba doping on the phase transition temperature. The samples were all measured between 220 and 520 K and a small endothermic peak was observed for every sample (*Figure 8.6. and Table 8.6*). This peak is attributed to the rise of the ferroelectric characteristics through a phase transition, which lowers the crystal symmetry and results in the bonding of Ge–O–Ge, which bridges the two tetrahedra in the  $[\text{Ge}_2\text{O}_7]^{6-}$  unit, no longer being identical. The subtle change involved in this phase transition means there is a very small change in enthalpy, therefore the resulting peak area with differential scanning calorimetry is also very small.



For the non-substituted phase,  $\text{Pb}_5\text{Ge}_3\text{O}_{11}$ , the phase transition temperature, 450 K, has been seen to fluctuate from one investigation to another (446 – 451 K).<sup>[298–300]</sup> This variation can actually be explained as the phase transition occurring being a continuous phase transition, which can be seen as a transition region, where the structural change and Curie temperature are located.<sup>[299]</sup> Taking this into account, the measured average value for non-substituted  $\text{Pb}_5\text{Ge}_3\text{O}_{11}$ , 418.1 K, fits well with the expected value.

Partial substitution of Ba onto the Pb position typically results in a considerable lowering of the transition temperature, at a rate of 18 K/at. % of Ba on the Pb position, and a broadening of the phase transition region.<sup>[298,299]</sup> While a decrease is observed in the measured average values of the Ba substituted phases, they are very small and do not fit with the established relationship of Ba content to phase transition temperature. The reason for this has so far proven elusive.

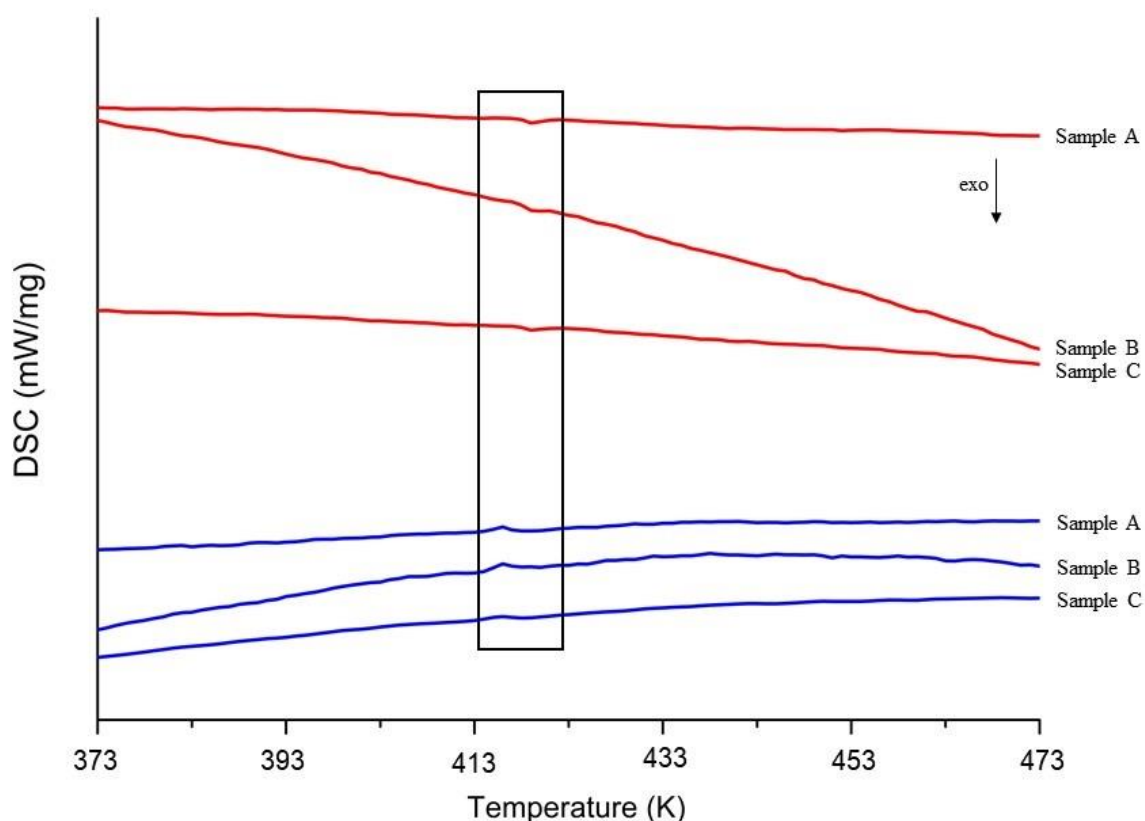


Figure 8.6. Selected differential scanning calorimetry measurements of each sample, between 373 and 473 K, showing the observed small peak, with lines corresponding to heating (red) and cooling (blue).

Table 8.6. Measured onset values and average of the endothermic peak, in K, on heating from DSC for  $\text{Pb}_{5-x}\text{Ba}_x\text{Ge}_3\text{O}_{11}$ , with stated compositions.

	1	2	3	4	5	Average
Sample A $x = 0$	419.8	420.3	418.2	417.8	414.25	418.1
Sample B $x = 0.15(2)$	418.9	417.3	415.3	416.9	415.45	416.8
Sample C $x = 0.29(2)$	416.8	416.7	416.2	417.8	416.4	416.8

#### 8.2.4. Discussion and conclusion

In this chapter, large single crystal samples of  $\text{Pb}_{5-x}\text{Ba}_x\text{Ge}_3\text{O}_{11}$  were synthesised. All of the samples crystallised in the low temperature structure, with the space group  $P3$  (No. 143). Crystal structure data obtained by both single crystal and powder X-ray diffraction showed that in general the unit cell increases with increasing Ba content (*Table 8.7*). A slight decrease in the  $a$  axis is actually observed for sample B in both sets of data obtained by X-ray diffraction techniques, which could be attributed to a variance in the thermal history of the sample in comparison to the other samples. Interestingly, the calculated unit cell parameters from powder X-ray diffraction for sample C are smaller than those calculated by single crystal X-ray diffraction. This variance could be evidence of varying Ba content between single crystals. However, powder X-ray diffraction techniques analyse more than just one microcrystal in the powder sample and so an averaged unit cell is observed by this method. This X-ray powder pattern has sharp and defined reflections and unit cell parameters with a low error. This would mean that small regions of the crystals have a homogenous composition and overall the whole crystal is comprised of these different regions with varying compositions. While energy dispersive spectroscopy was not used to measure across the entire surface of the crystal, it is expected to show a composition gradient.

Table 8.7. Comparison between unit cell parameters from powder X-ray diffraction refinement and single crystal X-ray diffraction refinement of  $\text{Pb}_{5-x}\text{Ba}_x\text{Ge}_3\text{O}_{11}$ , with compositions obtained by energy dispersive spectroscopy.

	Single crystal			Powder		
	$a/\text{\AA}$	$c/\text{\AA}$	$V/\text{\AA}^3$	$a/\text{\AA}$	$c/\text{\AA}$	$V/\text{\AA}^3$
Sample A $x = 0$	10.2131(1)	10.6496(2)	962.01	10.2323(4)	10.6673(4)	967.364
Sample B $x = 0.15(2)$	10.2056(1)	10.6712(1)	962.54	10.1926(3)	10.6448(4)	957.711
Sample C $x = 0.29(2)$	10.2145(2)	10.7070(2)	967.46	10.2028(3)	10.6699(4)	961.913

During synthesis of  $\text{Pb}_{5-x}\text{Ba}_x\text{Ge}_3\text{O}_{11}$  a predicted Ba content was calculated, from the ratios of reagents, for samples B and C,  $x = 0.125$  and  $0.225$  respectively. During refinement of the crystal structure data obtained by X-ray diffraction techniques, the Ba content of both samples was calculated (Table 8.8.). Standard X-ray diffraction techniques are typically not accurate with determining the amount of substitution, with errors being 3 to 4 times of what is shown. This would explain why there is a quite large discrepancy between the values predicted and calculated by this method. Energy dispersive spectroscopy measurement produced values which were more in agreement with those predicted. For each analytical measurement a different crystal was used. During the crystallisation process, a difference between the melt and crystal being grown begins to occur.<sup>[301–304]</sup> As the large single crystals are being removed from the flux, it affects the concentration of the melt. This happens due to the large crystal altering the composition of the melt, resulting in a larger concentration of Ba in the melt. This increase leads to a higher amount of Ba to be incorporated into the crystal structure.

Table 8.8. Comparison of values of  $x$  for  $\text{Pb}_{5-x}\text{Ba}_x\text{Ge}_3\text{O}_{11}$  obtained with different analytical methods.

	Expected	Values of $x$		
		Single Crystal	Powder Refinement	Energy dispersive spectroscopy
Sample B	0.125	0.24(5)	0.241	$0.15 \pm 0.02$
Sample C	0.225	0.31(4)	0.307	$0.29 \pm 0.02$

Investigations into the effect of Ba content on the phase transition temperature, and thus ferroelectric transition, showed that for these samples the small amount of Ba introduced had a minimal impact on the transition temperature. This goes against what has been reported so far. However, since the phase transition is better described as a phase transition range, the previously observed behaviours might vary from sample to sample.

While the crystal structure itself is not a novel structure, the effect of Ba content on the unit cell parameters and the phase transition does show behaviour which goes against what has been previously reported. These results can, perhaps, add further understanding to, what is appearing to be, a rather complex and conflicting relationship between Ba content in  $\text{Pb}_{5-x}\text{Ba}_x\text{Ge}_3\text{O}_{11}$  and the structural and physical characteristics.

### 8.3. Synthesis and characterisation of $\text{Pb}_5\text{Ge}_{3-x}\text{Si}_x\text{O}_{11}$

#### 8.3.1. Introduction

Several works have looked into the effects of substitution of the Ge atoms with isovalent Si atoms, which has been explored for a large range of Si content  $\text{Pb}_5\text{Ge}_{3-x}\text{Si}_x\text{O}_{11}$  ( $0 \leq x \leq 2.25$ ).<sup>[283,290,313,314,305–312]</sup> Introduction of Si into the system leads to a decrease in the Curie temperature, which lowers from 450 K, for  $x = 0$ , to 220 K, for  $x = 2.25$ . When sufficient amount of Si is present,  $x = 0.75$ , relaxator behaviour is observed. A separate investigation has pointed to a dramatic decrease of the ferroelectric transition temperature with increasing Si content, stating that for  $\text{Pb}_{4.95}\text{Ba}_{0.05}\text{Ge}_2\text{SiO}_{11}$  the transition temperature is as low as 167 K.<sup>[314]</sup>

The origin and relation of this behaviour with Si content has yet to be explained. Other properties, such as pyroelectric constants, permittivity and phase transition temperatures, vary substantially between different investigations.<sup>[283,285,306]</sup> This would imply that Si content is not the only factor that influences the properties. This has led to limited progress to be made about the nature and causes of the dependence on Si content for the changes in permittivity, as well as the origins of the relaxator behaviour.

### 8.3.2. Synthesis of $\text{Pb}_5\text{Ge}_{3-x}\text{Si}_x\text{O}_{11}$

Five charge mixtures were produced from weighing out a stoichiometric mixture of PbO, SiO<sub>2</sub> and GeO<sub>2</sub> (Table 8.9.) and treated using the method described earlier (see part 8.1.).

Table 8.9. Mixture composition used to grow single crystals of  $\text{Pb}_5\text{Ge}_{3-x}\text{Si}_x\text{O}_{11}$ . Data for sample A is taken from sample A in section 8.2.

	Reactant composition					
	wt%			mol%		
	PbO	SiO <sub>2</sub>	GeO <sub>2</sub>	PbO	SiO <sub>2</sub>	GeO <sub>2</sub>
Sample A $x = 0$	78.046	–	21.954	62.511	–	37.489
Sample B $x = 0.30(4)$	78.492	1.521	19.987	69.529	4.551	37.782
Sample C $x = 0.72(1)$	79.610	3.343	17.047	62.548	8.871	28.581
Sample D $x = 1.23(1)$	81.180	5.901	12.920	63.084	15.489	21.426
Sample E $x = 1.42(1)$	81.180	5.901	12.920	63.084	15.489	21.426

### 8.3.3. Characterisation

#### 8.3.3.1. Structure determination and crystal structure of $\text{Pb}_5\text{Ge}_{3-x}\text{Si}_x\text{O}_{11}$

Single crystals of each sample were measured using single X-ray diffraction and were indexed in the trigonal space group  $P3$  (No. 143), with varying unit cell parameters ( $a = 10.2131(1) \text{ \AA} - 10.1341(1) \text{ \AA}$  and  $c = 10.6496(2) \text{ \AA} - 10.5748(2) \text{ \AA}$ ). This is in agreement with the unit cell parameters seen for  $\text{Pb}_5\text{Ge}_3\text{O}_{11}$  ( $a = 10.190 \text{ \AA}$  and  $c = 10.624 \text{ \AA}$ ).<sup>[289]</sup> Refinement of the single crystal X-ray diffraction data of each sample confirmed each sample to be  $\text{Pb}_5\text{Ge}_{3-x}\text{Si}_x\text{O}_{11}$  (Table 8.10.) and which Ge crystallographic positions were substituted with Si (Tables B.2.1. and B.2.2.).

With increasing Si content there is a clear decrease in unit cell parameters, volume, density and  $F(000)$ . This decrease is a result of Si being smaller than Ge atoms, 0.26 Å and 0.40 Å respectively,<sup>[187]</sup> as well as being lighter and with fewer electrons. The change in unit cell parameters and volume appears to, with increasing Si content, decrease quite steadily (*Figure 8.7.*). For the value of the  $c$  axis, the decreasing values appear to begin to plateau after a certain Si content,  $x = 1.23(1)$ .

Table 8.10. Single crystal structural refinements of  $\text{Pb}_5\text{Ge}_{3-x}\text{Si}_x\text{O}_{11}$ . Data for sample A is taken from sample A in section 8.2.

	Sample A	Sample B	Sample C	Sample D	Sample E
Composition	$x = 0$	$x = 0.30(4)$	$x = 0.72(1)$	$x = 1.23(1)$	$x = 1.42(1)$
Crystal system	Trigonal	Trigonal	Trigonal	Trigonal	Trigonal
Space group	$P3$ (No. 143)	$P3$ (No. 143)	$P3$ (No. 143)	$P3$ (No. 143)	$P3$ (No. 143)
$Z$	3	3	3	3	3
$a/\text{Å}$	10.2131(1)	10.2028(1)	10.1608(1)	10.1453(1)	10.1341(1)
$c/\text{Å}$	10.6496(2)	10.6312(1)	10.5985(2)	10.5737(1)	10.5748(2)
$\rho_{\text{calc}}/\text{gcm}^{-3}$	7.404	7.200	7.282	7.322	7.258
Volume $V/\text{Å}^3$	962.01	958.41	947.61	942.51	940.53
Measurement temperature/K	293(2)	293(2)	293(2)	293(2)	293(2)
Index range	$-9 \leq h \leq 18$ $-18 \leq k \leq 18$ $-19 \leq l \leq 19$	$-20 \leq h \leq 19$ $-18 \leq k \leq 20$ $-15 \leq l \leq 20$	$-20 \leq h \leq 11$ $-17 \leq k \leq 20$ $-20 \leq l \leq 20$	$-18 \leq h \leq 18$ $-18 \leq k \leq 18$ $-12 \leq l \leq 19$	$-13 \leq h \leq 18$ $-18 \leq k \leq 15$ $-19 \leq l \leq 19$
Max. $2\theta$ /deg	61.29	67.17	64.55	61.31	61.27
$F(000)$	1782.0	1764.0	1740.0	1713.0	1706.4
$\mu/\text{mm}^{-1}$	39.39	39.15	39.09	38.79	38.63
Observed reflections	124791	138695	137417	140713	138434
Unique reflections	8106	9100	9940	6963	7921
Refined parameters	174	177	176	177	176
$R_{\text{int}}/R_{\sigma}$	0.0599/0.0202	0.0673/0.0422	0.0928/0.0484	0.0872/0.0452	0.0751/0.0339
$R_1/wR_2$	0.0346/0.0942	0.1060/0.0407	0.0624/0.1704	0.0678/0.1684	0.0312/0.0724
$Goof$	1.026	1.072	1.054	1.047	0.988
Remaining electron density max/min/ $\text{Å}^{-3}$	4.07/−3.11	4.01/−5.12	3.05/−5.27	6.66/−10.54	3.63/−3.95
BASF	0.494(2)	0.438(2)	0.505(5)	0.49(1)	
Twin matrix	−100 0−10 001	−100 0−10 001	−100 0−10 001	−100 0−10 001	

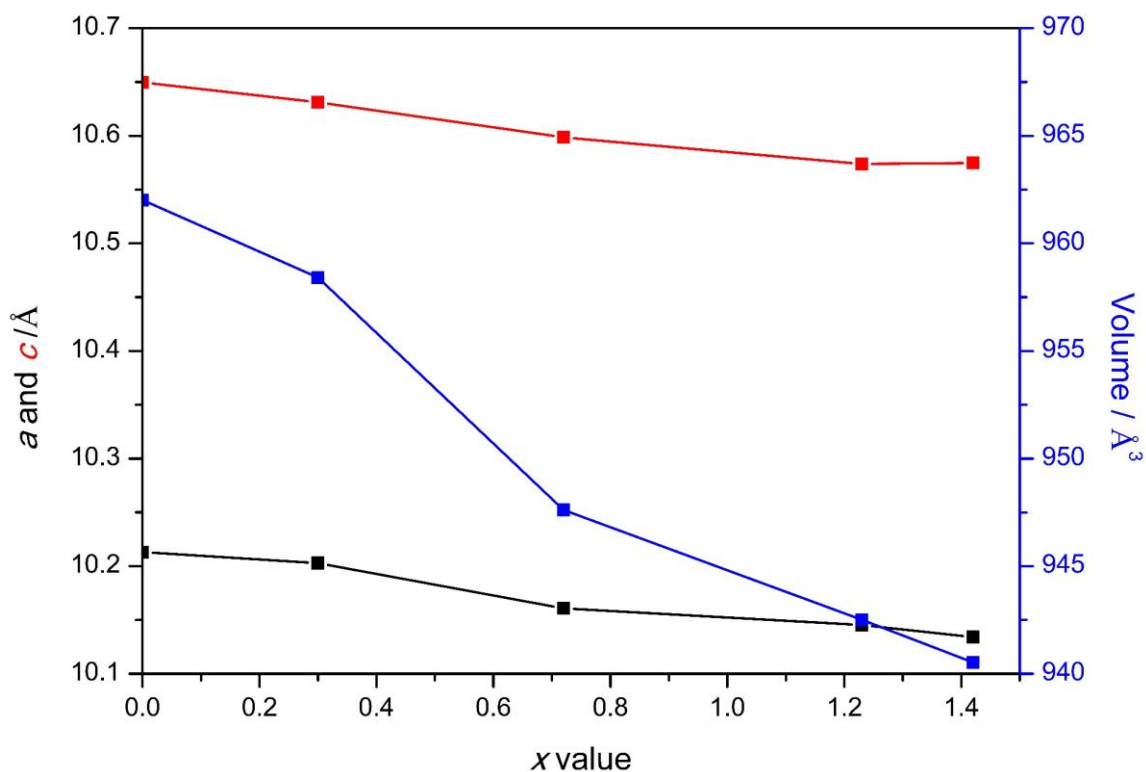


Figure 8.7. Relationship between value of  $x$  for  $\text{Pb}_5\text{Ge}_{3-x}\text{Si}_x\text{O}_{11}$  and unit cell parameters ( $a$  is shown in black,  $c$  is shown in red and volume is shown in blue). Data for sample A is taken from sample A in section 8.2.

The influence of the substitution of Ge by Si can be seen in the interatomic distances of the (Ge/Si) $\text{O}_4$  tetrahedra (Table 8.11.). For sample A, with no Si content, the interatomic distances between Ge and O (1.73(1) – 1.80(1) Å) are in agreement with those reported for  $\text{Pb}_5\text{Ge}_3\text{O}_{11}$  (1.71 – 1.84 Å).<sup>[289]</sup> As Si is introduced to the crystal structure, the Ge/Si – O interatomic distances decrease and tend towards the Si–O distances observed in the structurally similar  $\text{Pb}_3[\text{Si}_2\text{O}_7]$ , 1.61 Å – 1.67 Å.<sup>[315]</sup> From sample C,  $x = 0.72(1)$ , onwards the increasing Si content appears to have less of an effect on the interatomic distances between Ge/Si and O. This is likely due to the interatomic distances already being in the typical range for Si–O and therefore, the changes with further increasing Si content would be minimal. This could explain why a plateau is seen for the decrease in the  $c$ -axis, since along the  $c$  direction only the distance between Ge/Si and O changes with changing Si content. However, a lack of published data regarding this change in interatomic distances makes it challenging to compare with other phases of  $\text{Pb}_5\text{Ge}_3\text{O}_{11}$  substituted with Si.

Upon comparing the amount of Si content on each Ge/Si position in the crystal structure, a trend and distinct preference can be seen (Figure 8.8.). The Si atoms more readily substitute onto the Ge found on the isolated tetrahedra (Ge(1)/Si(1)), which would be expected since substitution on this site would have the least impact on the crystal structure as a whole. In general, the substitution appears to at first prefer the isolated Ge(1)/Si(1) site, but once the Si content on this position tends

towards 0.5, then the other Ge sites start to get substituted with Si. The substitution on the Ge(2)/Si(2) and Ge(3)/Si(3) sites have no discernible pattern, which would imply that the Si atoms have no preference between these two positions. This would fit with the fact that both these positions are near identical, so there is no chemical or structural difference that would make one position more preferable. An exception to this general trend can be seen for sample B, which is attributed to the Si content being so low for the Ge(2)/Si(2) and Ge(3)/Si(3) positions that it could just be a result of standard deviation and actually contains no Si, which would fit with the aforementioned trend.

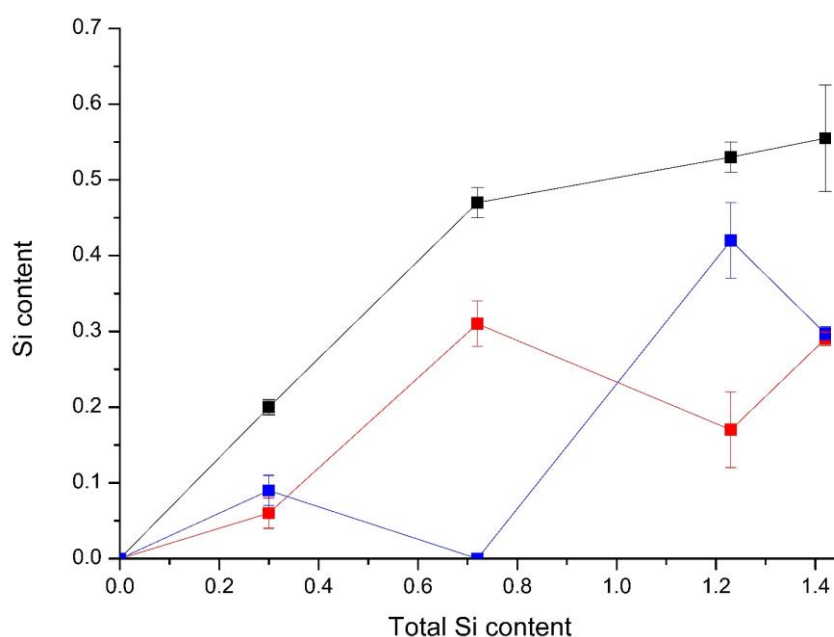


Figure 8.8. Comparison of the amount of Si content on the Ge/Si positions for each sample (Ge(1)/Si(1) – black, Ge(2)/Si(2) – blue and Ge(3)/Si(3) – red).

An interesting effect of increasing Si content is what happens to the tilting angle of the corner sharing (Ge/Si)O<sub>4</sub> tetrahedra. For sample A, the value calculated for the tilting angle is 127.8(7) °, which fits well with what is reported in the literature for Pb<sub>5</sub>Ge<sub>3</sub>O<sub>11</sub>, 126.1 °.<sup>[315]</sup> As the samples increase in Si content, the tilting angle also increases (*Table 8.11*). This increase also appears to plateau similar to the Ge/Si–O interatomic distances described earlier. There are currently no reports of the solely Si containing phase Pb<sub>5</sub>Si<sub>3</sub>O<sub>11</sub>, so it is unknown what the tilting angle between the corner sharing SiO<sub>4</sub> tetrahedra would be. However, a simplistic relationship can be proposed between the Ge/Si content and tilting angle by looking at the structurally similar lead Barysilite, Pb<sub>3</sub>Si<sub>2</sub>O<sub>7</sub>, and a Ge containing variant, Pb<sub>3-x</sub>Ba<sub>x</sub>Ge<sub>2</sub>O<sub>7</sub> (See chapter 8.4.), which also contain the corner sharing tetrahedra. In this structure the corner sharing GeO<sub>4</sub> tetrahedra of Pb<sub>3-x</sub>Ba<sub>x</sub>Ge<sub>2</sub>O<sub>7</sub> have a calculated tilting angle of 120.2(3) °, while the corner sharing SiO<sub>4</sub> tetrahedra in Pb<sub>3</sub>Si<sub>2</sub>O<sub>7</sub>



have a larger tilting angle of  $125.1^\circ$ .<sup>[315]</sup> While these values are not the same as those for  $\text{Pb}_5\text{Ge}_{3-x}\text{Si}_x\text{O}_{11}$ , it does show that the Si–O–Si tilting angle is larger than the angle for Ge–O–Ge, which is also observed for  $\text{Pb}_5\text{Ge}_{3-x}\text{Si}_x\text{O}_{11}$  with increasing Si content.

To determine the purity of the bulk sample, powdered samples of each product were analysed using powder X-ray diffraction and refined using the structural data obtained by single crystal refinement as a template. The powder diffraction refinements showed that the bulk sample of each measured product is single phase (*Tables 8.12. and B.2.3. and Figure 8.9.*). However, Pb cations are such large absorbers of X-rays, that refinement of the atomic positions of the lighter O anions was not possible. To compensate for this the refined atomic positions of O from the respective samples were used and fixed as the positions of O for the refinements (*Table B.2.3.*). Due to program limitation, the occupation of the mixed Ge/Si positions had to be refined manually, using values from single crystal refinement as a reference. This was achieved by gradual increasing and decreasing of the occupation until the best refinement values were obtained.

Sample B shows a slight deviation in the trend of decreasing unit cell parameters with increasing Si content. This deviation could have been caused when the large single crystals are being removed from the flux. As the crystal is removed the concentration of the melt changes. This happens due to the large crystal altering the composition of the melt, resulting in a larger concentration of Ba in the melt. This increase leads to a higher amount of Ba to be incorporated into the crystal structure.

Table 8.11. Interatomic distance range (Å) and angles (°) of Ge/Si and O for  $\text{Pb}_5\text{Ge}_{3-x}\text{Si}_x\text{O}_{11}$ .

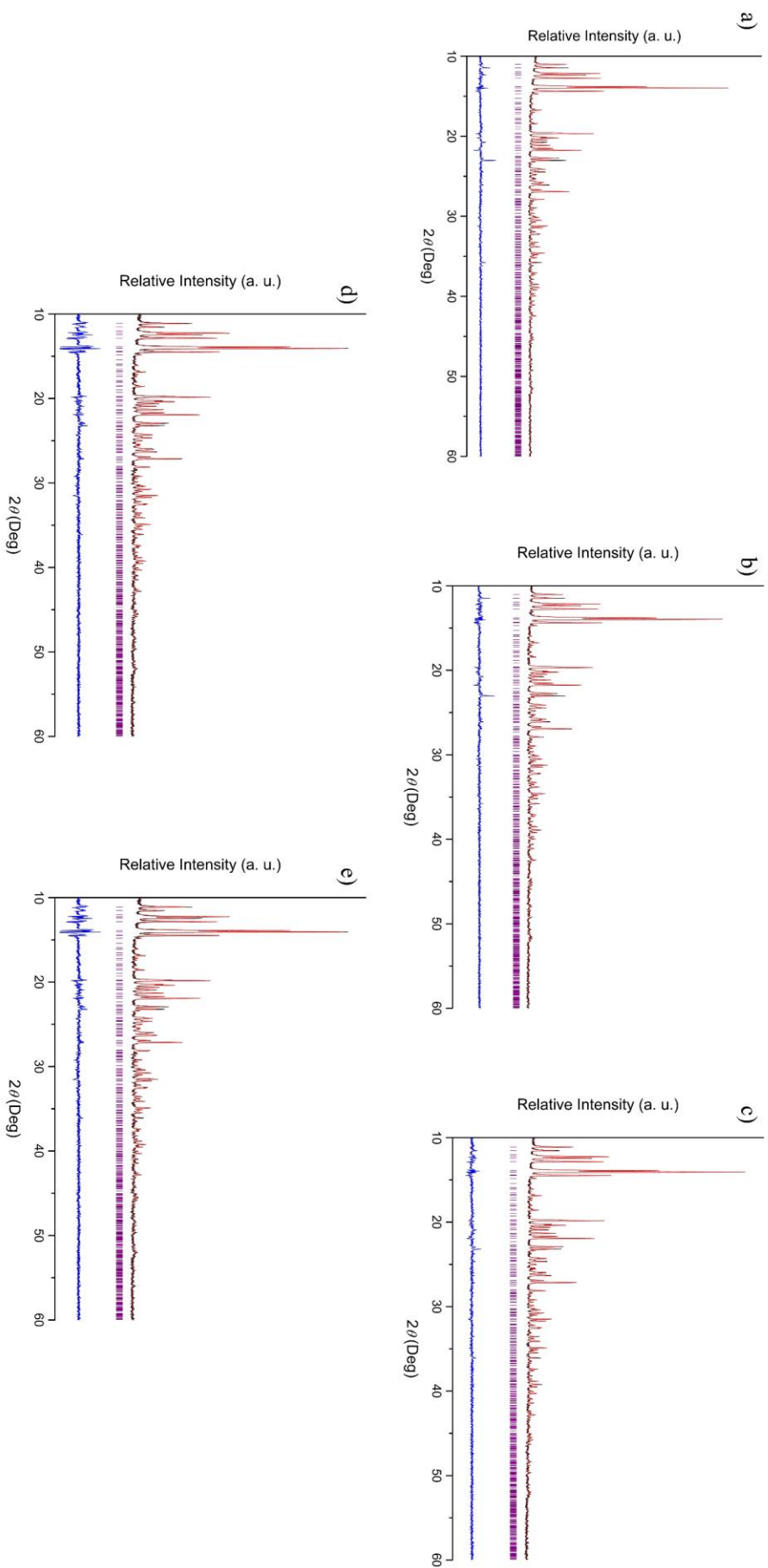
Data for sample A is taken from sample A in section 8.2.

	Ge(1)/Si(1) – O	Ge(2)/Si(2) – O	Ge(3)/Si(3) – O	Ge/Si(2) – O(9) – Ge/Si(3)
Sample A $x = 0$	1.73(1) – 1.76(1)	1.75(1) – 1.80(1)	1.72(2) – 1.80(1)	127.8(7)
Sample B $x = 0.30(4)$	1.72(1) – 1.75(2)	1.70(1) – 1.82(2)	1.75(2) – 1.78(2)	128.4(8)
Sample C $x = 0.72(1)$	1.69(2) – 1.74(4)	1.67(3) – 1.82(4)	1.65(3) – 1.79(5)	130(1)
Sample D $x = 1.23(1)$	1.67(5) – 1.71(2)	1.71(3) – 1.77(4)	1.62(4) – 1.81(5)	129(1)
Sample E $x = 1.42(1)$	1.679(9) – 1.694(7)	1.684(8) – 1.764(8)	1.688(8) – 1.759(7)	130.4(4)

Table 8.12. Unit cell parameters from the powder X-ray diffraction refinement of  $\text{Pb}_5\text{Ge}_{3-x}\text{Si}_x\text{O}_{11}$ .

Data for sample A is taken from sample A in section 8.2.

	Sample A $x = 0$	Sample B $x = 0.30(4)$	Sample C $x = 0.72(1)$	Sample D $x = 1.23(1)$	Sample E $x = 1.42(1)$
Space group	<i>P3</i>	<i>P3</i>	<i>P3</i>	<i>P3</i>	<i>P3</i>
$a/\text{Å}$	10.2323(4)	10.2313(3)	10.1490(3)	10.1462(3)	10.1104(3)
$c/\text{Å}$	10.66673(4)	10.666(4)	10.5815(3)	10.5810(4)	10.5417(4)
$V/\text{Å}^3$	967.364	966.958	943.899	943.334	933.207
$R_{wp}/\%$	7.71	6.46	7.15	6.70	6.02
$R_{Bragg}/\%$	9.41	7.24	7.26	8.00	6.35



### 8.3.3.2. Wavelength dispersive spectroscopy

Single crystals of samples B, C, D and E were measured using wavelength dispersive spectroscopy to determine the ratio between Ge and Si to calculate the value of  $x$  for  $\text{Pb}_5\text{Ge}_{3-x}\text{Si}_x\text{O}_{11}$ . Energy dispersive spectroscopy could not be used, due to Ge and Si producing overlapping signals with this method. Multiple measurements were conducted along the crystals, which showed a variation in Si content. The values obtained for every sample shows that a composition gradient is present in each sample (*Table 8.13.*) and the average of these values were used for the value of  $x$  for  $\text{Pb}_5\text{Ge}_{3-x}\text{Si}_x\text{O}_{11}$ . This gradient would be expected, since there appears to be no preference or limit for the Ge positions to be substituted with Si.

Table 8.13. Relative values from wavelength dispersive spectroscopy of for  $\text{Pb}_5\text{Ge}_{3-x}\text{Si}_x\text{O}_{11}$ .

Sample B	$w(\text{Ge})/\%$	$w(\text{Si})/\%$	$x$
1	14.03±0.13	1.60±0.02	0.307±0.004
2	14.18±0.07	1.57±0.02	0.299±0.038
3	14.63±0.13	1.70±0.02	0.312±0.004
4	14.44±0.13	1.57±0.02	0.293±0.004
5	14.13±0.13	1.57±0.02	0.300±0.004
6	14.34±0.13	1.68±0.02	0.315±0.004
Sample C	$w(\text{Ge})/\%$	$w(\text{Si})/\%$	$x$
1	11.97±0.13	3.81±0.03	0.724±0.006
2	12.12±0.13	3.80±0.03	0.716±0.006
3	12.02±0.13	3.80±0.03	0.721±0.006
Sample D	$w(\text{Ge})/\%$	$w(\text{Si})/\%$	$x$
1	8.52±0.13	8.38±0.02	1.488±0.004
2	8.45±0.13	7.60±0.02	1.421±0.004
3	8.25±0.13	7.22±0.02	1.400±0.004
4	8.08±0.13	7.32±0.02	1.426±0.004
5	8.03±0.13	7.42±0.03	1.441±0.006
6	8.28±0.13	7.19±0.02	1.394±0.004
7	8.34±0.13	7.03±0.02	1.372±0.004
8	8.51±0.13	7.43±0.02	1.398±0.004
Sample E	$w(\text{Ge})/\%$	$w(\text{Si})/\%$	$x$
1	10.31±0.13	6.31±0.02	1.139±0.004
2	9.84±0.13	6.63±0.02	1.208±0.004
3	10.09±0.13	6.34±0.02	1.158±0.004
4	9.84±0.13	6.53±0.02	1.179±0.004
5	9.73±0.13	6.06±0.02	1.151±0.004
6	9.73±0.13	6.09±0.02	1.550±0.004

### 8.3.3.3. Differential scanning calorimetry

Differential scanning calorimetry measurements were performed on each powdered sample to observe how the introduction of Si affects the phase transition temperature. The samples were all measured between 220 and 520 K and a small peak was observed for every sample (*Figure 8.10. and Table 8.14.*). This peak is attributed to a phase transition, which lowers the crystal symmetry and results in the interatomic distances of the bridging bonds Ge–O–Ge of the  $[\text{Ge}_2\text{O}_7]^{6-}$  unit no longer being identical. The subtle change involved in this phase transition means there is a very small change in enthalpy, therefore the resulting peak area with differential scanning calorimetry is also very small.

For the non-substituted phase,  $\text{Pb}_5\text{Ge}_3\text{O}_{11}$ , the phase transition temperature, 450 K, has been seen to fluctuate from one investigation to another (446 – 451 K).<sup>[298–300]</sup> This variation can actually be explained as the phase transition occurring as a continuous phase transition, which can be seen as a transition region, where the structural change and Curie temperature are located.<sup>[299]</sup> This explains the deviation between the transition temperature seen for the non-substituted  $\text{Pb}_5\text{Ge}_3\text{O}_{11}$ , 418.1 K, and the expected value from the literature. However, upon the introduction of Si there is no notable change in the transition temperature.

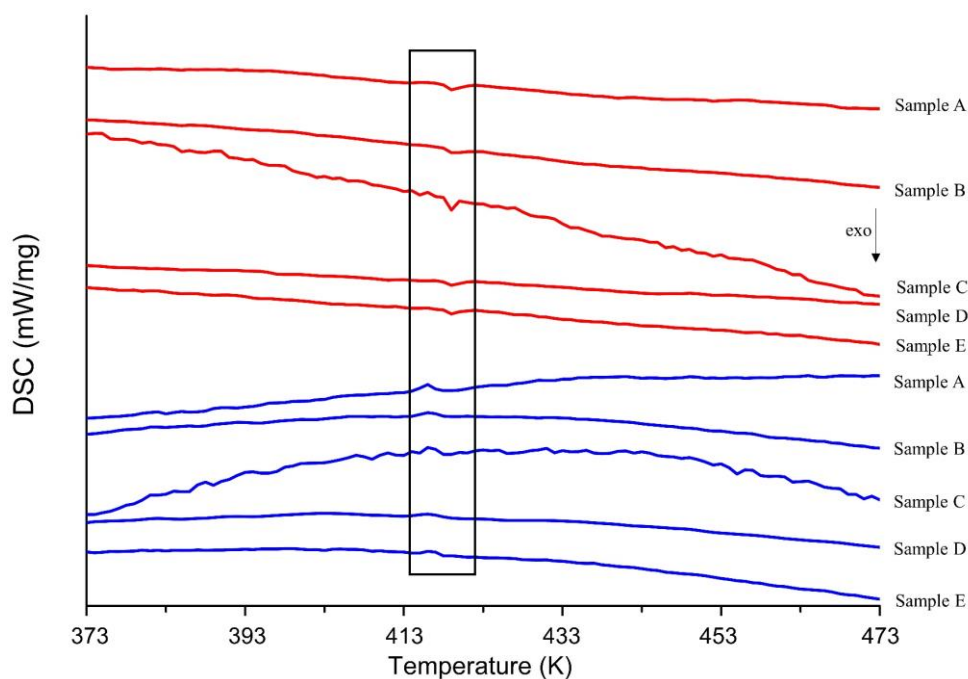


Figure 8.10. Selected differential scanning calorimetry measurements of each sample, between 373 and 473 K, showing the observed small peak, with lines corresponding to heating (red) and cooling (blue). Data for sample A is taken from sample A in section 8.2.

Table 8.14. Measured onset values and average of the endothermic peak, in K, on heating from DSC for  $\text{Pb}_5\text{Ge}_{3-x}\text{Si}_x\text{O}_{11}$ , with stated compositions. Data for sample A is taken from sample A in section 8.2.

	1	2	3	4	5	Average
Sample A $x = 0$	419.8	420.3	418.2	417.8	414.3	418.1
Sample B $x = 0.30(4)$	418.8	418.6	418.6	418.6	–	421.9
Sample C $x = 0.72(1)$	419.3	417.3	417.6	418.4	–	418.1
Sample D $x = 1.23(1)$	419.4	419.4	421.9	418.9	–	419.1
Sample E $x = 1.42(1)$	418.8	419.3	419.2	418.6	–	419.0

### 8.3.4. Discussion and conclusion

In this chapter several single crystals of the  $\text{Pb}_5\text{Ge}_{3-x}\text{Si}_x\text{O}_{11}$  series were produced. All samples crystallised in the low temperature phase with the space group  $P3$  (No. 143). Investigations of the crystal structure data, using both single crystal and powder X-ray diffraction techniques, showed that in general the unit cell parameters and volume decrease as the Si content increases (*Table 8.15*). A variation to this trend can be seen in the powder diffraction data of sample B, where the unit cell parameters are slightly larger than what the decreasing trend would suggest. This could arise from single crystals with varying Si which, due to the nature of powder X-ray diffraction, would result in an averaged unit cell of the powder.

A preference was seen for which Ge position would be substituted by Si. The Si was seen to prefer the isolated  $\text{GeO}_4$  tetrahedra and after a certain degree of substitution,  $x = 0.30(4)$ , the Si would also occupy the corner sharing tetrahedra, but no distinct preference was observed.

For each of the samples of  $\text{Pb}_5\text{Ge}_{3-x}\text{Si}_x\text{O}_{11}$  produced an estimated content of Si,  $x$ , was predicted from the amount of reactants involved. From the refinement of crystal structure data obtained by single crystal and powder X-ray diffraction, the Si content of each sample was calculated (*Table 8.16*). Even though standard X-ray diffraction techniques are not particularly accurate with determining the amount of substitution in a sample, the single crystal structure data fits well with what has been previously seen for the series  $\text{Pb}_5\text{Ge}_{3-x}\text{Si}_x\text{O}_{11}$ , with the exception of sample B. To obtain a more precise and accurate value for the amount of Si substitution, wavelength dispersive

spectroscopy was used. This method allowed the quantitative determination of Ge and Si in single crystals of each sample. The average values from this method fitted extremely well with the estimated values from the ratio of reagents, with the exception of sample E, which was slightly higher. The discrepancies between estimated values and those found through analytical techniques can be explained by there being varying compositions between each crystal. This would lead to some crystals being more Si rich than others and would also explain the difference in values between each analytical technique.

Table 8.15. Comparison between unit cell parameters from powder X-ray diffraction refinement and single crystal X-ray diffraction refinement of  $\text{Pb}_5\text{Ge}_{3-x}\text{Si}_x\text{O}_{11}$ , with predicted compositions. Data for sample A is taken from sample A in section 8.2.

	Single crystal			Powder		
	$a/\text{\AA}$	$c/\text{\AA}$	$V/\text{\AA}^3$	$a/\text{\AA}$	$c/\text{\AA}$	$V/\text{\AA}^3$
Sample A $x = 0$	10.2131(1)	10.6496(2)	962.01	10.2323(4)	10.6673(4)	967.364
Sample B $x = 0.30(4)$	10.2028(1)	10.6312(1)	958.41	10.2313(3)	10.666(4)	966.958
Sample C $x = 0.72(1)$	10.1608(1)	10.5985(2)	947.61	10.1490(3)	10.5815(3)	943.899
Sample D $x = 1.23(1)$	10.1453(1)	10.5737(1)	942.51	10.1462(3)	10.5810(4)	943.334
Sample E $x = 1.42(1)$	10.1341(1)	10.5748(2)	940.53	10.1104(3)	10.5417(4)	933.207

Table 8.16. Comparison of values of  $x$  for  $\text{Pb}_5\text{Ge}_{3-x}\text{Si}_x\text{O}_{11}$  obtained with different analytical methods.

	Expected	Values of $x$		
		Single Crystal	Powder Refinement	Wavelength dispersive spectroscopy
Sample B	0.26	0.4(1)	0.26	$0.30 \pm 0.04$
Sample C	0.72	0.77(6)	0.60	$0.72 \pm 0.01$
Sample D	1.23	1.1(4)	0.85	$1.23 \pm 0.01$
Sample E	1.23	1.33(5)	1.08	$1.42 \pm 0.01$

Determination of the amount of Si of the crystals revealed the presence of a composition gradient for each sample. This gradient would have resulted from the crystallisation process, where during crystallisation a difference between the melt and crystal being grown starts to occur.<sup>[301–304]</sup> The synthetic method used for each sample used relatively small amounts of SiO<sub>2</sub>, between 1.5 and 6 wt.%, leading to a low concentration of Si atoms in the melt. Upon crystallisation, the concentration of Si in the melt starts to increase, which then leads to an increase of Si within the crystal. This variation in Si content was observed by wavelength dispersive spectroscopy (*Table 8.13.*). The average Si content of each sample fits very well with what would be expected from the ratio of reagents used for the melt, but the composition within the crystal varies due to this relation between crystallisation and the concentrations of the melt.

Analysis of the effect of Si on the phase transition temperature, and by connection the ferroelectric transition temperature, showed that Si content had barely any effect on the transition temperature, even for the samples with the highest Si content. This goes against what has been previously reported, but since the phase transition can be better described as a phase transition range, the previously observed behaviours might vary from sample to sample.

Although compounds of the Pb<sub>5</sub>Ge<sub>3-x</sub>Si<sub>x</sub>O<sub>11</sub> series have been previously reported, there has been next to no information about the crystallographic effects of Si on the system. The crystallographic results presented here sheds light on how Si affects the crystal structure of Pb<sub>5</sub>Ge<sub>3-x</sub>Si<sub>x</sub>O<sub>11</sub> and this insight could contribute to the knowledge of how Si content affects the physical properties as a whole.



## 8.4. Synthesis and characterisation of $\text{Pb}_{3-x}\text{Ba}_x[\text{Ge}_2\text{O}_7]$

### 8.4.1. Introduction

The lead containing mineral Barysilite has seen several attempts, during the latter half of the 20<sup>th</sup> Century, to not only correctly determine its chemical formula, but also to produce it synthetically. Barysilite is defined as having the chemical formula  $\text{Pb}_3[\text{Si}_2\text{O}_7]$ <sup>[316]</sup> and is built up of isolated corner sharing double tetrahedra,  $[\text{Si}_2\text{O}_7]^{6-}$ . These tetrahedra are linked to each other via Pb cations to produce a framework, with channels running parallel along [001]. These channels are occupied with further Pb cations (*Figure 8.11.*).

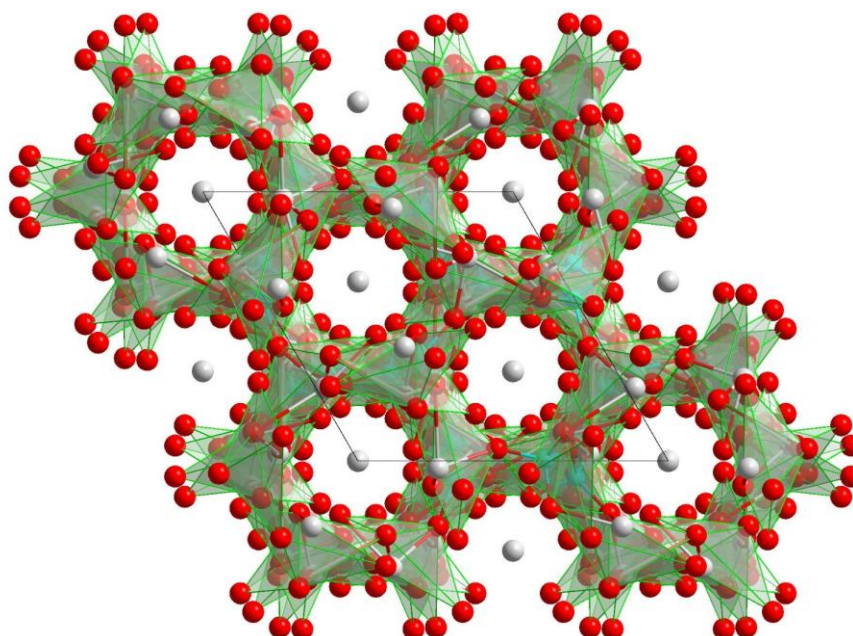


Figure 8.11. Crystal structure of Barysilite framework,  $\text{Pb}_3[\text{Si}_2\text{O}_7]$ , viewed along [001], consisting of Pb–grey, Si–turquoise and O–red. The framework is constructed from tetrahedra of  $\text{SiO}_4$ –green, with further Pb cations occupying the channels. Unit cell edges are shown in black.<sup>[315]</sup>

The chemical composition of naturally occurring Barysilite is not as idealised as the composition mentioned earlier. It is in fact considered to exist in the formula  $M\text{Pb}_8[\text{Si}_2\text{O}_7]_3$ , with  $M$  being primarily Mn, and replacing Pb cations along the channels.<sup>[317–319]</sup> Synthetic approaches have produced a wide variety of compounds for  $M\text{Pb}_8[\text{Si}_2\text{O}_7]_3$  ( $M = \text{Be} - \text{Sr}, \text{Mn}, \text{Co} - \text{Zn}$  and  $\text{Cd}$ ), with each of them substituting with Pb cations solely in the channels.<sup>[317,320]</sup>

Barysilite has also been produced, under synthetic conditions, on more than one occasion.<sup>[315,321]</sup> Further investigations lead to the substitution of Pb with two different cations, resulting in the compound (Pb,Sr,Ba)Pb<sub>8</sub>[Si<sub>2</sub>O<sub>7</sub>]<sub>3</sub>.<sup>[321]</sup> This, along with the large range of metals substitutions mentioned previously, shows that Barysilite has a large tolerance towards substitution. However, only one example of substitution on the Si site has been observed, where it was substituted by Ge cations.<sup>[300]</sup> Increasing substitution showed a substantial increase in the Curie temperature of the pyroelectric properties.

### 8.4.2. Synthesis of Pb<sub>3-x</sub>Ba<sub>x</sub>[Ge<sub>2</sub>O<sub>7</sub>]

The charge mixtures were produced from weighing out a stoichiometric mixture of PbO (72.064 wt.%, 57.749 mol%), BaCO<sub>3</sub> (4.993 wt.%, 4.526 mol%) and GeO<sub>2</sub> (22.064 wt.%, 37.733 mol%) and treated using the method described earlier (*see part 8.1.*).

### 8.4.3. Characterisation

#### 8.4.3.1. Structure determination and crystal structure of Pb<sub>3-x</sub>Ba<sub>x</sub>[Ge<sub>2</sub>O<sub>7</sub>]

Single crystal X-ray diffraction indexed the product with a rhombohedral unit cell ( $a = 10.2408(1) \text{ \AA}$  and  $c = 40.348(8) \text{ \AA}$ ), which are similar to those seen for Barysilite, Pb<sub>3</sub>[Si<sub>2</sub>O<sub>7</sub>], ( $a = 10.1264(3) \text{ \AA}$  and  $c = 38.678(2) \text{ \AA}$ ).<sup>[315]</sup> A notable enlargement can be seen, when compared with Barysilite, and this can be explained by the larger Ge atoms, compared with Si (0.40 and 0.26 Å respectively, CN = 6),<sup>[187]</sup> and the partial substitution of Pb<sup>2+</sup> by Ba<sup>2+</sup> (1.36 and 1.18 Å respectively, CN = 6).<sup>[187]</sup>

A refinement of the single crystal structure data showed that the sample was near isostructural to Barysilite and that the Ba substitution only occurs in the channels of the structure (*Tables 8.17., B.3.1. and B.3.2.*). A powder X-ray diffraction was also measured and the data was refined using the Rietveld refinement method, using values from single crystal refinement as a reference. This produced a very good refinement and showed that the sample is single phase (*Figure 8.12. and Tables 8.18. and B.3.3.*). Due to program limitation, the occupation of the mixed Pb/Ba positions was fixed to those calculated from the refinement of the single crystal structure data.

Table 8.17. Single crystal structural refinements of  $\text{Pb}_{3-x}\text{Ba}_x[\text{Ge}_2\text{O}_7]$  for  $x = 0.19(9)$ .

Crystal System	Trigonal
Space group	$R\bar{3}$ (No. 146)
$Z$	18
$a/\text{\AA}$	10.2408(1)
$c/\text{\AA}$	40.3477(8)
$\rho_{\text{calc}}/\text{gcm}^{-3}$	6.851
Volume $V/\text{\AA}^3$	3664.52
Measurement	293(2)
temperature/K	
	$-13 \leq h \leq 19$
Index range	$-19 \leq k \leq 19$
	$-75 \leq l \leq 75$
Max. $2\theta/\text{deg}$	63.88
$F(000)$	6410.0
$\mu/\text{mm}^{-1}$	33.38
Observed reflections	181270
Unique reflections	2877
Refined parameters	173
$R_{\text{int}}/R_{\sigma}$	0.0741/0.0377
$R_1/wR_2$	0.0391/0.1073
$Goof$	1.071
Remaining electron	3.78–3.16
density (max/min)/ $\text{\AA}^{-3}$	
BASF	0.46(2)
Twin matrix	010 100 00–1

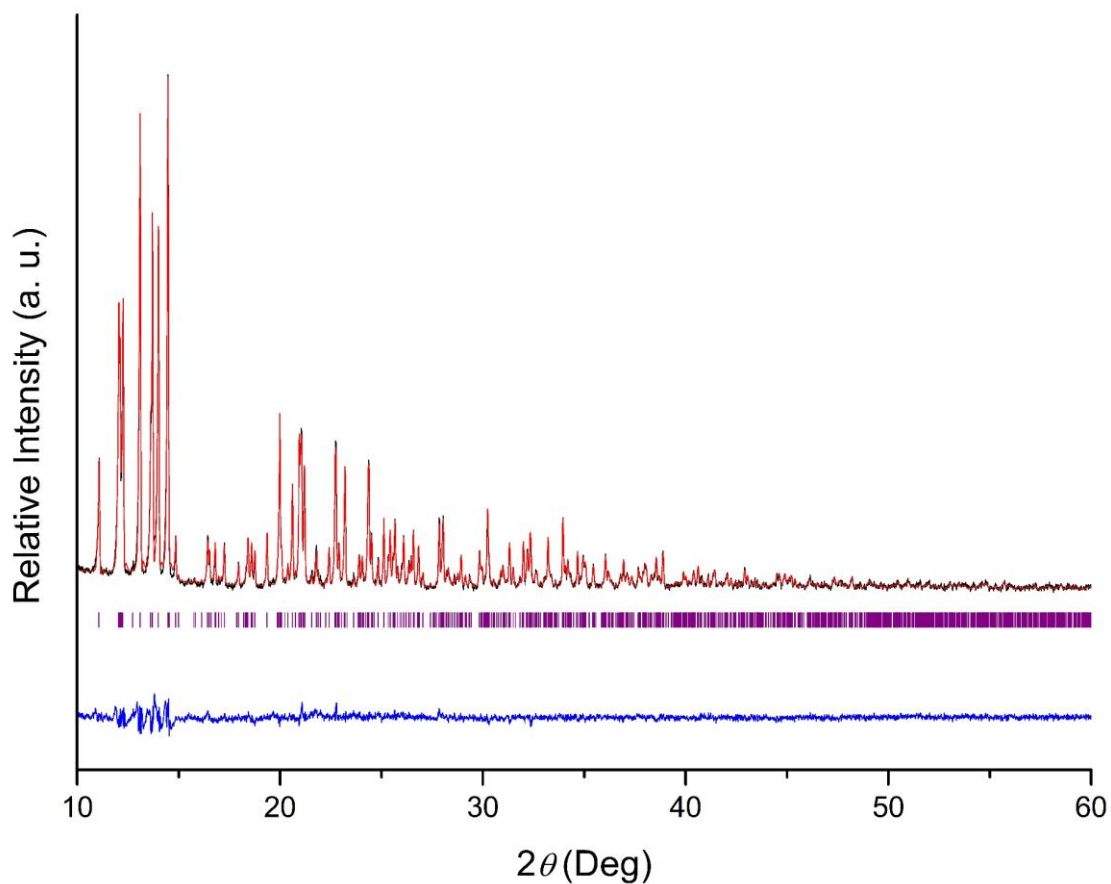


Figure 8.12. Graphical representation of Rietveld structural refinement of  $\text{Pb}_{3-x}\text{Ba}_x[\text{Ge}_2\text{O}_7]$  from powder X-ray diffraction measurements. The observed pattern is shown in black, the calculated one in red, Bragg marks in purple and the difference in blue. (Mo- $K_{\alpha 1}$ -wavelength,  $\lambda = 0.7093 \text{ \AA}$ ).

Table 8.18. Unit cell parameters from the powder X-ray diffraction refinement of  $\text{Pb}_{3-x}\text{Ba}_x[\text{Ge}_2\text{O}_7]$ , with the value of  $x$  coming from energy dispersive spectroscopy.

$x = 0.19(9)$	
Space Group	$R\bar{3}$
$a/\text{\AA}$	10.2948(3)
$c/\text{\AA}$	40.364(1)
$V/\text{\AA}^3$	3704.726
$R_{wp}/\%$	7.72
$R_{Bragg}/\%$	6.66

Originally, the crystal structure was thought to crystallise in  $R\bar{3}c$  (No. 167), the same as Barysilite. However, upon close inspection of the single crystal structural data refinement, a rather large remaining electron density ( $15.22/-12.30 \text{ \AA}^{-3}$ ) was observed near the Pb/Ba mixed positions. The reason for this high remaining electron density can be attributed to the stereochemically active lone pair of the  $\text{Pb}^{2+}$  cations. To reach a more stereochemically favourable position, the  $\text{Pb}^{2+}$  cations would occupy a position slightly different from that of  $\text{Ba}^{2+}$  cations. This slight difference in atomic positions would result in the loss of both the  $c$ -glide plane and inversion centre, due to the atomic positions produced by these symmetry elements no longer being identical (*Figure 8.13*). Another observation was that if a  $c$ -glide plane were present, then reflections for  $0kl$ , where  $l = 2n+1$ , would be systematically absent however, these reflections were observed. This led to the conclusion that  $R\bar{3}c$  was in fact the incorrect space group and the space group  $R3$  (No. 146) was taken instead, due to it producing a better single crystal structural data refinement and the comparison of the calculated and observed intensities for  $0kl$ , where  $l = 2n+1$ , fitted better than other potential space groups ( $R\bar{3}$ ,  $R32$ ,  $R3c$  and  $C2$ ). This produced a single crystal structural data refinement, with an inversion twin, which has significantly lower remaining electron density ( $3.78/-3.16 \text{ \AA}^{-3}$ ) and the reflections for  $0kl$ , where  $l = 2n+1$ , were observed and described.

This product crystallises very similar to  $\text{Pb}_3[\text{Si}_2\text{O}_7]$ , with Ge in place of Si and a partial substitution of Pb with Ba, which is only observed on the Pb positions that are located in the channels along  $[001]$  (*Figure 8.14*), as is observed for substituted variants of Barysilite.<sup>[317,320]</sup> The influence of the substitution of Ba becomes quite evident when observing the interatomic distances (*Table 8.19*). The interatomic distance range of the Pb sites without any Ba substitution ( $2.16(1) \text{ \AA} - 2.70(2) \text{ \AA}$ ) fits well with the range observed for the same position in  $\text{Pb}_3[\text{Si}_2\text{O}_7]$  ( $2.37 \text{ \AA} - 2.85 \text{ \AA}$ ).<sup>[315]</sup> However, the sites with the highest amount of Ba, Ba(8) and Ba(10), have an overall larger interatomic distance, between  $2.54(2)$  and  $3.27(2) \text{ \AA}$ , when compared to the same positions in the unsubstituted Barysilite,  $2.50 \text{ \AA}$  and  $2.61 \text{ \AA}$  respectively.<sup>[315]</sup> This change can be attributed to the interatomic distance tending towards that of  $d(\text{Ba}-\text{O}) = 2.759 \text{ \AA}$ ,<sup>[322]</sup> due to the larger ionic radius of Ba cations, which explains why a larger difference is seen for the site containing more Ba.

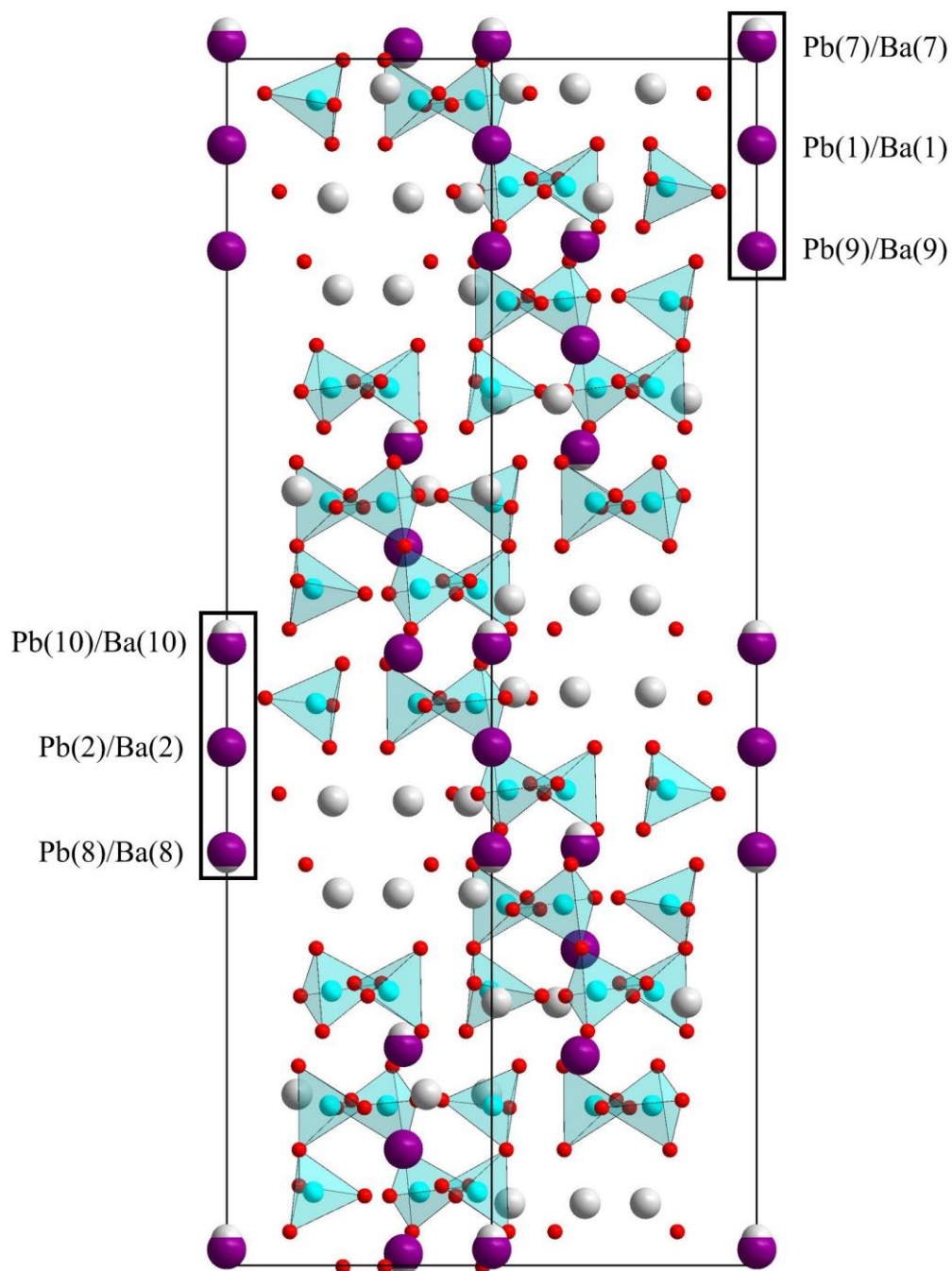


Figure 8.13. Section of the crystal structure of  $\text{Pb}_{3-x}\text{Ba}_x[\text{Ge}_2\text{O}_7]$ , viewed along  $[110]$ , showing the labelled Pb/Ba atoms, indicated by black boxes, that should be identical if a  $c$ -glide plane is present. With tetrahedra of  $\text{GeO}_4$ —turquoise and Pb—grey, Ba—purple, Ge—turquoise and O—red. Unit cell is shown in black.

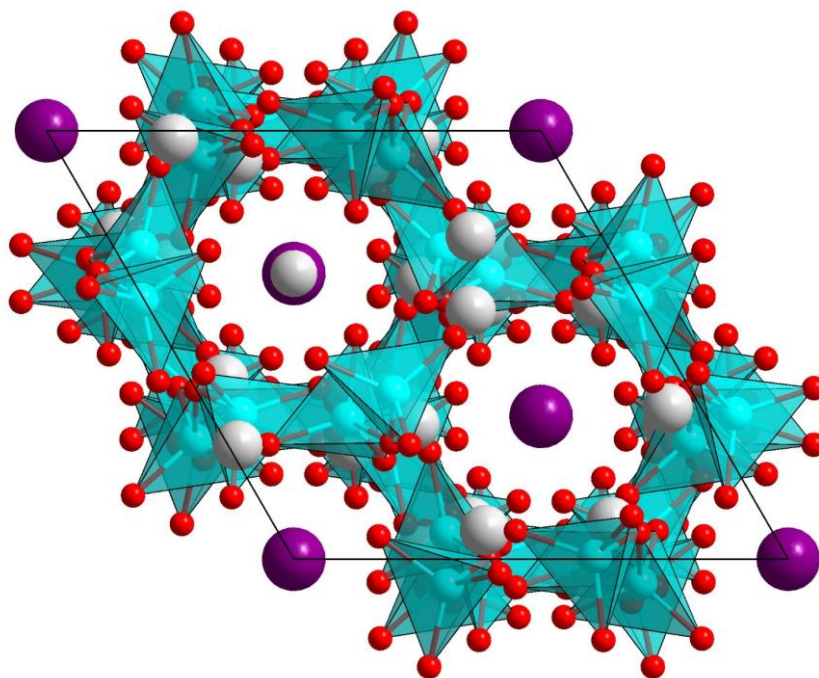


Figure 8.14. Section of the crystal structure of  $\text{Pb}_{3-x}\text{Ba}_x[\text{Ge}_2\text{O}_7]$ , viewed along  $[001]$ , with tetrahedra of  $\text{GeO}_4$ –turquoise and  $\text{Pb}$ –grey,  $\text{Ba}$ –purple,  $\text{Ge}$ –turquoise and  $\text{O}$ –red. Unit cell is shown in black.

The Ge cations are located inside tetrahedra of oxygen, with each tetrahedron corner sharing with another tetrahedron, which is also observed in  $\text{Pb}_3[\text{Si}_2\text{O}_7]$  for the Si and O tetrahedra. The interatomic distances between Ge and O ( $1.71(1) \text{ \AA} - 1.81(1) \text{ \AA}$ ) are longer than the ones observed for the Si variant ( $1.61 \text{ \AA} - 1.67 \text{ \AA}$ ),<sup>[315]</sup> which is due to Ge being larger than Si. Interestingly, there is a large difference in the angle between the corner sharing tetrahedra, with the angle for  $\text{Ge}(1)\text{--O}(1)\text{--Ge}(2)$  and  $\text{Ge}(3)\text{--O}(2)\text{--Ge}(4)$ ,  $118.4(5)^\circ$  and  $121.6(5)^\circ$  respectively, being smaller than that for  $\text{Si}\text{--O}\text{--Si}$ ,  $125.1^\circ$ , seen for  $\text{Pb}_3[\text{Si}_2\text{O}_7]$ .<sup>[315]</sup> This large difference is likely due to the larger radii of Ge cations, which causes the bridging angle to tend more towards  $180^\circ$  to reduce steric hindrance.

Table 8.19. Interatomic distances (Å) between selected atoms from  $\text{Pb}_{3-x}\text{Ba}[\text{Ge}_2\text{O}_7]$ .

Pb(1)/Ba(1) –O(3)	2.43(2)/2.54(2)		–O(12)	2.94(2)/3.04(2)	
	–O(4)	2.49(2)/2.39(2)	Pb(9)/Ba(9)	–O(4)	2.70(1)/2.71(2)
Pb(2)/Ba(2) –O(5)	2.45(2)/2.34(3)		–O(10)	2.70(2)/2.70(2)	
	–O(6)	2.38(8)/2.48(3)	–O(13)	2.98(2)/2.97(2)	
Pb(3) –O(5)	2.453(9)	Pb(10)/Ba(10)	–O(6)	2.763(2)/2.54(2)	
	–O(8)	2.35(1)	–O(7)	2.848(1)/2.95(1)	
	–O(9)	2.70(2)	–O(11)	3.037(2)/3.27(2)	
	–O(14)	2.16(1)	Ge(1)	–O(1)	1.81(1)
Pb(4) –O(4)	2.43(1)		–O(4)	1.77(1)	
	–O(7)	2.68(1)	–O(7)	1.75(1)	
	–O(10)	2.36(2)	–O(11)	1.74(1)	
	–O(11)	2.21(2)	Ge(2)	–O(1)	1.81(1)
Pb(5) –O(6)	2.46(1)		–O(3)	1.75(1)	
	–O(7)	2.30(1)	–O(8)	1.79(1)	
	–O(13)	2.16(1)	–O(12)	1.71(1)	
Pb(6) –O(3)	2.41(2)	Ge(3)	–O(2)	1.76(1)	
	–O(9)	2.32(2)	–O(5)	1.74(1)	
	–O(12)	2.22(1)	–O(9)	1.71(2)	
Pb(7)/Ba(7) –O(3)	2.74(1)/2.49(2)		–O(14)	1.73(1)	
	–O(9)	2.83(2)/2.96(2)	Ge(4)	–O(2)	1.76(1)
	–O(14)	–/3.29(2)	–O(6)	1.71(1)	
Pb(8)/Ba(8) –O(5)	2.71(2)/2.65(1)		–O(10)	1.74(2)	
	–O(8)	2.78(2)/2.74(2)	–O(13)	1.72(1)	



### 8.4.3.2. Energy Dispersive Spectroscopy

A single crystal of the sample was measured using energy dispersive spectroscopy to determine the ratio between Pb and Ba to calculate the value of  $x$  for  $\text{Pb}_{3-x}\text{Ba}_x[\text{Ge}_2\text{O}_7]$ . Since the surface of the crystal measured was not continuously flat, regions of flat areas were selected at points along the crystal (*Figure 8.15.*). Multiple measurements were conducted at these zones on the crystal, which showed a variation in Ba content (*Table 8.20.*). This variation shows there is a composition gradient along the crystal ( $0.019 \leq x \leq 0.28$ ), which is attributed to Ba substituting with the Pb along the channels in a disordered manner.

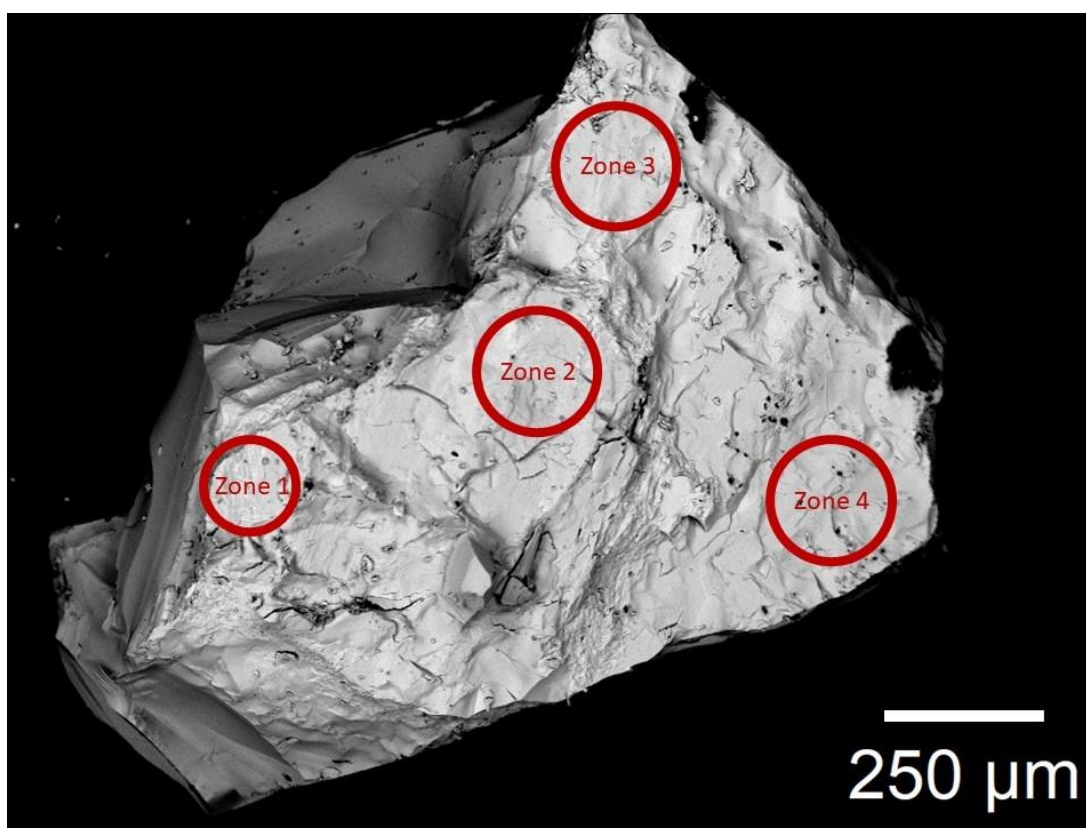


Figure 8.15. Selected zones used to measure the composition gradient along a single crystal of  $\text{Pb}_{3-x}\text{Ba}_x[\text{Ge}_2\text{O}_7]$ .

Table 8.20. Relative values from energy dispersive spectroscopy of for  $\text{Pb}_{3-x}\text{Ba}_x[\text{Ge}_2\text{O}_7]$ .

	w(Pb)/%	w(Ba)/%	x
Zone 1	38.22±0.18	0.24±0.09	0.019±0.007
Zone 2	27.71±0.14	1.82±0.15	0.18±0.02
	27.94±0.14	1.52±0.15	0.15±0.02
	36.69±0.17	2.17±0.19	0.17±0.01
Zone 3	27.87±0.14	2.15±0.15	0.21±0.02
	27.09±0.13	1.98±0.15	0.20±0.02
	30.90±0.15	0.91±0.16	0.22±0.02
Zone 4	12.76±0.07	1.00±0.09	0.22±0.02
	28.40±0.14	2.71±0.16	0.26±0.02
	25.11±0.53	2.61±0.43	0.28±0.05

#### 8.4.3.3. Differential scanning calorimetry

A differential scanning calorimetry measurement was conducted for a powdered sample. The sample was measured several times between 223 and 523 K, which produced a small endothermic peak, with an average of 417 K (*Figure 8.16. and Table 8.21.*).

This peak can be explained when compared with Barysilite and the substituted series  $\text{Pb}_3[\text{Si}_{2-x}\text{Ge}_x\text{O}_7]$  ( $0 \leq x \leq 1$ ).<sup>[300]</sup> The ferroelectric  $\text{Pb}_3[\text{Si}_2\text{O}_7]$  has an extrapolated Curie temperature of 173 K, which also corresponds to a phase transition from an as yet unidentified space group to  $R\bar{3}c$ . As the content of Ge increases in this system, the Curie temperature increases dramatically to a maximum of 448 K for the pure Ge variant,  $\text{Pb}_3[\text{Ge}_2\text{O}_7]$ . This would show that the observed peak at 417.8 K belongs to the same transition observed for the series  $\text{Pb}_3[\text{Si}_{2-x}\text{Ge}_x\text{O}_7]$  ( $0 \leq x \leq 1$ ). It would also suggest, when compared with  $\text{Pb}_3[\text{Ge}_2\text{O}_7]$ , that the introduction of Ba to the system in fact reduces the value of Curie temperature. For the series  $\text{Pb}_3[\text{Si}_{2-x}\text{Ge}_x\text{O}_7]$  ( $0 \leq x \leq 1$ ) a second peak was observed at 593 K, which is assigned to an as yet uncharacterised phase transition. A separate measurement was conducted, which went up to 650 K, and the second peak seen at 593 K for  $\text{Pb}_3[\text{Si}_{2-x}\text{Ge}_x\text{O}_7]$  ( $0 \leq x \leq 1$ ) was not observed.

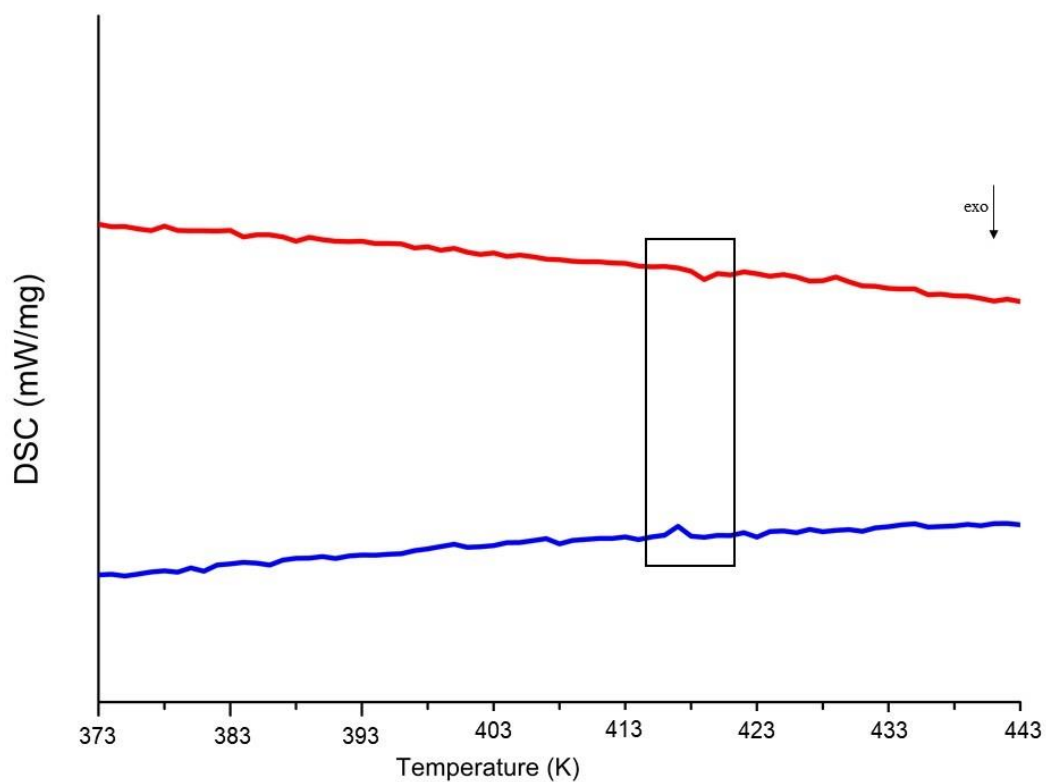


Figure 8.16. Differential scanning calorimetry of  $\text{Pb}_{3-x}\text{Ba}_x[\text{Ge}_2\text{O}_7]$ , between 373 and 443 K, showing the observed small peak, with lines corresponding to heating (red) and cooling (blue).

Table 8.21. Measured onset values and average of the endothermic peak, in K, on heating from DSC for  $\text{Pb}_{3-x}\text{Ba}_x[\text{Ge}_2\text{O}_7]$ , with stated compositions.

Scan 1	Scan 2	Scan 3	Scan 4	Scan 5	Average
419.4	415.4	417.1	416.4	420.6	417.8

#### 8.4.4. Discussion and conclusion

In this chapter a new germanium containing compound has been produced, which is nearly isostructural to the mineral Barysilite, and had a mixed occupation of Pb and Ba. Unit cell parameters obtained by single crystal and powder X-ray diffraction methods are larger than those reported for  $\text{Pb}_3[\text{Si}_2\text{O}_7]$ , which is caused by the presence of the larger Ge and Ba atoms. The unit cell parameters obtained for  $\text{Pb}_{3-x}\text{Ba}_x[\text{Ge}_2\text{O}_7]$  by powder X-ray diffraction are slightly larger than those calculated from single crystal X-ray diffraction (*Table 8.22.*). This is most likely due to there being varying compositions between each single crystal, which the overall average composition of the sample is measured by powder X-ray diffraction.

Table 8.22. Comparison between unit cell parameters from powder X-ray diffraction refinement and single crystal X-ray diffraction refinement of  $\text{Pb}_{3-x}\text{Ba}_x[\text{Ge}_2\text{O}_7]$ .

Single crystal			Powder		
$a/\text{\AA}$	$c/\text{\AA}$	$V/\text{\AA}^3$	$a/\text{\AA}$	$c/\text{\AA}$	$V/\text{\AA}^3$
10.2408(1)	40.3477(8)	3664.52	10.2946(2)	40.364(1)	3704.608

From the refinement of the crystal structure data obtained by single crystal and powder X-ray diffraction, the Ba content for the sample was calculated and compared with the expected composition (*Table 8.23.*). Standard X-ray diffraction techniques are not particularly accurate with determining the amount of substitution in a sample, with a large error being associated to this, which can be seen for the calculated Ba content from the single crystal structure data. However, the value obtained from Rietveld refinement of the crystal structure data, collected by powder X-ray diffraction, fits well with the expected value. To obtain a more precise and accurate value for the amount of Ba substitution, energy dispersive spectroscopy was used. This method allowed the quantitative determination of Pb and Ba by measuring a single crystal. The average value from this method fitted well with the estimated value and matched the value obtained from the Rietveld refinement. Along the crystal a composition gradient was observed, resulting in a variation of Ba content for  $\text{Pb}_{3-x}\text{Ba}_x[\text{Ge}_2\text{O}_7]$  ( $0.019 \leq x \leq 0.28$ ). The discrepancies between estimated values and those found through analytical techniques can be explained by there being varying compositions between each crystal. Since the substitution of Ba only occurs in the channels, the predicted highest possible Ba content for this phase would be  $\text{Pb}_2\text{Ba}[\text{Ge}_2\text{O}_7]$ .

The composition gradient of the single crystal of  $\text{Pb}_{3-x}\text{Ba}_x[\text{Ge}_2\text{O}_7]$  can be explained by looking at the crystallisation process. While slow crystallisation increases the overall quality of the crystal, it leads to differences in the concentrations between the melt and crystal being grown.<sup>[301–304]</sup> The crystal growth of  $\text{Pb}_{3-x}\text{Ba}_x[\text{Ge}_2\text{O}_7]$  used a relatively small amount of  $\text{BaCO}_3$  (4.993 wt.%), leading to the Ba cations having a low concentration in the melt. However, upon crystallisation of  $\text{Pb}_{3-x}\text{Ba}_x[\text{Ge}_2\text{O}_7]$ , the concentration of Ba cations in the melt increases. This leads to a higher concentration of Ba being brought into the crystal as crystallisation progresses and results in the appearance of a composition gradient along the crystal. This was observed by energy dispersive spectroscopy, where one end of the crystal was practically Ba free,  $\text{Pb}_{2.981(7)}\text{Ba}_{0.019(7)}[\text{Ge}_2\text{O}_7]$ , and Ba content was seen to increase along the crystal, until reaching the highest Ba content at the other end of the crystal,  $\text{Pb}_{2.72(5)}\text{Ba}_{0.28(5)}[\text{Ge}_2\text{O}_7]$  (*Figure 8.15. and Table 8.20.*).

Table 8.23. Comparison of values of  $x$  for  $\text{Pb}_{3-x}\text{Ba}_x[\text{Ge}_2\text{O}_7]$  obtained with different analytical methods.

Expected	Values of $x$		
	Single Crystal	Powder Refinement	Wavelength dispersive spectroscopy
0.21	0.17(5)	0.17	0.19±0.09

Investigations into the effect of Ba content on the phase transition temperature showed the phase transition occurs at a similar temperature as  $\text{Pb}_3[\text{Ge}_2\text{O}_7]$ . However, the measured temperature is slightly lower than that of  $\text{Pb}_3[\text{Ge}_2\text{O}_7]$ . This is attributed to the introduction of Ba, a behaviour that has been previously reported for other lead germanates.

Compounds of  $\text{Pb}_3[\text{Ge}_2\text{O}_7]$  have been previously reported<sup>[323]</sup> however, this is the first occurrence of substitution on the Pb site. This opens up a new field of investigation into determining the precise relationship in the Barysilite structure between Ba content and physical properties, as well as discovering if the upper limit of Ba substitution is in fact  $\text{Pb}_{3-x}\text{Ba}_x[\text{Ge}_2\text{O}_7]$  ( $x = 1$ ).



## 9. Summary & outlook

During this doctoral work a wide range of binary and higher nitride compounds, with increasing complexity, containing late 3d transition metals, were produced and characterised. These ranged from isolated  $N^{3-}$  containing NiAs-type FeN and  $\epsilon$ -Fe<sub>2</sub>MnN to substituted infinite chains of nitridometalate anions,  $[M_xN_y]^{z-}$ , such as SrLi<sub>2</sub>{Li[CoN<sub>2</sub>]} and Sr<sub>2</sub>[(Li<sub>1-x</sub>Ni<sub>x</sub>)Ni<sub>2</sub>N<sub>2</sub>]. In addition, the first nitridocuprate carbodiimide, Sr<sub>6</sub>N[CuN<sub>2</sub>][CN<sub>2</sub>], was also produced, which includes two nitrogen containing anions, the isolated  $N^{3-}$  and [CuN<sub>2</sub>]<sup>5-</sup>.

Utilising elevated pressure and temperature, new iron containing nitrides were produced and characterised. The first, NiAs-type FeN, is the only example of NiAs-type structure in a 3d-metal nitride, at the time of writing, and can be made from either elemental  $\alpha$ -Fe or  $\zeta$ -Fe<sub>2</sub>N. This phase is metastable at ambient conditions and, surprisingly, showed magnetic ordering that is stable to at least 45 GPa. The second iron containing nitride,  $\epsilon$ -Fe<sub>2</sub>MnN, was produced by using pressure to create a substituted phase of  $\epsilon$ -Fe<sub>3</sub>N and extend the series of 3d-transition metals that have been substituted into the  $\epsilon$ -Fe<sub>3</sub>N structure. This phase has the highest thermal stability out of the known 3d-transition metal substituted phases,  $\epsilon$ -Fe<sub>2</sub>MN ( $M = \text{Co, Ni}$ ), and  $\epsilon$ -Fe<sub>3</sub>N. Interestingly, the phase is a soft ferromagnet with an observed magnetic moment that is lower than expected.

A novel substituted nitridometalate, SrLi<sub>2</sub>{Li[CoN<sub>2</sub>]}, was synthesised and is a substituted phase of SrLi<sub>4</sub>N<sub>2</sub>, with Co substituting solely on the  $\frac{1}{\infty}$ [LiN<sub>2/2</sub>]<sup>2-</sup> chains. Originally, the phase was first thought to crystallise in the same space group as SrLi<sub>4</sub>N<sub>2</sub> and other substituted phases,  $I4_1/amd$ . However, after in depth investigation of X-ray diffraction data, the space group was revealed to be lower in symmetry,  $P2_1/c$ , and that there was a preference for ordering of Li and Co along the  $\frac{1}{\infty}$ [(Li,Co)N<sub>2/2</sub>]<sup>2-</sup> nitridometalate chains.

A new Cu containing phase was added to the series Sr<sub>6</sub>N[MN<sub>2</sub>][CN<sub>2</sub>] ( $M = \text{Fe and Co}$ ) and has a very similar crystal structure to the other known phases. The only discernible difference between the Cu containing phase and the others is the orientation of the [CN<sub>2</sub>]<sup>2-</sup> anions. For Sr<sub>6</sub>N[CuN<sub>2</sub>][CN<sub>2</sub>] these anions adopt a ‘criss-crossing’ arrangement, whereas the [CN<sub>2</sub>]<sup>2-</sup> anions for Sr<sub>6</sub>N[MN<sub>2</sub>][CN<sub>2</sub>] ( $M = \text{Fe and Co}$ ) are aligned. This results in Sr<sub>6</sub>N[CuN<sub>2</sub>][CN<sub>2</sub>] and Sr<sub>6</sub>N[MN<sub>2</sub>][CN<sub>2</sub>] ( $M = \text{Fe and Co}$ ) crystallising in different space groups. The cause of this

'criss-crossing' effect still proves elusive, but is thought to be an intrinsic trait of the Cu containing phase.

The rarely reported  $[\text{C}_2\text{N}]^{3-}$  was seen in two Sr containing compounds. The first was a acetonitriletriide carbodiimide,  $\text{Sr}_4\text{N}[\text{CN}_2][\text{C}_2\text{N}]$ , which is comprised of three different anionic components and shows that the  $[\text{C}_2\text{N}]^{3-}$  unit can be formed and stabilised using just three elements. The second compound was the first quasi-binary acetonitriletriide,  $\text{Sr}_3[\text{C}_2\text{N}]_2$ , where the crystal structure is solely comprised of bidisphenoid polyhedra of Sr, which contain  $[\text{C}_2\text{N}]^{3-}$  units. These bidisphenoid polyhedra were observed in both compounds and are perhaps crucial to stabilising the  $[\text{C}_2\text{N}]^{3-}$  anion.

The compounds presented in this thesis highlight the diverse nature of nitrides, as well as the important relationship between the synthetic technique employed and the resultant product. A common theme seen during this research was the importance of pressure and more specifically  $\text{N}_2$  pressure. For example, the NiAs-type FeN was only produced above 10 GPa of  $\text{N}_2$  during the synthesis. A more sensitive relationship was observed for the acetonitriletriide containing compounds,  $\text{Sr}_4\text{N}[\text{CN}_2][\text{C}_2\text{N}]$  and  $\text{Sr}_3[\text{C}_2\text{N}]_2$ , where the only difference in the synthesis of these compounds was the  $\text{N}_2$  pressure within the metal ampoule. This extreme sensitivity is thought to be the prime reason for these compounds having not been discovered sooner and the reason for single phase products not being produced.

Further work needed on each of the compounds reported in this thesis is the optimisation of the synthetic approach for each compound to produce bulk single phase product for further characterisation. These further characterisations would include magnetic property measurements of NiAs-type FeN and the series  $\text{Sr}_2[(\text{Li}_{1-x}\text{Ni}_x)\text{Ni}_2\text{N}_2]$ . A further topic of interest would be to investigate if other alkaline earth metals can be used in the synthesis of the acetonitriletriide containing compounds,  $\text{AE}_3[\text{C}_2\text{N}]_2$  and  $\text{AE}_4\text{N}[\text{CN}_2][\text{C}_2\text{N}]$  ( $\text{AE} = \text{Mg} - \text{Ba}$ ).



## References

- [1] A. F. Hollemann, E. Wiberg, N. Wiberg, *Anorganische Chemie*, De Gruyter, **2017**.
- [2] M. Bykov, E. Bykova, G. Aprilis, K. Glazyrin, E. Koemets, I. Chuvashova, I. Kuppenko, C. McCammon, M. Mezouar, V. Prakapenka, et al., *Nat. Commun.* **2018**, 1–8.
- [3] W. Schnick, *Angew. Chem. Int. Ed.* **1993**, 32, 806–818.
- [4] N. Dubrovinskaia, V. L. Solozhenko, N. Miyajima, V. Dmitriev, O. O. Kurakevych, L. Dubrovinsky, *Appl. Phys. Lett.* **2007**, 90, 38–41.
- [5] M. Hasegawa, T. Yagi, *J. Alloy. Compd.* **2005**, 403, 131–142.
- [6] W. Chen, J. Z. Jiang, *J. Alloy. Compd.* **2010**, 499, 243–254.
- [7] N. Schönberg, *Acta Chem. Scand.* **1954**, 8, 199–203.
- [8] H. A. Wriedt, N. A. Gokcen, R. H. Nafziger, *Bull. Alloy Phase. Diagr.* **1987**, 8, 355–377.
- [9] K. Zhang, Y. Feng, F. Wang, Z. Yang, J. Wang, *J. Mater. Chem. C* **2017**, 5, 11992–12022.
- [10] E. Kroke, A. Zerr, M. Schwarz, R. Boehler, G. Miehe, H. Fueß, P. Kroll, R. Riedel, G. Serghiou, *Nature* **2002**, 400, 340–342.
- [11] E. Zhao, J. Wang, J. Meng, Z. Wu, *Comput. Mater. Sci.* **2010**, 47, 1064–1071.
- [12] C. M. Caskey, R. M. Richards, D. S. Ginley, A. Zakutayev, *Mater. Horiz.* **2014**, 1, 424–430.
- [13] Y. Ito, R. Hagiwara, K. Hachiya, H. Tsujimura, T. Goto, K. Toyoura, *Thin Solid Films* **2005**, 492, 88–92.
- [14] H. M. Kim, Y. H. Cho, H. Lee, S. I. I. Kim, S. R. Ryu, D. Y. Kim, T. W. Kang, K. S. Chung, *Nano Lett.* **2004**, 4, 1059–1062.
- [15] P. Boch, J. C. Glandus, J. Jarrige, J. P. Lecompte, J. Mexmain, *Ceram. Int.* **1982**, 8, 34–40.
- [16] G. Liu, J. Shi, F. Zhang, Z. Chen, J. Han, C. Ding, S. Chen, Z. Wang, H. Han, C. Li, *Angew. Chem. Int. Ed.* **2014**, 53, 7295–7299.
- [17] S. A. Medvedev, I. A. Trojan, M. I. Eremets, T. Palasyuk, T. M. Klapötke, J. Evers, *J. Phy. Condens. Matter* **2009**, 21, 195404.
- [18] V. S. Bhadram, D. Y. Kim, T. a. Strobel, *Chem. Mater.* **2016**, 28, 1616–1620.
- [19] G. Paniconi, Z. Stoeva, H. Doberstein, R. I. Smith, B. L. Gallagher, D. H. Gregory, *Solid State Sci.* **2007**, 9, 907–913.
- [20] N. Schönberg, *Acta Chem. Scand.* **1954**, 8, 204–207.
- [21] A. P. Gazhulina, M. O. Marychev, *J. Solid State Chem.* **2016**, 239, 170–177.
- [22] M. G. Barker, M. J. Begley, P. P. Edwards, D. H. Gregory, S. E. Smith, *J. Chem. Soc., Dalton Trans.* **1996**, 1–5.
- [23] A. F. Young, C. Sanloup, E. Gregoryanz, S. Scandolo, R. J. Hemley, H. K. Mao, *Phys. Rev. Lett.* **2006**, 96, 1–4.

- [24] H. Wang, Q. Li, Y. Li, Y. Xu, T. Cui, A. R. Oganov, Y. Ma, *Phy. Rev. B* **2009**, *79*, 1–4.
- [25] J. C. Crowhurst, A. F. Goncharov, B. Sadigh, J. M. Zaug, D. Aberg, Y. Meng, V. B. Prakapenka, *J. Mater. Res.* **2008**, *23*, 1–5.
- [26] A. F. Young, J. A. Montoya, C. Sanloup, M. Lazzeri, E. Gregoryanz, S. Scandolo, *Phys. Rev. B* **2006**, *73*, 2–5.
- [27] M. Wessel, R. Dronskowski, *Chem. Eur. J.* **2011**, *17*, 2598–2603.
- [28] J. A. Montoya, A. D. Hernandez, C. Sanloup, E. Gregoryanz, S. Scandolo, *Appl. Phys. Lett.* **2007**, *90*, 2005–2008.
- [29] X. Luo, W. Xing, Z. Li, G. Wu, X. Chen, *Phys. Rev. B* **2007**, *75*, 1–8.
- [30] W. Chen, J. S. Tse, J. Z. Jiang, *J. Phys. Condens. Matter* **2010**, *22*.
- [31] M. Bykov, E. Bykova, G. Aprilis, K. Glazyrin, E. Koemets, I. Chuvashova, I. Kuppenko, C. McCammon, M. Mezouar, V. Prakapenka, et al., *Nat. Commun.* **2018**, *9*, 1–8.
- [32] K. Niwa, T. Terabe, D. Kato, S. Takayama, M. Kato, K. Soda, M. Hasegawa, *Inorg. Chem.* **2017**, *56*, 6410–6418.
- [33] K. Niwa, D. Dzivenko, K. Suzuki, R. Riedel, I. Troyan, M. Eremets, M. Hasegawa, *Inorg. Chem.* **2014**, *53*, 697–699.
- [34] F. Kawamura, H. Yusa, T. Taniguchi, *Appl. Phys. Lett.* **2012**, *100*, 2–5.
- [35] J. C. Crowhurst, *Science* **2006**, *311*, 1275–1278.
- [36] S. B. Schneider, R. Frankovsky, W. Schnick, *Inorg. Chem.* **2012**, *51*, 2366–2373.
- [37] S. B. Schneider, R. Frankovsky, W. Schnick, *Angew. Chem. Int. Ed.* **2012**, *51*, 1873–1875.
- [38] S. B. Schneider, M. Seibald, V. L. Deringer, R. P. Stoffel, R. Frankovsky, G. M. Friederichs, H. Laqua, V. Duppel, G. Jeschke, R. Dronskowski, et al., *J. Am. Chem. Soc.* **2013**, *135*, 16668–16679.
- [39] S. B. Schneider, R. Frankovsky, W. Schnick, *Inorg. Chem.* **2012**, *51*, 2366–2373.
- [40] S. B. Schneider, R. Frankovsky, W. Schnick, *Angew. Chem. Int. Ed.* **2012**, *51*, 1873–1875.
- [41] J. Binns, M.-E. Donnelly, M. Peña-Alvarez, M. Wang, E. Gregoryanz, A. Hermann, P. Dalladay-Simpson, R. T. Howie, *J. Phys. Chem. Lett.* **2019**, *10*, 1109–1114.
- [42] G. E. Pringle, D. E. Noakes, *Acta. Crystallogr. B* **1968**, *24*, 262–269.
- [43] U. Müller, *Z. Anorg. Allg. Chem.* **1972**, *392*, 159–166.
- [44] X. Liu, J. George, S. Maintz, R. Dronskowski, *Angew. Chem. Int. Ed.* **2015**, *54*, 1954–1959.
- [45] G. C. Guo, Q. M. Wang, T. C. W. Mak, *J. Chem. Crystallogr.* **1999**, *29*, 561–564.
- [46] P. Nockemann, U. Cremer, U. Ruschewitz, G. Meyer, *Z. Anorg. Allg. Chem.* **2003**, *629*, 2079–2082.
- [47] F. Karau, W. Schnick, *Z. Anorg. Allg. Chem.* **2005**, *631*, 2315–2320.

- [48] C. S. Choi, E. Prince, W. L. Garrett, *Acta Cryst. B* **2002**, *33*, 3536–3537.
- [49] R. Haiges, J. A. Boatz, R. Bau, S. Schneider, T. Schroer, M. Yousufuddin, K. O. Christe, *Angew. Chem. Int. Ed.* **2005**, *44*, 1860–1865.
- [50] D. Williams, B. Pleune, K. Leinenweber, J. Kouvetakis, *J. Solid State Chem.* **2001**, *159*, 244–250.
- [51] U. Berger, W. Schnick, *J. Alloy. Compd.* **1994**, *206*, 179–184.
- [52] M. Becker, M. Jansen, *Acta Crystallogr. C* **2001**, *57*, 347–348.
- [53] G. Baldinozzi, B. Malinowska, M. Rakib, G. Durand, *J. Mater. Chem.* **2002**, *12*, 268–272.
- [54] X. Liu, A. Decker, D. Schmitz, R. Dronskowski, *Z. Anorg. Allg. Chem.* **2000**, *626*, 103–105.
- [55] O. Reckeweg, F. J. DiSalvo, *Z. Anorg. Allg. Chem.* **2003**, *629*, 177–179.
- [56] A. Frank, N. Caro, *Ger. Pat.* **1895**, 88363.
- [57] X. Liu, M. Krott, P. Müller, C. Hu, H. Lueken, R. Dronskowski, *Inorg. Chem.* **2005**, *44*, 3001–3003.
- [58] X. Liu, L. Stork, M. Speldrich, H. Lueken, R. Dronskowski, *Chem. Eur. J.* **2009**, *15*, 1558–1561.
- [59] M. Krott, X. Liu, B. P. T. Fokwa, M. Speldrich, H. Lueken, R. Dronskowski, *Inorg. Chem.* **2007**, *46*, 2204–2207.
- [60] X. Liu, M. A. Wankeu, H. Lueken, R. Dronskowski, *Z. Naturforsch. B* **2005**, *60*, 593–596.
- [61] M. G. Down, M. J. Haley, P. Hubberstey, R. J. Pulham, A. E. Thunder, *J. Chem. Soc., Chem. Commun.* **1978**, 52.
- [62] M. Becker, J. Nuss, M. Jansen, *Z. Naturforsch. B* **2000**, *55*, 383–385.
- [63] M. Jansen, M. Becker, *Z. Anorg. Allg. Chem.* **2000**, 1639–1641.
- [64] K. B. Sterri, C. Besson, A. Houben, P. Jacobs, M. Hoelzel, R. Dronskowski, *New J. Chem.* **2016**, *40*, 10512–10519.
- [65] E. Hennings, H. Schmidt, W. Voigt, *Z. Anorg. Allg. Chem.* **2011**, *637*, 1199–1202.
- [66] O. Reckeweg, A. Schulz, B. Leonard, F. J. DiSalvo, *Z. Naturforsch. B* **2010**, *65*, 528–532.
- [67] H. Nambu, M. Ichikawa, T. Gustafsson, I. Olovsson, *J. Phys. Chem. Solids* **2003**, *64*, 2269–2272.
- [68] T. C. Waddington, *J. Chem. Soc.* **1959**, *0*, 2499–2502.
- [69] C. L. Schmidt, M. Jansen, *Z. Anorg. Allg. Chem.* **2012**, *638*, 275–278.
- [70] F. Jach, S. I. Brückner, A. Ovchinnikov, A. Isaeva, M. Bobnar, M. F. Groh, E. Brunner, P. Höhn, M. Ruck, *Angew. Chem. Int. Ed.* **2017**, *56*, 2919–2922.
- [71] F. Jach, P. Höhn, Y. Prots, M. Ruck, *Eur. J. Inorg. Chem.* **2019**, *2019*, 1207–1211.
- [72] T. A. Strobel, O. O. Kurakevych, D. Y. Kim, Y. Le Godec, W. Crichton, J. Guignard, N.

- Guignot, G. D. Cody, A. R. Oganov, *Inorg. Chem* **2014**, *53*, 7020–7027.
- [73] H.-J. Meyer, *Z. Anorg. Allg. Chem.* **1991**, *593*, 186–192.
- [74] P. Srepusharawoot, A. Blomqvist, C. M. Araújo, R. H. Scheicher, R. Ahuja, *Phys. Rev. B* **2010**, *82*, 1–6.
- [75] A. J. Karttunen, T. F. Fässler, M. Linnolahti, T. A. Pakkanen, *Inorg. Chem.* **2011**, *50*, 1733–1742.
- [76] M. Krings, G. Montana, R. Dronskowski, C. Wickleder, *Chem. Mater.* **2011**, *23*, 1694–1699.
- [77] S. Yuan, Y. Yang, F. Chevire, F. Tessier, X. Zhang, G. Chen, *J. Am. Chem. Soc.* **2010**, *93*, 3052–3055.
- [78] J. Sinko, *Patent-US6139610A*, **1998**.
- [79] M. Kubus, R. Heinicke, M. Ströbele, D. Enseling, T. Jüstel, H. J. Meyer, *Mater. Res. Bull.* **2015**, *62*, 37–41.
- [80] M. Kubus, C. Castro, D. Enseling, T. Jüstel, *Opt. Mater.* **2016**, *59*, 126–129.
- [81] Q. Liu, Y. Liu, G. Dai, L. Tian, J. Xu, G. Zhao, N. Zhang, Y. Fang, *Appl. Surf. Sci.* **2015**, *357*, 745–749.
- [82] M. T. Sougrati, A. Darwiche, X. Liu, A. Mahmoud, R. P. Hermann, S. Jouen, L. Monconduit, R. Dronskowski, L. Stievano, *Angew. Chem. Int. Ed.* **2016**, *55*, 5090–5095.
- [83] A. Eguía-Barrio, E. Castillo-Martínez, X. Liu, R. Dronskowski, M. Armand, T. Rojo, *J. Mater. Chem. A* **2016**, *4*, 1608–1611.
- [84] C. Liu, C. Zhang, H. Fu, X. Nan, G. Cao, *Adv. Energy Mater.* **2017**, *7*, 1601127.
- [85] A. Eguia-Barrio, E. Castillo-Martinez, X. Liu, R. Dronskowski, L. Lezama, M. Armand, T. Rojo, *MRS Adv.* **2017**, *2*, 1165–1176.
- [86] A. Eguia-Barrio, E. Castillo-Martínez, F. Klein, R. Pinedo, L. Lezama, J. Janek, P. Adelhelm, T. Rojo, *J. Power Sources* **2017**, *367*, 130–137.
- [87] A. Gudat, S. Haag, R. Kniep, A. Rabenau, *Z. Naturforsch. B* **2015**, *45*, 111–120.
- [88] R. Niewa, F. R. Wagner, W. Schnelle, O. Hochrein, R. Kniep, *Inorg. Chem.* **2001**, *40*, 5215–5222.
- [89] L. Ren, N. Vii, O. Hochrein, H. Borrmann, È. Kniep, *Z. Anorg. Allg. Chem.* **2001**, *627*, 37–42.
- [90] J. Bendyna, Dissertation, TU Dresden, **2009**.
- [91] R. Juza, W. Sachsze, *Z. Anorg. Chem.* **1945**, *253*, 95–108.
- [92] Z. Stoeva, R. Gomez, D. H. Gregory, G. B. Hix, J. J. Titman, *Dalton Trans.* **2004**, 3093–3097.
- [93] J. B. Ducros, S. Bach, J. P. Pereira-Ramos, P. Willmann, *Electrochem. commun.* **2007**, *9*, 2496–2500.

- [94] M. Widenmeyer, R. Niewa, T. C. Hansen, H. Kohlmann, *Z. Anorg. Allg. Chem.* **2013**, 639, 285–295.
- [95] R. Niewa, D. Zherebtsov, Z. Hu, *Inorg. Chem.* **2003**, 42, 2538–2544.
- [96] A. Tennstedt, C. Röhr, R. Kniep, *Z. Naturforsch. B* **1993**, 48, 1831–1834.
- [97] J. K. Bendyna, P. Höhn, R. Kniep, *Z. Kristallogr.* **2009**, 224, 5–6.
- [98] J. K. Bendyna, P. Höhn, A. Ormeci, W. Schnelle, R. Kniep, *J. Alloy. Compd.* **2009**, 480, 138–140.
- [99] J. Klatyk, R. Kniep, *Z. Kristallogr. - New Cryst. Struct.* **1999**, 214, 445–446.
- [100] J. Klatyk, R. Kniep, *Z. Kristallogr. - New Cryst. Struct.* **1999**, 214, 447–448.
- [101] P. Ehrlich, H. J. Seifert, G. Brauer, *Handbuch Der Präparativen Anorganischen Chemie Vol. 2*, Ferdinand Enke Verlag, Stuttgart, **1978**.
- [102] A. Leineweber, H. Jacobs, S. Hull, *Inorg. Chem.* **2001**, 40, 5818–5822.
- [103] G. Hüttig, *Z. Anorg. Allg. Chem.* **1920**, 109, 162–173.
- [104] C. E. Weir, E. R. Lippincott, A. Van Valkenburg, E. N. Bunting, *J. Res. Natl. Bur. Stand. Sect. A* **1959**, 63A, 55.
- [105] L. C. Ming, W. A. Bassett, *Rev. Sci. Instrum.* **1974**, 45, 1115–1118.
- [106] L. Dubrovinsky, N. Dubrovinskaia, V. B. Prakapenka, A. M. Abakumov, *Nat. Commun.* **2012**, 3, 1163–1167.
- [107] Y. Akahama, H. Kawamura, *High Pressure Res.* **2007**, 27, 473–482.
- [108] A. W. Webb, D. U. Gubser, L. C. Towle, *Rev. Sci. Instrum.* **1976**, 47, 59–62.
- [109] R. Boehler, *Rev. Geophys.* **2000**, 38, 221–245.
- [110] H. Olijnyk, *J. Chem. Phys.* **1990**, 93, 8968–8972.
- [111] H. K. Mao, J. Xu, P. M. Bell, *J. Geophys. Res.* **1986**, 91, 4673.
- [112] R. Boehler, D. Santamaría-Pérez, D. Errandonea, M. Mezouar, *J. Phys. Conf. Ser.* **2008**, 121.
- [113] I. Kupenko, L. Dubrovinsky, N. Dubrovinskaia, C. McCammon, K. Glazyrin, E. Bykova, T. B. Ballaran, R. Sinmyo, A. I. Chumakov, V. Potapkin, et al., *Rev. Sci. Instrum.* **2012**, 83, 124501.
- [114] A. Wosylus, U. Schwarz, L. Akselrud, M. G. Tucker, M. Hanfland, K. Rabia, C. Kuntscher, J. von Appen, R. Dronskowski, D. Rau, et al., *Z. Anorg. Allg. Chem.* **2009**, 635, 1959–1968.
- [115] H. Huppertz, *Z. Anorg. Allg. Chem.* **2004**, 219, 330–338.
- [116] D. C. Rubie, *Phase Transit.* **1999**, 68, 431–451.
- [117] M. Ladd, R. Palmer, in *Structure Determination by X-Ray Crystallography*, Springer US, Boston, MA, **2013**.

- [118] L. Spieß, G. Teichert, R. Schwarzer, H. Behnken, C. Genzel, *Moderne Röntgenbeugung*, Vieweg+Teubner, Wiesbaden, **2009**.
- [119] G. M. Sheldrick, Program SHELX-97, **1997**.
- [120] Stoe & Cie GmbH, Program X-RED 32, **2005**.
- [121] Stoe & Cie GmbH, Program X-STEP 32, **2000**.
- [122] Stoe & Cie GmbH, Program X-SHAPE 32, **1999**.
- [123] W. Massa, *Crystal Structure Determination*, Springer Berlin Heidelberg, Berlin, Heidelberg, **2004**.
- [124] Stoe & Cie GmbH, Program WINXPOW, **2001**.
- [125] Fullprof Team, Program Fullprof Suite, **2011**.
- [126] H. M. Rietveld, *J. Appl. Crystallogr.* **1969**, 2, 65–71.
- [127] L. B. McCusker, R. B. Von Dreele, D. E. Cox, D. Louër, P. Scardi, *J. Appl. Crystallogr.* **1999**, 32, 36–50.
- [128] V. Potapkin, A. I. Chumakov, G. V. Smirnov, J. P. Celse, R. Rüffer, C. McCammon, L. Dubrovinsky, *J. Synchrotron Radiat.* **2012**, 19, 559–569.
- [129] L. C. Berthollet, L. J. Thénard, *Traite de Chimie* **1834**, 1, 435.
- [130] O. Silvestri, *Pogg. Ann. Chem.* **1867**, 157, 165–172.
- [131] K. Suzuki, H. Morita, T. Kaneko, H. Yoshida, H. Fujimori, *J. Alloys Compd.* **1993**, 201, 11–16.
- [132] J. M. D. Coey, P. A. I. Smith, *J. Magn. Magn. Mater.* **1999**, 200, 405–424.
- [133] B. C. Frazer, *Phys. Rev.* **1958**, 112, 751–754.
- [134] I. Dirba, C. A. Schwöbel, L. V. B. Diop, M. Duerrschnabel, L. Molina-Luna, K. Hofmann, P. Komissinskiy, H.-J. Kleebe, O. Gutfleisch, *Acta Mater.* **2017**, 123, 214–222.
- [135] A. Leineweber, H. Jacobs, F. Hüning, H. Lueken, H. Schilder, W. Kockelmann, *J. Alloys Compd.* **1999**, 288, 79–87.
- [136] Z. Yang, S. Guo, X. Pan, J. Wang, X. Bao, *Energ. Environ. Sci.* **2011**, 4, 4500.
- [137] Y. Namiki, S. Matsunuma, T. Inoue, S. Koido, A. Tsubota, Y. Kuse, N. T, in *Nanocrystal*, InTech, **2011**.
- [138] K. H. Jack, *Proc. Royal Soc. Lond. A* **1948**, 195, 41–55.
- [139] K. H. Jack, *Acta Crystallogr.* **1952**, 5, 404–411.
- [140] K. H. Jack, *Proc. Royal Soc. Lond. A* **1951**, 208, 200–215.
- [141] A. Leineweber, H. Jacobs, F. Hüning, H. Lueken, W. Kockelmann, *J. Alloy. Compd.* **2001**, 316, 21–38.
- [142] B. J. Kooi, M. A. J. Somers, E. J. Mittemeijer, *Metall. Mater. Trans. A* **1996**, 27, 1063–1071.

- [143] M. Widenmeyer, T. C. Hansen, R. Niewa, *Z. Anorg. Allg. Chem.* **2013**, 639, 2851–2859.
- [144] M. Widenmeyer, L. Shlyk, A. Senyshyn, R. Mönig, R. Niewa, *Z. Anorg. Allg. Chem.* **2015**, 641, 348–354.
- [145] R. Niewa, D. Rau, A. Wosylus, K. Meier, M. Hanfland, M. Wessel, R. Dronskowski, D. Dzivenko, R. Riedel, U. Schwarz, *Chem. Mater.* **2009**, 21, 392–398.
- [146] J. F. Adler, Q. Williams, *J. Geophys. Res. B* **2005**, 110, 1–11.
- [147] S. Minobe, Y. Nakajima, K. Hirose, Y. Ohishi, *Geophys. Res. Lett.* **2015**, 3, 1–6.
- [148] D. Laniel, A. Dewaele, G. Garbarino, *Inorg. Chem.* **2018**, 57, 6245–6251.
- [149] R. Niewa, D. Rau, A. Wosylus, K. Meier, M. Wessel, M. Hanfland, R. Dronskowski, U. Schwarz, *J. Alloy. Compd.* **2009**, 480, 76–80.
- [150] K. Guo, D. Rau, J. von Appen, Y. Prots, W. Schnelle, R. Dronskowski, R. Niewa, U. Schwarz, *High Pressure Res.* **2013**, 33, 684–696.
- [151] H. Jacobs, J. Bock, *J. Less-Common Met.* **1987**, 134, 215–220.
- [152] H. Jacobs, D. Rechenbach, U. Zachwieja, *J. Alloys Compd.* **1995**, 227, 10–17.
- [153] U. Schwarz, A. Wosylus, M. Wessel, R. Dronskowski, M. Hanfland, D. Rau, R. Niewa, *Eur. J. Inorg. Chem.* **2009**, 2009, 1634–1639.
- [154] D. M. Borsa, D. O. Boerma, *Hyperfine Interact.* **2003**, 151–152, 31–48.
- [155] E. Andrzejewska, R. Gonzalez-Arrabal, D. Borsa, D. O. Boerma, *Nucl. Instrum. Methods Phys. Res. B* **2006**, 249, 838–842.
- [156] I. Jouanny, P. Weisbecker, V. Demange, M. Grafoute, O. Pena, E. Bauer-Grosse, *Thin Solid Films* **2010**, 518, 1883–1891.
- [157] H. Shimizu, M. Shirai, N. Suzuki, *J. Phys. Soc. Jpn.* **1998**, 67, 922–926.
- [158] A. Filippetti, W. E. Pickett, *Phys. Rev. B* **1999**, 59, 8397–8400.
- [159] A. Houari, S. F. Matar, M. A. Belkhir, M. Nakhl, *Phys. Rev. B* **2007**, 75, 1–6.
- [160] Y. Kong, *J. Phys. Condens. Matter* **2000**, 12, 4161–4173.
- [161] B. Eck, R. Dronskowski, M. Takahashi, S. Kikkawa, *J. Mater. Chem.* **1999**, 9, 1527–1537.
- [162] P. Lukashev, W. R. L. Lambrecht, *Phys. Rev. B* **2004**, 70, 1–8.
- [163] A. Kartsev, N. Bondarenko, *Thermodynamic Properties of NiAs-FeN Phase from First Principles [Abstract]*, SMMS2015, Chiang Mai, Thailand, **2015**.
- [164] G. V Vajenine, G. Auffermann, Y. Prots, W. Schnelle, R. K. Kremer, A. Simon, *Inorg. Chem.* **2001**, 4866–4870.
- [165] G. Auffermann, Y. Prots, R. Kniep, *Angew. Chem. Int. Ed.* **2001**, 40, 547–549.
- [166] E. Gregoryanz, C. Sanloup, M. Somayazulu, J. Badro, G. Fiquet, H.-K. Mao, R. J. Hemley, *Nat. Mater.* **2004**, 3, 294–7.

- [167] R. D. Taylor, M. P. Pasternak, R. Jeanloz, *J. Appl. Phys.* **1991**, *69*, 6126–6128.
- [168] D. Bancroft, E. L. Peterson, S. Minshall, *J. Appl. Phys.* **1956**, *27*, 291–298.
- [169] P. M. Giles, M. H. Longenbach, A. R. Marder, *J. Appl. Phys.* **1971**, *42*, 4290–4295.
- [170] Q. Williams, R. Jeanloz, J. Bass, B. Svendsen, T. J. Ahrens, *Science* **1987**, *236*, 181–182.
- [171] V. Ksenofontov, S. Reiman, M. Waldeck, R. Niewa, R. Kniep, P. Gütlich, *Z. Anorg. Allg. Chem.* **2003**, *629*, 1787–1794.
- [172] M. Widenmeyer, T. C. Hansen, E. Meissner, R. Niewa, *Z. Anorg. Allg. Chem.* **2014**, *640*, 1265–1274.
- [173] D. Rechenbach, H. Jacobs, *J. Alloys Compd.* **1996**, *235*, 15–22.
- [174] A. F. Wells, *Structural Inorganic Chemistry*, **1962**.
- [175] C. Ravi, *Calphad* **2009**, *33*, 469–477.
- [176] E. Zhao, J. Wang, Z. Wu, *Phys. Status Solidi B* **2010**, *247*, 1207–1213.
- [177] N. Terao, *J. Less-Common Met.* **1971**, *23*, 159–169.
- [178] J. C. Fontbonne, A. Gilles, *Rev. Int. Hautes Temp.* **1969**, 181–192.
- [179] T. Takahashi, W. A. Bassett, H.-K. Mao, *J. Geophys. Res.* **1968**, *73*, 4717–4725.
- [180] N. Alsén, *Geol. Foren. Stock. For.* **1925**, *47*, 19–72.
- [181] M. Onoda, H. Wada, *J. Less-Common Met.* **1987**, *132*, 195–207.
- [182] N. Schönberg, W. G. Overend, A. Munthe-Kaas, N. A. Sørensen, *Acta Chem. Scand.* **1954**, *8*, 226–239.
- [183] C. Prescher, C. McCammon, L. Dubrovinsky, *J. Appl. Crystallogr.* **2012**, *45*, 329–331.
- [184] R. Dronskowski, P. E. Bloechl, *J. Phys. Chem.* **1993**, *97*, 8617–8624.
- [185] G. A. Landrum, R. Dronskowski, *Angew. Chem. Int. Ed.* **2000**, *39*, 1560–1585.
- [186] B. Cordero, V. Gómez, A. E. Platero-Prats, M. Revés, J. Echeverría, E. Cremades, F. Barragán, S. Alvarez, *Dalton Trans.* **2008**, 2832.
- [187] R. D. Shannon, C. T. Prewitt, *J. Inorg. Nucl. Chem.* **1970**, *32*, 1427–1441.
- [188] R. Dronskowski, *Computational Chemistry of Solid State Materials*, Wiley-VCH Verlag GmbH & Co. KGaA, Weinheim, Germany, **2005**.
- [189] D. Laniel, A. Dewaele, S. Anzellini, N. Guignot, *J. Alloys Compd.* **2018**, *733*, 53–58.
- [190] S. Li, X. Cui, Z.-F. Liu, T.-L. Song, *J. Alloys Compd.* **2019**, *771*, 322–326.
- [191] A. Kartsev, O. D. Feyta, N. Bondarenko, A. G. Kvashnin, *Physical Chemistry Chemical Physics* **2019**, *21*, 5262–5273.
- [192] C. Scott, S. Allain, M. Faral, N. Guelton, *Rev. Metall. Paris* **2006**, *103*, 293–302.
- [193] J. E. Jin, Y. K. Lee, *Mater. Sci. Eng. A* **2009**, *527*, 157–161.
- [194] A. Saeed-Akbari, J. Imlau, U. Prahl, W. Bleck, *Metall. Mater. Trans. A* **2009**, *40*, 3076–3090.



- [195] A. S. Hamada, L. P. Karjalainen, M. C. Somani, *Mater. Sci. Eng. A* **2007**, *467*, 114–124.
- [196] O. Grässel, L. Krüger, G. Frommeyer, L. W. Meyer, *Int. J. Plast.* **2000**, *16*, 1391–1409.
- [197] D. Xue, F. Li, J. Yang, Y. Kong, M. Gao, *J. Magn. Magn. Mater.* **1997**, *172*, 165–172.
- [198] C. A. Kuhnen, R. S. De Figueiredo, A. V. Dos Santos, *J. Magn. Magn. Mater.* **2000**, *219*, 58–68.
- [199] A. Houben, P. Müller, J. Von Appen, H. Lueken, R. Niewa, R. Dronskowski, *Angew. Chem. Int. Ed.* **2005**, *44*, 7212–7215.
- [200] A. Houben, J. Burghaus, R. Dronskowski, *Chem. Mater.* **2009**, *21*, 4332–4338.
- [201] N. S. Gajbhiye, R. S. Ningthoujam, S. Bhattacharyya, *Hyperfine Interact.* **2006**, *164*, 17–26.
- [202] N. S. Gajbhiye, S. Bhattacharyya, *Mater. Chem. Phys.* **2008**, *108*, 201–207.
- [203] N. S. Gajbhiye, S. Bhattacharyya, S. Sharma, *Pram. J. Phys.* **2008**, *70*, 367–373.
- [204] P. P. Mishra, M. M. Raja, R. N. Panda, *Mater. Res. Bull.* **2016**, *75*, 127–133.
- [205] K. Guo, D. Rau, L. Toffoletti, C. Müller, U. Burkhardt, W. Schnelle, R. Niewa, U. Schwarz, *Chem. Mater.* **2012**, *24*, 4600–4606.
- [206] K. Guo, D. Rau, W. Schnelle, U. Burkhardt, R. Niewa, U. Schwarz, *Z. Anorg. Allg. Chem.* **2014**, *640*, 814–818.
- [207] Y. S. Zhao, M. Wang, Y. Q. Ma, *J. Mater. Sci. Mater. Electron.* **2018**, *29*, 20071–20080.
- [208] X. Lei, Z. Ye, Y. Qie, Z. Fan, X. Chen, Z. Shi, H. Yang, *J. Mater. Sci. Mater. Electron.* **2019**, *30*, 277–283.
- [209] H. Jacobs, C. Stüve, *J. Less-Common Met.* **1984**, *96*, 323–329.
- [210] A. Leineweber, R. Niewa, H. Jacobs, W. Kockelmann, *J. Mater. Chem.* **2000**, *10*, 2827–2834.
- [211] W. Sachsze, R. Juza, *Z. Anorg. Chem.* **1949**, *259*, 278–290.
- [212] L. Pauling, *Phys. Rev.* **1938**, *54*, 899–904.
- [213] J. C. Slater, *J. Appl. Phys.* **1937**, *8*, 385–390.
- [214] E. A. Brandes, G. B. Brook, *Smithells Metals Reference Book*, **1997**.
- [215] E. Oberg, F. D. Jones, H. L. Horton, H. H. Ryffel, *Machinery's Handbook*, **2008**.
- [216] T. Weber, L. de Wit, F. W. Saris, A. Königer, B. Rauschenbach, G. K. Wolf, S. Krauss, *Mater. Sci. Eng. A* **1995**, *199*, 205–210.
- [217] M. Guemmaz, A. Mosser, J.-J. Grob, R. Stuck, *Surf. Coat. Technol.* **1998**, *100–101*, 353–357.
- [218] D. H. Gregory, *Chem. Rec.* **2008**, *8*, 229–239.
- [219] A. Rabenau, *Solid State Ionics* **1982**, *6*, 277–293.
- [220] R. Kniep, *Pure Appl. Chem.* **1997**, *69*, 185–191.
- [221] R. Niewa, H. Jacobs, *Chem. Rev.* **1996**, *96*, 2053–2062.
- [222] F. J. DiSalvo, S. J. Clarke, *Curr. Opin. Solid State Mater. Sci.* **1996**, *1*, 241–249.

- [223] R. Dronskowski, S. Kikkawa, A. Stein, *Handbook of Solid State Chemistry*, Wiley-VCH Verlag GmbH & Co. KGaA, Weinheim, Germany, **2017**.
- [224] A. Rabenau, H. Schulz, *J. Alloy. Compd.* **1976**, *50*, 155–159.
- [225] G. Cordier, A. Gudat, R. Kniep, A. Rabenau, *Angew. Chem. Int. Ed.* **1989**, *28*, 1702–1703.
- [226] A. Mehta, P. Höhn, W. Schnelle, V. Petzold, H. Rosner, U. Burkhardt, R. Kniep, *Chem. Eur. J.* **2006**, *12*, 1667–1676.
- [227] R. Niewa, F. DiSalvo, D. Yang, D. Zax, H. Luo, W. Yelon, *J. Alloy. Compd.* **1998**, *266*, 32–38.
- [228] A. Yamada, S. Matsumoto, Y. Nakamura, *J. Mater. Chem.* **2011**, *21*, 10021–10025.
- [229] M. Nishijima, *Solid State Ionics* **1996**, *83*, 107–111.
- [230] A. Ovchinnikov, P. Höhn, H. Borrmann, M. Kazancioğlu, R. Kniep, *Z. Kristallogr.* **2015**, *230*, 3–4.
- [231] Z. Stoeva, R. I. Smith, D. H. Gregory, *Chem. Mater.* **2006**, *18*, 313–320.
- [232] S. Bach, J. P. Pereira-Ramos, J. B. Ducros, P. Willmann, *Solid State Ionics* **2009**, *180*, 231–235.
- [233] J. Klatyk, R. Kniep, *Z. Kristallogr. - New Cryst. Struct.* **1999**, *214*, 449–450.
- [234] A. Gudat, R. Kniep, A. Rabenau, *Thermochim. Acta* **1990**, *160*, 49–56.
- [235] J. Jäger, R. Kniep, *Z. Naturforsch., B: Chem. Sci.* **1992**, *47*, 1290–1296.
- [236] P. Höhn, R. Kniep, *Z. Naturforsch. B* **1992**, *47*, 434–436.
- [237] A. Gudat, R. Kniep, A. Rabenau, *Z. Anorg. Allg. Chem.* **1991**, *597*, 61–67.
- [238] D. H. Gregory, P. M. O’Meara, A. G. Gordon, J. P. Hodges, S. Short, J. D. Jorgensen, *Chem. Mater.* **2002**, *14*, 2063–2070.
- [239] A. G. Gordon, D. H. Gregory, A. J. Blake, D. P. Weston, M. O. Jones, *Int. J. Inorg. Mater.* **2001**, *3*, 973–981.
- [240] D. H. Gregory, P. M. O. Meara, A. G. Gordon, D. J. Siddons, A. J. Blake, M. G. Barker, T. A. Hamor, P. P. Edwards, *J. Alloy. Compd.* **2001**, *318*, 237–244.
- [241] J. B. Ducros, S. Bach, J. P. Pereira-Ramos, P. Willmann, *J. Power Sources* **2008**, *175*, 517–525.
- [242] A. L. Spek, Program PLATON, **2006**.
- [243] H. Bärnighausen, *MATCH Commun. Math. Comput. Chem.* **1980**, *9*, 139–175.
- [244] T. Nishizawa, K. Ishida, *Bull. Alloy Phase Diagr.* **1983**, *4*, 387–390.
- [245] R. Niewa, Z.-L. Huang, W. Schnelle, Z. Hu, R. Kniep, *Z. Anorg. Allg. Chem.* **2003**, *629*, 1778–1786.
- [246] A. Gudat, R. Kniep, A. Rabenau, *Z. Anorg. Allg. Chem.* **1992**, *607*, 8–12.

- [247] G. V. Vajenine, A. Grzechnik, K. Syassen, I. Loa, M. Hanfland, A. Simon, *C. R. Chimie* **2005**, *8*, 1897–1905.
- [248] O. Reckeweg, F. J. DiSalvo, *Z. Anorg. Allg. Chem.* **2001**, *627*, 371–377.
- [249] M. B. Robin, P. Day, *Advances in Inorganic Chemistry and Radiochemistry*, Academic Press Inc., Cambridge, **1967**.
- [250] S. Van Houten, *J. Phys. Chem. Solids* **1960**, *17*, 7–17.
- [251] X. Liu, P. Müller, P. Kroll, R. Dronskowski, *Inorg. Chem.* **2002**, *41*, 4259–4265.
- [252] X. Tang, H. Xiang, X. Liu, M. Speldrich, R. Dronskowski, *Angew. Chem. Int. Ed.* **2010**, *49*, 4738–4742.
- [253] U. Berger, W. Milius, W. Schnick, *Z. Anorg. Allg. Chem.* **1995**, *621*, 2075–2082.
- [254] O. Reckeweg, F. J. DiSalvo, *Angew. Chem. Int. Ed.* **2000**, *39*, 412–414.
- [255] Z. A. Gál, P. M. Mallinson, S. J. Clarke, *Acta Crystallogr. E* **2005**, *61*, i221–i222.
- [256] M. Becker, M. Jansen, *J. Chem. Res.* **1998**, 86–87.
- [257] M. Becker, M. Jansen, A. Lieb, W. Milius, W. Schnick, *Z. Anorg. Allg. Chem.* **1998**, *624*, 113–118.
- [258] R. Niewa, P. Höhn, R. Kniep, A. Weiske, H. Jacobs, *Z. Kristallogr. - New Cryst. Struct.* **2001**, *216*, 357–358.
- [259] J. K. Bendyna, P. Höhn, W. Schnelle, R. Kniep, *Sci. Technol. Adv. Mater.* **2007**, *8*, 393–398.
- [260] A. J. Corkett, P. M. Konze, R. Dronskowski, *Z. Anorg. Allg. Chem.* **2017**, *643*, 1456–1461.
- [261] O. Reckeweg, F. J. DiSalvo, *Z. Naturforsch. B* **2008**, *63*, 530–536.
- [262] P. Höhn, R. Kniep, *Z. Anorg. Allg. Chem.* **2002**, *628*, 2173.
- [263] O. Reckeweg, F. J. DiSalvo, *Z. Naturforsch. B* **2003**, *58*, 201–204.
- [264] R. Niewa, F. J. DiSalvo, *J. Alloy. Compd.* **1998**, *279*, 153–160.
- [265] J. Nyvlt, *Cryst. Res. Technol.* **1995**, *30*, 443–449.
- [266] C. E. Shannon, W. Weaver, *The Mathematical Theory of Communication*, Univ. of Illinois Press, **1963**.
- [267] S. V. Krivovichev, *Angew. Chem. Int. Ed.* **2014**, *53*, 654–661.
- [268] J. F. Cordes, *Z. Naturforsch. B* **1958**, 622–623.
- [269] T. M. Klapötke, *Angew. Chem. Int. Ed.* **1994**, *33*, 1575–1576.
- [270] R. West, G. A. Gornowicz, *J. Am. Chem. Soc.* **2005**, *93*, 1714–1720.
- [271] W. Zarges, M. Marsch, K. Harms, *Chem. Ber.* **1989**, *2*, 1307–1311.
- [272] M. Haeberlen, J. Glaser, H.-J. Meyer, *Z. Anorg. Allg. Chem.* **2002**, *628*, 1959–1962.
- [273] M. Würle, H. Meyer zu Altenschildesche, R. Nesper, *J. Alloys Compd.* **1998**, *264*, 107–114.
- [274] A. Simon, K. Peters, *Acta Crystallogr. B* **1980**, *36*, 2750–2751.

- [275] M. I. Eremets, M. Y. Popov, I. A. Trojan, V. N. Denisov, R. Boehler, R. J. Hemley, *J. Chem. Phys.* **2004**, *120*, 10618–10623.
- [276] T. V Blankenship, A. Lita, S. E. Lattturner, *Inorg. Chem.* **2012**, *51*, 13345–13350.
- [277] M. Somer, W. Carrillo-cabrera, A. Zu, U. Herterich, C. Jan, K. Peters, G. Von Schnering, N. Ternary, N. B. N. Anion, *Z. Anorg. Allg. Chem.* **2000**, *626*, 625–633.
- [278] J. F. Sullivan, S. K. Nandy, M. J. Lee, J. R. Durig, *J. Raman Spectrosc.* **1992**, *23*, 51–60.
- [279] O. Reckeweg, A. Schulz, F. J. DiSalvo, *Z. Naturforsch.* **2010**, *65b*, 1409–1415.
- [280] B. Jürgens, E. Irran, W. Schnick, *J. Solid State Chem.* **2001**, *157*, 241–249.
- [281] P. Höhn, F. Jach, B. Karabiyik, Y. Prots, S. Agrestini, F. R. Wagner, M. Ruck, L. H. Tjeng, R. Kniep, *Angew. Chem. Int. Ed.* **2011**, *50*, 9361–9364.
- [282] P. Höhn, M. Armbrüster, G. Auffermann, U. Burkhardt, F. Haarmann, A. Mehta, R. Kniep, *Z. Anorg. Allg. Chem.* **2006**, *632*, 2129–2129.
- [283] A. A. Bush, Y. N. Venevstev, *NIITEKhIM* **1981**.
- [284] G. R. Jones, N. Shaw, A. W. Vere, *Electron. Lett.* **1972**, *8*, 345.
- [285] R. Watton, C. Smith, G. R. Jones, *Ferroelectr.* **1976**, *14*, 719–721.
- [286] T. Li, S. T. Hsu, *Integr. Ferroelectr.* **2001**, *34*, 55–63.
- [287] S. Mendricks, X. Yue, R. Pankrath, H. Hesse, D. Kip, *Appl. Phys. B* **1999**, *68*, 887–891.
- [288] H. J. Reyher, N. Hausfeld, M. Pape, K. T. Stevens, L. E. Halliburton, S. D. Setzler, M. A. Laruhin, H. J. Van Es, *J. Phys. Condens. Matter* **2001**, *13*, 3767–3778.
- [289] M. I. Kay, R. E. Newnham, R. W. Wolfe, *Ferroelectr.* **1975**, *9*, 1–6.
- [290] H. Iwasaki, K. Sugii, T. Yamada, N. Niizeki, *Appl. Phys. Lett.* **1971**, *18*, 444–445.
- [291] J. P. Dougherty, E. Sawaguchi, L. E. Cross, *Appl. Phys. Lett.* **1972**, *20*, 364–365.
- [292] G. R. Barsch, L. J. Bonczar, R. E. Newnham, *Phys. Status Solidi A* **1975**, *29*, 241–250.
- [293] H. Iwasaki, T. Yamada, N. Niizeki, H. Toyoda, H. Kubota, *Jpn. J. Appl. Phys.* **1968**, *7*, 185–186.
- [294] T. Yamada, H. Iwasaki, N. Niizeki, *J. Appl. Phys.* **1970**, *41*, 4141–4147.
- [295] W. Królikowski, M. Cronin-Golomb, B. S. Chen, *Appl. Phys. Lett.* **1990**, *57*, 7–9.
- [296] X. Yue, S. Mendricks, Y. Hu, H. Hesse, D. Kip, *J. Appl. Phys.* **1998**, *83*, 3473.
- [297] X. F. Yue, S. Mendricks, T. Nikolajsen, H. Hesse, D. Kip, E. Kratzig, *J. Opt. Soc. Am. B* **1999**, *16*, 389–394.
- [298] A. V Stepanov, A. A. Bush, K. E. Kamentsev, *Inorg. Mater.* **2017**, *53*, 744–750.
- [299] R. N. P. Choudhary, N. K. Misra, *J. Phys. Chem. Solids* **1998**, *59*, 605–610.
- [300] V. D. Salnikov, S. Y. Stephanovitch, V. V. Chetchkin, M. V. Pentegova, Y. Y. Tomashpolskii, Y. N. Venevtsev, *Ferroelectr.* **1974**, *8*, 491–493.

- [301] J. A. Burton, R. C. Prim, W. P. Slichter, *J. Chem. Phys.* **1953**, *21*, 1987–1991.
- [302] R. H. McFee, *J. Chem. Phys.* **1947**, *15*, 856–861.
- [303] H. Neumann, J. Mead, C. J. Vitaliano, *Geochim. Cosmochim. Acta* **1954**, *6*, 90–99.
- [304] W. G. Pfann, *JOM* **1952**, *4*, 747–753.
- [305] W. Eysel, R. W. Wolfe, R. E. Newnham, *J. Am. Ceram.* **1973**, *56*, 185.
- [306] S. Y. Stefanovich, V. V Chechkin, V. D. Sal'nikov, Y. N. Venevstev, *Kristallografiya* **1976**, *21*, 540.
- [307] A. G. Belous, V. V Dem'yanov, Y. N. Venevstev, *Fiz. Tverd. Tela* **1977**, *19*, 1694.
- [308] W. Muller-Lierhein, W. Gebhardt, H. H. Otto, G. Busse, *Ferroelectr.* **1978**, *20*, 299.
- [309] E. V Sinyakov, V. V Gene, A. Y. Krøecherek, *Fiz. Tverd. Tela* **1979**, *21*, 1223.
- [310] M. Polomska, M. Malinowski, H. H. Otto, *Phys. Status Solidi A* **1979**, *56*, 335.
- [311] A. A. Bush, Y. N. Venevstev, *Kristallografiya* **1981**, *26*, 349.
- [312] A. A. Bush, E. A. Popova, *Fiz. Tverd. Tela* **2004**, *46*, 875.
- [313] K. Takahashi, S. Shirasaki, K. Takamatsu, N. Kobayasm, Y. Mitarai, K. Kakegawa, *Jpn. J. Appl. Phys.* **1983**, *22*, 73.
- [314] N. K. Misra, R. Sati, R. N. P. Choudhary, *Ferroelectr.* **1996**, *189*, 39–42.
- [315] W. Petter, A. B. Harnik, U. Keppler, A. B. Harnik, U. Keppler, *Z. Kristallogr.* **1971**, *133*, 445–458.
- [316] H. Strunz, E. H. Nickel, *Strunz Mineralogical Tables*, **2001**.
- [317] P. J. Lajzerowicz, *Acta Crystallogr.* **1965**, *20*, 357–363.
- [318] J. Ito, C. Frondel, *Am. Mineral.* **1967**, *52*, 1077–1084.
- [319] U. Kolitsch, D. Holtstam, *Mineral. Mag.* **2002**, *66*, 353–363.
- [320] J. Ito, C. Frondel, *Am. Mineral.* **1967**, *52*, 1077–1084.
- [321] H. W. Billhardt, *Am. Mineral.* **1969**, *54*, 510–521.
- [322] W. Gerlach, *Z. Phys.* **1922**, *9*, 184–192.
- [323] H. H. Otto, *J. Appl. Crystallogr.* **1983**, *16*, 430.



## Appendix

### A– Crystallographic data for the series $\text{Sr}_2[(\text{Li}_{1-x}\text{Ni}_x)\text{Ni}_2\text{N}_2]$

Table A.1. Atomic positions and occupations for the refinement of  $\text{Sr}_2[(\text{Li}_{1-x}\text{Ni}_x)\text{Ni}_2\text{N}_2]$ .

Sample A $x = 0.032(2)$	Wyckoff Position	$x/a$	$y/b$	$z/c$	Occupation	$U_{eq}$
Sr(1)	8 <i>f</i>	0	0.16336(6)	0.09708(7)	1	0.0151(3)
Li(1)/Ni(1)	4 <i>b</i>	0	$\frac{1}{2}$	0	0.968/0.0323(7)	0.024(4)
Ni(2)	8 <i>e</i>	$\frac{1}{4}$	0.41038(8)	$\frac{1}{4}$	1	0.0131(3)
N(1)	8 <i>f</i>	0	0.4130(5)	0.2503(7)	1	0.014(1)
Sample B $x = 0.038(2)$	Wyckoff Position	$x/a$	$y/b$	$z/c$	Occupation	$U_{eq}$
Sr(1)	8 <i>f</i>	0	0.16341(7)	0.09714(8)	1	0.0188(3)
Li(1)/Ni(1)	4 <i>b</i>	0	$\frac{1}{2}$	0	0.962/0.038(7)	0.031(5)
Ni(2)	8 <i>e</i>	$\frac{1}{4}$	0.41038(9)	$\frac{1}{4}$	1	0.0169(3)
N(1)	8 <i>f</i>	0	0.4133(6)	0.2504(8)	1	0.019(1)
Sample C $x = 0.080(1)$	Wyckoff Position	$x/a$	$y/b$	$z/c$	Occupation	$U_{eq}$
Sr(1)	8 <i>f</i>	0	0.16381(4)	0.09702(5)	1	0.0169(2)
Li(1)/Ni(1)	4 <i>b</i>	0	$\frac{1}{2}$	0	0.920/0.080(2)	0.024(2)
Ni(2)	8 <i>e</i>	$\frac{1}{4}$	0.41084(5)	$\frac{1}{4}$	1	0.0150(2)
N(1)	8 <i>f</i>	0	0.4136(4)	0.2504(5)	1	0.0161(9)
Sample D $x = 0.127(1)$	Wyckoff Position	$x/a$	$y/b$	$z/c$	Occupation	$U_{eq}$
Sr(1)	8 <i>f</i>	0	0.16397(4)	0.09676(5)	1	0.0156(2)
Li(1)/Ni(1)	4 <i>b</i>	0	$\frac{1}{2}$	0	0.873/0.127(5)	0.024(2)
Ni(2)	8 <i>e</i>	$\frac{1}{4}$	0.41117(5)	$\frac{1}{4}$	1	0.0133(2)
N(1)	8 <i>f</i>	0	0.4135(4)	0.2512(5)	1	0.0147(9)
Sample E $x = 0.132(2)$	Wyckoff Position	$x/a$	$y/b$	$z/c$	Occupation	$U_{eq}$
Sr(1)	8 <i>f</i>	0	0.16387(5)	0.09674(7)	1	0.0143(3)
Li(1)/Ni(1)	4 <i>b</i>	0	$\frac{1}{2}$	0	0.868/0.132(7)	0.024(2)
Ni(2)	8 <i>e</i>	$\frac{1}{4}$	0.41102(6)	$\frac{1}{4}$	1	0.0124(3)
N(1)	8 <i>f</i>	0	0.4140(4)	0.2510(6)	1	0.013(1)

Table A.2. Anisotropic displacement parameters for the refinement of  $\text{Sr}_2[(\text{Li}_{1-x}\text{Ni}_x)\text{Ni}_2\text{N}_2]$ .

Sample A $x = 0.032(2)$	$U_{11}$	$U_{22}$	$U_{33}$	$U_{23}$	$U_{13}$	$U_{12}$	$U_{eq}$
Sr(1)	0.0165(4)	0.0137(4)	0.0147(4)	-0.0008(2)	0	0	0.0151(3)
Li(1)/Ni(1)	0.021(7)	0.020(7)	0.031(7)	0.001(5)	0	0	0.024(4)
Ni(2)	0.0084(4)	0.0157(5)	0.0148(4)	0	-0.0001(3)	0	0.0131(3)
N(1)	0.015(3)	0.016(3)	0.011(2)	-0.000(2)	0	0	0.014(1)
Sample B $x = 0.038(2)$	$U_{11}$	$U_{22}$	$U_{33}$	$U_{23}$	$U_{13}$	$U_{12}$	$U_{eq}$
Sr(1)	0.0187(4)	0.0195(4)	0.0181(4)	-0.0003(3)	0	0	0.0188(3)
Li(1)/Ni(1)	0.035(8)	0.021(7)	0.037(8)	0.004(6)	0	0	0.031(5)
Ni(2)	0.0107(5)	0.0218(6)	0.0183(5)	0	0.0001(4)	0	0.0169(3)
N(1)	0.019(3)	0.022(4)	0.016(3)	0.000(2)	0	0	0.019(1)
Sample C $x = 0.080(1)$	$U_{11}$	$U_{22}$	$U_{33}$	$U_{23}$	$U_{13}$	$U_{12}$	$U_{eq}$
Sr(1)	0.0185(3)	0.0149(3)	0.0172(3)	-0.0008(4)	0	0	0.0169(2)
Li(1)/Ni(1)	0.032(4)	0.018(3)	0.022(3)	0.002(2)	0	0	0.024(2)
Ni(2)	0.0103(4)	0.0177(4)	0.0171(3)	0	0.0001(2)	0	0.0150(2)
N(1)	0.013(2)	0.022(2)	0.013(2)	-0.02(1)	0	0	0.0161(9)
Sample D $x = 0.127(1)$	$U_{11}$	$U_{22}$	$U_{33}$	$U_{23}$	$U_{13}$	$U_{12}$	$U_{eq}$
Sr(1)	0.0177(3)	0.0124(3)	0.166(3)	-0.0007(1)	0	0	0.0156(2)
Li(1)/Ni(1)	0.037(3)	0.017(3)	0.017(2)	0.005(2)	0	0	0.024(2)
Ni(2)	0.0094(4)	0.0094(4)	0.0158(4)	0	0.0003(2)	0	0.0133(2)
N(1)	0.012(2)	0.017(2)	0.015(2)	0.001(1)	0	0	0.0147(9)
Sample E $x = 0.132(2)$	$U_{11}$	$U_{22}$	$U_{33}$	$U_{23}$	$U_{13}$	$U_{12}$	$U_{eq}$
Sr(1)	0.0175(4)	0.0118(4)	0.0135(4)	-0.0008(2)	0	0	0.0143(3)
Li(1)/Ni(1)	0.031(3)	0.020(3)	0.022(3)	-0.000(2)	0	0	0.024(2)
Ni(2)	0.0098(5)	0.0143(5)	0.0130(5)	0	0.0001(2)	0	0.0124(3)
N(1)	0.009(2)	0.016(2)	0.014(3)	0.002(2)	0	0	0.013(1)



Table A.3. Atomic positions from the powder X-ray diffraction refinement of  $\text{Sr}_2[(\text{Li}_{1-x}\text{Ni}_x)\text{Ni}_2\text{N}_2]$ .

Sample A $x = 0.032(2)$	Wyckoff Position	$x/a$	$y/b$	$z/c$	Occupation
Sr(1)	8 <i>f</i>	0	0.1641(3)	0.0961(2)	1
Li(1)/Ni(1)	4 <i>b</i>	0	$1/2$	0	0.968/0.0323(7)
Ni(2)	8 <i>e</i>	$1/4$	0.4083(4)	$1/4$	1
N(1)	8 <i>f</i>	0	0.4131(1)	0.264(2)	1
Sample B $x = 0.038(2)$	Wyckoff Position	$x/a$	$y/b$	$z/c$	Occupation
Sr(1)	8 <i>f</i>	0	0.1657(2)	0.0953(2)	1
Li(1)/Ni(1)	4 <i>b</i>	0	$1/2$	0	0.962/0.038(7)
Ni(2)	8 <i>e</i>	$1/4$	0.4046(3)	$1/4$	1
N(1)	8 <i>f</i>	0	0.413(1)	0.243(2)	1
Sample C $x = 0.080(1)$	Wyckoff Position	$x/a$	$y/b$	$z/c$	Occupation
Sr(1)	8 <i>f</i>	0	0.162(1)	0.0931(1)	1
Li(1)/Ni(1)	4 <i>b</i>	0	$1/2$	0	0.920/0.080(2)
Ni(2)	8 <i>e</i>	$1/4$	0.410(2)	$1/4$	1
N(1)	8 <i>f</i>	0	0.407(6)	0.225(6)	1
Sample D $x = 0.127(1)$	Wyckoff Position	$x/a$	$y/b$	$z/c$	Occupation
Sr(1)	8 <i>f</i>	0	0.1648(3)	0.099(2)	1
Li(1)/Ni(1)	4 <i>b</i>	0	$1/2$	0	0.873/0.127(5)
Ni(2)	8 <i>e</i>	$1/4$	0.4065(4)	$1/4$	1
N(1)	8 <i>f</i>	0	0.422(1)	0.276(1)	1
Sample E $x = 0.132(2)$	Wyckoff Position	$x/a$	$y/b$	$z/c$	Occupation
Sr(1)	8 <i>f</i>	0	0.1607(3)	0.0995(3)	1
Li(1)/Ni(1)	4 <i>b</i>	0	$1/2$	0	0.868/0.132(7)
Ni(2)	8 <i>e</i>	$1/4$	0.4094(5)	$1/4$	1
N(1)	8 <i>f</i>	0	0.426(2)	0.253(2)	1

## B – Crystallographic data of lead germanates

### B.1. – Crystallographic data of $\text{Pb}_{5-x}\text{Ba}_x\text{Ge}_3\text{O}_{11}$

Table B.1.1. Atomic positions from the single crystal X-ray diffraction refinement of  $\text{Pb}_{5-x}\text{Ba}_x\text{Ge}_3\text{O}_{11}$ .

Sample A $x = 0$	Wyckoff Position	$x/a$	$y/b$	$z/c$	Occupation	$U_{eq}$
Pb(1)	1b	$1/3$	$2/3$	0.0511(2)	1	0.0211(2)
Pb(2)	1a	0	0	0.0649(1)	1	0.0197(2)
Pb(3)	1a	0	0	0.7242(2)	1	0.0175(2)
Pb(4)	3d	0.41276(6)	0.07493(7)	0.54273(7)	1	0.0158(1)
Pb(5)	1b	$1/3$	$2/3$	0.3999(1)	1	0.0182(2)
Pb(6)	1a	0	0	0.3893(1)	1	0.0182(2)
Pb(7)	1b	$1/3$	$2/3$	0.7279(2)	1	0.0151(1)
Pb(8)	3d	0.39666(6)	0.06509(7)	0.90871(6)	1	0.0190(1)
Pb(9)	3d	0.40846(7)	0.32844(7)	0.24224(7)	1	0.0196(1)
Ge(1)	3d	0.0587(2)	0.3389(2)	0.2297(2)	1	0.0123(2)
Ge(2)	3d	0.2768(2)	0.3262(2)	0.5700(2)	1	0.0127(3)
Ge(3)	3d	0.2698(2)	0.3125(2)	0.8735(2)	1	0.0141(3)
O(1)	3d	0.185(1)	0.044(1)	0.228(2)	1	0.016(2)
O(2)	3d	0.341(2)	0.504(1)	0.890(2)	1	0.022(2)
O(3)	3d	0.378(2)	0.524(2)	0.561(1)	1	0.021(3)
O(4)	3d	0.071(1)	0.211(2)	0.877(2)	1	0.026(3)
O(5)	3d	0.080(2)	0.242(2)	0.561(2)	1	0.029(4)
O(6)	3d	0.250(2)	0.412(2)	0.255(2)	1	0.030(4)
O(7)	3d	0.035(2)	0.416(2)	0.091(2)	1	0.027(3)
O(8)	3d	0.343(2)	0.245(2)	0.460(1)	1	0.024(3)
O(9)	3d	0.310(1)	0.267(1)	0.720(1)	1	0.017(2)
O(10)	3d	0.340(2)	0.239(2)	0.982(2)	1	0.031(4)
O(11) <sup>1</sup>	3d	-0.013(2)	0.409(2)	0.345(2)	1	0.023(3)

<sup>1</sup> Non-asymmetric unit given for ease of comparison. Asymmetric unit: 0.422(2), 0.013(2), 0.345(2).

Table B.1.1. *cont.*

Sample B $x = 0.15(2)$	Wyckoff Position	$x/a$	$y/b$	$z/c$	Occupation	$U_{eq}$
Pb(1)/Ba(1)	1 <i>b</i>	$1/3$	$2/3$	0.0512(1)	0.847/0.153(7)	0.0128(2)
Pb(2)	1 <i>a</i>	0	0	0.0643(1)	1	0.0128(1)
Pb(3)/Ba(3)	1 <i>a</i>	0	0	0.7266(1)	0.841/0.159(6)	0.0117(2)
Pb(4)	3 <i>d</i>	0.40597(7)	0.07102(7)	0.54319(6)	1	0.0205(1)
Pb(5)/Ba(5)	1 <i>b</i>	$1/3$	$2/3$	0.4021(1)	0.831/0.169(7)	0.0255(4)
Pb(6)	1 <i>a</i>	0	0	0.3890(1)	1	0.0227(2)
Pb(7)/Ba(7)	1 <i>b</i>	$1/3$	$2/3$	0.7266(1)	0.755/0.245(6)	0.0182(3)
Pb(8)	3 <i>d</i>	0.40599(7)	0.07105(7)	0.90991(6)	1	0.0206(1)
Pb(9)	3 <i>d</i>	0.40977(8)	0.32889(8)	0.2266(1)	1	0.0310(2)
Ge(1)	3 <i>d</i>	0.0575(2)	0.3384(2)	0.2266(2)	1	0.0147(2)
Ge(2)	3 <i>d</i>	0.2736(2)	0.3195(2)	0.5748(2)	1	0.0172(2)
Ge(3)	3 <i>d</i>	0.2734(2)	0.3193(2)	0.8782(2)	1	0.0174(3)
O(1)	3 <i>d</i>	0.185(1)	0.047(2)	0.227(1)	1	0.019(2)
O(2)	3 <i>d</i>	0.361(2)	0.513(2)	0.892(1)	1	0.032(3)
O(3)	3 <i>d</i>	0.362(2)	0.514(2)	0.561(2)	1	0.035(3)
O(4)	3 <i>d</i>	0.073(2)	0.227(2)	0.888(2)	1	0.029(3)
O(5)	3 <i>d</i>	0.073(2)	0.226(2)	0.568(2)	1	0.030(3)
O(6)	3 <i>d</i>	0.249(2)	0.409(2)	0.228(2)	1	0.047(6)
O(7)	3 <i>d</i>	0.012(2)	0.414(2)	0.100(1)	1	0.036(4)
O(8)	3 <i>d</i>	0.338(2)	0.242(2)	0.465(1)	1	0.034(3)
O(9)	3 <i>d</i>	0.311(1)	0.265(1)	0.726(1)	1	0.019(2)
O(10)	3 <i>d</i>	0.336(2)	0.241(2)	0.989(1)	1	0.033(3)
O(11)	3 <i>d</i>	0.011(2)	0.414(1)	0.354(1)	1	0.034(4)

Table B.1.1 *cont.*

Sample C $x = 0.29(2)$	Wyckoff Position	$x/a$	$y/b$	$z/c$	Occupation	$U_{eq}$
Pb(1)/Ba(1)	1 <i>b</i>	$1/3$	$2/3$	0.0509(1)	0.750/0.250(6)	0.0273(4)
Pb(2)	1 <i>a</i>	0	0	0.0643(1)	1	0.0235(2)
Pb(3)/Ba(3)	1 <i>a</i>	0	0	0.7266(1)	0.796/0.204(5)	0.0217(3)
Pb(4)	3 <i>d</i>	0.40625(6)	0.07125(6)	0.54292(5)	1	0.0201(1)
Pb(5)/Ba(5)	1 <i>b</i>	$1/3$	$2/3$	0.4024(1)	0.753/0.247(6)	0.0273(4)
Pb(6)	1 <i>a</i>	0	0	0.3890(1)	1	0.0235(2)
Pb(7)/Ba(7)	1 <i>b</i>	$1/3$	$2/3$	0.72664(9)	0.774/0.226(5)	0.0179(3)
Pb(8)	3 <i>d</i>	0.40624(6)	0.07118(6)	0.91016(5)	1	0.0200(1)
Pb(9)	3 <i>d</i>	0.40931(7)	0.32913(7)	0.2265(1)	1	0.0317(2)
Ge(1)	3 <i>d</i>	0.0571(2)	0.3384(2)	0.2266(2)	1	0.0147(2)
Ge(2)	3 <i>d</i>	0.2738(2)	0.3196(2)	0.5754(1)	1	0.0167(3)
Ge(3)	3 <i>d</i>	0.2738(2)	0.3197(2)	0.8778(1)	1	0.0168(3)
O(1)	3 <i>d</i>	0.186(1)	0.046(1)	0.226(1)	1	0.020(2)
O(2)	3 <i>d</i>	0.364(2)	0.512(1)	0.889(1)	1	0.030(3)
O(3)	3 <i>d</i>	0.363(2)	0.515(1)	0.563(1)	1	0.029(3)
O(4)	3 <i>d</i>	0.074(2)	0.229(2)	0.887(1)	1	0.031(3)
O(5)	3 <i>d</i>	0.076(2)	0.229(2)	0.567(2)	1	0.033(3)
O(6)	3 <i>d</i>	0.249(2)	0.410(2)	0.226(2)	1	0.041(4)
O(7)	3 <i>d</i>	0.011(2)	0.414(1)	0.100(1)	1	0.033(3)
O(8)	3 <i>d</i>	0.338(2)	0.242(1)	0.464(1)	1	0.032(3)
O(9)	3 <i>d</i>	0.310(1)	0.265(1)	0.7268(9)	1	0.020(2)
O(10)	3 <i>d</i>	0.338(2)	0.242(2)	0.989(1)	1	0.033(3)
O(11)	3 <i>d</i>	0.012(2)	0.415(1)	0.353(1)	1	0.035(3)

Table B.1.2. Anisotropic displacement parameters from the single crystal refinement of  $\text{Pb}_{5-x}\text{Ba}_x\text{Ge}_3\text{O}_{11}$ .

Sample A	$U_{11}$	$U_{22}$	$U_{33}$	$U_{23}$	$U_{13}$	$U_{12}$	$U_{eq}$
$x = 0$							
Pb(1)	0.0228(3)	$U_{11}$	0.0175(5)	0	0	0.0114(2)	0.0211(2)
Pb(2)	0.0212(3)	$U_{11}$	0.0167(5)	0	0	0.0106(2)	0.017(2)
Pb(3)	0.0182(2)	$U_{11}$	0.0160(3)	0	0	0.0091(1)	0.0175(2)
Pb(4)	0.0171(2)	0.0156(2)	0.0156(2)	-0.0014(2)	-0.0014(2)	0.0089(2)	0.0158(1)
Pb(5)	0.0189(2)	$U_{11}$	0.0167(5)	0	0	0.0095(1)	0.0182(2)
Pb(6)	0.0197(2)	$U_{11}$	0.0153(5)	0	0	0.0098(1)	0.0182(2)
Pb(7)	0.0146(2)	$U_{11}$	0.0163(4)	0	0	0.0073(1)	0.0151(1)
Pb(8)	0.0210(2)	0.0219(2)	0.0174(2)	0.0037(2)	0.0035(2)	0.0132(2)	0.0190(1)
Pb(9)	0.0160(2)	0.0177(2)	0.0271(4)	-0.0009(2)	0.000(2)	0.0099(2)	0.0196(1)
Ge(1)	0.0119(5)	0.0097(5)	0.0148(5)	-0.0011(6)	0.0006(5)	0.0050(4)	0.0123(2)
Ge(2)	0.0127(7)	0.0120(6)	0.0143(7)	-0.0002(5)	0.0000(4)	0.0068(6)	0.0127(3)
Ge(3)	0.0146(6)	0.0108(5)	0.0157(6)	-0.002(4)	0.0000(4)	0.0055(5)	0.0141(3)
O(1)	0.0111(4)	0.019(5)	0.024(5)	0.004(5)	0.001(5)	0.012(3)	0.016(2)
O(2)	0.029(6)	0.011(4)	0.022(5)	-0.00(4)	-0.000(5)	0.007(4)	0.022(2)
O(3)	0.024(7)	0.013(5)	0.025(7)	0.005(4)	0.003(5)	0.010(5)	0.021(3)
O(4)	0.012(4)	0.017(5)	0.038(8)	-0.07(5)	0.005(4)	0.000(4)	0.026(3)
O(5)	0.019(6)	0.028(8)	0.036(9)	0.006(6)	-0.003(5)	0.009(6)	0.029(4)
O(6)	0.010(4)	0.013(5)	0.06(1)	-0.003(5)	-0.002(5)	0.003(4)	0.030(4)
O(7)	0.044(9)	0.016(5)	0.020(6)	0.003(4)	-0.003(6)	0.014(6)	0.027(3)
O(8)	0.045(9)	0.030(6)	0.012(5)	0.003(4)	0.007(5)	0.030(7)	0.024(3)
O(9)	0.022(4)	0.025(5)	0.010(4)	0.002(4)	0.001(4)	0.016(4)	0.017(2)
O(10)	0.06(1)	0.022(6)	0.018(6)	-0.000(5)	-0.012(6)	0.020(6)	0.031(4)
O(11)	0.036(7)	0.023(5)	0.020(5)	0.003(4)	0.006(5)	0.022(5)	0.023(3)

Table B.1.2. *cont.*

Sample B	$U_{11}$	$U_{22}$	$U_{33}$	$U_{33}$	$U_{13}$	$U_{12}$	$U_{eq}$
$x = 0.15(2)$							
Pb(1)/Ba(1)	0.0256(4)	$U_{11}$	0.0268(6)	0	0	0.0128(2)	0.015(1)
Pb(2)	0.0256(3)	$U_{11}$	0.0164(4)	0	0	0.0128(1)	0.015(1)
Pb(3)/Ba(3)	0.0235(4)	$U_{11}$	0.0176(4)	0	0	0.0117(2)	0.015(1)
Pb(4)	0.0251(3)	0.0234(2)	0.0152(2)	-0.0028(2)	-0.0031(2)	0.0138(2)	0.016(1)
Pb(5)/Ba(5)	0.0251(4)	$U_{11}$	0.0262(6)	0	0	0.0126(2)	0.015(1)
Pb(6)	0.0259(3)	$U_{11}$	0.0163(4)	0	0	0.0130(1)	0.0156(8)
Pb(7)/Ba(7)	0.0187(3)	$U_{11}$	0.0172(5)	0	0	0.0094(2)	0.012(1)
Pb(8)	0.0254(3)	0.0236(2)	0.0152(2)	-0.0027(2)	0.0032(2)	0.0141(2)	0.012(1)
Pb(9)	0.0188(3)	0.0210(3)	0.0555(5)	0.0000(3)	-0.0001(3)	0.0117(2)	0.012(1)
Ge(1)	0.0148(6)	0.0134(5)	0.0159(5)	-0.0000(4)	-0.0000(5)	0.0070(5)	0.007(3)
Ge(2)	0.0193(6)	0.0182(6)	0.0142(6)	-0.0006(5)	-0.0005(5)	0.0094(5)	0.012(3)
Ge(3)	0.0192(6)	0.0180(6)	0.0150(6)	0.0006(5)	-0.0006(5)	0.0094(5)	0.011(3)
O(1)	0.017(4)	0.029(5)	0.020(5)	-0.002(4)	-0.000(3)	0.018(4)	0.019(2)
O(2)	0.05(1)	0.019(5)	0.024(6)	-0.007(4)	-0.011(6)	0.019(6)	0.032(3)
O(3)	0.06(1)	0.022(6)	0.030(7)	0.005(5)	0.006(6)	0.021(7)	0.035(3)
O(4)	0.019(5)	0.030(6)	0.038(7)	0.006(5)	0.008(5)	0.012(5)	0.029(3)
O(5)	0.021(5)	0.26(6)	0.042(8)	-0.006(5)	-0.012(5)	0.012(5)	0.030(3)
O(6)	0.017(5)	0.010(4)	0.11(2)	0.010(7)	0.003(8)	0.002(4)	0.047(6)
O(7)	0.06(1)	0.027(6)	0.015(5)	-0.000(4)	-0.021(6)	0.019(6)	0.036(4)
O(8)	0.07(1)	0.036(7)	0.013(4)	0.002(4)	0.006(6)	0.040(8)	0.034(3)
O(9)	0.022(4)	0.026(5)	0.011(3)	-0.000(3)	0.000(3)	0.013(4)	0.019(2)
O(10)	0.07(1)	0.028(6)	0.014(4)	-0.002(4)	-0.005(5)	0.033(7)	0.033(3)
O(11)	0.06(1)	0.022(5)	0.018(5)	0.003(4)	0.019(6)	0.018(6)	0.034(4)

Table B.1.2. *cont.*

Sample C	$U_{11}$	$U_{22}$	$U_{33}$	$U_{23}$	$U_{13}$	$U_{12}$	$U_{eq}$
$x = 0.29(2)$							
Pb(1)/Ba(1)	0.0246(4)	$U_{11}$	0.0327(7)	0	0	0.0123(2)	0.0273(4)
Pb(2)	0.0262(3)	$U_{11}$	0.0182(3)	0	0	0.0131(1)	0.0235(2)
Pb(3)/Ba(3)	0.0221(4)	$U_{11}$	0.0209(4)	0	0	0.0111(2)	0.0217(3)
Pb(4)	0.0244(2)	0.0226(2)	0.0154(2)	-0.0024(2)	-0.0027(2)	0.0132(2)	0.0201(1)
Pb(5)/Ba(5)	0.0243(4)	$U_{11}$	0.0332(7)	0	0	0.0122(2)	0.0273(4)
Pb(6)	0.0261(3)	$U_{11}$	0.0183(3)	0	0	0.0131(1)	0.0235(2)
Pb(7)/Ba(7)	0.0171(3)	$U_{11}$	0.0195(4)	0	0	0.0086(2)	0.0179(3)
Pb(8)	0.0242(2)	0.0226(2)	0.0154(2)	0.0023(2)	0.0027(2)	0.0133(2)	0.0200(1)
Pb(9)	0.0185(3)	0.0204(3)	0.0586(5)	-0.0001(3)	-0.0000(3)	0.0115(2)	0.0317(2)
Ge(1)	0.0152(6)	0.0128(5)	0.0161(5)	-0.0002(4)	0.0001(4)	0.0072(5)	0.0147(2)
Ge(2)	0.0187(6)	0.0175(6)	0.0146(5)	-0.0006(4)	-0.0004(4)	0.0095(5)	0.0167(3)
Ge(3)	0.0182(6)	0.0179(6)	0.0149(5)	0.0003(4)	0.0003(4)	0.0095(5)	0.0168(3)
O(1)	0.019(5)	0.025(5)	0.023(5)	-0.000(4)	-0.000(4)	0.017(4)	0.020(2)
O(2)	0.053(9)	0.021(5)	0.021(5)	-0.005(4)	-0.005(4)	0.020(6)	0.030(3)
O(3)	0.044(8)	0.018(5)	0.028(6)	0.009(4)	0.009(4)	0.017(5)	0.029(3)
O(4)	0.023(5)	0.032(7)	0.037(7)	0.003(5)	0.003(5)	0.013(5)	0.031(3)
O(5)	0.026(6)	0.033(7)	0.042(7)	-0.000(6)	-0.000(6)	0.016(5)	0.033(3)
O(6)	0.021(6)	0.016(5)	0.08(1)	-0.002(6)	-0.002(6)	0.005(5)	0.041(4)
O(7)	0.057(9)	0.020(5)	0.015(4)	0.001(4)	0.001(4)	0.015(5)	0.033(3)
O(8)	0.063(9)	0.028(6)	0.017(5)	0.001(4)	0.001(4)	0.031(6)	0.032(3)
O(9)	0.022(4)	0.029(5)	0.010(3)	0.002(3)	0.002(3)	0.013(4)	0.020(2)
O(10)	0.07(1)	0.034(6)	0.013(4)	-0.004(4)	-0.004(4)	0.036(7)	0.033(3)
O(11)	0.066(9)	0.023(5)	0.013(4)	-0.001(4)	-0.001(4)	0.021(6)	0.035(3)

Table B.1.3. Atomic positions from the powder X-ray diffraction refinement of  $\text{Pb}_{5-x}\text{Ba}_x\text{Ge}_3\text{O}_{11}$ .

Sample A $x = 0$	Wyckoff Position	$x/a$	$y/b$	$z/c$	Occupation
Pb(1)	1 <i>b</i>	$1/3$	$2/3$	0.040(5)	1
Pb(2)	1 <i>a</i>	0	0	0.043(5)	1
Pb(3)	1 <i>a</i>	0	0	0.714(6)	1
Pb(4)	3 <i>d</i>	0.408(2)	0.077(2)	0.541(4)	1
Pb(5)	1 <i>b</i>	$1/3$	$2/3$	0.376(5)	1
Pb(6)	1 <i>a</i>	0	0	0.386(5)	1
Pb(7)	1 <i>b</i>	$1/3$	$2/3$	0.709(5)	1
Pb(8)	3 <i>d</i>	0.405(7)	0.086(1)	0.901(5)	1
Pb(9)	3 <i>d</i>	0.401(1)	0.316(1)	0.219(4)	1
Ge(1)	3 <i>d</i>	0.045(3)	0.334(4)	0.218(6)	1
Ge(2)	3 <i>d</i>	0.279(2)	0.351(4)	0.567(5)	1
Ge(3)	3 <i>d</i>	0.279(2)	0.319(5)	0.879(5)	1
O(1) <sup>1</sup>	3 <i>d</i>	0.185(1)	0.044(1)	0.228(2)	1
O(2) <sup>1</sup>	3 <i>d</i>	0.341(2)	0.504(1)	0.890(2)	1
O(3) <sup>1</sup>	3 <i>d</i>	0.378(2)	0.524(2)	0.561(1)	1
O(4) <sup>1</sup>	3 <i>d</i>	0.071(1)	0.211(2)	0.877(2)	1
O(5) <sup>1</sup>	3 <i>d</i>	0.080(2)	0.242(2)	0.561(2)	1
O(6) <sup>1</sup>	3 <i>d</i>	0.250(2)	0.412(2)	0.255(2)	1
O(7) <sup>1</sup>	3 <i>d</i>	0.035(2)	0.416(2)	0.091(2)	1
O(8) <sup>1</sup>	3 <i>d</i>	0.343(2)	0.245(2)	0.460(1)	1
O(9) <sup>1</sup>	3 <i>d</i>	0.310(1)	0.267(1)	0.720(1)	1
O(10) <sup>1</sup>	3 <i>d</i>	0.340(2)	0.239(2)	0.982(2)	1
O(11) <sup>1,2</sup>	3 <i>d</i>	-0.013(2)	0.409(2)	0.345(2)	1

<sup>1</sup>Values taken from single crystal refinement of  $\text{Pb}_{5-x}\text{Ba}_x\text{Ge}_3\text{O}_{11}$  ( $x = 0$ ).

<sup>2</sup>Non-asymmetric unit given for ease of comparison. Asymmetric unit: 0.422(2), 0.013(2), 0.345(2).

$B_{iso}$  values were fixed to the default value (1) for the refinements.



Table B.1.3. *cont.*

Sample B $x = 0.15(2)$	Wyckoff Position	$x/a$	$y/b$	$z/c$	Occupation
Pb(1)/Ba(1)	1 <i>b</i>	$\frac{1}{3}$	$\frac{2}{3}$	0.05(1)	0.82817/0.16183
Pb(2)/Ba(2)	1 <i>a</i>	0	0	0.059(9)	0.94437/0.05563
Pb(3)/Ba(3)	1 <i>a</i>	0	0	0.72(1)	0.87684/0.12316
Pb(4)/Ba(4)	3 <i>d</i>	0.406(1)	0.058(1)	0.546(9)	0.97488/0.2512
Pb(5)/Ba(5)	1 <i>b</i>	$\frac{1}{3}$	$\frac{2}{3}$	0.39(1)	0.85509/0.14491
Pb(6)	1 <i>a</i>	0	0	0.39(1)	1
Pb(7)/Ba(7)	1 <i>b</i>	$\frac{1}{3}$	$\frac{2}{3}$	0.72(1)	0.82629/0.17371
Pb(8)	3 <i>d</i>	0.411(1)	0.081(2)	0.909(9)	1
Pb(9)	3 <i>d</i>	0.397(3)	0.316(2)	0.227(9)	1
Ge(1)	3 <i>d</i>	0.053(4)	0.338(4)	0.22(1)	1
Ge(2)	3 <i>d</i>	0.281(7)	0.323(6)	0.57(1)	1
Ge(3)	3 <i>d</i>	0.277(4)	0.314(5)	0.88(1)	1
O(1) <sup>1</sup>	3 <i>d</i>	0.185(1)	0.047(2)	0.227(1)	1
O(2) <sup>1</sup>	3 <i>d</i>	0.361(2)	0.513(2)	0.892(1)	1
O(3) <sup>1</sup>	3 <i>d</i>	0.362(2)	0.514(2)	0.561(2)	1
O(4) <sup>1</sup>	3 <i>d</i>	0.073(2)	0.227(2)	0.888(2)	1
O(5) <sup>1</sup>	3 <i>d</i>	0.073(2)	0.226(2)	0.568(2)	1
O(6) <sup>1</sup>	3 <i>d</i>	0.249(2)	0.409(2)	0.228(2)	1
O(7) <sup>1</sup>	3 <i>d</i>	0.012(2)	0.414(2)	0.100(1)	1
O(8) <sup>1</sup>	3 <i>d</i>	0.338(2)	0.242(2)	0.465(1)	1
O(9) <sup>1</sup>	3 <i>d</i>	0.311(1)	0.265(1)	0.726(1)	1
O(10) <sup>1</sup>	3 <i>d</i>	0.336(2)	0.241(2)	0.989(1)	1
O(11) <sup>1</sup>	3 <i>d</i>	0.011(2)	0.414(1)	0.354(1)	1

<sup>1</sup>Values taken from single crystal refinement of  $\text{Pb}_{5-x}\text{Ba}_x\text{Ge}_3\text{O}_{11}$  ( $x = 0.24(5)$ ).

$B_{iso}$  values were fixed to the default value (1) for the refinements.

Table B.1.3. *cont.*

Sample C $x = 0.29(2)$	Wyckoff Position	$x/a$	$y/b$	$z/c$	Occupation
Pb(1)/Ba(1)	1 <i>b</i>	$1/3$	$2/3$	0.047(8)	0.83817/0.16183
Pb(2)/Ba(2)	1 <i>a</i>	0	0	0.0450(7)	0.96/0.04
Pb(3)/Ba(3)	1 <i>a</i>	0	0	0.717(8)	0.83448/0.16552
Pb(4)	3 <i>d</i>	0.406(1)	0.057(1)	0.540(6)	1
Pb(5)/Ba(5)	1 <i>b</i>	$1/3$	$2/3$	0.384(8)	0.71193/0.28807
Pb(6)	1 <i>a</i>	0	0	0.384(7)	1
Pb(7)/Ba(7)	1 <i>b</i>	$1/3$	$2/3$	0.717(9)	0.82629/0.17371
Pb(8)	3 <i>d</i>	0.410(1)	0.078(1)	0.904(7)	1
Pb(9)	3 <i>d</i>	0.409(3)	0.330(2)	0.220(6)	1
Ge(1)	3 <i>d</i>	0.055(5)	0.327(4)	0.218(9)	1
Ge(2)	3 <i>d</i>	0.305(4)	0.359(4)	0.566(7)	1
Ge(3)	3 <i>d</i>	0.277(7)	0.329(7)	0.874(7)	1
O(1) <sup>1</sup>	3 <i>d</i>	0.186(1)	0.046(1)	0.226(1)	1
O(2) <sup>1</sup>	3 <i>d</i>	0.364(2)	0.512(1)	0.889(1)	1
O(3) <sup>1</sup>	3 <i>d</i>	0.363(2)	0.515(1)	0.563(1)	1
O(4) <sup>1</sup>	3 <i>d</i>	0.074(2)	0.229(2)	0.887(1)	1
O(5) <sup>1</sup>	3 <i>d</i>	0.076(2)	0.229(2)	0.567(2)	1
O(6) <sup>1</sup>	3 <i>d</i>	0.249(2)	0.410(2)	0.226(2)	1
O(7) <sup>1</sup>	3 <i>d</i>	0.011(2)	0.414(1)	0.100(1)	1
O(8) <sup>1</sup>	3 <i>d</i>	0.338(2)	0.242(1)	0.464(1)	1
O(9) <sup>1</sup>	3 <i>d</i>	0.310(1)	0.265(1)	0.7268(9)	1
O(10) <sup>1</sup>	3 <i>d</i>	0.338(2)	0.242(2)	0.989(1)	1
O(11) <sup>1</sup>	3 <i>d</i>	0.012(2)	0.415(1)	0.353(1)	1

<sup>1</sup>Values taken from single crystal refinement of  $\text{Pb}_{5-x}\text{Ba}_x\text{Ge}_3\text{O}_{11}$  ( $x = 0.31(4)$ ).

$B_{iso}$  values were fixed to the default value (1) for the refinements.

## B.2. – Crystallographic data of $\text{Pb}_5\text{Ge}_{3-x}\text{Si}_x\text{O}_{11}$

Table B.2.1. Atomic positions from the single crystal X-ray diffraction refinement of  $\text{Pb}_5\text{Ge}_{3-x}\text{Si}_x\text{O}_{11}$ .

Sample A $x = 0$	Wyckoff Position	$x/a$	$y/b$	$z/c$	Occupation	$U_{eq}$
Pb(1)	1 <i>b</i>	$1/3$	$2/3$	0.0511(2)	1	0.0211(2)
Pb(2)	1 <i>a</i>	0	0	0.0649(1)	1	0.0197(2)
Pb(3)	1 <i>a</i>	0	0	0.7242(2)	1	0.0175(2)
Pb(4)	3 <i>d</i>	0.41276(6)	0.07493(7)	0.54273(7)	1	0.0158(1)
Pb(5)	1 <i>b</i>	$1/3$	$2/3$	0.3999(1)	1	0.0182(2)
Pb(6)	1 <i>a</i>	0	0	0.3893(1)	1	0.0182(2)
Pb(7)	1 <i>b</i>	$1/3$	$2/3$	0.7279(2)	1	0.0151(1)
Pb(8)	3 <i>d</i>	0.39666(6)	0.06509(7)	0.90871(6)	1	0.0190(1)
Pb(9)	3 <i>d</i>	0.40846(7)	0.32844(7)	0.24224(7)	1	0.0196(1)
Ge(1)	3 <i>d</i>	0.0587(2)	0.3389(2)	0.2297(2)	1	0.0123(2)
Ge(2)	3 <i>d</i>	0.2768(2)	0.3262(2)	0.5700(2)	1	0.0127(3)
Ge(3)	3 <i>d</i>	0.2698(2)	0.3125(2)	0.8735(2)	1	0.0141(3)
O(1)	3 <i>d</i>	0.185(1)	0.044(1)	0.228(2)	1	0.016(2)
O(2)	3 <i>d</i>	0.341(2)	0.504(1)	0.890(2)	1	0.022(2)
O(3)	3 <i>d</i>	0.378(2)	0.524(2)	0.561(1)	1	0.021(3)
O(4)	3 <i>d</i>	0.071(1)	0.211(2)	0.877(2)	1	0.026(3)
O(5)	3 <i>d</i>	0.080(2)	0.242(2)	0.561(2)	1	0.029(4)
O(6)	3 <i>d</i>	0.250(2)	0.412(2)	0.255(2)	1	0.030(4)
O(7)	3 <i>d</i>	0.035(2)	0.416(2)	0.091(2)	1	0.027(3)
O(8)	3 <i>d</i>	0.343(2)	0.245(2)	0.460(1)	1	0.024(3)
O(9)	3 <i>d</i>	0.310(1)	0.267(1)	0.720(1)	1	0.017(2)
O(10)	3 <i>d</i>	0.340(2)	0.239(2)	0.982(2)	1	0.031(4)
O(11) <sup>1</sup>	3 <i>d</i>	-0.013(2)	0.409(2)	0.345(2)	1	0.023(3)

<sup>1</sup>Non-asymmetric unit given for ease of comparison. Asymmetric unit: 0.425(2), 0.014(2), 0.345(2).

Data is taken from sample A in section 8.2.

Table B.2.1. *cont.*

$x = 0.30(4)$	Wyckoff Position	$x/a$	$y/b$	$z/c$	Occupation	$U_{eq}$
Pb(1)	1 <i>b</i>	$1/3$	$2/3$	0.0528(2)	1	0.0174(2)
Pb(2)	1 <i>a</i>	0	0	0.0632(1)	1	0.0176(2)
Pb(3)	1 <i>a</i>	0	0	0.7281(2)	1	0.0159(2)
Pb(4)	3 <i>d</i>	0.39782(7)	0.06574(8)	0.54312(7)	1	0.0176(1)
Pb(5)	1 <i>b</i>	$1/3$	$2/3$	0.4000(2)	1	0.0192(3)
Pb(6)	1 <i>a</i>	0	0	0.3876(1)	1	0.0185(3)
Pb(7)	1 <i>b</i>	$1/3$	$2/3$	0.7245(2)	1	0.0136(2)
Pb(8)	3 <i>d</i>	0.41234(8)	0.07475(8)	0.91003(7)	1	0.0148(1)
Pb(9)	3 <i>d</i>	0.40826(8)	0.32860(8)	0.21185(8)	1	0.0187(2)
Ge(1)/Si(1)	3 <i>d</i>	0.0586(2)	0.3389(2)	0.2245(3)	0.80/0.20(1)	0.0115(4)
Ge(2)/Si(2)	3 <i>d</i>	0.2703(2)	0.3133(2)	0.5791(2)	0.94/0.06(2)	0.0128(5)
Ge(3)/Si(3)	3 <i>d</i>	0.2771(3)	0.3262(3)	0.8831(2)	0.91/0.09(2)	0.0106(5)
O(1)	3 <i>d</i>	0.187(1)	0.043(1)	0.226(2)	1	0.018(2)
O(2)	3 <i>d</i>	0.378(2)	0.524(2)	0.895(1)	1	0.018(3)
O(3)	3 <i>d</i>	0.342(2)	0.503(1)	0.563(2)	1	0.021(3)
O(4)	3 <i>d</i>	0.080(2)	0.243(2)	0.891(2)	1	0.024(4)
O(5)	3 <i>d</i>	0.072(2)	0.211(2)	0.578(2)	1	0.023(3)
O(6)	3 <i>d</i>	0.250(2)	0.413(2)	0.199(2)	1	0.031(5)
O(7) <sup>1</sup>	3 <i>d</i>	-0.013(2)	0.408(2)	0.111(2)	1	0.025(4)
O(8)	3 <i>d</i>	0.341(2)	0.240(2)	0.471(2)	1	0.029(4)
O(9)	3 <i>d</i>	0.310(1)	0.268(1)	0.735(2)	1	0.017(2)
O(10)	3 <i>d</i>	0.343(2)	0.246(2)	0.994(2)	1	0.023(3)
O(11)	3 <i>d</i>	0.028(3)	0.416(2)	0.361(2)	1	0.031(4)

<sup>1</sup>Non-asymmetric unit given for ease of comparison. Asymmetric unit: 0.421(2), 0.013(2), 0.111(2).

Table B.2.1. *cont.*

$x = 0.72(1)$	Wyckoff Position	$x/a$	$y/b$	$z/c$	Occupation	$U_{eq}$
Pb(1)	1 <i>b</i>	$\frac{1}{3}$	$\frac{2}{3}$	0.0531(4)	1	0.0226(5)
Pb(2)	1 <i>a</i>	0	0	0.0633(4)	1	0.0226(6)
Pb(3)	1 <i>a</i>	0	0	0.7252(5)	1	0.0199(2)
Pb(4)	3 <i>d</i>	0.4026(2)	0.0688(2)	0.5416(2)	1	0.0220(3)
Pb(5)	1 <i>b</i>	$\frac{1}{3}$	$\frac{2}{3}$	0.3992(4)	1	0.0249(7)
Pb(6)	1 <i>a</i>	0	0	0.3877(4)	1	0.0232(6)
Pb(7)	1 <i>b</i>	$\frac{1}{3}$	$\frac{2}{3}$	0.7241(5)	1	0.0182(2)
Pb(8)	3 <i>d</i>	0.4087(2)	0.0723(2)	0.9091(2)	1	0.0195(3)
Pb(9)	3 <i>d</i>	0.40890(9)	0.3290(1)	0.2195(4)	1	0.0265(3)
Ge(1)/Si(1)	3 <i>d</i>	0.0582(3)	0.3387(3)	0.228(1)	0.53/0.47(2)	0.0139(6)
Ge(2)/Si(2)	3 <i>d</i>	0.2728(5)	0.3178(5)	0.5758(6)	0.69/0.31(3)	0.016(1)
Ge(3)	3 <i>d</i>	0.2749(5)	0.3221(6)	0.8795(5)	1	0.0189(9)
O(1)	3 <i>d</i>	0.188(1)	0.043(2)	0.224(4)	1	0.020(3)
O(2)	3 <i>d</i>	0.362(5)	0.517(4)	0.891(3)	1	0.033(9)
O(3)	3 <i>d</i>	0.356(3)	0.508(3)	0.561(4)	1	0.030(6)
O(4)	3 <i>d</i>	0.087(4)	0.245(4)	0.880(4)	1	0.033(8)
O(5)	3 <i>d</i>	0.068(3)	0.214(3)	0.569(4)	1	0.025(5)
O(6)	3 <i>d</i>	0.249(2)	0.412(3)	0.206(4)	1	0.03(1)
O(7)	3 <i>d</i>	0.009(5)	0.417(4)	0.106(4)	1	0.033(7)
O(8)	3 <i>d</i>	0.338(5)	0.235(3)	0.467(4)	1	0.031(7)
O(9)	3 <i>d</i>	0.310(2)	0.271(2)	0.725(4)	1	0.031(4)
O(10)	3 <i>d</i>	0.347(4)	0.256(3)	0.986(4)	1	0.028(6)
O(11)	3 <i>d</i>	0.016(6)	0.409(3)	0.359(5)	1	0.05(1)

Table B.2.1. *cont.*

$x = 1.23(1)$	Wyckoff Position	$x/a$	$y/b$	$z/c$	Occupation	$U_{eq}$
Pb(1)	1 <i>b</i>	$1/3$	$2/3$	0.0528(6)	1	0.022(1)
Pb(2)	1 <i>a</i>	0	0	0.0642(6)	1	0.021(1)
Pb(3)	1 <i>a</i>	0	0	0.7265(9)	1	0.0183(2)
Pb(4)	3 <i>d</i>	0.4064(3)	0.0709(3)	0.5429(3)	1	0.0196(6)
Pb(5)	1 <i>b</i>	$1/3$	$2/3$	0.3989(6)	1	0.022(1)
Pb(6)	1 <i>a</i>	0	0	0.3893(6)	1	0.021(1)
Pb(7)	1 <i>b</i>	$1/3$	$2/3$	0.7266(8)	1	0.0174(2)
Pb(8)	3 <i>d</i>	0.4051(3)	0.0705(3)	0.9106(3)	1	0.0190(5)
Pb(9)	3 <i>d</i>	0.40887(9)	0.3288(1)	0.2245(8)	1	0.0247(2)
Ge(1)/Si(1)	3 <i>d</i>	0.0575(3)	0.3382(4)	0.226(2)	0.47/0.53(2)	0.0122(8)
Ge(2)/Si(2)	3 <i>d</i>	0.2737(9)	0.319(1)	0.577(1)	0.83/0.17(5)	0.017(2)
Ge(3)/Si(3)	3 <i>d</i>	0.274(1)	0.321(1)	0.880(1)	0.58/0.42(5)	0.011(2)
O(1)	3 <i>d</i>	0.188(2)	0.043(2)	0.235(7)	1	0.017(6)
O(2)	3 <i>d</i>	0.343(4)	0.504(4)	0.890(4)	1	0.016(6)
O(3)	3 <i>d</i>	0.376(4)	0.519(4)	0.556(5)	1	0.022(8)
O(4)	3 <i>d</i>	0.073(5)	0.241(5)	0.882(5)	1	0.03(1)
O(5)	3 <i>d</i>	0.079(3)	0.219(4)	0.566(4)	1	0.017(5)
O(6)	3 <i>d</i>	0.248(2)	0.408(2)	0.247(2)	1	0.021(5)
O(7)	3 <i>d</i>	0.019(5)	0.419(5)	0.101(4)	1	0.029(9)
O(8)	3 <i>d</i>	0.361(6)	0.256(6)	0.467(6)	1	0.03(1)
O(9)	3 <i>d</i>	0.313(2)	0.273(2)	0.725(5)	1	0.024(4)
O(10)	3 <i>d</i>	0.328(4)	0.237(4)	0.987(4)	1	0.016(6)
O(11)	3 <i>d</i>	0.002(7)	0.405(5)	0.347(4)	1	0.04(1)

Table B.2.1. *cont.*

$x = 1.42(1)$	Wyckoff Position	$x/a$	$y/b$	$z/c$	Occupation	$U_{eq}$
Pb(1)	1 <i>b</i>	$\frac{1}{3}$	$\frac{2}{3}$	0.05253(7)	1	0.0206(1)
Pb(2)	1 <i>a</i>	0	0	0.06280(7)	1	0.0194(1)
Pb(3)	1 <i>a</i>	0	0	0.72535(6)	1	0.0167(1)
Pb(4)	3 <i>d</i>	0.40555(4)	0.07044(4)	0.54133(4)	1	0.01746(7)
Pb(5)	1 <i>b</i>	$\frac{1}{3}$	$\frac{2}{3}$	0.39820(7)	1	0.0205(1)
Pb(6)	1 <i>a</i>	0	0	0.38795(7)	1	0.0194(1)
Pb(7)	1 <i>b</i>	$\frac{1}{3}$	$\frac{2}{3}$	0.72534(6)	1	0.0158(1)
Pb(8)	3 <i>d</i>	0.40557(4)	0.07038(4)	0.90926(4)	1	0.01736(7)
Pb(9)	3 <i>d</i>	0.40890(4)	0.32870(5)	0.22528(6)	1	0.02325(9)
Ge(1)/Si(1)	3 <i>d</i>	0.0577(2)	0.3381(2)	0.2253(2)	0.445/0.555(7)	0.0103(4)
Ge(2)/Si(2)	3 <i>d</i>	0.2737(2)	0.3199(1)	0.5742(1)	0.710/0.290(9)	0.0132(3)
Ge(3)/Si(3)	3 <i>d</i>	0.2740(2)	0.3201(1)	0.8765(1)	0.703/0.297(9)	0.0127(3)
O(1)	3 <i>d</i>	0.1895(8)	0.0443(9)	0.2251(6)	1	0.014(1)
O(2)	3 <i>d</i>	0.357(1)	0.511(1)	0.8920(8)	1	0.025(2)
O(3)	3 <i>d</i>	0.357(1)	0.5103(9)	0.5589(8)	1	0.025(2)
O(4)	3 <i>d</i>	0.0774(9)	0.229(1)	0.8814(9)	1	0.027(2)
O(5)	3 <i>d</i>	0.0772(9)	0.229(1)	0.5684(9)	1	0.028(2)
O(6)	3 <i>d</i>	0.247(1)	0.410(1)	0.225(1)	1	0.038(3)
O(7)	3 <i>d</i>	0.013(1)	0.4115(9)	0.1006(8)	1	0.029(2)
O(8)	3 <i>d</i>	0.342(1)	0.2449(9)	0.4645(8)	1	0.028(2)
O(9)	3 <i>d</i>	0.3111(8)	0.2732(8)	0.7256(7)	1	0.018(1)
O(10)	3 <i>d</i>	0.340(1)	0.2449(9)	0.9855(8)	1	0.026(2)
O(11)	3 <i>d</i>	0.011(1)	0.4108(9)	0.3496(8)	1	0.031(2)

Table B.2.2. Anisotropic displacement parameters from the single crystal refinement of  $\text{Pb}_5\text{Ge}_{3-x}\text{Si}_x\text{O}_{11}$ .

Sample A	$U_{11}$	$U_{22}$	$U_{33}$	$U_{23}$	$U_{13}$	$U_{12}$	$U_{eq}$
$x = 0$							
Pb(1)	0.0228(3)	$U_{11}$	0.0175(5)	0	0	0.0114(2)	0.0211(2)
Pb(2)	0.0212(3)	$U_{11}$	0.0167(5)	0	0	0.0106(2)	0.017(2)
Pb(3)	0.0182(2)	$U_{11}$	0.0160(3)	0	0	0.0091(1)	0.0175(2)
Pb(4)	0.0171(2)	0.0156(2)	0.0156(2)	-0.0014(2)	-0.0014(2)	0.0089(2)	0.0158(1)
Pb(5)	0.0189(2)	$U_{11}$	0.0167(5)	0	0	0.0095(1)	0.0182(2)
Pb(6)	0.0197(2)	$U_{11}$	0.0153(5)	0	0	0.0098(1)	0.0182(2)
Pb(7)	0.0146(2)	$U_{11}$	0.0163(4)	0	0	0.0073(1)	0.0151(1)
Pb(8)	0.0210(2)	0.0219(2)	0.0174(2)	0.0037(2)	0.0035(2)	0.0132(2)	0.0190(1)
Pb(9)	0.0160(2)	0.0177(2)	0.0271(4)	-0.0009(2)	0.000(2)	0.0099(2)	0.0196(1)
Ge(1)	0.0119(5)	0.0097(5)	0.0148(5)	-0.0011(6)	0.0006(5)	0.0050(4)	0.0123(2)
Ge(2)	0.0127(7)	0.0120(6)	0.0143(7)	-0.0002(5)	0.0000(4)	0.0068(6)	0.0127(3)
Ge(3)	0.0146(6)	0.0108(5)	0.0157(6)	-0.002(4)	0.0000(4)	0.0055(5)	0.0141(3)
O(1)	0.011(4)	0.019(5)	0.024(5)	0.004(5)	0.001(5)	0.012(3)	0.016(2)
O(2)	0.029(6)	0.011(4)	0.022(5)	-0.00(4)	-0.000(5)	0.007(4)	0.022(2)
O(3)	0.024(7)	0.013(5)	0.025(7)	0.005(4)	0.003(5)	0.010(5)	0.021(3)
O(4)	0.012(4)	0.017(5)	0.038(8)	-0.07(5)	0.005(4)	0.000(4)	0.026(3)
O(5)	0.019(6)	0.028(8)	0.036(9)	0.006(6)	-0.003(5)	0.009(6)	0.029(4)
O(6)	0.010(4)	0.013(5)	0.06(1)	-0.003(5)	-0.002(5)	0.003(4)	0.030(4)
O(7)	0.044(9)	0.016(5)	0.020(6)	0.003(4)	-0.003(6)	0.014(6)	0.027(3)
O(8)	0.045(9)	0.030(6)	0.012(5)	0.003(4)	0.007(5)	0.030(7)	0.024(3)
O(9)	0.022(4)	0.025(5)	0.010(4)	0.002(4)	0.001(4)	0.016(4)	0.017(2)
O(10)	0.06(1)	0.022(6)	0.018(6)	-0.000(5)	-0.012(6)	0.020(6)	0.031(4)
O(11)	0.036(7)	0.023(5)	0.020(5)	0.003(4)	0.006(5)	0.022(5)	0.023(3)

Data is taken from sample A in section 8.2.



Table B.2.2. *cont.*

$x = 0.30(4)$	$U_{11}$	$U_{22}$	$U_{33}$	$U_{23}$	$U_{13}$	$U_{12}$	$U_{eq}$
Pb(1)	0.0197(3)	$U_{11}$	0.0128(5)	0	0	0.0099(2)	0.0174(2)
Pb(2)	0.0202(3)	$U_{11}$	0.0125(6)	0	0	0.0101(2)	0.0176(2)
Pb(3)	0.0172(3)	$U_{11}$	0.0133(4)	0	0	0.0086(1)	0.0159(2)
Pb(4)	0.0205(3)	0.0209(3)	0.0146(3)	-0.0032(2)	-0.0032(2)	0.0128(2)	0.0176(1)
Pb(5)	0.0223(4)	$U_{11}$	0.0131(6)	0	0	0.0111(2)	0.0192(3)
Pb(6)	0.0210(4)	$U_{11}$	0.0133(6)	0	0	0.0105(2)	0.0185(3)
Pb(7)	0.0141(2)	$U_{11}$	0.0128(4)	0	0	0.0070(1)	0.0136(2)
Pb(8)	0.0165(3)	0.0154(3)	0.0135(2)	0.0018(2)	0.0019(2)	0.0088(3)	0.0148(1)
Pb(9)	0.0158(3)	0.0175(3)	0.0246(4)	0.0009(2)	-0.0000(2)	0.0097(2)	0.0187(2)
Ge(1)/Si(1)	0.0113(8)	0.0088(7)	0.0133(7)	0.0014(8)	0.0009(8)	0.0041(6)	0.0115(4)
Ge(2)/Si(2)	0.0145(9)	0.0100(8)	0.0123(8)	0.0002(5)	0.0002(5)	0.0049(6)	0.0128(5)
Ge(3)/Si(3)	0.012(1)	0.0109(9)	0.0111(9)	0.0000(6)	0.0001(5)	0.0069(8)	0.0106(5)
O(1)	0.013(5)	0.017(5)	0.030(7)	-0.003(7)	0.002(7)	0.011(4)	0.018(2)
O(2)	0.028(8)	0.013(6)	0.013(6)	-0.002(4)	-0.005(5)	0.010(6)	0.018(3)
O(3)	0.036(7)	0.012(5)	0.016(5)	0.001(4)	0.004(6)	0.012(5)	0.021(3)
O(4)	0.022(7)	0.021(7)	0.028(9)	-0.003(5)	0.005(5)	0.010(6)	0.024(4)
O(5)	0.015(5)	0.019(6)	0.034(9)	0.000(5)	-0.000(5)	0.006(5)	0.023(3)
O(6)	0.010(5)	0.025(7)	0.06(1)	0.006(7)	0.008(6)	0.009(5)	0.031(5)
O(7)	0.05(1)	0.024(7)	0.017(6)	0.004(5)	0.001(6)	0.026(7)	0.025(4)
O(8)	0.05(1)	0.026(7)	0.023(8)	0.002(6)	0.008(7)	0.026(7)	0.029(4)
O(9)	0.020(5)	0.022(5)	0.012(5)	0.003(5)	0.002(5)	0.012(4)	0.017(2)
O(10)	0.039(9)	0.019(6)	0.019(6)	-0.003(5)	-0.008(6)	0.019(6)	0.023(3)
O(11)	0.04(1)	0.024(7)	0.021(8)	-0.007(6)	0.003(7)	0.011(7)	0.031(4)

Table B.2.2. *cont.*

$x = 0.72(1)$	$U_{11}$	$U_{22}$	$U_{33}$	$U_{33}$	$U_{13}$	$U_{12}$	$U_{eq}$
Pb(1)	0.0271(7)	$U_{11}$	0.014(2)	0	0	0.0135(3)	0.0226(5)
Pb(2)	0.0270(7)	$U_{11}$	0.014(2)	0	0	0.0135(3)	0.0226(6)
Pb(3)	0.0221(3)	$U_{11}$	0.0154(5)	0	0	0.0111(2)	0.0199(2)
Pb(4)	0.0273(6)	0.0266(6)	0.0161(7)	-0.0035(6)	-0.0042(5)	0.0165(5)	0.0220(3)
Pb(5)	0.0278(8)	$U_{11}$	0.019(2)	0	0	0.0139(4)	0.0249(7)
Pb(6)	0.0270(8)	$U_{11}$	0.015(2)	0	0	0.0135(4)	0.0232(6)
Pb(7)	0.0197(3)	$U_{11}$	0.0151(5)	0	0	0.0099(1)	0.0182(2)
Pb(8)	0.0226(6)	0.0217(6)	0.0154(7)	0.0014(6)	0.0015(5)	0.0120(5)	0.0195(3)
Pb(9)	0.0206(3)	0.0223(3)	0.0385(7)	-0.0004(7)	-0.0009(8)	0.0123(3)	0.0265(3)
Ge(1)/Si(1)	0.016(1)	0.0122(9)	0.013(1)	0.002(3)	0.000(2)	0.0065(8)	0.0139(6)
Ge(2)/Si(2)	0.019(2)	0.016(2)	0.014(2)	0.000(2)	0.001(1)	0.009(2)	0.016(1)
Ge(3)	0.020(2)	0.024(6)	0.017(2)	0.002(2)	0.002(1)	0.010(2)	0.0189(9)
O(1)	0.014(4)	0.024(6)	0.018(7)	-0.01(1)	-0.00(1)	0.007(4)	0.020(3)
O(2)	0.06(2)	0.02(1)	0.02(1)	-0.002(9)	-0.02(1)	0.02(1)	0.033(9)
O(3)	0.03(1)	0.019(9)	0.04(2)	0.01(1)	-0.01(1)	0.015(8)	0.030(6)
O(4)	0.02(1)	0.02(1)	0.05(2)	-0.01(1)	-0.01(1)	0.001(9)	0.033(8)
O(5)	0.023(9)	0.02(1)	0.02(1)	-0.002(9)	-0.011(8)	0.008(8)	0.025(5)
O(6)	0.018(7)	0.027(8)	0.05(3)	0.01(1)	0.01(1)	0.006(6)	0.03(1)
O(7)	0.05(2)	0.05(2)	0.01(1)	0.00(1)	-0.01(1)	0.03(1)	0.033(7)
O(8)	0.06(2)	0.018(8)	0.02(1)	-0.002(7)	0.01(1)	0.02(1)	0.031(7)
O(9)	0.021(6)	0.033(8)	0.04(1)	0.01(1)	-0.02(1)	0.010(6)	0.031(4)
O(10)	0.04(1)	0.02(1)	0.03(2)	-0.003(9)	-0.01(1)	0.021(9)	0.028(6)
O(11)	0.09(3)	0.012(8)	0.04(2)	0.00(1)	0.02(2)	0.03(1)	0.05(1)

Table B.2.2. *cont.*

$x = 1.23(1)$	$U_{11}$	$U_{22}$	$U_{33}$	$U_{23}$	$U_{13}$	$U_{12}$	$U_{eq}$
Pb(1)	0.024(1)	$U_{11}$	0.019(3)	0	0	0.0119(7)	0.022(1)
Pb(2)	0.024(1)	$U_{11}$	0.016(2)	0	0	0.0120(7)	0.021(1)
Pb(3)	0.0181(3)	$U_{11}$	0.0187(5)	0	0	0.0090(2)	0.0183(2)
Pb(4)	0.021(1)	0.020(1)	0.021(1)	-0.003(1)	-0.004(1)	0.012(1)	0.0196(6)
Pb(5)	0.024(1)	$U_{11}$	0.018(3)	0	0	0.0119(7)	0.022(1)
Pb(6)	0.022(1)	$U_{11}$	0.019(2)	0	0	0.0110(7)	0.021(1)
Pb(7)	0.0167(3)	$U_{11}$	0.0188(5)	0	0	0.0084(2)	0.0174(2)
Pb(8)	0.022(1)	0.021(1)	0.016(1)	0.003(1)	0.003(1)	0.013(1)	0.0190(5)
Pb(9)	0.0158(3)	0.0178(3)	0.0427(7)	0.000(2)	-0.001(2)	0.0100(3)	0.0247(2)
Ge(1)/Si(1)	0.011(1)	0.009(1)	0.017(1)	-0.001(6)	-0.002(5)	0.006(1)	0.0122(8)
Ge(2)/Si(2)	0.017(4)	0.015(4)	0.020(4)	-0.002(3)	-0.001(3)	0.008(3)	0.017(2)
Ge(3)/Si(3)	0.011(4)	0.009(4)	0.012(3)	-0.002(3)	-0.001(3)	0.005(3)	0.011(2)
O(1)	0.012(6)	0.018(7)	0.02(2)	0.01(1)	-0.001(9)	0.005(5)	0.017(6)
O(2)	0.02(2)	0.02(1)	0.013(8)	-0.008(8)	-0.01(1)	0.02(1)	0.016(6)
O(3)	0.02(1)	0.010(9)	0.03(2)	-0.004(9)	0.00(1)	-0.000(9)	0.022(8)
O(4)	0.03(2)	0.02(2)	0.05(2)	-0.02(1)	-0.01(1)	0.02(1)	0.03(1)
O(5)	0.006(8)	0.01(1)	0.04(1)	-0.006(9)	-0.012(8)	0.006(7)	0.017(5)
O(6)	0.021(8)	0.019(8)	0.02(1)	-0.002(6)	-0.000(7)	0.010(7)	0.021(5)
O(7)	0.03(1)	0.02(1)	0.03(2)	0.01(1)	-0.01(1)	0.01(1)	0.029(9)
O(8)	0.05(3)	0.03(2)	0.03(2)	0.01(2)	0.02(2)	0.03(2)	0.03(1)
O(9)	0.028(8)	0.022(8)	0.026(8)	-0.02(1)	-0.01(2)	0.016(7)	0.024(4)
O(10)	0.02(1)	0.011(9)	0.02(1)	0.005(8)	0.003(9)	0.006(8)	0.016(6)
O(11)	0.08(3)	0.01(1)	0.02(1)	0.01(1)	0.00(1)	0.02(2)	0.04(1)

Table B.2.2. *cont.*

$x = 1.42(1)$	$U_{11}$	$U_{22}$	$U_{33}$	$U_{23}$	$U_{13}$	$U_{12}$	$U_{eq}$
Pb(1)	0.0240(2)	$U_{11}$	0.0137(3)	0	0	0.0120(1)	0.0206(1)
Pb(2)	0.0229(2)	$U_{11}$	0.0124(3)	0	0	0.0115(1)	0.0194(1)
Pb(3)	0.0183(2)	$U_{11}$	0.0136(3)	0	0	0.00914(9)	0.0167(1)
Pb(4)	0.0213(2)	0.0204(2)	0.0134(1)	-0.0027(1)	-0.0032(1)	0.0124(2)	0.01746(7)
Pb(5)	0.0241(2)	$U_{11}$	0.0134(3)	0	0	0.0120(1)	0.0205(1)
Pb(6)	0.0229(2)	$U_{11}$	0.0125(3)	0	0	0.0115(1)	0.0194(1)
Pb(7)	0.0168(2)	$U_{11}$	0.0138(3)	0	0	0.00841(9)	0.0158(1)
Pb(8)	0.0212(2)	0.0202(2)	0.0133(1)	0.0027(1)	0.0031(1)	0.0123(2)	0.01736(7)
Pb(9)	0.0156(2)	0.0174(2)	0.0389(2)	0.0001(2)	0.0001(2)	0.0100(2)	0.02325(9)
Ge(1)/Si(1)	0.0109(7)	0.0090(6)	0.0107(6)	0.0001(4)	0.0002(5)	0.0048(5)	0.0103(4)
Ge(2)/Si(2)	0.0152(6)	0.0125(6)	0.0118(5)	-0.0005(4)	-0.0002(4)	0.0069(4)	0.0132(3)
Ge(3)/Si(3)	0.0143(6)	0.0117(6)	0.0118(5)	0.0002(4)	0.0001(4)	0.0064(4)	0.0127(3)
O(1)	0.012(3)	0.018(3)	0.017(3)	-0.002(2)	-0.002(2)	0.010(3)	0.014(1)
O(2)	0.038(5)	0.021(4)	0.023(4)	-0.005(3)	-0.003(3)	0.019(4)	0.025(2)
O(3)	0.040(5)	0.020(4)	0.021(4)	0.006(3)	0.006(3)	0.019(4)	0.025(2)
O(4)	0.014(3)	0.033(4)	0.031(4)	-0.006(4)	0.003(3)	0.010(3)	0.027(2)
O(5)	0.014(3)	0.031(4)	0.035(5)	0.007(4)	-0.008(3)	0.008(3)	0.028(2)
O(6)	0.018(4)	0.016(4)	0.083(9)	0.003(5)	0.005(5)	0.012(3)	0.038(3)
O(7)	0.046(5)	0.018(4)	0.018(3)	-0.002(3)	-0.010(4)	0.013(4)	0.029(2)
O(8)	0.049(5)	0.024(4)	0.018(3)	0.005(3)	0.006(4)	0.024(4)	0.028(2)
O(9)	0.017(3)	0.021(4)	0.017(3)	-0.001(3)	-0.000(3)	0.010(3)	0.018(1)
O(10)	0.048(5)	0.022(4)	0.015(3)	-0.004(3)	-0.009(3)	0.022(4)	0.026(2)
O(11)	0.052(6)	0.020(4)	0.021(4)	0.002(3)	0.010(4)	0.018(4)	0.031(2)

Table B.2.3. Atomic positions from the powder X-ray diffraction refinement of  $\text{Pb}_5\text{Ge}_{3-x}\text{Si}_x\text{O}_{11}$ .

Sample A $x = 0$	Wyckoff Position	$x/a$	$y/b$	$z/c$	Occupation
Pb(1)	1 <i>b</i>	$1/3$	$2/3$	0.040(5)	1
Pb(2)	1 <i>a</i>	0	0	0.043(5)	1
Pb(3)	1 <i>a</i>	0	0	0.714(6)	1
Pb(4)	3 <i>d</i>	0.408(2)	0.077(2)	0.541(4)	1
Pb(5)	1 <i>b</i>	$1/3$	$2/3$	0.376(5)	1
Pb(6)	1 <i>a</i>	0	0	0.386(5)	1
Pb(7)	1 <i>b</i>	$1/3$	$2/3$	0.709(5)	1
Pb(8)	3 <i>d</i>	0.405(7)	0.086(1)	0.901(5)	1
Pb(9)	3 <i>d</i>	0.401(1)	0.316(1)	0.219(4)	1
Ge(1)	3 <i>d</i>	0.045(3)	0.334(4)	0.218(6)	1
Ge(2)	3 <i>d</i>	0.279(2)	0.351(4)	0.567(5)	1
Ge(3)	3 <i>d</i>	0.279(2)	0.319(5)	0.879(5)	1
O(1) <sup>1</sup>	3 <i>d</i>	0.185(1)	0.044(1)	0.228(2)	1
O(2) <sup>1</sup>	3 <i>d</i>	0.341(2)	0.504(1)	0.890(2)	1
O(3) <sup>1</sup>	3 <i>d</i>	0.378(2)	0.524(2)	0.561(1)	1
O(4) <sup>1</sup>	3 <i>d</i>	0.071(1)	0.211(2)	0.877(2)	1
O(5) <sup>1</sup>	3 <i>d</i>	0.080(2)	0.242(2)	0.561(2)	1
O(6) <sup>1</sup>	3 <i>d</i>	0.250(2)	0.412(2)	0.255(2)	1
O(7) <sup>1</sup>	3 <i>d</i>	0.035(2)	0.416(2)	0.091(2)	1
O(8) <sup>1</sup>	3 <i>d</i>	0.343(2)	0.245(2)	0.460(1)	1
O(9) <sup>1</sup>	3 <i>d</i>	0.310(1)	0.267(1)	0.720(1)	1
O(10) <sup>1</sup>	3 <i>d</i>	0.340(2)	0.239(2)	0.982(2)	1
O(11) <sup>1,2</sup>	3 <i>d</i>	-0.013(2)	0.409(2)	0.345(2)	1

<sup>1</sup>Values taken from single crystal refinement of  $\text{Pb}_5\text{Ge}_{3-x}\text{Si}_x\text{O}_{11}$  ( $x = 0$ ).

<sup>2</sup>Non-asymmetric unit given for ease of comparison. Asymmetric unit: 0.425(2), 0.014(2), 0.345(2).

$B_{iso}$  values were fixed to the default value (1) for the refinements.

Data is taken from sample A in section 8.2.

Table B.2.3. *cont.*

$x = 0.30(4)$	Wyckoff Position	$x/a$	$y/b$	$z/c$	Occupation
Pb(1)	1 <i>b</i>	$1/3$	$2/3$	0.069(7)	1
Pb(2)	1 <i>a</i>	0	0	0.071(7)	1
Pb(3)	1 <i>a</i>	0	0	0.735(7)	1
Pb(4)	3 <i>d</i>	0.389(1)	0.065(1)	0.545(7)	1
Pb(5)	1 <i>b</i>	$1/3$	$2/3$	0.404(7)	1
Pb(6)	1 <i>a</i>	0	0	0.401(7)	1
Pb(7)	1 <i>b</i>	$1/3$	$2/3$	0.727(8)	1
Pb(8)	3 <i>d</i>	0.416(1)	0.078(2)	0.908(6)	1
Pb(9)	3 <i>d</i>	0.403(2)	0.324(2)	0.223(6)	1
Ge(1)	3 <i>d</i>	0.056(4)	0.335(7)	0.569(7)	1
Ge(2)/Si(2)	3 <i>d</i>	0.281(5)	0.329(8)	0.569(7)	0.79/0.21
Ge(3)/Si(3)	3 <i>d</i>	0.293(4)	0.351(4)	0.885(6)	0.95/0.05
O(1) <sup>1</sup>	3 <i>d</i>	0.187(1)	0.043(1)	0.226(2)	1
O(2) <sup>1</sup>	3 <i>d</i>	0.378(2)	0.524(2)	0.895(1)	1
O(3) <sup>1</sup>	3 <i>d</i>	0.342(2)	0.503(1)	0.563(2)	1
O(4) <sup>1</sup>	3 <i>d</i>	0.080(2)	0.243(2)	0.891(2)	1
O(5) <sup>1</sup>	3 <i>d</i>	0.072(2)	0.211(2)	0.578(2)	1
O(6) <sup>1</sup>	3 <i>d</i>	0.250(2)	0.413(2)	0.199(2)	1
O(7) <sup>1,2</sup>	3 <i>d</i>	-0.013(2)	0.408(2)	0.111(2)	1
O(8) <sup>1</sup>	3 <i>d</i>	0.341(2)	0.240(2)	0.471(2)	1
O(9) <sup>1</sup>	3 <i>d</i>	0.310(1)	0.268(1)	0.735(2)	1
O(10) <sup>1</sup>	3 <i>d</i>	0.343(2)	0.246(2)	0.994(2)	1
O(11) <sup>1</sup>	3 <i>d</i>	0.028(3)	0.416(2)	0.361(2)	1

<sup>1</sup>Values taken from single crystal refinement of  $\text{Pb}_5\text{Ge}_{3-x}\text{Si}_x\text{O}_{11}$  ( $x = 0.30(4)$ ).

<sup>2</sup>Non-asymmetric unit given for ease of comparison. Asymmetric unit: 0.421(2), 0.013(2), 0.111(2).  $B_{iso}$  values were fixed to the default value (1) for the refinements.

Table B.2.3. *cont.*

$x = 0.72(1)$	Wyckoff Position	$x/a$	$y/b$	$z/c$	Occupation
Pb(1)	1 <i>b</i>	$\frac{1}{3}$	$\frac{2}{3}$	0.054(8)	1
Pb(2)	1 <i>a</i>	0	0	0.051(8)	1
Pb(3)	1 <i>a</i>	0	0	0.713(9)	1
Pb(4)	3 <i>d</i>	0.402(2)	0.066(2)	0.538(6)	1
Pb(5)	1 <i>b</i>	$\frac{1}{3}$	$\frac{2}{3}$	0.388(8)	1
Pb(6)	1 <i>a</i>	0	0	0.389(7)	1
Pb(7)	1 <i>b</i>	$\frac{1}{3}$	$\frac{2}{3}$	0.715(8)	1
Pb(8)	3 <i>d</i>	0.412(2)	0.082(1)	0.902(6)	1
Pb(9)	3 <i>d</i>	0.3984(9)	0.317(1)	0.220(5)	1
Ge(1)	3 <i>d</i>	0.038(2)	0.317(1)	0.204(6)	1
Ge(2)/Si(2)	3 <i>d</i>	0.285(7)	0.352(9)	0.557(7)	0.605/0.395
Ge(3)/Si(3)	3 <i>d</i>	0.289(4)	0.337(7)	0.869(5)	0.8/0.2
O(1) <sup>1</sup>	3 <i>d</i>	0.188(1)	0.043(2)	0.224(4)	1
O(2) <sup>1</sup>	3 <i>d</i>	0.362(5)	0.517(4)	0.891(3)	1
O(3) <sup>1</sup>	3 <i>d</i>	0.356(3)	0.508(3)	0.561(4)	1
O(4) <sup>1</sup>	3 <i>d</i>	0.087(4)	0.245(4)	0.880(4)	1
O(5) <sup>1</sup>	3 <i>d</i>	0.068(3)	0.214(3)	0.569(4)	1
O(6) <sup>1</sup>	3 <i>d</i>	0.249(2)	0.412(3)	0.206(4)	1
O(7) <sup>1</sup>	3 <i>d</i>	0.009(5)	0.417(4)	0.106(4)	1
O(8) <sup>1</sup>	3 <i>d</i>	0.338(5)	0.235(3)	0.467(4)	1
O(9) <sup>1</sup>	3 <i>d</i>	0.310(2)	0.271(2)	0.725(4)	1
O(10) <sup>1</sup>	3 <i>d</i>	0.347(4)	0.256(3)	0.986(4)	1
O(11) <sup>1</sup>	3 <i>d</i>	0.016(6)	0.409(3)	0.359(5)	1

<sup>1</sup>Values taken from single crystal refinement of  $\text{Pb}_5\text{Ge}_{3-x}\text{Si}_x\text{O}_{11}$  ( $x = 0.72(1)$ ).

$B_{iso}$  values were fixed to the default value (1) for the refinements.

Table B.2.3. *cont.*

$x = 1.23(1)$	Wyckoff Position	$x/a$	$y/b$	$z/c$	Occupation
Pb(1)	1 <i>b</i>	$1/3$	$2/3$	0.065(8)	1
Pb(2)	1 <i>a</i>	0	0	0.070(7)	1
Pb(3)	1 <i>a</i>	0	0	0.739(7)	1
Pb(4)	3 <i>d</i>	0.418(2)	0.076(2)	0.545(6)	1
Pb(5)	1 <i>b</i>	$1/3$	$2/3$	0.406(7)	1
Pb(6)	1 <i>a</i>	0	0	0.404(7)	1
Pb(7)	1 <i>b</i>	$1/3$	$2/3$	0.735(8)	1
Pb(8)	3 <i>d</i>	0.396(2)	0.068(3)	0.91(2)	1
Pb(9)	3 <i>d</i>	0.399(3)	0.326(2)	0.23(2)	1
Ge(1)	3 <i>d</i>	0.054(7)	0.328(6)	0.23(2)	1
Ge(2)/Si(2)	3 <i>d</i>	0.28(2)	0.344(9)	0.58(2)	0.477/0.523
Ge(3)/Si(3)	3 <i>d</i>	0.293(6)	0.307(4)	0.87(2)	0.673/0.327
O(1) <sup>1</sup>	3 <i>d</i>	0.188(2)	0.043(2)	0.235(7)	1
O(2) <sup>1</sup>	3 <i>d</i>	0.343(4)	0.504(4)	0.890(4)	1
O(3) <sup>1</sup>	3 <i>d</i>	0.376(4)	0.519(4)	0.556(5)	1
O(4) <sup>1</sup>	3 <i>d</i>	0.073(5)	0.241(5)	0.882(5)	1
O(5) <sup>1</sup>	3 <i>d</i>	0.079(3)	0.219(4)	0.566(4)	1
O(6) <sup>1</sup>	3 <i>d</i>	0.248(2)	0.408(2)	0.247(2)	1
O(7) <sup>1</sup>	3 <i>d</i>	0.019(5)	0.419(5)	0.101(4)	1
O(8) <sup>1</sup>	3 <i>d</i>	0.361(6)	0.256(6)	0.467(6)	1
O(9) <sup>1</sup>	3 <i>d</i>	0.313(2)	0.273(2)	0.725(5)	1
O(10) <sup>1</sup>	3 <i>d</i>	0.328(4)	0.237(4)	0.987(4)	1
O(11) <sup>1</sup>	3 <i>d</i>	0.002(7)	0.405(5)	0.347(4)	1

<sup>1</sup>Values taken from single crystal refinement of  $\text{Pb}_5\text{Ge}_{3-x}\text{Si}_x\text{O}_{11}$  ( $x = 1.23(1)$ ).

$B_{iso}$  values were fixed to the default value (1) for the refinements.



Table B.2.3. *cont.*

$x = 1.42(1)$	Wyckoff Position	$x/a$	$y/b$	$z/c$	Occupation
Pb(1)	1 <i>b</i>	$\frac{1}{3}$	$\frac{2}{3}$	0.06(2)	1
Pb(2)	1 <i>a</i>	0	0	0.06(2)	1
Pb(3)	1 <i>a</i>	0	0	0.72(2)	1
Pb(4)	3 <i>d</i>	0.419(2)	0.082(3)	0.54(2)	1
Pb(5)	1 <i>b</i>	$\frac{1}{3}$	$\frac{2}{3}$	0.40(2)	1
Pb(6)	1 <i>a</i>	0	0	0.40(2)	1
Pb(7)	1 <i>b</i>	$\frac{1}{3}$	$\frac{2}{3}$	0.73(2)	1
Pb(8)	3 <i>d</i>	0.406(2)	0.064(4)	0.911(6)	1
Pb(9)	3 <i>d</i>	0.408(1)	0.336(1)	0.229(6)	1
Ge(1)	3 <i>d</i>	0.044(3)	0.341(3)	0.238(6)	1
Ge(2)/Si(2)	3 <i>d</i>	0.27(2)	0.05(1)	0.579(9)	0.38/0.62
Ge(3)/Si(3)	3 <i>d</i>	0.28(1)	0.317(7)	0.873(7)	0.54/0.46
O(1) <sup>1</sup>	3 <i>d</i>	0.1895(8)	0.0443(9)	0.2251(6)	1
O(2) <sup>1</sup>	3 <i>d</i>	0.357(1)	0.511(1)	0.8920(8)	1
O(3) <sup>1</sup>	3 <i>d</i>	0.357(1)	0.5103(9)	0.5589(8)	1
O(4) <sup>1</sup>	3 <i>d</i>	0.0774(9)	0.229(1)	0.8814(9)	1
O(5) <sup>1</sup>	3 <i>d</i>	0.0772(9)	0.229(1)	0.5684(9)	1
O(6) <sup>1</sup>	3 <i>d</i>	0.247(1)	0.410(1)	0.225(1)	1
O(7) <sup>1</sup>	3 <i>d</i>	0.013(1)	0.4115(9)	0.1006(8)	1
O(8) <sup>1</sup>	3 <i>d</i>	0.342(1)	0.2449(9)	0.4645(8)	1
O(9) <sup>1</sup>	3 <i>d</i>	0.3111(8)	0.2732(8)	0.7256(7)	1
O(10) <sup>1</sup>	3 <i>d</i>	0.340(1)	0.2449(9)	0.9855(8)	1
O(11) <sup>1</sup>	3 <i>d</i>	0.011(1)	0.4108(9)	0.3496(8)	1

<sup>1</sup>Values taken from single crystal refinement of  $\text{Pb}_5\text{Ge}_{3-x}\text{Si}_x\text{O}_{11}$  ( $x = 1.42(1)$ ).

$B_{iso}$  values were fixed to the default value (1) for the refinements.

### B.3. – Crystallographic data of $\text{Pb}_{3-x}\text{Ba}_x[\text{Ge}_2\text{O}_7]$

Table B.3.1. Atomic positions from the single crystal X-ray diffraction refinement of  $\text{Pb}_{3-x}\text{Ba}_x[\text{Ge}_2\text{O}_7]$ .

$x = 0.19(9)$	Wyckoff Position	$x/a$	$y/b$	$z/c$	Occupation	$U_{eq}$
Pb(1)	3a	$2/3$	$1/3$	0.2633(1)	0.585(3)	0.011(1)
Ba(1)	3a	$2/3$	$1/3$	0.2636(3)	0.415(3)	0.017(4)
Pb(2)	3a	$1/3$	$2/3$	0.0968(1)	0.622(4)	0.0117(9)
Ba(2)	3a	$1/3$	$2/3$	0.0962(4)	0.378(4)	0.026(4)
Pb(3)	9b	0.41991(8)	0.06777(8)	0.05160(2)	1	0.0184(1)
Pb(4)	9b	0.26540(8)	0.24647(8)	0.21822(2)	1	0.0179(1)
Pb(5)	9b	0.01891(9)	0.26580(8)	0.14198(2)	1	0.0191(2)
Pb(6)	9b	0.35249(8)	0.41917(1)	0.30869(2)	1	0.0184(2)
Pb(7)	3a	0	0	0.0213(1)	0.533(6)	0.0202(9)
Ba(7)	3a	0	0	0.0131(4)	0.467(6)	0.022(2)
Pb(8)	3a	$1/3$	$2/3$	0.0040(4)	0.256(6)	0.011(1)
Ba(8)	3a	$1/3$	$2/3$	0.0093(2)	0.744(6)	0.009(1)
Pb(9)	3a	$2/3$	$1/3$	0.1734(2)	0.633(7)	0.027(2)
Ba(9)	3a	$2/3$	$1/3$	0.1729(4)	0.367(7)	0.034(4)
Pb(10)	3a	$1/3$	$2/3$	0.18892(1)	0.291(6)	0.0098(8)
Ba(10)	3a	$1/3$	$2/3$	0.1817(3)	0.709(6)	0.030(1)
Ge(1)	9b	0.0076(2)	0.3963(2)	0.22760(5)	1	0.0129(4)
Ge(2)	9b	0.3273(2)	0.0560(2)	0.29935(5)	1	0.0150(4)
Ge(3)	9b	0.2722(2)	0.3277(2)	0.06101(5)	1	0.0121(4)
Ge(4)	9b	0.3934(2)	0.3890(2)	0.13261(5)	1	0.0140(4)
O(1)	9b	0.0702(9)	0.345(1)	0.2642(2)	1	0.013(1) <sup>1</sup>
O(2)	9b	0.321(1)	0.2679(2)	0.0975(3)	1	0.015(2) <sup>1</sup>
O(3)	9b	0.519(1)	0.130(1)	0.3049(3)	1	0.021(3) <sup>1</sup>
O(4)	9b	0.467(1)	0.191(1)	0.2246(3)	1	0.015(2) <sup>1</sup>
O(5)	9b	0.386(1)	0.524(1)	0.0577(3)	1	0.015(2) <sup>1</sup>
O(6)	9b	0.285(1)	0.470(1)	0.1386(3)	1	0.019(2) <sup>1</sup>
O(7)	9b	0.099(1)	0.353(1)	0.1953(2)	1	0.019(2) <sup>1</sup>
O(8)	9b	0.385(1)	0.107(1)	0.3324(3)	1	0.021(2) <sup>1</sup>
O(9)	9b	0.317(1)	0.238(1)	0.0285(2)	1	0.017(1) <sup>1</sup>
O(10)	9b	0.386(1)	0.284(1)	0.1663(3)	1	0.024(2) <sup>1</sup>
O(11)	9b	0.415(1)	0.474(1)	0.2371(3)	1	0.025(2) <sup>1</sup>
O(12)	9b	0.257(1)	0.173(1)	0.2980(3)	1	0.018(1) <sup>1</sup>
O(13)	9b	0.5850(9)	0.5130(9)	0.1322(2)	1	0.015(1) <sup>1</sup>
O(14)	9b	0.081(1)	0.276(1)	0.0693(3)	1	0.023(2) <sup>1</sup>

<sup>1</sup> Value was treated isotropically during refinement.

Table B.3.2. Anisotropic displacement parameters from the single crystal refinement of  $\text{Pb}_{3-x}\text{Ba}_x[\text{Ge}_2\text{O}_7]$ .

$x = 0.19(9)$	$U_{11}$	$U_{22}$	$U_{33}$	$U_{23}$	$U_{13}$	$U_{12}$	$U_{eq}$
Pb(1)	0.010(1)	$U_{11}$	0.013(2)	0	0	0.0052(6)	0.011(1)
Ba(1)	0.026(4)	$U_{11}$	0.001(4)	0	0	0.013(2)	0.017(4)
Pb(2)	0.013(1)	$U_{11}$	0.010(1)	0	0	0.0063(7)	0.0117(9)
Ba(2)	0.023(6)	$U_{11}$	0.032(8)	0	0	0.012(3)	0.026(4)
Pb(3)	0.0180(3)	0.0159(3)	0.0208(4)	-0.0011(3)	0.0004(3)	0.0082(3)	0.0184(1)
Pb(4)	0.0166(3)	0.0138(3)	0.0183(3)	0.0003(3)	0.0010(3)	0.0039(2)	0.0179(1)
Pb(5)	0.0157(3)	0.0161(3)	0.0243(4)	0.0035(3)	-0.0001(3)	0.0070(2)	0.0191(2)
Pb(6)	0.0150(3)	0.0202(3)	0.0215(4)	0.0010(3)	-0.0010(3)	0.0098(3)	0.0184(2)
Pb(7)	0.0214(9)	$U_{11}$	0.018(2)	0	0	0.0107(4)	0.0202(9)
Ba(7)	0.015(1)	$U_{11}$	0.035(5)	0	0	0.0075(7)	0.022(2)
Pb(8)	0.007(2)	$U_{11}$	0.013(3)	0	0	0.0033(8)	0.011(1)
Ba(8)	0.023(2)	$U_{11}$	0.036(4)	0	0	0.0115(8)	0.009(1)
Pb(9)	0.0150(9)	$U_{11}$	0.048(3)	0	0	0.0075(4)	0.027(2)
Ba(9)	0.045(5)	$U_{11}$	0.013(4)	0	0	0.022(2)	0.034(4)
Pb(10)	0.012(1)	$U_{11}$	0.006(2)	0	0	0.0058(6)	0.0098(8)
Ba(10)	0.023(1)	$U_{11}$	0.043(3)	0	0	0.0117(7)	0.030(1)
Ge(1)	0.0141(8)	0.0124(7)	0.0101(9)	0.0012(7)	0.0020(7)	0.0051(6)	0.0129(4)
Ge(2)	0.0135(8)	0.0181(9)	0.0093(9)	0.0007(7)	-0.0024(7)	0.0048(7)	0.0150(4)
Ge(3)	0.0158(8)	0.0091(7)	0.0116(9)	-0.0011(6)	-0.0016(7)	0.0063(6)	0.0121(4)
Ge(4)	0.0176(9)	0.0166(9)	0.0111(9)	-0.0042(7)	-0.0027(7)	0.0111(8)	0.0140(4)

Table B.3.3. Atomic positions from the powder X-ray diffraction refinement of  $\text{Pb}_{3-x}\text{Ba}_x[\text{Ge}_2\text{O}_7]$ .

$x = 0.19(9)$	Wyckoff Position	$x/a$	$y/b$	$z/c$	Occupation
Pb(1)/Ba(1)	$3a$	$2/3$	$1/3$	0.260(1)	0.18852/0.1448
Pb(2)/Ba(2)	$3a$	$1/3$	$2/3$	0.093(1)	0.19546/0.13786
Pb(3)	$9b$	0.417(2)	0.066(2)	0.0465(5)	1
Pb(4)	$9b$	0.275(1)	0.245(2)	0.2151(5)	1
Pb(5)	$9b$	0.018(2)	0.259(1)	0.1383(5)	1
Pb(6)	$9b$	0.345(2)	0.414(2)	0.3048(5)	1
Pb(7)	$3a$	0	0	0.014(1)	0.19455
Ba(7)	$3a$	0	0	0.1079(9)	0.13878
Pb(8)/Pb(8)	$3a$	$1/3$	$2/3$	0.003(1)	0.006421/0.2691
Pb(9)/Ba(9)	$3a$	$2/3$	$1/3$	0.1720(7)	0.19029/0.17329
Pb(10)/Ba(10)	$3a$	$1/3$	$2/3$	0.1843(8)	0.10743/0.22588
Ge(1)	$9b$	0.009(4)	0.392(5)	0.223(1)	1
Ge(2)	$9b$	0.314(3)	0.038(3)	0.2973(9)	1
Ge(3)	$9b$	0.281(3)	0.339(3)	0.0603(8)	1
Ge(4)	$9b$	0.402(3)	0.403(3)	0.130(1)	1
O(1) <sup>1</sup>	$9b$	0.0702(9)	0.345(1)	0.2642(2)	1
O(2) <sup>1</sup>	$9b$	0.321(1)	0.2679(2)	0.0975(3)	1
O(3) <sup>1</sup>	$9b$	0.519(1)	0.130(1)	0.3049(3)	1
O(4) <sup>1</sup>	$9b$	0.467(1)	0.191(1)	0.2246(3)	1
O(5) <sup>1</sup>	$9b$	0.386(1)	0.524(1)	0.0577(3)	1
O(6) <sup>1</sup>	$9b$	0.285(1)	0.470(1)	0.1386(3)	1
O(7) <sup>1</sup>	$9b$	0.099(1)	0.353(1)	0.1953(2)	1
O(8) <sup>1</sup>	$9b$	0.385(1)	0.107(1)	0.3324(3)	1
O(9) <sup>1</sup>	$9b$	0.317(1)	0.238(1)	0.0285(2)	1
O(10) <sup>1</sup>	$9b$	0.386(1)	0.284(1)	0.1663(3)	1
O(11) <sup>1</sup>	$9b$	0.415(1)	0.474(1)	0.2371(3)	1
O(12) <sup>1</sup>	$9b$	0.257(1)	0.173(1)	0.2980(3)	1
O(13) <sup>1</sup>	$9b$	0.5850(9)	0.5130(9)	0.1322(2)	1
O(14) <sup>1</sup>	$9b$	0.081(1)	0.276(1)	0.0693(3)	1

<sup>1</sup>Values taken from single crystal refinement of  $\text{Pb}_{3-x}\text{Ba}_x[\text{Ge}_2\text{O}_7]$ .

$B_{\text{iso}}$  values were fixed to the default value (1) for the refinements.

## C – Synthesis and crystallographic data of $\text{Sr}_{2-x}\text{Ni}_x\text{N}$

The phase  $\text{Sr}_{2-x}\text{Ni}_x\text{N}$  was accidentally found while attempting to produce a more Ni rich phase of  $\text{Sr}_2[(\text{Li}_{1-x}\text{Ni}_x)\text{Ni}_2\text{N}_2]$ . This particular compound is placed in the appendix of this doctoral thesis, since further characterisation needs to be conducted, as well as determining the reproducibility of this phase.

A mixture of  $\alpha\text{-Li}_3\text{N}$  (0.021 g, 0.603 mmol), prepared using the method seen in Chapter 2.1., elemental Sr (0.041 g, 0.468 mmol), Ni powder (0.080 g, 1.363 mmol) and  $\text{Sr}(\text{N}_3)_2$  (0.018 g, 0.105 mmol) were mixed and filled in a Ni ampoule, along with elemental Na (0.120 g) as a fluxing agent. The ampoule was then sealed by an arc welder and inserted into a fused silica tube, which was then heated, under Ar flow, to 1073 K and allowed to cool at a controlled rate of 1 K/h. After opening the ampoule, the Na flux was removed using liquid ammonia leaving a sample containing a mixture  $\text{Sr}_2\text{N}$  and metallic dark blue plates, which were identified as  $\text{Sr}_{2-x}\text{Ni}_x\text{N}$ .

A metallic dark blue plate was measured using single crystal X-ray diffraction and was indexed in a monoclinic unit cell ( $a = 6.6228(4) \text{ \AA}$ ,  $b = 3.8221(2) \text{ \AA}$ ,  $c = 6.6701(4) \text{ \AA}$ ,  $\beta = 109.317(4)^\circ$ ). Refinement single crystal structural data showed the structure crystallises in the space group  $P2_1/m$  (No. 11) (Tables C.1., C.2. and C.3.), which is a subgroup of the space group of the anti- $\text{CdCl}_2$ -type  $\text{Sr}_2\text{N}$  ( $R\bar{3}m$ , No. 166) and results in a splitting of the Sr position. Confirmation of the Ni content was conducted by energy dispersive spectroscopy (Table C.4.), which showed a small composition gradient for  $\text{Sr}_{2-x}\text{Ni}_x\text{N}$  ( $0.62(2) \leq x \leq 0.64(1)$ ). There is a clear discrepancy between the Ni content determined by refinement single crystal structural data and energy dispersive spectroscopy. Different crystals were used for each method, which implies that varying compositions are present between each crystal in the sample.

Table C.1. Single crystal structural refinement of Sr<sub>2-x</sub>Ni<sub>x</sub>N.

Crystal System	Monoclinic
Space Group	<i>P2<sub>1</sub>/m</i>
<i>Z</i>	4
<i>a</i> /Å	6.6228(4)
<i>b</i> /Å	3.8221(2)
<i>c</i> /Å	6.6701(4)
$\beta$ /°	109.317(4)
$\rho_{\text{calc}}/\text{gcm}^{-3}$	3.643
Volume <i>V</i> /Å <sup>3</sup>	159.33
Measurement temperature/K	293(2)
Index range	$-8 \leq h \leq 8$ $-4 \leq k \leq 4$ $-8 \leq l \leq 8$
Max. $2\theta$ /deg	55.05
<i>F</i> (000)	156.0
$\mu/\text{mm}^{-1}$	27.75
Measured reflections	4542
Observed reflections	414
Refined parameters	22
$R_{\text{int}}/R_{\sigma}$	12.83/0.0437
$R_1/wR_2$	0.0471/0.1130
<i>Goof</i>	1.273
Remaining electron density (max/min)/Å <sup>-3</sup>	1.54/-1.09
BASF	0.08(3)
Twin matrix	010 0-10 100

Table C.2. Atomic positions for the refinement of Sr<sub>2-x</sub>Ni<sub>x</sub>N.

	Wyckoff Position	$x/a$	$y/b$	$z/c$	Occupation	$U_{eq}$
Sr(1)/Ni(1)	2e	0.9880(3)	¼	0.2173(3)	0.74/0.26(3)	0.0118(9)
Sr(2)	2e	0.5103(3)	¼	0.7840(3)	1	0.0176(8)
N(1)	2e	0.247(3)	¼	0.000(3)	1	0.018(2)

Table C.3. Anisotropic displacement parameters from the refinement of the crystal structure data of Sr<sub>2-x</sub>Ni<sub>x</sub>N.

	$U_{11}$	$U_{22}$	$U_{33}$	$U_{23}$	$U_{13}$	$U_{12}$	$U_{eq}$
Sr(1)/Ni(1)	0.011(1)	0.013(1)	0.015(1)	0	0.0083(8)	0	0.0118(9)
Sr(2)	0.020(1)	0.014(1)	0.017(1)	0	0.0044(8)	0	0.0176(8)
N(1)	0.017(5)	0.014(5)	0.025(6)	0	0.008(4)	0	0.018(2)

Table C.4. Relative values from energy dispersive spectroscopy of Sr and Ni for samples of Sr<sub>2-x</sub>Ni<sub>x</sub>N.

	w(Sr)/%	w(Ni)/%	$x$
1	37.44±0.22	16.88±0.33	0.62±0.02
2	39.55±0.18	18.69±0.20	0.64±0.01
3	38.94±0.16	18.03±0.14	0.633±0.007





## Publications

- W. P. Clark, S. Steinberg, R. Dronskowski, C. McCammon, I. Kuppenko, M. Bykov, L. Dubrovinsky, L. G. Akselrud, U. Schwarz and R. Niewa, "High-Pressure NiAs-Type Modification of FeN", *Angew. Chem. Int. Ed.*, **2017**, 56, 25, 7302–7306., "Eine NiAs-artige Hochdruckmodifikation von FeN", *Angew. Chem.*, 129, 25, 7408–7412.
  - Also featured in "Extreme Magnetism" by Jon Cartwright, ESRF news, No. 78 and included as a highlight of research for the year 2017 in the Annual GDCH trend review and Jülich Aachen Research Alliance annual report.
- W. P. Clark and R. Niewa, "Li and Co ordering in the nitridocobaltate(I)  $SrLi_2\{Li[CoN_2]\}$ ", *Crystals*, **2018**, 8, 7, 268–277.
- U. Schwarz, K. Guo, W. P. Clark, U. Burkhardt, M. Bobnar, R. Castillo, L. Akselrud and R. Niewa, "Ferromagnetic  $\epsilon$ -Fe<sub>2</sub>MnN: High-pressure synthesis, Hardness and Magnetic Properties", *Materials*, **2019**, 12, 12, 1993–2002.
- W. P. Clark and R. Niewa, "Synthesis and characterisation of the Nitridocuprate(I) Nitride Carbodiimide ( $Sr_6N$ )[CuN<sub>2</sub>][CN<sub>2</sub>]", *Z. Anorg. Allg. Chem.* **2020**. 646, 114–119.
- W. P. Clark, A. Köhn and R. Niewa, "The Quasi-Binary Acetonitriletriide  $Sr_3[C_2N]_2$ ", *Angew. Chem. Int. Ed.*, **2020**, 59, 1, 339–342., "Das quasi-binäre Acetonitriltriid  $Sr_3[C_2N]_2$ ", *Angew. Chem.*, **2020**, 132, 1, 347–350.

## Publications in preparation

- W. P. Clark, P. Höhn and R. Niewa, "Synthesis and structure of novel nitride series  $Sr_2(Li_{1-x}Ni_x)Ni_2N_2$ ", **2020**.

## Conference contributions

- W. P. Clark, S. Steinberg, R. Dronskowski, C. McCammon, I. Kупenko, M. Bykov, L. Dubrovinsky, L. G. Akselrud, U. Schwarz and R. Niewa: "*Novel High-pressure NiAs-Type Modification of FeN*", poster presentation at the 25<sup>th</sup> Annual Meeting of the German Crystallographic Society, Karlsruhe, Germany (27<sup>th</sup> – 30<sup>th</sup> March 2017).
- W. P. Clark, S. Steinberg, R. Dronskowski, C. McCammon, I. Kупenko, M. Bykov, L. Dubrovinsky, L. G. Akselrud, U. Schwarz and R. Niewa: "*Novel High-pressure NiAs-Type Modification of FeN*", poster presentation at the 16<sup>th</sup> European Conference on Solid State Chemistry, Glasgow, UK (23<sup>rd</sup> – 30<sup>th</sup> July 2017).
- W. P. Clark, K. Guo, D. Rau, U. Burkhardt, M. Bobnar, R. Castillo, L. Akselrud, R. Niewa and U. Schwarz: "*High-pressure–high-temperature synthesis, hardness and magnetic properties of the metastable ferromagnet  $\epsilon$ -Fe<sub>2</sub>MnN*", poster presentation at the 26<sup>th</sup> Annual Meeting of the German Crystallographic Society, Essen, Germany (5<sup>th</sup> – 8<sup>th</sup> March 2018).
- W. P. Clark and R. Niewa: "*Crystal structure and synthesis of SrLi<sub>2</sub>{Li[CoN<sub>2</sub>]}: a novel quaternary nitridocobaltate(I) with evidence of Li and Co ordering*", poster presentation at the 19<sup>th</sup> Vortragstagung für Anorganische Chemie der Fachgruppen Wöhler-Vereinigung und Festkörperchemie und Materialforschung in Regensburg, Germany (24<sup>th</sup> – 27<sup>th</sup> September 2018).

## PERSONAL INFORMATION

---

Name	William Peter Clark
Address	Beim Wasserturm 32, 71332 Waiblingen, Germany
Date of Birth	02/07/1991
City and country of birth	Derby, United Kingdom
Nationality	British

---

## EDUCATION

---

Since Nov. 2014	PhD Thesis research in solid state chemistry, which a focus on iron nitrides and ternary and higher nitrides (Supervised by Prof. Dr. R. Niewa) at the Institute for Inorganic Chemistry, University of Stuttgart.
March 2017	Attended a workshop on X-ray, synchrotron and neutron diffraction at KIT Karlsruhe, including a tour of the synchrotron facility ANKA
June 2014	Graduated from the University of Hull with Master of Chemistry degree
October 2013 – June 2014	Master Thesis: "Ionic Substitution in the $A_2BX_4$ -type Structure" (Supervised by Dr. M. G. Francesconi) at the Inorganic chemistry department, University of Hull, UK
September 2010 – June 2014	Undergraduate Chemistry studies at the University of Hull, UK
September 2007 – June 2009	A-Levels at South East Derbyshire College, UK
September 2002 – June 2007	GCSE level education at Bennerley Grammar School, UK

---

## EMPLOYMENT

---

Since Nov. 2014	Scientific assistant for practical courses at the Institute for Inorganic Chemistry, University of Stuttgart
August 2009 – August 2010	Teacher at St. Ignatius Secondary School, Lethem, Guyana, South America

---